UNIVERSITY OF GENOA

POLYTECHNIC SCHOOL

DIME

Department of Mechanical, Energy, Management

and Transportation Engineering

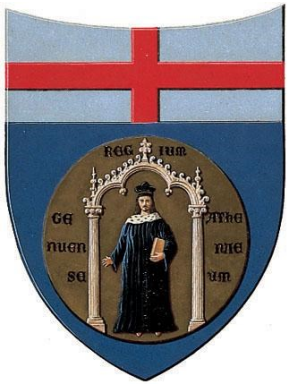

RESEARCH DOCTORATE THESIS - XXXIII CYCLE

MACHINE AND SYSTEMS ENGINEERING FOR ENERGY,
THE ENVIRONMENT AND TRANSPORT
CURRICULUM
MACHINE AND SYSTEMS ENGINEERING FOR ENERGY,
THE ENVIRONMENT AND PROPULSION

Application of Uncertainty Quantification techniques to CFD simulation of twin entry radial turbines

Candidate:

Andrea Ottonello

Supervisor:

Chiar.mo Prof. Ing. Carlo Cravero

May 2021

Applicazione delle tecniche di Uncertainty Quantification alla simulazione CFD di turbine radiali twin entry

Sommario

L'argomento principale della tesi è l'applicazione delle tecniche di quantificazione dell'incertezza (UQ) alla simulazione numerica (CFD) di turbine radiali twin entry impiegate nella turbosovralimentazione automobilistica.
Lo studio approfondito di questo tipo di turbomacchine è affrontato nel capitolo 3, finalizzato alla comprensione dei principali parametri che caratterizzano e influenzano le prestazioni fluidodinamiche delle turbine twin scroll. Il capitolo 4 tratta di una piattaforma per l'analisi UQ sviluppata internamente tramite il set di strumenti open source 'Dakota'. La piattaforma è stata testata dapprima su un caso di interesse industriale, ovvero un ugello de Laval supersonico (capitolo 5); l'analisi ha evidenziato l'utilizzo pratico delle tecniche di quantificazione dell'incertezza nella previsione delle prestazioni di un ugello affetto da condizioni di fuori progetto con complessità fluidodinamica dovuta alla forte non linearità.
L'esperienza maturata con l'approccio UQ ha agevolato l'identificazione di metodi idonei per applicare la propagazione dell'incertezza alla simulazione CFD di turbine radiali twin scroll (capitolo 6). In tal caso sono state studiate e messe in pratica diverse tecniche di quantificazione dell'incertezza al fine di acquisire un'esperienza approfondita sull'attuale stato dell'arte. Il confronto dei risultati ottenuti dai diversi approcci e la discussione dei pro e dei contro relativi a ciascuna tecnica hanno portato a conclusioni interessanti, che vengono proposte come linee guida per future applicazioni di quantificazione dell'incertezza alla simulazione CFD delle turbine radiali.
L'integrazione di modelli e metodologie UQ, oggi utilizzati solo da alcuni centri di ricerca accademica, con solutori CFD commerciali consolidati ha permesso di raggiungere l'obiettivo finale della tesi di dottorato: dimostrare all'industria l'elevato potenziale delle tecniche UQ nel migliorare, attraverso distribuzioni di probabilità, la previsione delle prestazioni relative ad un componente soggetto a diverse fonti di incertezza.
Lo scopo dell'attività di ricerca consiste pertanto nel fornire ai progettisti dati prestazionali associati a margini di incertezza che consentano di correlare meglio simulazione e applicazione reale.

Per accordi di riservatezza, i parametri geometrici relativi alla turbina twin entry in oggetto sono forniti adimensionali, i dati sensibili sugli assi dei grafici sono stati omessi e nelle figure si è reso necessario eliminare le legende dei contours ed ogni eventuale riferimento dimensionale.

Application of Uncertainty Quantification techniques to CFD simulation of twin entry radial turbines

Abstract

The main topic of the thesis is the application of uncertainty quantification (UQ) techniques to the numerical simulation (CFD) of twin entry radial turbines used in automotive turbocharging.
The detailed study of this type of turbomachinery is addressed in chapter 3, aimed at understanding the main parameters which characterize and influence the fluid dynamic performance of twin scroll turbines. Chapter 4 deals with the development of an in-house platform for UQ analysis through 'Dakota' open source toolset. The platform was first tested on a test case of industrial interest, i.e. a supersonic de Laval nozzle (chapter 5); the analysis highlighted the practical use of uncertainty quantification techniques in predicting the performance of a nozzle affected by off-design conditions with fluid dynamic complexity due to strong non-linearity.
The experience gained with the UQ approach facilitated the identification of suitable methods for applying the uncertainty propagation to the CFD simulation of twin entry radial turbines (chapter 6). In this case different uncertainty quantification techniques have been investigated and put into practice in order to acquire in-depth experience on the current state of the art. The comparison of the results coming from the different approaches and the discussion of the pros and cons related to each technique led to interesting conclusions, which are proposed as guidelines for future uncertainty quantification applications to the CFD simulation of radial turbines.
The integration of UQ models and methodologies, today used only by some academic research centers, with well established commercial CFD solvers allowed to achieve the final goal of the doctoral thesis: to demonstrate to industry the high potential of UQ techniques in improving, through probability distributions, the prediction of the performance relating to a component subject to different sources of uncertainty.
The purpose of the research activity is therefore to provide designers with performance data associated with margins of uncertainty that allow to better correlate simulation and real application.

Due to confidentiality agreements, geometrical parameters concerning the studied twin entry radial turbine are provided dimensionless, confidential data on axes of graphs are omitted and legends of the contours as well as any dimensional reference have been shadowed.

Acknowledgments

I want to dedicate this doctoral thesis to my parents Giuseppina and Giovanni, my sister Valentina and my fiancée Erika, you are my true strength.

Thank you mom for the love and time you have always dedicated to me, thank you dad for the work culture you taught me every day and thanks sister for the precious advice and affection that you have never let me lack.
At the beginning of this PhD I was lucky enough to meet Erika, a wonderful woman who has been able to understand my passion for research work and above all how much time this passion requires to be cultivated to the level I want.

Among the personal affections, I also want to dedicate this thesis to my grandfathers Carlo and Antonio, my aunt Adriana and my grandmothers Maria and Mina.
A special dedication goes to my giant dog Thor and my little cats Missi, Max and Pepperly.
I can't forget to thank my sister's husband, Paolo, my girlfriend's family, Mauro, Tiziana and Stefano, and finally my friends, Andrea and Elena, with whom I spent unforgettable moments of fun and serenity.

Among the people I have worked with, I want to mention my dear colleagues Davide, Emanuele, Gabriele, Marcello and Stephane, each of whom taught me something different during this exciting experience.
I am very grateful to the referees of the doctoral thesis, Dr. Vittorio Michelassi and Prof. Alessandro Corsini, who offered their precious scientific contribution to improve this thesis.

Finally I want to express my gratitude to my academic mentor Professor Carlo Cravero, who supervised the development of the thesis and directed my research activity during the PhD, allowing me to acquire new skills and form scientific experience in an international context.
I will always be grateful to Professor Cravero, first of all a special person with whom I had the privilege of collaborating from the Bachelor's and Master's degrees up to the Doctorate.

"Non scholae sed vitae discimus"

Contents

Chapter 1

Twin scroll radial turbines: literature overview

Inflow radial turbines are gaining an increasing importance in several engineering applications because of the possibility to implement very compact solutions with high specific power. Today this kind of turbomachinery is extensively used for distributed power generation with micro-gas turbines and as a driving machine in turbochargers for automotive applications.
Turbocharging is a well established technique for increasing internal combustion engines specific power and consequent downsizing of the power unit: on the one hand it allows to reduce engine cylinders overall volume in order to decrease specific fuel consumption and greenhouse gas emissions, on the other hand it permits to keep high performance and specific power, key factors in the racing sector. In this scenario the performance evaluation and flow characterization of the turbine represent a basic prerequisite for a correct matching with the internal combustion engine.
This chapter summarizes some literature information necessary to characterize radial turbines operation, focusing then on the 'twin entry' turbines, which will be the main research subject of the thesis.

1.1. Pulse turbocharging

IFR turbines are widely used for turbocharging in automotive field: the air entering the intake manifold is compressed by a centrifugal impeller driven by a radial turbine placed on the same axis (Fig. 1.1); this practice aims to optimize the quantity of charge introduced into the cylinder per engine cycle, leading to an improvement in the ICE performance.
Among possible turbocharging schemes, pulse turbocharging is a convenient solution for the possibility to take advantage of the pressure fluctuations generated by the periodic opening of the engine discharge valves through exhaust manifolds characterized by small diameters and lengths (low damping volume). Following the impulse turbocharging scheme [1], the phenomena of propagation and reflection of pressure waves are exploited:

1) in the spontaneous discharge phase ('blowdown'), immediately after the discharge valve opening. The goal is to keep the p_d (discharge pressure) greater than the p_{atm} (atmospheric pressure);
2) during the crossing phase, when intake and exhaust valves are open simultaneously, the target is instead $p_d < p_{atm}$.

Following the two points just exposed, it is possible to take advantage of the compression wave generated by the opening of the discharge valve in the first phase (1) and then to exploit its reflection at the open end of the exhaust manifold in a wave of the opposite type (i.e. expansion): in fact in the second phase (2) if the expansion wave reaches the discharge valve before its closing the p_d is reduced, decreasing the work required by the piston during the forced unloading of the cylinder.
This technique requires a careful tuning of the turbo-ICE matching because introduces issues related to the possible negative interaction of pressure waves coming from different cylinders and to periods of zero exhaust gas mass flow, which can jeopardize the positive effect of pulsating flow. Considering that the mass flow passing through the turbine in pulsating condition is lower than in the stationary case, in order to make the gas supply to the turbine as homogeneous as possible (thus optimizing the performance of the turbine), it is important to group the cylinders gas exhaust into different manifolds.

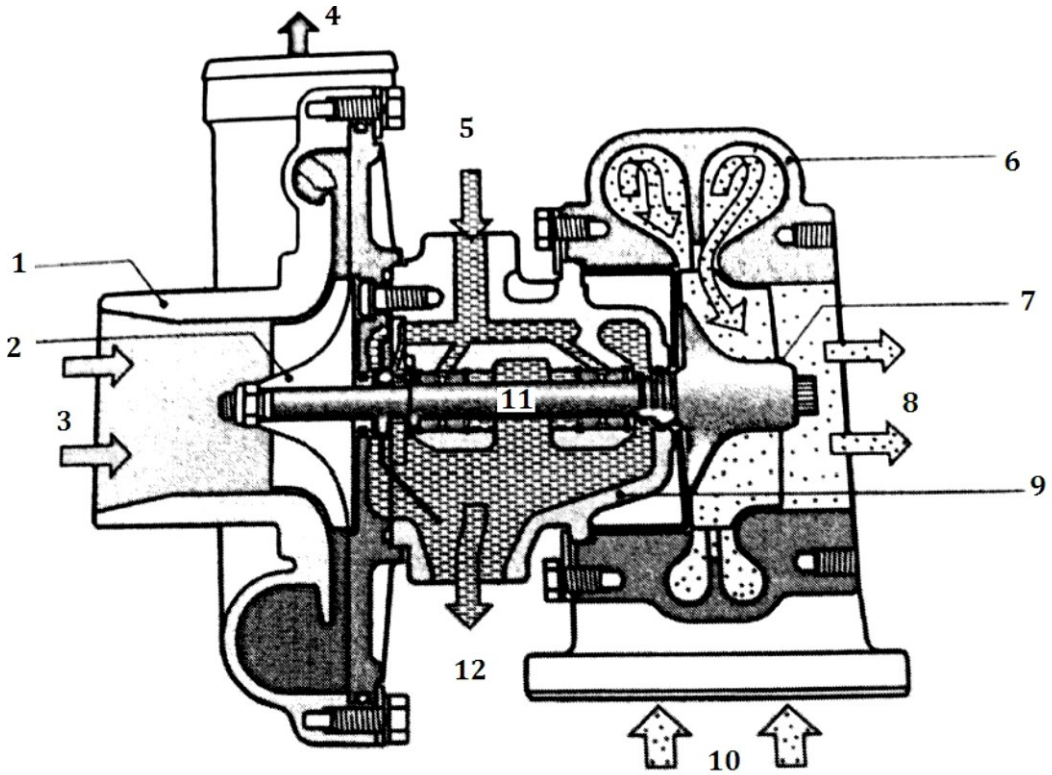

Fig. 1.1 – Meridian section of an impulse turbocharger. The numbers in figure respectively identify: 1. centrifugal compressor casing; 2. centrifugal impeller; 3. air inlet; 4. compressed air outlet; 5. lubricating oil inlet; 6. centripetal turbine casing; 7. turbine impeller; 8. exhaust gas outlet; 9. case for bearing housing; 10. exhaust gas inlet into the turbine; 11. connecting shaft; 12. lubricating oil outlet [2]

The main problem in pulse turbocharging is the choice of which cylinders have to be connected together. With reference to the distribution diagram of a four stroke engine, the opening advance angle of the discharge valve is typically ϑ_{od} = 40 ° ÷ 70 °, while the closing delay angle of the discharge valve ϑ_{cd}= 40 ° ÷ 60 °; therefore the discharge phase has an angular extension of approximately $\Delta\vartheta_d$ = 260 ° ÷ 310 °.
In order to obtain a correct washing of each cylinder which discharges into the same manifold, it is necessary that the blowdown pressure wave (spontaneous discharge) of the next cylinder according to the firing sequence reaches the cylinder discharge valve in washing phase only after its closure, otherwise a high pressure at the discharge of the cylinder could be registered, preventing the correct charge replacement.
The actual angular phase shift between two cylinders which discharge the exhaust gases in the same manifold may be less than the values of $\Delta\vartheta_d$ indicated above, mainly because there is a delay between the beginning of the discharge valve opening and the pressure increase in the manifold and also because a certain interval of time is required for the perturbation to propagate from the cylinder in discharge phase to the one in washing phase.
The non-interference condition will be respected if the ignition intervals between cylinders which discharge into the same manifold are greater than or equal to 240 °.
In order to provide a practical example, the case of a six-cylinder engine can be considered: the typical configuration is to divide the exhaust manifolds into two groups of three, each of which feeds only one of the two inlets of the turbine volute. If the engine operating cycle covers 720° of crank angle and there are 6 cylinders, the ignition interval

between a cylinder and the next one is $\Delta\vartheta_{firing} = (720°)/6 = 120°$. Therefore in this case to avoid interference between the respective washing phases it would be sufficient to connect the cylinders which have an angular phase shift of 240° according to the firing sequence. The superimposition of three equally spaced pressure pulses during an engine cycle generally provides the best condition, minimizing the periods of zero mass flow and ensuring higher average turbine efficiency over an engine cycle.

Pulse turbocharging often leads to the adoption of peculiar turbine volute geometries in order to preserve the pressure pulsations of the exhaust gas inside the ICE manifolds. A fundamental distinction between the two main types of double inlet turbines is made on the basis of the type of flow subdivision:

- 'double entry' turbines have a volute that splits the exhaust gas flow from the ICE manifolds so that each volute inlet feeds a different angular sector of the rotor in circumferential direction: e.g. 0-180° for 'outer entry' and 180-360° for 'inner entry', as in Fig. 1.2a. These sectors can be easily identified considering the volute tongues;
- 'twin entry' or 'twin scroll' turbines are characterized by a volute which presents a single septum divider (called 'divider wall' in Fig. 1.2b) that runs on the entire perimeter of the casing so that each volute inlet feeds the entire annular section at impeller inlet, but only within a certain percentage of the channel height: for example hub scroll from the hub (0%) up to midspan (50%) while shroud scroll from 50% of the span up to the shroud (100%).

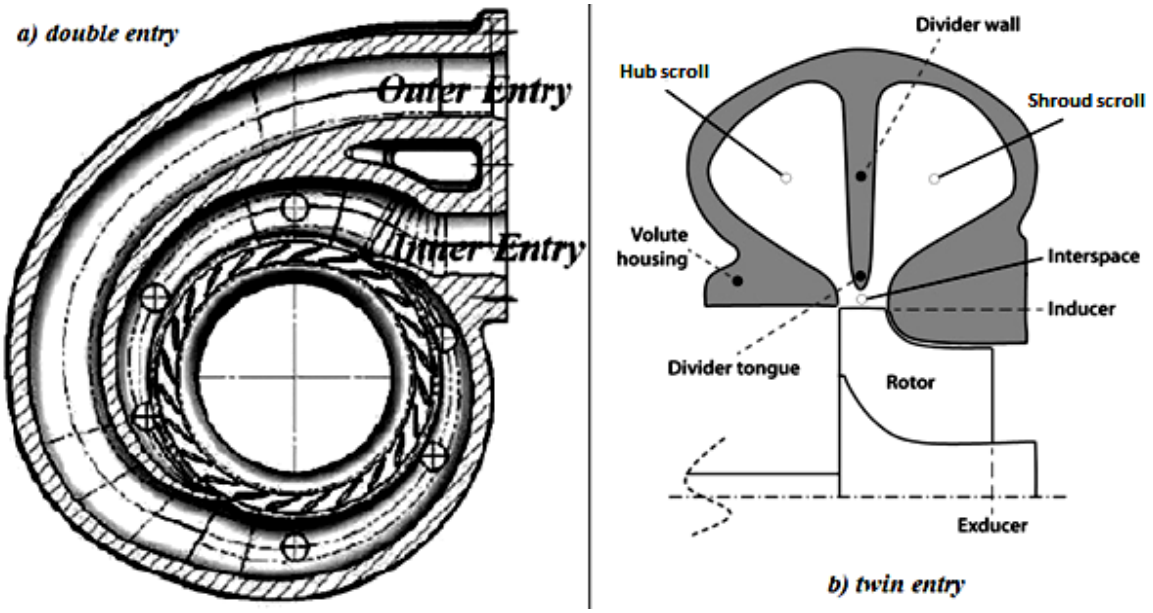

Fig. 1.2 – Different designs of double inlet radial turbines [3,4]

Both types of double inlet volute described above serve the purpose of preserving the energy of the exhaust gases and make easier the charge replacement in the engine cylinders. However, 'twin entry' turbines are more popular among designers and manufacturers for simpler and less expensive design than 'double entry' ones.
The next paragraph is dedicated to the description of a generic radial turbine stage from a theoretical point of view.

1.2. Radial turbines: basic concepts on each component

This section summarizes the operating principles of a radial turbine, analyzing separately each component: volute, rotor and diffuser.

1.2.1. Volute

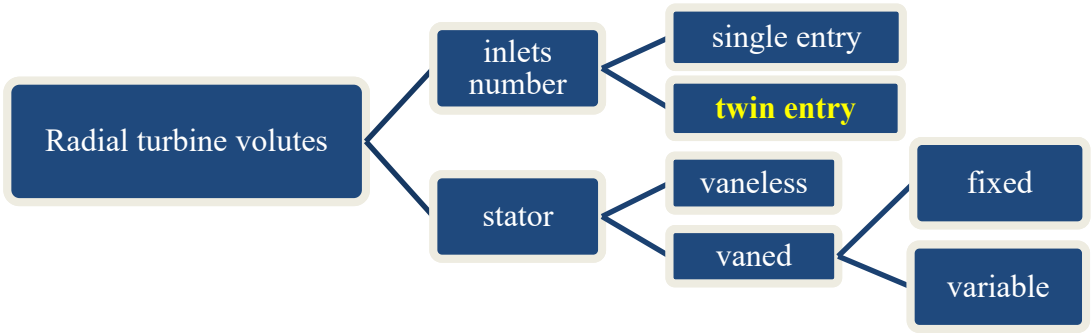

Fig. 1.3 – Possible design choices for a radial turbine volute

The flow enters the volute with a direction that is roughly tangential to the rotor (see Fig. 1.4). Crossing the volute, the exhaust gases experience a pressure gradient in radial direction that directs the flow towards the impeller, while a high circumferential velocity component is preserved to distribute it peripherally. In case of vaneless distributor, the flow is also subject to pressure pulsations linked to the periodic passage of the rotor blades. The portion of flow that sweeps the entire channel around the rotor in circumferential direction must return and mix with the mainstream flow at the volute tongue.

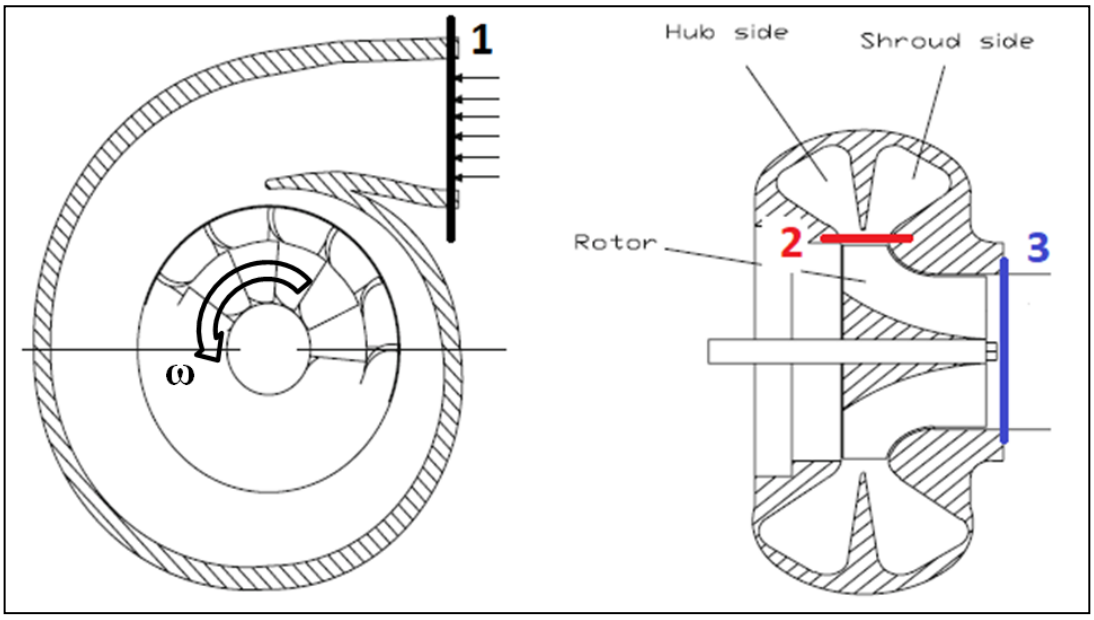

Fig. 1.4 – Cross section of the twin entry radial inflow turbine [5]

The simplest volute flow models simulate only the through flow and the radial velocity components without taking into account the secondary flows or the mixing of the flow re-

entering the mainstream under the tongue.
In an "ideal" volute (no losses) the angular momentum must be preserved, hence the flow will be a free vortex centered on the turbine axis:

$$rc_\theta = cost. \tag{1.1}$$

The volute inlet conditions are often set by external limits, such as the project of the ICE exhaust manifolds; to understand its influence on the design of the scrolls, it is necessary to apply equation (1.1) between control sections 1 and 2 (volute inlet and outlet in Fig. 1.4):

$$c_2 \sin\alpha_2 \, r_2 = c_1 \sin\alpha_1 \, r_1 \tag{1.2}$$

Assuming that the volute is adiabatic, there's no work exchange in the stator hence $dh_0 = 0$. Given that $T_{01} = T_{02}$, the ratio r_1/r_2 can be expressed as below:

$$\frac{r_1}{r_2} = \frac{\sin\alpha_2}{\sin\alpha_1} \frac{c_2}{\sqrt{kRT_2}} \frac{\sqrt{kRT_1}}{c_1} \frac{\sqrt{T_2}}{\sqrt{T_1}} \frac{\sqrt{T_{01}}}{\sqrt{T_{02}}} \tag{1.3}$$

So remembering from gas dynamics theory that $T_0/T = f(M,k)$:

$$\frac{r_1}{r_2} = \frac{M_2 \sin\alpha_2}{M_1 \sin\alpha_1} \left\{ \frac{1 + \left[\frac{k-1}{2}\right] {M_1}^2}{1 + \left[\frac{k-1}{2}\right] {M_2}^2} \right\}^{1/2} \tag{1.4}$$

The last equation allows to derive the ratio between the inlet and outlet volute radii for each specific inlet Mach number and flow angle.
Rather compact scrolls (therefore small r_1/r_2 ratios) require higher inlet Mach numbers as shown in Fig. 1.5; this inevitably leads to additional frictional losses in the volute due to the increasing flow speed levels.

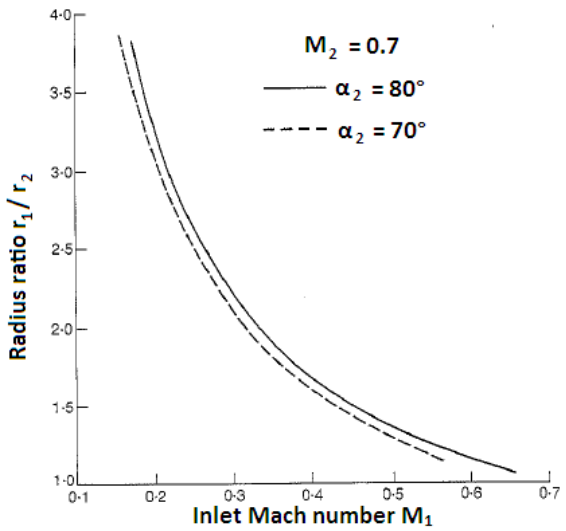

Fig. 1.5 – Inlet Mach number effect on volute area and radius ratio [6]

The volute area ratio can be derived through the application of the continuity equation. The non-dimensional mass flow rates at volute inlet and outlet are respectively given by:

$$\theta_1 = \left\{\sin\alpha_1 \, M_1\left[1 + 0.5(k-1){M_1}^2\right]^{-(k+1)/2(k-1)}\right\} \tag{1.5}$$

$$\theta_2 = \left\{\cos\alpha_2 \, M_2\left[1 + 0.5(k-1){M_2}^2\right]^{-(k+1)/2(k-1)}\right\} \tag{1.6}$$

The volute inlet to exit area ratio may then be written as:

$$\frac{A_1}{A_2} = \frac{\theta_2}{\theta_1}\frac{p_{02}}{p_{01}} \tag{1.7}$$

In the ideal case of isentropic flow $p_{02} = p_{01}$ and the volute area ratio can be determined from equation (1.7) directly. In a real case instead, a stator efficiency (including entry duct, volute and nozzle blades if present) must be specified and used to calculate the total pressure ratio. In practice, a reduction of the volute efficiency from 100% (ideal case) to 90% (a reasonable real case) has a negligible effect on the results.
For what concerns volute outlet conditions, if the mass flow rate and therefore the flow velocity are uniform around the exit periphery of the scroll, the flow angle at volute outlet is given by:

$$\tan\alpha_2 = c_{\theta 2}/c_{m2} \tag{1.8}$$

To obtain $c_{\theta 2}$, the free vortex equation between stations 1 (volute inlet) and 2 (volute outlet/rotor inlet) is applied:

$$c_{\theta 2} = (c_{\theta 1} r_1)/r_2 = (c_1 r_1)/r_2 \tag{1.9}$$

where it is assumed that at volute inlet the absolute speed is only tangential ($c_{\theta 1} = c_1$). Then the continuity equation is applied to calculate the meridian velocity:

$$c_{m2} = \dot{m}/(\rho_2 A_2) = [(\rho_1 A_1)/(\rho_2 A_2)]c_1 \tag{1.10}$$

In fact, at section 1 the mass flow rate is determined by the tangential component, while at section 2 by the meridian component (vector sum between the axial and radial velocity components). Once substituted the equations (1.9) and (1.10) in (1.8), the absolute flow angle at volute outlet can be obtained:

$$\alpha_2 = \tan^{-1}\left(\frac{\rho_2}{\rho_1}\frac{A_2}{A_1}\frac{r_1}{r_2}\right) \tag{1.11}$$

Considering a twin scroll turbine, which has two different inlets, given that the geometric quantities A_2 and r_2 are fixed by the component immediately downstream of the volute (which may be the nozzle or directly the rotor), the absolute flow angle at each branch outlet is determined uniquely by the choice of the corresponding volute inlet area and radius (the ratio ρ_2/ρ_1 has a small effect).
The flow angle of the fluid approaching the wheel has a strong influence on the mass flow swallowing capacity of the turbine and this aspect is often used by vaneless volute manufacturers to adjust the turbine for a specific application: for a given rotor a range of different volute casings (identified by an $A\ /\ r$ value) is produced.

Considering the complexity of the flow evolution in this component, there is little agreement between the designers regarding the "optimal" geometry to be adopted for the volute and the selected configuration can play a significant role in the overall performance of the turbine.
Some researchers [7] measured up to 1.5% variation in the turbine total to total efficiency due to changes made to the volute cross section profile and this is probably due to the fact that different volutes distribute the flow to the rotor in a different and non-uniform way, playing a key role on the potential work that can be extracted from the impeller.
As measured experimentally by Chappie [8], any static pressure circumferential non-uniformity at volute exit propagates right through the wheel and can also be found at the impeller exit plane; at rotor inlet these non-uniformities can promote detrimental rotor blade vibrations.
Scrimshaw and Williams [9] performed flow measurements around the outlet of a vaneless volute: three geometrically similar turbine were studied, with the same ratio between tongue clearance and rotor tip diameter (D_2), but different absolute values of clearance. In the examined cases evident changes in flow angle, static pressure and total pressure loss (especially in the region near the tongue) occurred. The static pressure increase and total pressure drop which characterize the tongue region (see Fig. 1.6 below) can be interpreted as an injector-type suction of the recirculating flow under the tongue by the main flow entering the volute, with a slowing and mixing effect. The magnitude of this "injector" effect varies with the movement of blades under the volute tongue, which can give rise to strong pressure waves at the blade passing frequency. The latter can play a remarkable role in the possible fatigue failure of the blades.

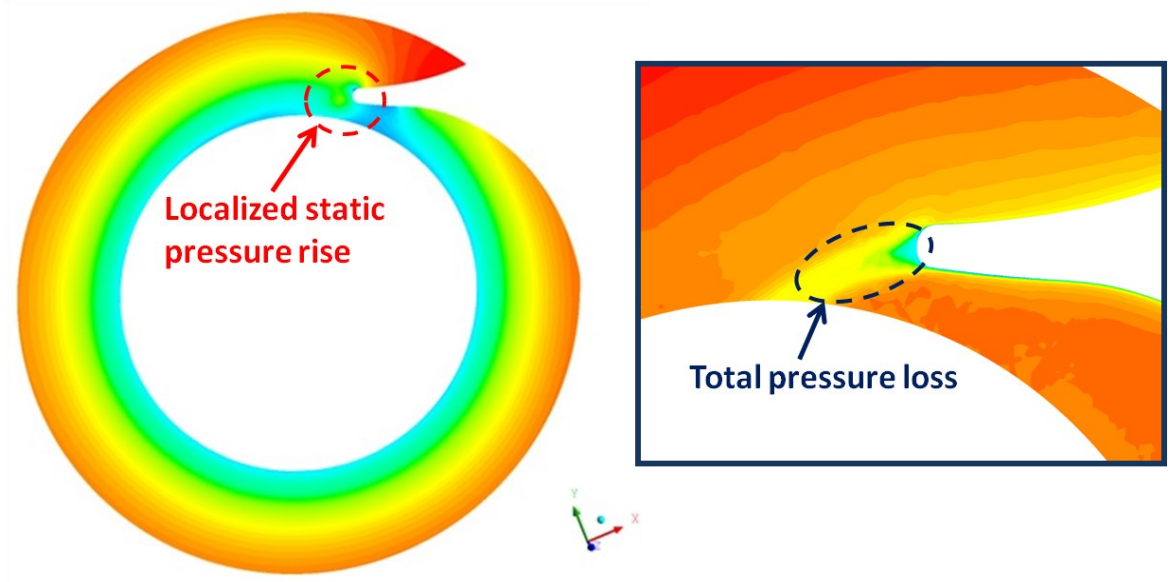

Fig. 1.6 – Static pressure contours on a front view volute cross section (on the left) and total pressure contours on an enlarged view of the tongue region (on the right)

1.2.2. Rotor

In a centripetal turbine energy is transferred from the fluid to the rotor passing from a greater radius to a smaller one. Following the principle that considers as positive the incoming heat and the work leaving the machine, for the generation of a positive work it is

necessary that the product between the peripheral and circumferential speed at wheel inlet is greater than the corresponding one at impeller outlet.
This is usually achieved by providing the flow, through the volute, with a strong tangential speed component at rotor inlet and reducing the 'absolute' (or 'stationary frame') swirl angle at the outlet. Euler's equation for turbines is written as in equation (1.12):

$$L_{2,3} = u_2 c_{\theta 2} - u_3 c_{\theta 3} \tag{1.12}$$

Typically the blade inlet (control section 2) construction angle is zero with respect to the radial direction and this design choice is dictated by two factors: the material resistance and the exhaust gas high temperatures at impeller inlet. The rotor blades are subject to high levels of stress, caused by the centrifugal force field together with a pulsating and unsteady flow of high temperature gases. Despite possible performance gains, the use of swept blades is generally avoided because of the additional stresses which result from bending.
From station 2 the rotor blades extend radially inward and turn the flow into the axial direction. The final part of the blades, called the 'exducer', is curved to remove most of the absolute tangential velocity component at wheel outlet.
The exhaust gas discharged from the impeller may have a considerable velocity (c_3) and an axial diffuser is normally placed before turbine tailpipe exit in order to recover the kinetic specific energy ($1/2\ c_3{}^2$) which would otherwise be wasted.

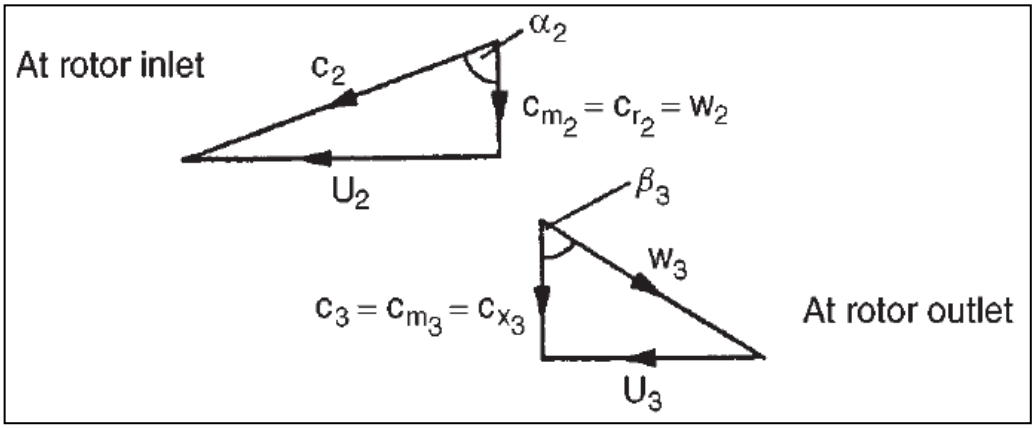

Fig. 1.7 – Velocity diagrams for a 90 [deg] inward flow radial turbine at design point [10]

In Fig. 1.7 the velocity triangles are drawn to suggest that the inlet relative velocity (w_2) is totally radial, i.e. zero incidence flow, and the absolute velocity at rotor exit (c_3) is purely axial. This configuration of the velocity triangles, popular with designers for many years, is called the "nominal design condition" [10] .

The flow reaching rotor inlet has an absolute velocity equal to c_2 and an absolute flow angle α_2 determined by the geometry of the volute and, if present, by the nozzle blades. Once the flow enters the impeller, the work extraction process is quickly accomplished with fast reduction of the absolute circumferential velocity component and peripheral speed, while the flow radius decreases. These strong speed variations correspond to a high blade loading and hence to a large pressure gradient across the passage, which tends to

move the flow from the pressure side to the suction side, contrary to the rotation direction of the impeller.
If the rotor has an angular speed equal to +ω and the viscosity of the incoming flow is neglected, the motion field between two blades is irrotational (the vorticity is zero far from the boundary layer); to preserve this state, a vortex is generated at rotor channel inlet which rotates at -ω in the relative reference, as visible in Fig. 1.8 (red arrows).

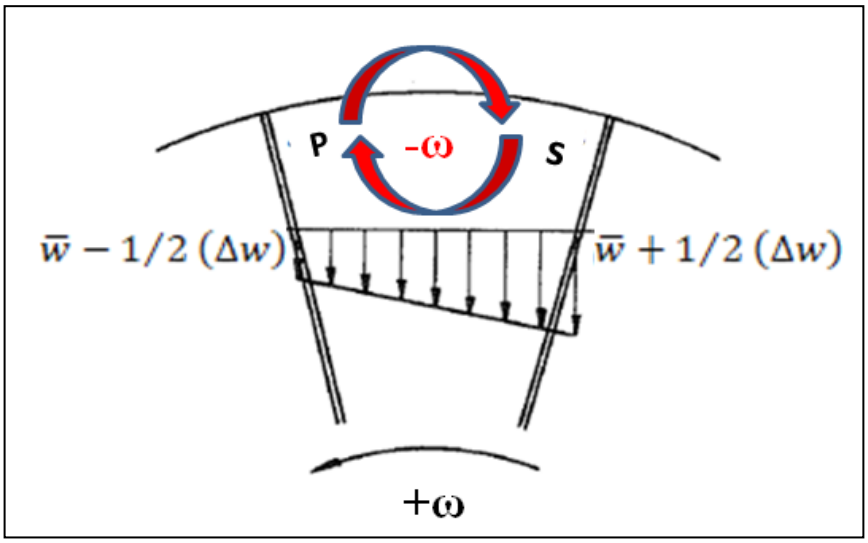

Fig. 1.8 – Rotor inlet: relative flow velocity variation in circumferential direction [6]

In order to better understand the phenomenon described above, a fluid particle can be considered in the rotor channel as it migrates in radial direction towards the rotation axis: for a 90° rotation of the impeller in the direction indicated by ω there's a particle counter rotation of -90° in the relative reference: this means that in the absolute reference the particle actually does not rotate on itself.
The effect is ideally the same described in literature for the flow that leaves the rotor of a centrifugal compressor (the so-called 'slip effect'). In the case of the centrifugal impeller the slip effect causes an over-deflection (w_θ grows) of the streamlines leaving the wheel: if the peripheral speed is the same, a reduction of the absolute circumferential velocity component and consequently of the exchanged work is expected.
For the discussed case of the centripetal turbine, the slip effect at rotor inlet produces a relative flow speed (w_2) deflected in opposite direction to the rotation: with the same peripheral speed (u_2), the slip effect causes a lower $c_{\theta 2}$ and therefore it reduces the work potentially extractable from the flow (see equation (1.12)), resulting in performance deterioration.
As a consequence of combining an irrotational flow at rotor inlet with a counter-rotating vortex, the relative speed on the pressure side of the blade decreases while the one on the suction side grows (Fig. 1.9). The torque transmitted to the rotor by the fluid manifests itself as a pressure difference inside each inter-blade channel. Therefore there must be a pressure gradient in circumferential direction in the space between two consequent blades.
Considering the flow as stationary ($d\omega/dt = 0$), the second law of dynamics (Newton) is applied in circumferential direction for a fluid element in the space (r, ϑ, z):

$$dpdr = 2\omega w(\rho r d\vartheta dr) \qquad (1.13)$$

where $2\omega w$ is the Coriolis acceleration while $\rho r d\vartheta dr$ is the mass of the fluid element per unit of depth (z).
If the flow is assumed incompressible ($\rho = cost.$) and the viscosity is neglected, the relative total pressure is constant ($d(p_{0rel}/\rho) = -dL_a = 0$) according to the energy equation in mechanical form written for the relative reference. The relative total pressure $p_{0rel} = p + 1/2\,\rho w^2 - 1/2\,\rho u^2$ is defined with respect to ϑ as follows:

$$\frac{1}{\rho}\frac{\partial p}{\partial \vartheta} = -w\frac{\partial w}{\partial \vartheta} \tag{1.14}$$

From the combination of suitably simplified equations (1.13) and (1.14) it is possible to obtain the relative speed gradient in circumferential direction:

$$\frac{\partial w}{\partial \vartheta} = -2\omega r \tag{1.15}$$

Therefore the relative velocity is not uniform across the inter-blade channel, decreasing in rotation direction ($\partial\vartheta > 0$):

$$w_{P.S.} = \overline{w} - 1/2\,(\Delta w) = \overline{w} - \omega r \Delta\vartheta \tag{1.16}$$

$$w_{S.S.} = \overline{w} + 1/2\,(\Delta w) = \overline{w} + \omega r \Delta\vartheta \tag{1.17}$$

where $\overline{w}$ is the average relative flow velocity and $\Delta\vartheta = 2\pi/z_b$ represents the angular opening between two consequent impeller blades (z_b is the number of rotor blades).

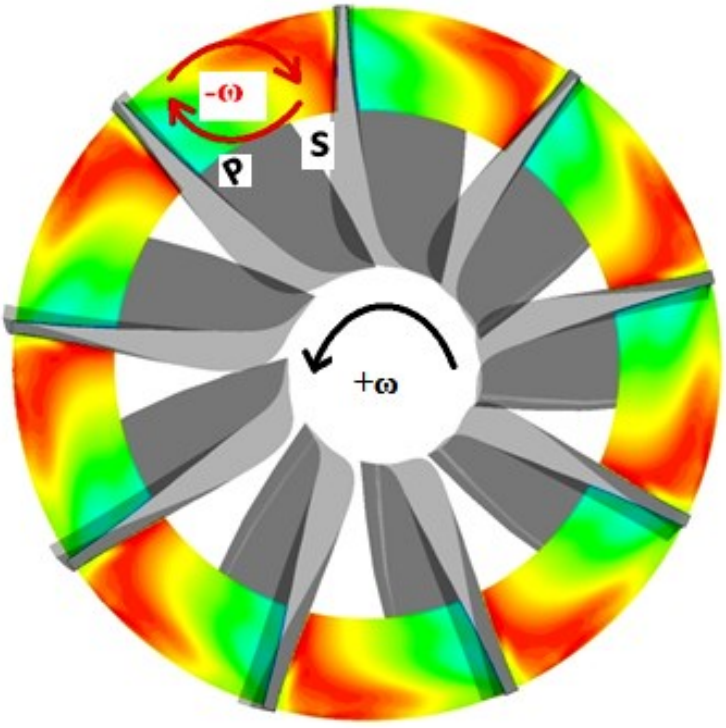

Fig. 1.9 - Relative speed contours on a rotor cross section – impeller back view

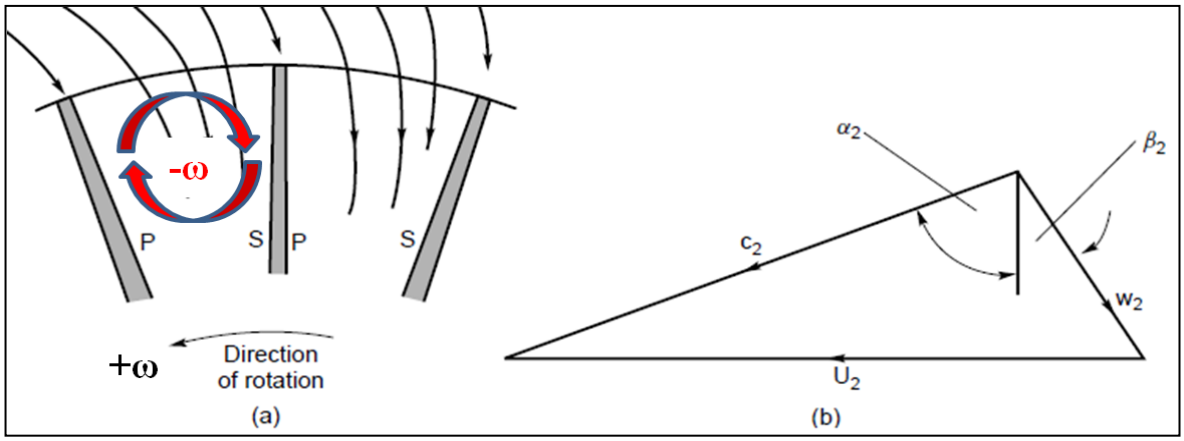

Fig. 1.10 – (a) Flow streamlines at rotor inlet. (b) Flow velocity diagram averaged along the pitch [10]

In Fig. 1.10 the relative velocity vector enters the rotor with an angle $\beta_2 \neq 0$ and if the blade metal angle (β_{c2}) is zero, the flow has a positive incidence on the rotor equal to β_2; depending on the number of impeller blades this angle can vary between -20° and -40° (minus sign because opposite to the rotation direction).

Whitfield and Baines [6] have defined an 'incidence factor' λ, with a meaning similar to the 'slip factor' used in centrifugal compressors, namely:

$$\lambda = \frac{c_{\theta 2\, effective}}{c_{\theta 2\, ideal}} = \frac{c_{\theta 2\, effective}}{u_2} \tag{1.18}$$

where "ideal" stands for cases with no slip effect, i.e. with $w_{\theta 2} = 0$ (as shown in Fig. 1.7). In order to determine the relative flow angle at rotor inlet the most practical and rapid use correlation for non-viscous 2D flow is the Stanitz [11] correlation:

$$\lambda = 1 - \frac{0{,}63\pi}{z_b} \approx 1 - \frac{2}{z_b} \tag{1.19}$$

From equation (1.19) it is therefore clear that the optimal incidence (β_2) on the rotor depends on the number of blades:

$$\beta_2 = \tan^{-1}\left[\frac{w_{\theta 2}}{w_{m2}}\right] = \tan^{-1}\left[\frac{c_{\theta 2} - u_2}{w_{m2}}\right] = \tan^{-1}\left[\frac{-(2/z_b)\,u_2}{c_{m2}}\right] \tag{1.20}$$

The minus sign at numerator inside the square brackets is due to the convention: the flow angles measured in opposite direction to the peripheral speed are negative. From last equation stems that to determine β_2 it is necessary to know at least the flow coefficient $\varphi_2 = c_{m2}/u_2$ and the number of blades z_b.
In addition, equation (1.20) highlights that the slip effect is lower if the blades number raises ($\lambda \rightarrow 1$). However, especially for small rotors, the blades number cannot be increased too much: otherwise the flow blockage effect would be excessive at the impeller outlet and the wheel inertia would grow, amplifying the well-known 'turbolag' problem

(common issue in turbocharging setups). Finally, a large number of blades produces a greater wetted surface, hence a negative increase in friction losses.
In the context of a radial turbine ideal design, the absolute speed is required to be mainly axial and small in absolute value at rotor outlet. This is due to the fact that the associated kinetic energy would be lost if the flow is not effectively diffused (in some installations this may not be possible).
Supposing that the meridian component of the flow speed at the exit (c_{m3}) is constant along the radius and there is no swirl ($c_{\theta 3} = 0$), since the peripheral speed at blade trailing edge varies proportionally with the radius (while the leading edge is located entirely at the same radius r_2), the blade metal angle at rotor exit can be calculated along the span from:

$$r_3/\beta_{c3} = cost \tag{1.21}$$

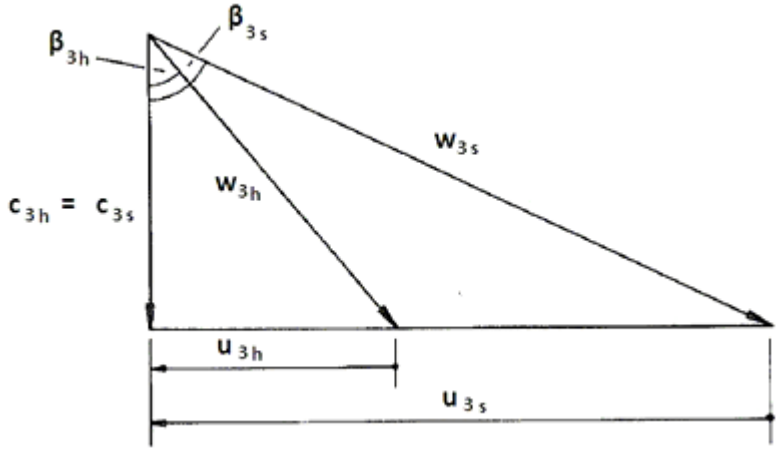

Fig. 1.11 – Hub ('h' subscript) and shroud ('s' subscript) speed triangles at rotor exit [6]

From Fig. 1.11 it can be noted that both the degree of deflection and the relative speed are greater near the blade tip than close to the root. With regard to the relative flow angle at impeller exit ($\beta_3 = tan(\, w_{\theta 3}/w_{m3})$, values between -55° and -75° are usual.
If the application of the turbine is such that the flow velocity at rotor exit can be effectively diffused, a smaller relative flow angle is advisable, in order to have a higher meridian component of the speed ($w_{m3} = c_{m3}$) and reduce kinetic energy losses. Otherwise, if an effective diffusion is not possible, it is better to minimize exit losses by reducing the meridian component, which implies a greater relative flow deflection.

1.2.3. Diffuser

The main task of the diffuser downstream of the wheel is to recover the residual kinetic energy at impeller exit, which would otherwise be lost. This component allows the turbine rotor to take advantage of a final pressure recovery up to the tailpipe discharge pressure (generally close to atmospheric value). In this way, compared to the case without diffuser, the pressure at rotor exit can be further decreased, ensuring a greater rotor enthalpy drop and therefore a higher extraction of specific work. The advantages deriving from the use of a diffuser can be quite significant, particularly where the rotor outlet diameter must be made smaller than what is fluid-dynamically advisable, for example in order to reduce the

rotating inertia or the stress at the blade root due to the centrifugal force ($F_{centrifugal} = mr\omega^2$), which grows linearly with the distance from the rotation axis.
The diffuser has generally a conical or annular geometry (see Fig. 1.12) and can have straight or shaped walls, depending on the installation and efficiency requirements. The performance of a diffuser is essentially a function of:

- geometric parameters: $AR = A_4/A_3$ (area ratio), δ (half-opening angle), l/D_3 for conical diffusers (length to inlet diameter ratio), $\bar{l}/b_3$ for annular diffusers (where $\bar{l} = (l_o + l_i)/2$);
- inlet fluid properties: speed profile, rotor outlet swirl angle (α_3), blockage factor due to the boundary layer, Mach and Reynolds numbers, turbulence intensity.

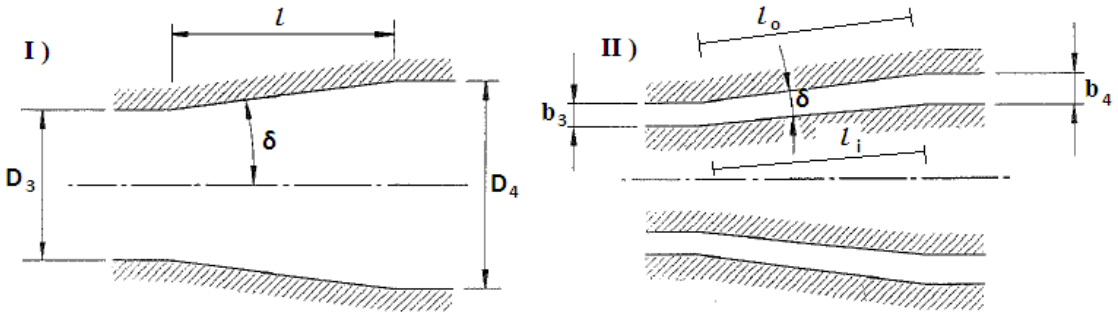

Fig. 1.12 – Diffuser types for a radial turbine: I) conical ; II) annular [6]

The diffuser performance parameters are essentially two:

- static pressure recovery $C_p = (p_4 - p_3)/(1/2\,\rho {c_3}^2)$;
- total pressure drop $\pi_d = p_{04}/p_{03}$.

Sovran and Klomp [12] design diagrams (see Fig. 1.13) link diffuser performance with its geometric parameters: constant C_p lines are plotted over the borderlines ${C_p}^*$ e ${C_p}^{**}$ which in turn identify, for a given length ratio (l/D_3) or area ratio (AR) respectively, the maximum static pressure recovery coefficient without diffuser stall.

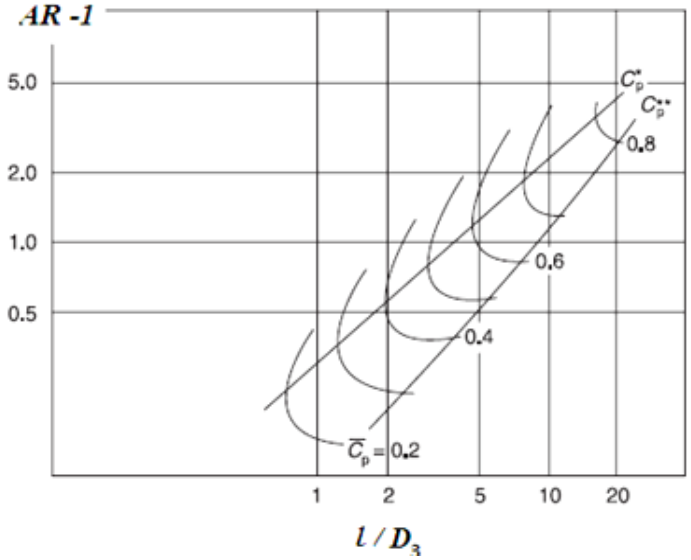

Fig. 1.13 – Contour plots of the static pressure recovery in a conical diffuser [12]

The flow in an annular diffuser can be divided into two areas: the main stream and the boundary layer near the walls. In the conical diffusers instead there is a third zone, i.e. the low momentum core located at the diffuser meanline, just downstream the rotor fixing nut.

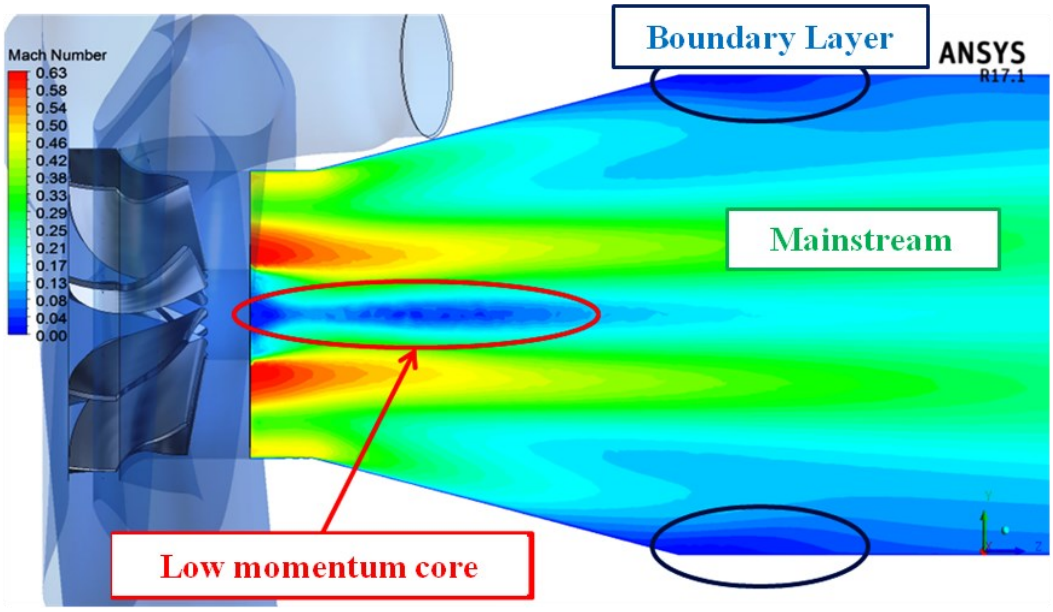

Fig. 1.14 – Main flow regions in a conical diffuser

The diffuser performance is roughly determined by the efficiency in controlling the growth of the boundary layer on the walls and for this reason some velocity, swirl or turbulence profiles can bring a benefit if they carry momentum inside the boundary layer.
In real turbines operation, flow non-uniformities or distortions of the speed profile on the inlet and outlet section of the diffuser can remarkably reduce the pressure recovery ideally achievable. Assuming the fluid as incompressible and using the continuity and energy equations between sections '3' and '4' (diffuser inlet and outlet respectively), through a sequence of steps omitted here for brevity, it is possible to derive the 'ideal' pressure recovery coefficient ($C_{p\,id}$) in case of non-uniform flow:

$$C_{p\,id} = \chi_3 - \chi_4 \frac{1}{\mathrm{AR}^2} \tag{1.22}$$

$$\chi = \frac{1}{\mathrm{A}} \int \left(\frac{c}{\bar{c}}\right)^3 dA \tag{1.23}$$

where χ is the "kinetic energy flux coefficient" [10] of the velocity profile, calculated through equation (1.23) with the flow average velocity on the control section ($\bar{c}$).
If the flow is uniform $\chi = 1$, otherwise $\chi > 1$; generally $\chi_3 = 1$ is a good approximation because the boundary layer is very small at diffuser inlet, while at the outlet the higher χ_4 is, the lower the pressure recovery ideally obtainable by the diffuser will be.

1.3. Twin scroll radial turbines

Previous paragraph summarizes some general information on radial turbines; the discussion turns now to the specific case of twin entry turbines. The volute divided in two

different scrolls or 'branches' is an interesting solution to preserve exhaust gas energy and ease engine cylinders charge replacement. Despite the engine manufacturers growing interest towards twin scroll IFR turbines, there are few research centers that support and study the development of this kind of turbomachinery. Flow investigations on twin entry volutes need a careful analysis of fluid dynamic phenomena occurring within such type of component. In fact, during the operation of an ICE, turbine feeding is discontinuous and consequently the flow distribution inside the two scrolls of the volute varies frequently.

1.3.1. Admission conditions classification

As a consequence of the division of the volute in two limbs, a twin scroll turbine has several combinations of admission conditions (see Tab. 1.1 below). In order to identify these 'states', it is useful to introduce the admission ratio λ [4], defined as:

$$\lambda = \frac{\dot{m}_{hub}}{\dot{m}_{hub} + \dot{m}_{shroud}} \tag{1.24}$$

where each of the two branches is denoted on the basis that it is located on the hub or shroud side of the rotor with respect to the divider wall (see Fig. 1.15).

Tab. 1.1 – Combinations of admission conditions for a twin scroll turbine [4]

Case	λ	Hub scroll	Shroud scroll
a	λ<0.0	Back flow	Full flow
b	λ=0.0	Zero flow	Full flow
c	0.0< λ<0.5	Lower flow	Higher flow
d	λ=0.5	Equal flow	Equal flow
e	0.5< λ<1.0	Higher flow	Lower flow
f	λ=1.0	Full flow	Zero flow
g	λ>1.0	Full flow	Back flow

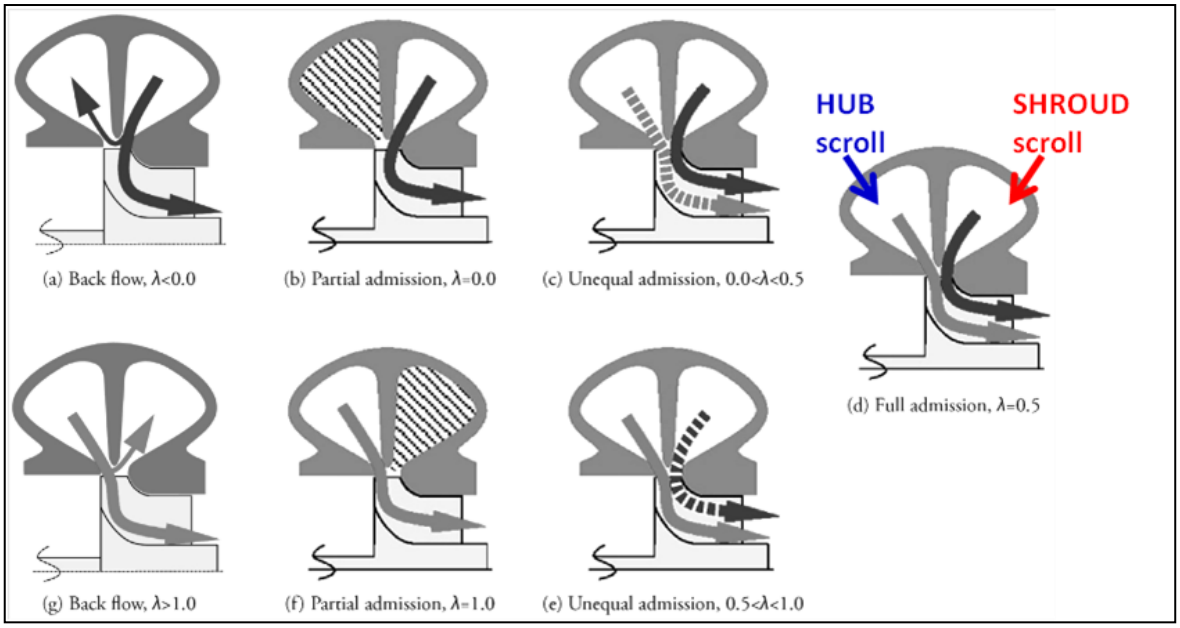

Fig. 1.15 – Flow admission conditions of a twin scroll turbine [4,13] – ref. Tab. 1.1

It is possible to collect the above mentioned operating conditions under three main cases:

- 'full' or 'equal' refers to the case in which both volute branches are fed and crossed approximately by the same mass flow rate (exception for small differences due to the asymmetry of the two sectors);
- 'unequal' describes the most usual operating conditions of the turbine coupled to the internal combustion engine, when the individual pressure pulsations that pass through the two volute branches arrive at the turbine out of phase. This is an unavoidable phenomenon in pulse turbocharging, dictated by the cylinders firing sequence and their grouping in engine manifolds as described in paragraph 1.1;
- 'partial' instead identifies the extreme case of unequal admission in which there's zero mass flow in one of the two branches.

1.3.2. Twin scroll turbines main performance parameters

The following list collects the fluid dynamic parameters commonly used for the description of the performance of a twin scroll turbine:

- mass flow parameter (MFP) is a pseudo-dimensionless parameter which is used to calculate the swallowing capacity of the turbine:

$$MFP_{twin\ entry} = \dot{m}_{tot} \frac{\sqrt{MFR_{sh} T_{01\,sh} + MFR_{hub} T_{01\,hub}}}{\frac{p_{01\,sh} + p_{01\,hub}}{2}} \tag{1.25}$$

  where $\dot{m}_{tot} = \dot{m}_{sh} + \dot{m}_{hub}$ and $MFR_i = \dot{m}_i / \dot{m}_{tot}$ is the ratio between the mass flow passing through the *'i-th'* scroll and the overall mass flow processed by the turbine.
  From the energy equation, the stagnation temperature is calculated considering the contribution of each limb on the overall flow capacity. It is noteworthy to consider that if the inlet total temperatures of the two branches are the same ($T_{01\,sh} = T_{01\,hub}$) and the mass flow rate that feeds the two entries is similar ($\dot{m}_{sh} \approx \dot{m}_{hub}$), the equation (1.25) can be simplified to the standard mass flow parameter definition:

$$MFP = \dot{m}\sqrt{T_{01}} / p_{01} \tag{1.26}$$

- pressure ratio flow (PRF - or total to static expansion ratio) represents the ratio between the volute inlet total pressure and the turbine tailpipe outlet static pressure. For a twin entry turbine, the PRF corresponds to an area average value of the pressure ratios related to the two scrolls (if the turbine outlet static pressure is the same for the two branches, the inlet total pressure is different). Denoting the volute inlet section with '1' and the tailpipe outlet section with '4':

$$PRF_{twin\ entry} = \frac{A_{1\,sh}}{A_{tot}} \frac{p_{01\,sh}}{p_4} + \frac{A_{1\,hub}}{A_{tot}} \frac{p_{01\,hub}}{p_4} \tag{1.27}$$

  If, as often occurs, the inlet section of each of the two manifolds that feed the volute branches is equal ($A_{1\,sh} = A_{1\,hub}$) the definition (1.27) is simplified into:

$$PRF_{twin\ entry} = (p_{01\,sh} + p_{01\,hub}) / (2p_4) \tag{1.28}$$

- 'both' volute inlet total pressure, a parameter used for volute losses assessment and efficiency evaluation:

$$p_{01\,both} = \left[\frac{MFR_{hub}T_{01\,hub}}{T_{01\,both}}(p_{01\,hub})^{\frac{1-k}{k}} + \frac{MFR_{sh}T_{01\,sh}}{T_{01\,both}}(p_{01\,sh})^{\frac{1-k}{k}}\right]^{\frac{k}{1-k}} \quad (1.29)$$

where $T_{01\,both}$ is an average of the two inlet total temperatures. If the difference between $T_{01\,sh}$ and $T_{01\,hub}$ is neglected, the following formulation may be derived:

$$p_{01\,both} = \left[MFR_{hub}(p_{01\,hub})^{\frac{1-k}{k}} + MFR_{sh}(p_{01\,shroud})^{\frac{1-k}{k}}\right]^{\frac{k}{1-k}} \quad (1.30)$$

- reduced speed, i.e. the ratio between the turbo rotational speed and the square root of the exhaust gas total temperature at volute inlet:

$$N_{rid} = N/\sqrt{T_{01}} \quad (1.31)$$

- total to static efficiency, i.e. the ratio between the actual total enthalpy drop $(h_{01} - h_{04})$ and the total to static enthalpy variation in case of isentropic transformation:

$$\eta_{ts} = \frac{h_{01} - h_{04}}{h_{01} - h_{4ss}} = \frac{1 - \frac{T_{04}}{T_{01}}}{\left[1 - \left(\frac{p_4}{p_{01\,both}}\right)^{(k-1)/k}\right]} \quad (1.32)$$

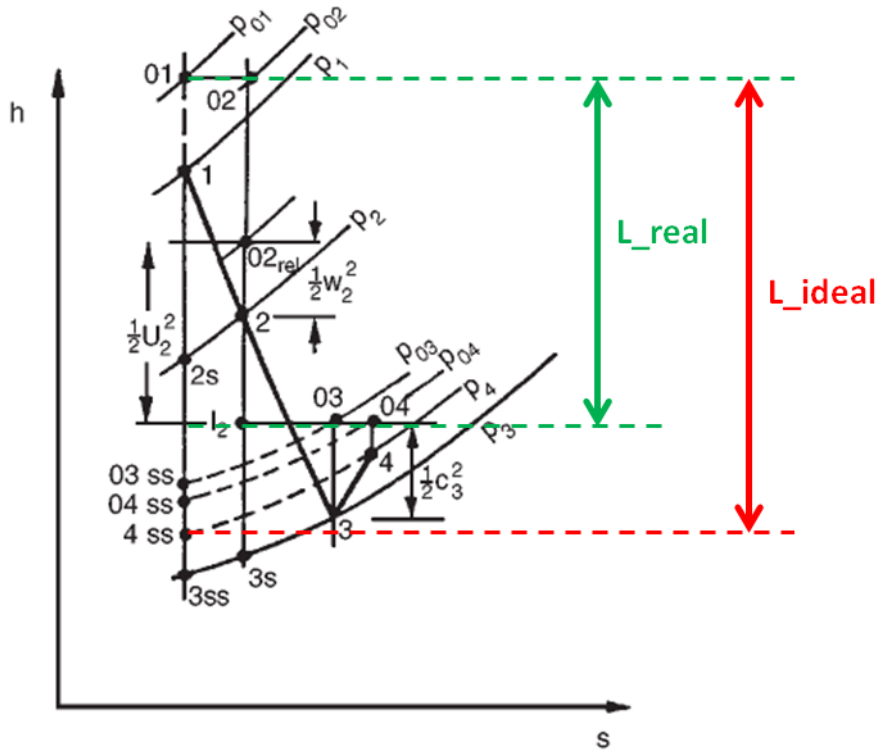

Fig. 1.16 – Mollier diagram for an IFR turbine with diffuser (at the design point) [10]

- total to total efficiency, defined as η_{ts} but replacing the 'total to static' expansion ratio ($\varepsilon_{ts} = p_{01\,both}/p_4$) with the 'total to total' one ($\varepsilon_{tt} = p_{01\,both}/p_{04}$):

$$\eta_{tt} = \frac{1 - \frac{T_{04}}{T_{01}}}{\left[1 - \left(\frac{p_{04}}{p_{01\,both}}\right)^{(k-1)/k}\right]} \tag{1.33}$$

1.3.3. Twin scroll turbines performance in unbalanced admission conditions

Twin entry turbochargers usually exhibit an imbalance of flow conditions between the two entries which is caused by the engine cylinders firing sequence. In 1.3.1 three main admission cases have been identified: equal, unequal and partial; however, it must be considered that the partial admission condition is difficult to take place under normal engine operating conditions. Even in the extreme case when the flow in one scroll drops to zero and backflow might occur in the other, the remaining flow is distributed by the volute around the entire periphery of the rotor. Nevertheless the importance of partial admission conditions becomes clear when it is necessary to evaluate fluid dynamic losses and translate these into the real pulsating operation of the turbocharger coupled with the ICE.
Baines et al. [14] measured the performance of a vaneless twin entry radial turbine under full and partial admission conditions. The results of these investigations showed that if one of the volute inlets is completely closed, large recirculations from one branch of the volute to the other are detectable, with consequent penalties in terms of efficiency. These evidences indicate that a remarkable portion of entry loss in case of unbalanced admission is represented by incidence losses in the twin-scroll flow housing.
Other researchers [5] studied in detail the direction of the flow at volute branches exit in partial admission: by plotting velocity vectors on a volute cross cut, it was noted that, in addition to back flow in the unpowered branch, the mixing of the streams coming from the two limbs occurs downstream of the divider septum in a decentralized position towards the no flow entry side of the volute.

Turbocharged power unit manufacturers often devote significant investments in the development of turbine behaviour predictive models to optimize the coupling with the engine. In this context the study of partial admission conditions reveals to be particularly useful in software set up where twin entry turbines modelling can be improved by a calibration procedure which includes the partial admission case besides the full.
The results of the experimental tests on twin entry turbines discussed by Romagnoli in his PhD thesis [15] suggest that the MFP definition previously provided in equation (1.25) seems to work in equal and unequal admission conditions, but not in partial admission. As visible in Fig. 1.17, the problem lies in considering the partial admission mass flow rate as half the full admission one, assimilating the twin entry turbine to an half-size single entry (light blue dots), without accounting for the existing interactions between the two branches. Although in partial admission there's no exhaust gas mass flow at one inlet of the volute, stagnant air at near atmospheric pressure is still present within the no flow branch. Consequently Romagnoli et al. [16] assumed that in partial admission both the mass flow rate and inlet total pressure of the open limb are equal to half the corresponding quantities in equal admission and atmospheric pressure is present in the stagnant scroll, leading to a new MFP formulation (see the black line in Fig. 1.17).

Labels “inner open” and “outer open” in Fig. 1.17 refer to the condition in which the outer or inner limb is blanked-off respectively (“inner” or “outer” relates instead to the position of the volute branch within the test-rig).

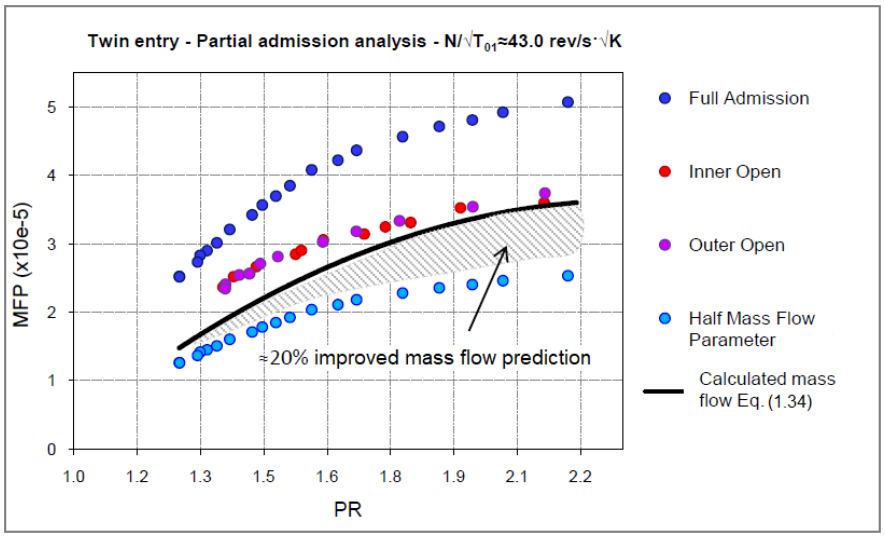

Fig. 1.17 – Improved mass flow prediction in partial admission [15]

$$MFP_{partial} = \dot{m}_{partial}\frac{\sqrt{T_{0,partial}}}{p_{0,partial}} \approx \left(\frac{\dot{m}_{full}}{2}\right)\frac{\sqrt{T_{0,full}}}{\frac{p_{0,full}}{2}+\frac{p_{atm}}{2}} \tag{1.34}$$

The interest is now shifted towards unequal admission conditions, which, as mentioned, characterize the normal functioning of the turbine coupled to the ICE. Unlike what was observed for partial admission, the unequal admission condition generally presents flow capacity similar to that in full admission: this suggests that in unequal admission the flows leaving the two branches of the volute are in favourable conditions to expand in the turbine stage, similarly to what happens in equal admission.

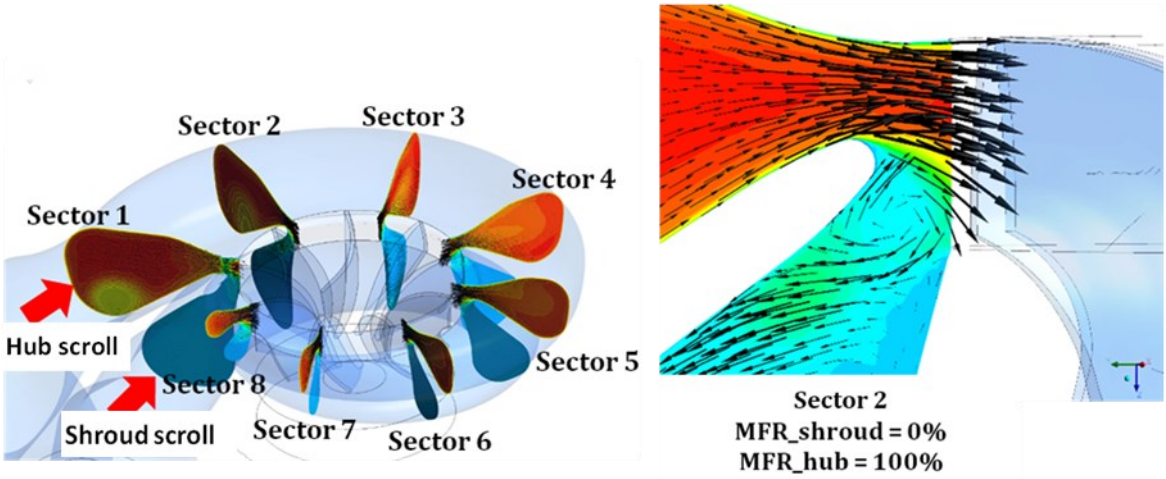

Fig. 1.18 – Total pressure on various twin scroll volute cross sections (left); enlarged view of the mixing region with marked recirculation in the no flow limb (right)

When one of the volute inlets is completely closed (partial admission), the incoming flow from the other side expands into a low pressure region (almost atmospheric), causing a detrimental axial distribution of the absolute velocity and flow angle at rotor inlet. The flow tends to migrate from one branch to the other, causing a remarkable recirculation (see Fig. 1.18) or even backflow, which leads to a flow coefficient drop.
In unequal admission even if a small amount of the overall mass flow rate passes through one volute branch ("lower flow" condition – see cases 'c' and 'e' in Tab. 1.1), this turns out to be sufficient to prevent any flow recirculation. The results similarity between equal and unequal admission suggests that a common pattern can be found between the overall mass flow and that one passing through the individual branches.

In the steady experimental tests led by Romagnoli [15] the unequal admission conditions were obtained by keeping the pressure ratio constant in one branch (therefore called "constant pressure limb") and leaving the other free to vary ("free flow limb") with the purpose of matching the required operating condition.
Comparing the mass flow curves under unequal admission with those of the so-called "free flow limb", it can be noted that the shape of the trends is almost the same, but the mass flow in the free flow limb covers a wider range of pressure ratios (see Fig. 1.19).

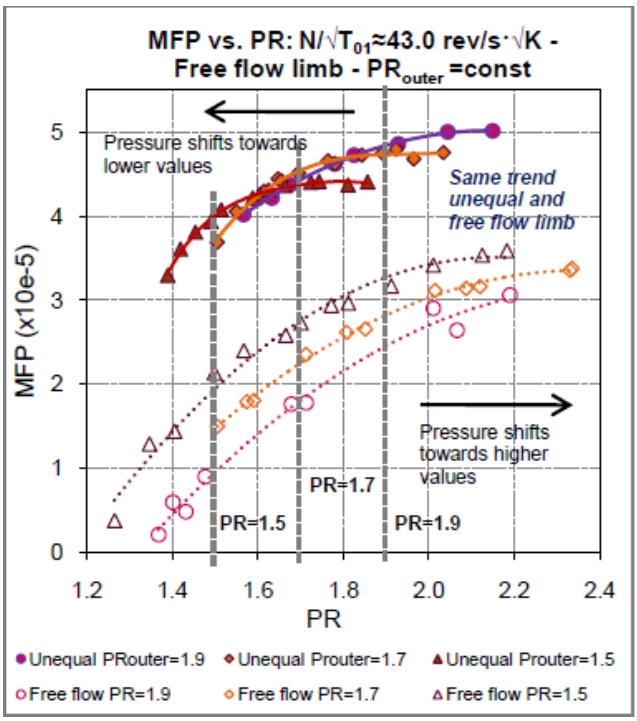

Fig. 1.19 - Overall and free flow limb mass flow parameter in unequal admission. The outer limb pressure ratio is kept constant [15]

Observing previous equation (1.27) it is clear that if the pressure ratio in one branch (e.g. the outer or shroud branch) is kept constant, the 'overall' PR shifts towards higher or lower values than those of the 'free flow' PR depending on whether the pressure ratio in the free flow limb is lower or higher than that one in the constant pressure limb (see Fig. 1.19); this forces the MFP in unequal admission conditions to vary in a narrow pressure ratios range, while maintaining trend and values very similar to those measured in full admission.

Is there a correlation between the mass flow in unequal admission and that in the free flow limb (computed by equation (1.26))? In order to check this, Romagnoli et al. [16] calculated the ratios between the corresponding Mass Flow Parameter and Pressure Ratio, leading to the definition of two dimensionless parameters called respectively Mass Flow Parameter Ratio (MFP_R) and Unequal Expansion Ratio (ER_U).

$$MFP_R = \frac{MFP_{unequal}}{MFP_{free\ flow}} = \frac{\dot{m}_{tot}\dfrac{\sqrt{\dfrac{\dot{m}_{free\ flow}}{\dot{m}_{tot}}T_{0,free\ flow} + \dfrac{\dot{m}_{const}}{\dot{m}_{tot}}T_{0,const}}}{\dfrac{p_{0,free\ flow}}{2} + \dfrac{p_{0,const}}{2}}}{\dot{m}_{free\ flow}\dfrac{\sqrt{T_{0,free\ flow}}}{p_{0,free\ flow}}} \tag{1.35}$$

where 'const' subscript in equations (1.35) and (1.36) stands for "constant pressure limb".

$$ER_U = \frac{PR_{un}}{PR_{free\ flow}} = \frac{\dfrac{PR_{free\ flow}}{2} + \dfrac{PR_{const}}{2}}{PR_{free\ flow}} \tag{1.36}$$

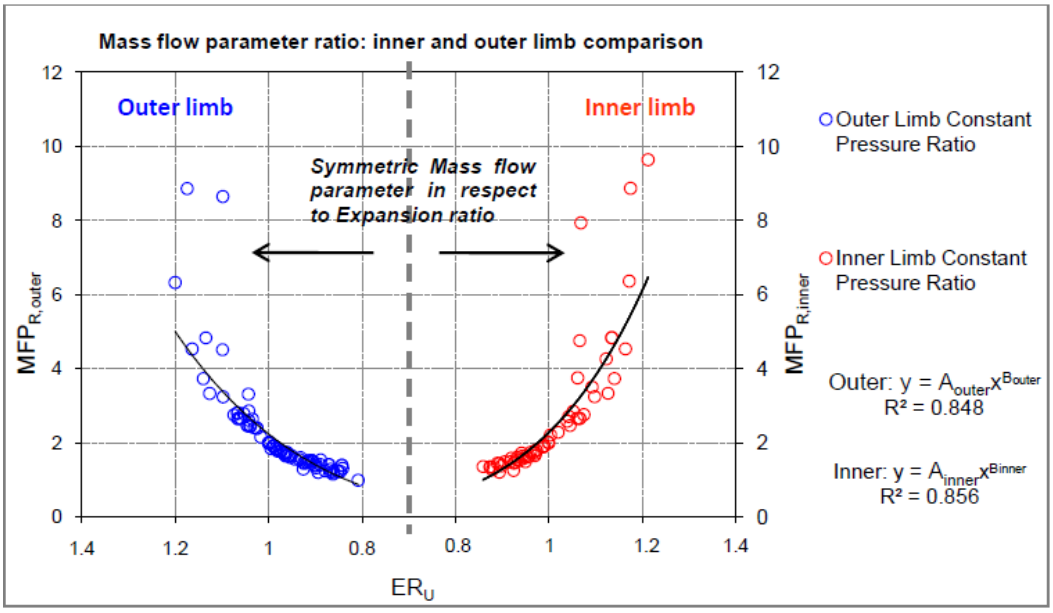

Fig. 1.20 - Mass flow parameter ratio as a function of the unequal expansion ratio [15]

Romagnoli [15] plotted the experimental data according to these new parameters (MFP_R and ER_U), discovering that for each scroll (outer/inner) all the measured points can be regressed through a unique curve (black line in Fig. 1.20), which is speed and pressure ratio independent. This relevant result suggested to the scientific community that a single power trend correlation exists between the mass flow parameter in unequal admission ($MFP_{unequal}$) and that calculated in the free flow scroll ($MFP_{free\ flow}$), as in the following equation (1.37).

$$MFP_R = \frac{MFP_{unequal}}{MFP_{free\ flow}} = A(ER_U)^B \tag{1.37}$$

The similarity previously observed between the unequal and full admission mass flow trends supported the assumption that the MFP_R in equation (1.37) was comparable with the ratio between the full admission mass flow and that passing through the free flow limb:

$$\frac{MFP_{unequal}}{MFP_{free\ flow}} \approx \frac{MFP_{full}}{MPF_{free\ flow}} = \frac{\dot{m}_{full}\dfrac{\sqrt{T_{0,full}}}{p_{0,full}}}{\dot{m}_{free\ flow}\dfrac{\sqrt{T_{0,free\ flow}}}{p_{0,free\ flow}}} =$$

$$= \frac{\dot{m}_{full}}{\dot{m}_{free\ flow}}\left(\frac{p_{0,free\ flow}}{p_{0,full}}\right) = \frac{\dot{m}_{full}}{\dot{m}_{free\ flow}}(ER_U)^{-1} \tag{1.38}$$

where $T_{0,full} = T_{0,free\ flow}$ and the term $(p_{0,free\ flow}/p_{0,full})$ corresponds to the inverse of the unequal pressure ratio.
By substituting the equation (1.37) in (1.38), Romagnoli et al. [16] finally derived the relationship which correlates the volute branch mass flow in unequal admission with the corresponding one in full admission. The mass flow through each scroll is therefore uniquely identified for a given value of the total pressure in the scroll itself:

$$\dot{m}_{limb} = \left(\frac{MFP_{full}}{MFP_{free\ flow}}\right)^{-1}\dot{m}_{full}(ER_U)^{-1} =$$

$$= \frac{\dot{m}_{full}}{A}\left(\frac{1}{ER_U}\right)^{B+1} = \frac{\dot{m}_{full}}{A}\left(\frac{p_{0,limb}}{p_{0,full}}\right)^{B+1} \tag{1.39}$$

This paragraph led to the classification of the different admission conditions which characterize twin scroll turbines functioning and to the identification of the main figures of merit capable of quantifying their performance.
Section 1.3.3, on the other hand, showed the reader some interesting literature results on the behaviour of twin entry turbines in unbalanced admission conditions, which can be correlated to full admission maps by introducing ad hoc parameters. Twin entry turbine modelling remains an open field of research.

Chapter 2

Uncertainty quantification in CFD: a new engineering test bench

Over the past three decades, computer simulation tools have achieved widespread use in the design and analysis of engineering devices. This shortened the overall product design cycle (physical experiments may be impossible during early design stages) and also provided better understanding of the operating behaviour of the systems under investigation. As a consequence, numerical simulation led to a reduction of physical prototyping and to lower costs for manufacturing production chains.
Despite this success, it remains difficult to provide objective confidence levels in quantitative information derived from numerical predictions. The complexity arises from the amount of uncertainties related to the inputs of any computation attempting to represent a physical system. As a result, especially in the area of reliability and safety, physical testing remains the dominant certification mechanism of new devices.

One of the key aspects in Computational Fluid Dynamics is the level of confidence of numerical results, boundary conditions, physical properties or model parameters, as they contains numerical errors and uncertainties. Thus, the understanding and quantification of these errors is a critical aspect in order to provide the uncertainty level of the CFD results. In the next future rigorous quantification of the errors and uncertainties introduced in numerical simulations will be required to establish objectively their predictive capabilities.
The U.S. Department of Energy provided a general definition for the Uncertainty Quantification (UQ):
"UQ studies all sources of error and uncertainty, including the following: systematic and stochastic measurement error; ignorance; limitations of theoretical models; limitations of numerical representations of those models; limitations of the accuracy and reliability of computations, approximations, and algorithms; and human error. A more precise definition is UQ is the end-to-end study of the reliability of scientific inferences" [17].

Procedures to establish the quality of numerical simulations have been organized within the framework of 'Verification and Validation' (V&V) activities. It is possible to distinguish:

- 'Verification' is a mathematical process that aims at answering the question: *"are we solving the equations correctly?"*. Thus the objective is to quantify the errors associated to the algorithms used to obtain the solution of the governing equations;
- 'Validation' on the other hand points at answering the question: *"are we solving the correct equations?"*. Then in this second case the goal is to identify the appropriateness of the selected mathematical/physical formulation to represent the device to be analyzed.

Validation always involves comparisons of the numerical predictions to reality, whereas verification only involves numerical analysis and tests. There's a growing recognition of the fact that validation cannot be carried out without explicitly accounting for the uncertainties present in both the measurements and the computations. Experimentalists are typically required to report uncertainty bars to clearly identify the repeatability and the errors associated to the measurements. Validation must be carried out by acknowledging the nature of the experimental uncertainties and providing a similar indication for the computational error bars.

As a general conclusion of this introduction, uncertainty quantification has two main goals:
1) the construction of a framework to estimate the error bars associated with given predictions;
2) the evaluation of the likelihood of a certain outcome [18]; this obviously leads to better understanding of risks and improves the decision making process.

2.1. Uncertainty characterization

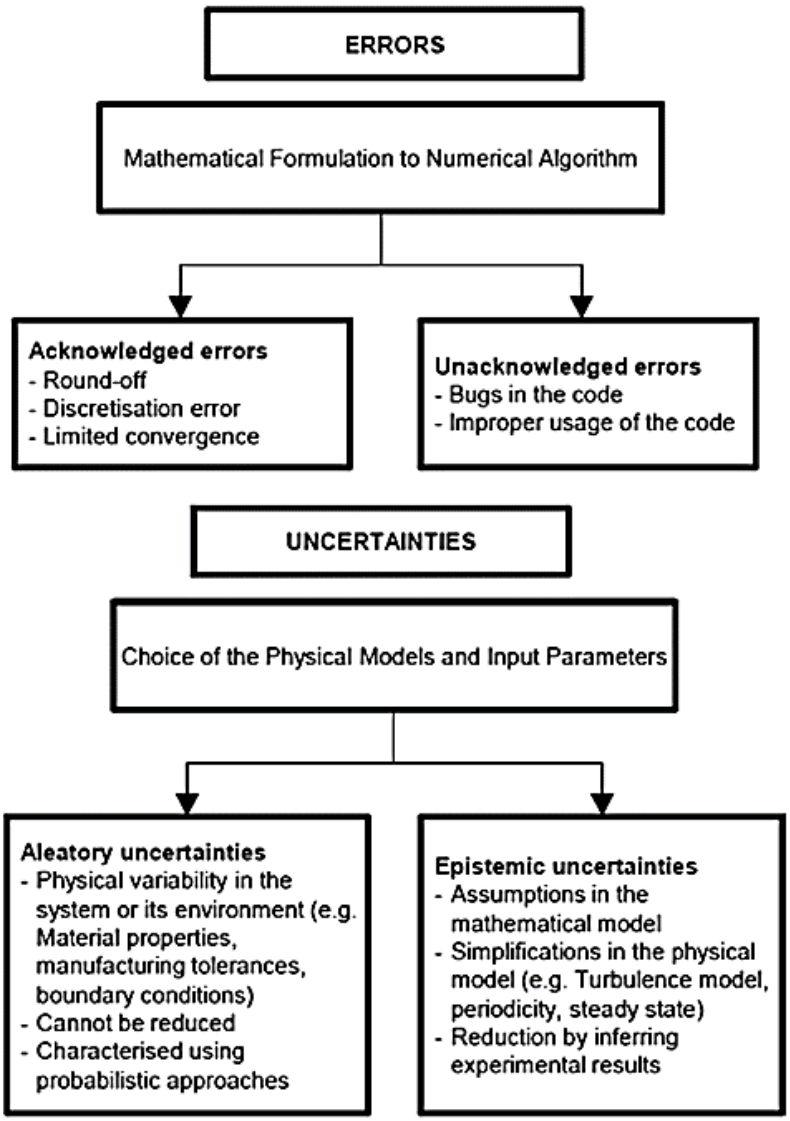

Fig. 2.1 – Errors and uncertainties definitions [19]

The American Institute of Aeronautics and Astronautics (AIAA) guidelines [20] clearly distinguished:

- ‘Uncertainty’ is a potential deficiency in any phase or activity of the modelling process that is due to the lack of knowledge;
- ‘Error’ is a recognizable deficiency in any phase or activity of the modelling process that is not due to the lack of knowledge.

This definition is not completely satisfactory as it does not precisely discriminate between mathematics and physics.

It is more useful to define errors as associated to the translation of a mathematical formulation into a numerical algorithm (and a computational code). Usually errors are further classified in two categories:

- 'acknowledged' errors, that are known to be present but their effect on the results is deemed negligible. Examples are round-off errors and limited convergence of certain iterative algorithms;
- 'unacknowledged' errors (which could be considered "uncertainties" according AIAA definition) on the other hand are not recognizable but might be present; implementation mistakes (bugs) or usage errors can only be characterized by verification tests and procedures.

Using the present definition of errors, the uncertainties are naturally associated with the choice of the physical models and the specification of the input parameters required for performing the analysis. As an example, numerical simulations require the exact specification of boundary conditions and typically only limited information are available from corresponding experiments and observations; variability or incompleteness in this information introduce uncertainties in the numerical simulations.

In order to meet the pragmatic point of view of the industrial user and make easier the management of each uncertainty class by the software developer, the 'source' of uncertainty lead to a distinction in three main categories of uncertainty:

1) operational, related to operating conditions issues;
2) geometrical, associated to the system geometry, like geometrical tolerance due to the system manufacturing process;
3) numerical, connected to modelling issues and numerical errors.

A more precise characterization is based on the distinction between two uncertainty types:

- 'aleatory' (from the Latin "*alea"*, meaning a die) refers to uncertainty about an inherently variable phenomenon. Uncertainties can be defined aleatory if linked to the intrinsic physical variability of the system or its environment (material properties, manufacturing tolerances, boundary conditions etc.). These stochastic uncertainties are not strictly due to lack of knowledge and cannot be removed completely; naturally this kind of uncertainty is often defined in probabilistic framework.
  The previous instance of specifying the boundary conditions in a CFD simulation is a classic example of an aleatory uncertainty. The information required for the numerical simulations should be inferred from observation of the system of interest or specific experiments. Given the limited degree of repeatability of experimental measurements and the errors associated to measurement techniques, these quantities are known with a certain degree of uncertainty, typically specified as an interval, $x \pm u\%$. Probabilistic approaches treat these quantities, that overall characterize the aleatory uncertainty, as random variables assuming values within specified intervals. In mathematical terms this corresponds to the definition of random variables with a specified probability distribution function (PDF). In the context of probabilistic approaches, the goal of uncertainty characterization is therefore to define PDFs of each input quantity used in the computational tool. Once the PDFs are defined, the uncertainties can be propagated through the mathematical model and the overall output uncertainty may be determined. The challenge of justifying the choice of a specific analytic distribution (Gaussian, uniform, beta, etc.) basing it solely on experimental data is tricky because of the limited amount of data typically available [21]. Different choices regarding the definition of input distributions can lead to ambiguous or conflicting estimates.

- ‘epistemic’ (from the Greek *“ἐπιστήμη”,* meaning knowledge) refers to uncertainty arising from lack of knowledge (as indicated in the AIAA Guide [20]). Uncertainties may be denoted as ‘epistemic’ if they are reducible and associated with assumptions introduced in the derivation of the mathematical model used or deriving from simplifications related to the correlation or dependence between physical processes.
  It is possible to reduce the epistemic uncertainty by using, for example, a combination of calibration, inference from experimental observations and improvement of the physical models. Epistemic uncertainty is not well characterized by probabilistic approaches because it might be difficult to deduce any statistical information due to the nominal lack of knowledge. The important consequence is that epistemic uncertainties have a fixed, but poorly known, value in the analysis; for instance the turbulent viscosity in a CFD simulation is known to be subject to the many assumptions associated with the turbulence model selection. Numerical errors induced, for example, by an incorrect discretization of the computational grid or by an unsuitable turbulence model are not intrinsic errors of the system under examination, but are linked to its incorrect modelling.

In conclusion, the epistemic uncertainties of a mathematical model represents the level of uncertainty in reproducing the real system, while the aleatory uncertainties are a strict property of the system being analyzed. This distinction is not always clear since lack of knowledge is relative and depends on current theory and experimental capabilities. One of the targets of uncertainty quantification is to reformulate epistemic uncertainties as aleatory uncertainties where the probabilistic analysis is applicable.

2.2. Sensitivity vs. Uncertainty analysis

Sensitivity analysis (SA) investigates the connection between inputs and outputs of a computational model; more specifically, it allows to identify how the variability in an output quantity of interest is connected to a model input and which input sources dominate the response of the system. On the other hand, Uncertainty quantification (UQ) aims at identifying the overall output uncertainty in a given system.
The main difference is therefore that SA does not require input data uncertainty characterization from a real device; it can be conducted purely based on the mathematical form of the model. As a consequence, large sensitivities of the output (identified through SA) do not necessarily translate in significant uncertainties because the input uncertainty might be very small in a device of interest.
Sensitivity analysis can be intended as understanding how a generic output function $f(x_1, ..., x_n)$ depends on variations not only in x_i individually, but also on combined or correlated effects among x_i. There are two main classes of SA:

- ‘local’ sensitivity studies the sensitivity of f to changes in its inputs at or near a particular base point, as exemplified by the computation of derivatives;
- ‘global’ sensitivity deals with the "average" sensitivity of f to changes in its inputs in the domain of definition of the output function.

SA is often based on the concept of the gradient of the output of interest with respect to input variables. The overall sensitivity is then evaluated using a Taylor series expansion, that, to first order, would be equal to a linear relationship between inputs and outputs.
The uncertainty quantification (UQ) is somewhat related to the sensitivity analysis since the common goal is to obtain an understanding on how input parameters variations can affect the response functions of any engineering design problem.

However for the UQ some (or all) components of the input parameters vector are considered 'uncertain' as specified by a particular probability distribution (e.g. normal, exponential, etc.). By assigning specific probability density functions (PDF) to the inputs, it is possible to deduce the distribution structure for the outputs (i.e. the response statistics). This distinguishes the sensitivity analysis, which is more qualitative in nature, from the UQ which is instead a more strictly quantitative analysis.
Uncertainty quantification is therefore the process that involves:

(1) the characterization of input uncertainties;
(2) the propagation of these uncertainties through a computational model;
(3) the determination of the response functions statistics.

2.3. Fundamental theoretical prerequisites to perform UQ

Computer simulations of an engineering device are performed following a series of steps:

1. initially the system of interest and related performance measures are defined. Then the geometrical characterization of the device, its operating conditions and the physical processes involved are identified and their relative importance must be quantified. The definition of the system response of interest is a fundamental aspect of this phase;
2. next step is the formulation of a mathematical representation of the system. It is necessary to define the governing equations and the phenomenological models required to capture the relevant physical processes; in addition, the precise geometrical definition of the device is presented. This step introduces simplification with respect to the real system: for example, small geometrical components are eliminated, or artificial boundaries are introduced to reduce the scope of the analysis;
3. after that, a discretized representation of the system has to be formulated: numerical methods are developed to convert the continuous form of the governing equations into an algorithm which produces the solution. This phase typically requires, for example, the generation of the computational grid, which acts as a sort of 'filter' of the physical domain, providing the basis for the approximation of the calculated variables (and the discretization of the governing equations);
4. finally the numerical analysis can be carried out.

The introduction of uncertainty in numerical simulations does not affect the structure of the above process, but involves considerable complexity in each phase.

A possible scheme to perform UQ analyses on CFD simulations is proposed in Fig. 2.2 (this approach was used for the UQ applications presented in chapters 5 and 6) and the different workflow stages will be treated in more detail in the following sections.

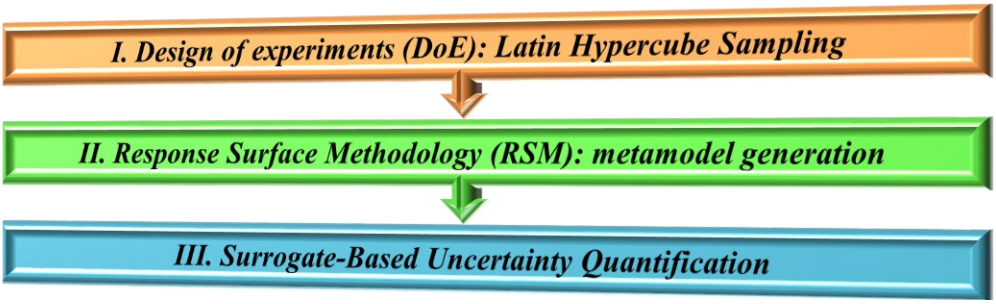

Fig. 2.2 – Workflow for the Surrogate-Based UQ approach

2.3.1. Design of experiments: Latin hypercube sampling

The main target of the first phase (I. in Fig. 2.2) is to collect the maximum amount of information about the analyzed system inside the region of interest (space of variation of the input variables). In particular it is required to use the minimum amount of resources to:

- understand how much the input variables affect the system under investigation;
- reshape the design space for further sampling (if needed);
- provide the information necessary for the generation of a response surface.

Classical 'Design of Experiments' (DoE) methods and the more modern 'Design and Analysis of Computer Experiments' (DACE) methods are both techniques which aim to extract as much trend data from a parametric space as possible, using a limited number of samples. Classical DoE techniques derived from technical disciplines that assumed some randomness and non-repeatability in field experiments (e.g., agricultural yield, experimental chemistry). DoE approaches such as central composite design, Box-Behnken design, and full and fractional factorial design generally place sampling points at the ends of the parametric space, as these designs offer more reliable trend extraction in the event of non-repeatability. DACE methods are different from DoE methods because the non-repeatability component may be omitted as computer simulations are involved. In these cases, space filling designs like orthogonal array sampling and 'Latin Hypercube Sampling' (LHS) are more frequently used in order to accurately infer trend information.

In Latin hypercube designs the parameters space (with dimensions equal to the problem variables) is subdivided into an orthogonal grid with '*N*' elements of the same length per parameter. Within the multidimensional grid, *N* sub-volumes are identified so that only one sub-volume is chosen along each row and column of the grid.
In Fig. 2.3, the selected sub-volumes are blackened giving, in two dimensions, the typical crosswords-like graphical representation of Latin hypercube designs. Inside each sub-volume a sample is randomly chosen.

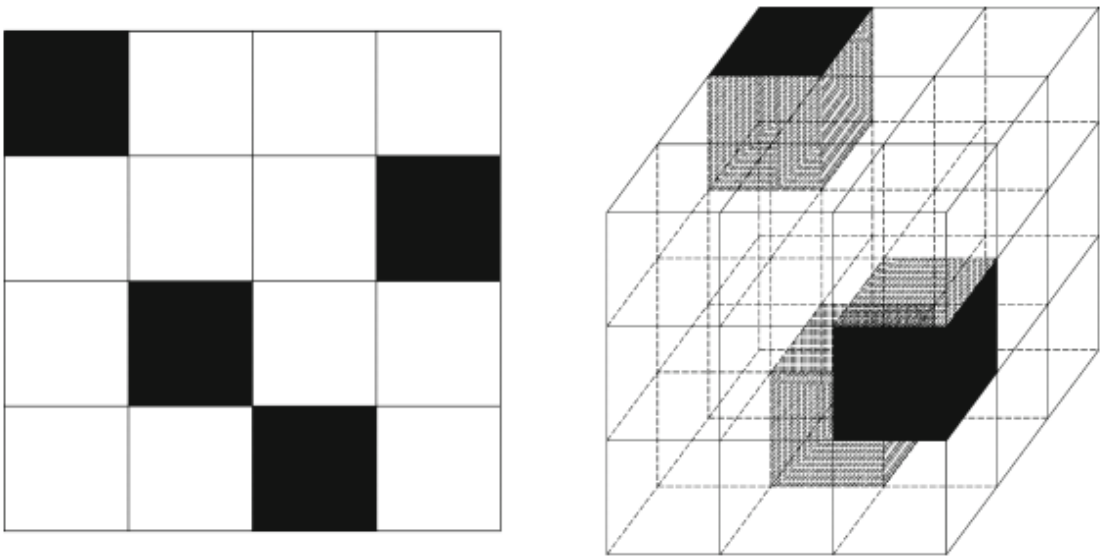

Fig. 2.3 – Example of Latin hypercube designs [22]

From the standpoint of UQ analysis, LHS can be used for any input variable of the problem, provided that spurious correlations among the variables are avoided. It is therefore fundamental to select the sub-volumes in order to spread the samples all over the region of interest. For example, a set of samples along the design space diagonal would satisfy the requirements of a Latin hypercube design, although it would show a strong correlation between the dimensions and would leave most of the design space unexplored.
Considering to apply the LHS technique to the case of k parameters and N samples, two matrices $Q_{N\times k}$ and $R_{N\times k}$ are built [22] to compute a set of Latin hypercube samples. Assuming that each parameter has range [0, 1], the sampling matrix $S_{N\times k}$ containing the samples in its rows is given by:

$$S = \frac{1}{N}(Q - R) \tag{2.1}$$

where:
- $Q_{N\times k}$ is a matrix whose columns are random permutations of the integers from 1 to N;
- $R_{N\times k}$ is a matrix with random values uniformly distributed in [0,1].

The LHS method is widely used because:

- it ensures a better coverage of the design space and a faster convergence than the basic Monte Carlo method;
- generally behaves better to generate a metamodel in case of irregular response functions (like the one shown in Fig. 2.4).

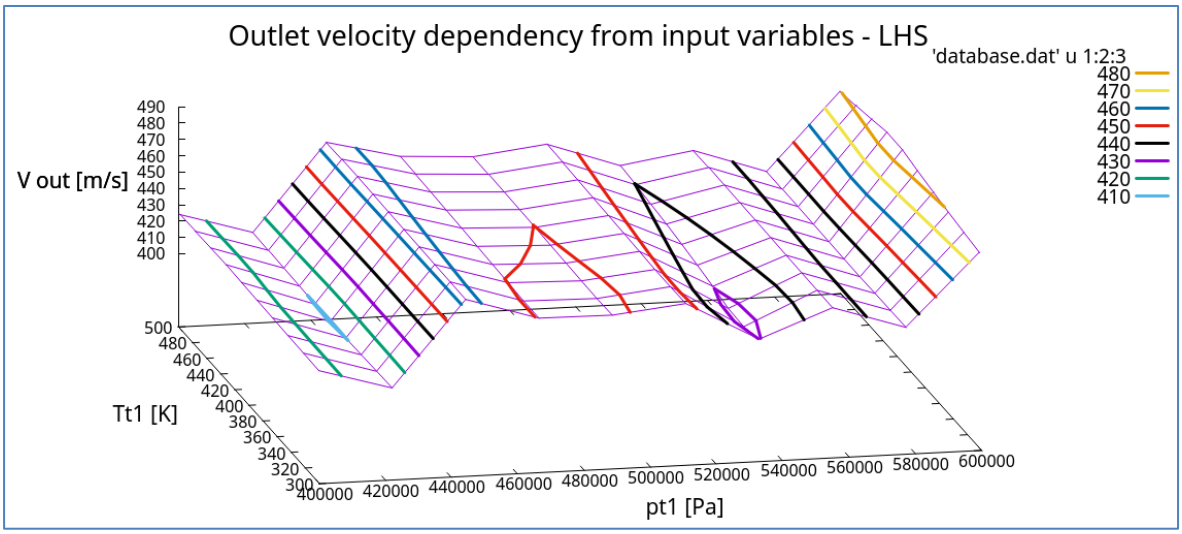

Fig. 2.4 – Example of LHS design: nozzle outlet flow speed (purple grid) is a non-smooth and irregular function (local minima and maxima) of the two input parameters (nozzle inlet total pressure and temperature)

2.3.2. Response Surface Methodology: metamodel generation

Response surface modelling, or response surface methodology (RSM), is closely related to DoE because the main concept is to use the results of a DoE run to create an approximation of the system response functions in the design space. The approximation is called 'response surface' or 'metamodel' and can be built for any objective function: if y is an

unknown function of the input parameters (x), then the response surface $\hat{y}$ differs from y by an error $\varepsilon(x)$:

$$y = f(x) = \hat{f}(x) + \varepsilon(x) \Rightarrow \hat{y} = \hat{f}(x) \tag{2.2}$$

Therefore the outcome of a DoE made of N experiments consists in N (x_i , y_i) pairs in which a point x_i within the design space is associated with the result of the experiment y_i.
The response surface is called:

- 'interpolating' if for each DoE sample point $y_i = \hat{f}(x_i)$;
- 'approximating' if $\varepsilon(x_i) \neq 0$.

To help visualize the shape of a response surface, contour plots are often used. In contour plots constant-value lines are drawn for the response in the design space (as in Fig. 2.4 for the nozzle outlet flow velocity).

The goal of generating a surrogate is to produce an inexpensive approximate model that is intended to capture the salient features of an expensive high-fidelity model (i.e. the actual "physical" model, with which the DoE was generated).
In the UQ perspective, RSM (II. step in Fig. 2.2) can be very functional: although a response surface is an approximation of the 'real' system (CFD model in numerical simulations), it can be used to perform uncertainty quantification analyses through sampling based techniques, which require a large number of response function evaluations to obtain converging statistics (PDF) of the outputs.
The response surface is an analytical function, so an uncertainty quantification analysis based on that model is very fast and computationally low-cost because it requires no additional experiments or simulations to be performed.
Despite the fact that metamodel implementation can be very advantageous, it is important to remark that the design space exploration (made with the DoE) and the response variable behaviour can remarkably affect the results of any analysis performed on the surrogate model. If the design space exploration is poor and the response functions are particularly irregular, the result of the Surrogate-Based Uncertainty Quantification (SBUQ) may be far from the truth because of the bad estimation of the model coefficients or the choice of an unsuitable model.

The surface fitting process consists of three stages:

1) selection of a set of design points;
2) evaluation of the "true" response values (e.g. from a user-supplied simulation code) at these design points;
3) use of response data (from the DoE) to solve for the unknown coefficients (e.g. polynomial coefficients, neural network weights, kriging correlation factors) in the surface fit model.

The first two steps (1 and 2) refer to the DoE already presented in subparagraph 2.3.1, while the third step is the subject of this subsection.
A surrogate of the 'data fit' type is a non-physics-based approximation that typically involves the interpolation or regression of a data set generated from the original model. Data fit surrogates can be further characterized by the number of data points used in the fit:

- 'local' approximation (e.g. first or second-order Taylor series) uses data from a single point;

- ‘multi-point’ approximation (e.g. two-point exponential approximations or two-point adaptive non-linearity approximations) employs a small number of data points often drawn from previous iterations of a peculiar algorithm;
- ‘global’ approximation (e.g. polynomial response surfaces, kriging/Gaussian process, neural networks, radial basis functions, splines) uses a set of data points spread over the domain of interest, frequently generated using a design of computer experiments (this is the type of data fit surrogate used in the following chapters for UQ analyses).

RSM was firstly introduced in 1951 by Box and Wilson [23], who suggested the use of a first-degree polynomial model to approximate a response variable. Since then, many RSM techniques were developed: one of the most common is the ‘Gaussian Process’.
Gaussian Processes (GP) [24, 25] are ‘Bayesian’ methods for RSM. Bayesian probability is an interpretation of the concept of probability, in which probability is interpreted as reasonable expectation representing a state of knowledge or as quantification of a personal belief instead of frequency or propensity of some phenomenon.
In a generic parametric approach the unknown function $y = f(\bar{x})$ is approximated in terms of a function $\hat{y} = \hat{f}(\bar{x}, \bar{\lambda})$, parameterized by the parameters $\bar{\lambda}$:

$$\hat{f}(\bar{x}, \bar{\lambda}) = \sum_{i=1}^{H} \lambda_i \varphi_i(\bar{x}) \tag{2.3}$$

the functions $\varphi_i(\bar{x})$, i = 1, . . . , H are called ‘basis functions’ and may be nonlinear while $\hat{f}(\bar{x}, \bar{\lambda})$ is linear in $\bar{\lambda}$. Many RSM methods differ in the set of basis functions used and in the way the weights are computed.
If the results of a DoE run $(\bar{x}_i, y_i)$ (where i = 1, . . . , N and $\bar{x}_i$ is a k-dimensional vector) are considered, the matrix of input variables $X_{k\times N}$ is the $k \times N$ matrix whose columns are the x_i, $\bar{y}$ is the vector of the y_i (response function) values, $\hat{y}$ is the vector of the response surface at the DoE points and finally $\Phi_{N\times H}$ is the $N \times H$ matrix, whose generic element is:

$$\Phi_{i,j} = \varphi_j(\bar{x}_i) \tag{2.4}$$

So it follows that:

$$\hat{y}_i = \sum_{j=1}^{H} \Phi_{i,j}\, \lambda_j \tag{2.5}$$

In conclusion, it stems from the above that the response surface value $\hat{f}(\bar{x}, \bar{\lambda})$ can be found in a generic point $\bar{x}$ by computing the weights $\bar{\lambda}$.

The surrogate models developed for the analyses discussed in chapters 5 and 6 implement the Gaussian Process method through an uncertainty quantification platform set up using ‘Dakota’, an open source toolset provided with a large number of optimization and uncertainty quantification utilities.
The Gaussian Process involves techniques elaborated in geostatistics and spatial statistics communities [26, 27] to produce smooth surface fit models of response functions starting

from a data set; the correlation function defines the number of times the fitted surface is differentiable. The analytical form of the GP model [28] is:

$$\hat{f}(\bar{x}) \approx \bar{g}(\bar{x})^T \bar{\beta} + \bar{r}(\bar{x})^T \bar{\bar{R}}^{-1} (\bar{f} - \bar{\bar{G}} \bar{\beta}) \tag{2.6}$$

where:

- $\bar{x}$ is the current point in n-dimensional parameter space;
- $\bar{g}(\bar{x})$ is the vector of trend basis functions evaluated at $\bar{x}$;
- $\bar{\beta}$ is a vector containing the generalized least squares estimates of the trend basis function coefficients;
- $\bar{r}(\bar{x})$ is the correlation vector of terms between $\bar{x}$ and the data points;
- $\bar{\bar{R}}$ is the correlation matrix for all of the data points;
- $\bar{f}$ is the vector of response values;
- $\bar{\bar{G}}$ is the matrix containing the trend basis functions evaluated at all data points.

The terms in the correlation vector and matrix are calculated using a Gaussian correlation function and are dependent on an n-dimensional vector of correlation parameters $\bar{\theta} = \{\theta_1, \ldots \theta_n\}^T$ determined using a 'Maximum Likelihood Estimation' (MLE) procedure.
The GP has a hyper-parametric error model, hence it can be used to model surfaces with slope discontinuities along with multiple local minima and maxima; this makes the Gaussian Process a very flexible tool for modelling response functions deriving from the simulation of complex fluid dynamic problems.

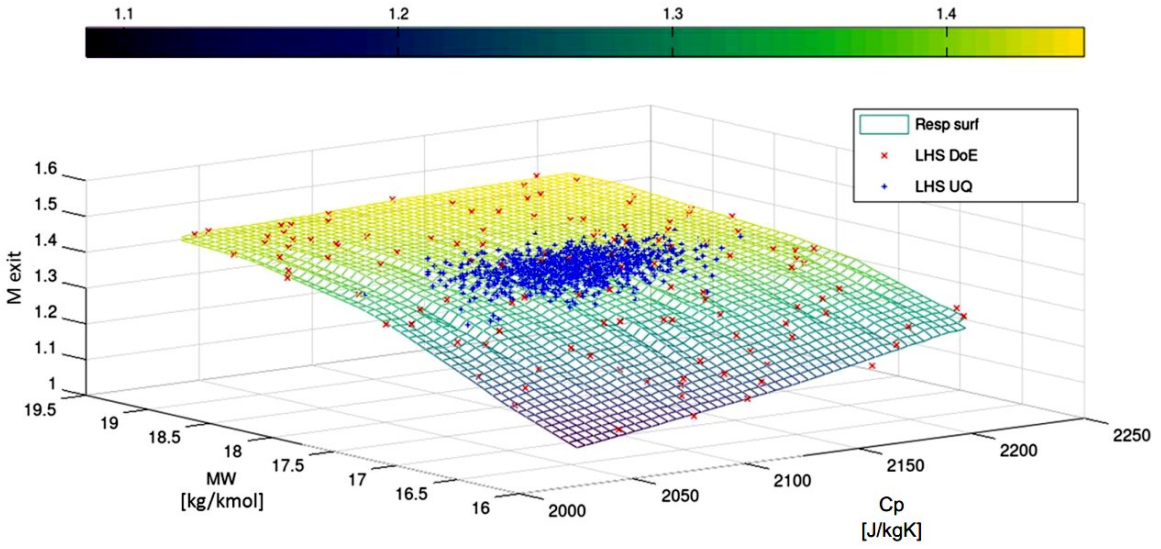

Fig. 2.5 – Example of application of the Gaussian Process to the case of a nozzle subject to off-design conditions due to uncertainty on fluid properties (C_p and MW)

2.3.3. Basic concepts of probability theory

Within a probabilistic framework, the uncertainty propagation consists in the generation of the PDFs of the outcomes, given the distribution of all the input parameters. Assuming that $\bar{x} = (x_1, \ldots x_D)$ is the vector containing the input quantities to the computational model, $y = g(\bar{x})$ is the output of interest, where g is possibly the result of a complex fluid

dynamic simulation. In probabilistic uncertainty quantification approaches, the stochastic input quantities $\bar{x}$ are represented as independent continuous random variables $x_i(\omega_i)$, mapping the sample space Ω_i to real numbers x_i: $\Omega_i \rightarrow \mathbb{R}$.
In practical terms, this assumption increases the dimensionality of the problem: the original deterministic outcome $y = f(x_1, \dots, x_i, \dots x_D)$ becomes a stochastic quantity $y = f(x_1, \dots, x_i, \dots x_D: \omega_1, \dots, \omega_i, \dots \omega_D)$. The target is to compute f_y, i.e. the PDF of y, in order to evaluate the likelihood of a certain outcome or, in general, the statistics of y. The expected value $E[y]$ and the variance $Var[y]$ are defined as [29]:

$$E[y] = \int_{-\infty}^{+\infty} z\, f_y(z) dz \tag{2.7}$$

$$Var[y] = \int_{-\infty}^{+\infty} (z - E[y])^2 f_y(z) dz = E[y^2] - (E[y])^2 \tag{2.8}$$

Note that y is a stochastic variable, while the expected value and the variance are deterministic quantities.

Now consider a continuous function $X(\omega) \in \{0,1\}$, defined on the probability space (Ω, B, P), where Ω is the outcome space, B the events and P is the probability measure.
$X(\omega)$ is a continuous random variable that maps each result ω from the random measurement in an element x of $\mathbb{R}$, and for each event $A_i \in B \subseteq \Omega$ in an interval $B_i \subseteq \mathbb{R}$, as shown in Fig. 2.6 below:

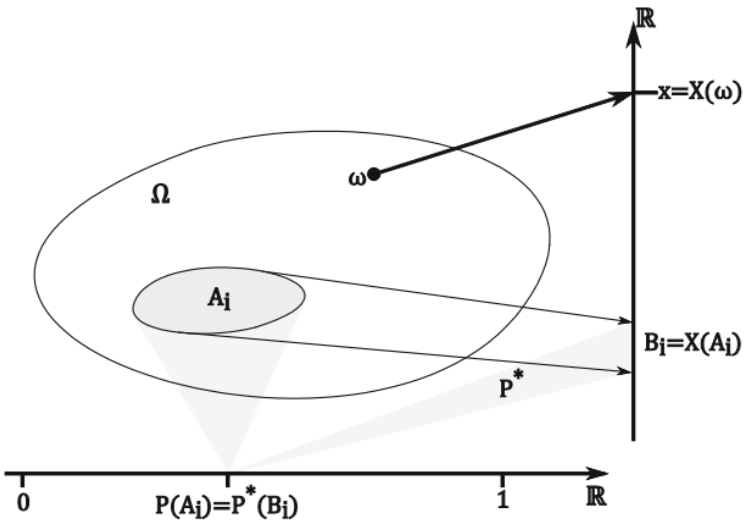

Fig. 2.6 – Mapping of each result ω in an element $x \in \mathbb{R}$ and association of each event A_i in an interval B_i which composes the field B^* on $X(\Omega) \subseteq \mathbb{R}$ [19]

The impossible event $\emptyset \in \Omega$ is associated with the empty set of the real numbers, and the certain event Ω is associated with the interval $X(\Omega) \subseteq \mathbb{R}$. Therefore the random variable $X(\omega)$ assumes a value $x \in \mathbb{R}$ with a defined probability which is induced in $X(\Omega) \subseteq \mathbb{R}$ by the probability $P(\omega)$ that $\omega \in \Omega$ occurs.

A random variable $X(\omega)$ defined in the probability space (Ω, B, P) has a distribution function determined by:

$$F_x(x) = P(X(\omega) \leq x) \tag{2.9}$$

In equation (2.9) the left hand side is called *'Cumulative Distribution Function'* (CDF) of $X(\omega)$, defining the probability distribution in a random experiment. In particular the CDF measures the probability that the random variable $X(\omega)$ assumes values lower or equal to the value *x*; as a consequence of this definition, this function is always not negative and monotonically increasing between 0 and 1.
The *'Probability Density Function'* (PDF) of $X(\omega)$ is instead an integrable function $f_x(x)$ whose integral on a defined set $B \subseteq X(\Omega)$ measures the probability that $X(\omega)$ assumes values $x \in B$:

$$\int_B f_x(x)dx = P(X \in B) \tag{2.10}$$

Consequently, by combining equations (2.9) and (2.10) it is possible to deduce that the PDF is the first derivative of the CDF:

$$f_x(x) = \frac{dF_x(x)}{dx} \rightarrow F_x(x) = \int_B f_x(x)dx \tag{2.11}$$

For a better understanding of the above definitions, a graphical example of PDF and CDF for a generic Gaussian distribution is given in the following Fig. 2.7:

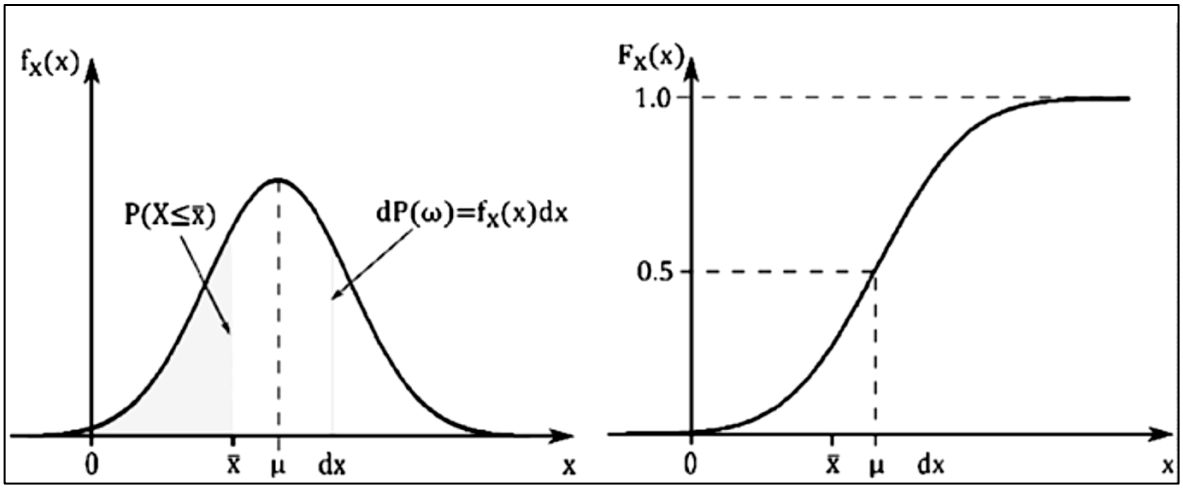

Fig. 2.7 – Gaussian density (left) and cumulative (right) distribution functions [19]

A real random variable $X(\omega)$ has a normal or Gaussian distribution $N(\mu, \sigma^2)$ if the probability density function is in the following analytical form:

$$f_x(x) = \frac{1}{\sqrt{2\pi}\sigma} exp\left[-\frac{1}{2}\left(\frac{x-\mu}{\sigma}\right)^2\right] \tag{2.12}$$

$$\sigma = \sqrt{\sum_{i=1}^{N} \frac{1}{N-1}(x_i - \mu)^2} \tag{2.13}$$

where:
- $\mu \in \mathbb{R}$ is the average value of the PDF (or 1st order moment);
- $\sigma^2 \in \mathbb{R}$ is called variance (or 2nd order moment);
- σ is the standard deviation (equal to variance square root);
- N is the number of samples on which the statistical moments are evaluated.

According to equation (2.11) the Gaussian CDF is then the integral of f_x in (2.12):

$$F_x(x) = \frac{1}{2}\left(1 + \text{erf}\left(\frac{x-\mu}{\sigma\sqrt{2}}\right)\right) \tag{2.14}$$

where the term $erf(z) = \frac{1}{\sqrt{2\pi}} \int_0^z e^{-\frac{1}{2}(t)^2} dt$ is called 'error function'.

Analyzing equation (2.12), in case of a Gaussian function $f_x(x) = exp[-(x)^2]$, the PDF is 'shifted' of the mean value $(x - \mu)$ and then 'stretched' through the standard deviation σ, which defines the dispersion of the variable around the mean value (see Fig. 2.8). In addition, by the definition of the cumulative distribution function in equation (2.9), the CDF value always falls between 0 and 1, depending on the integration region; the integral of the PDF between $-\infty$ and $+\infty$ must be equal to 1, therefore the Gaussian function is normalized with a multiplying factor $\frac{1}{\sqrt{2\pi\sigma}}$.
For example, in a normal distribution the 68.27% of the area under the $f_x(x)$ function falls within the interval $\pm\sigma$, the 95.45% is included in $\pm 2\sigma$ and the 99.73% is inside $\pm 3\sigma$ range.

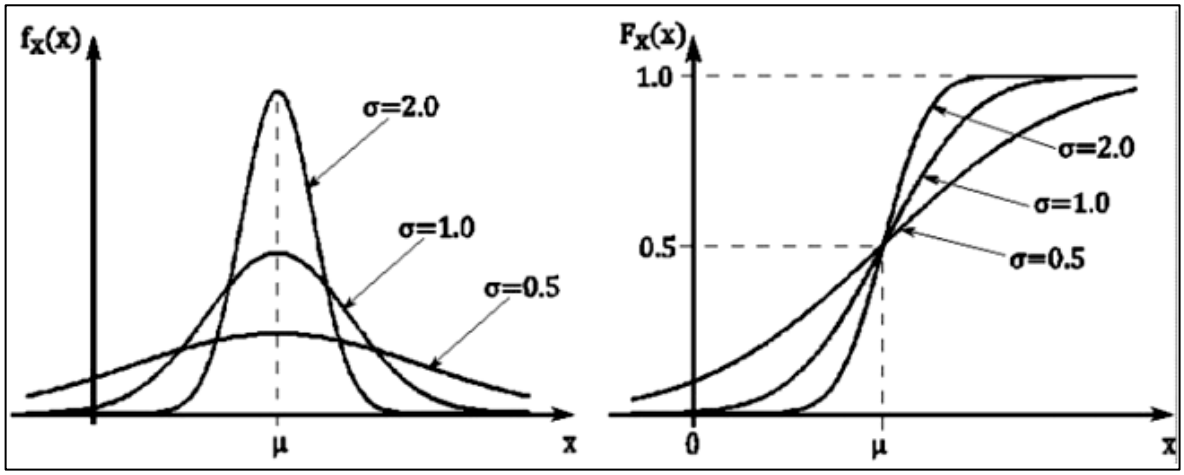

Fig. 2.8 – Gaussian PDF and CDF shape variation for different standard deviations [19]

2.3.4. Sampling-based techniques

Once recalled some basic probability theory concepts, it is now time to focus on sampling-based uncertainty quantification techniques; these ones are the simplest approaches to

propagate uncertainty in numerical simulations: they involve repeated simulations (also called ‘realizations’) with an appropriate selection of the input values. All results are then collected to generate a statistical characterization of the outcome.
The ‘Monte-Carlo’ method (MCM) is the oldest sampling approach. It involves random sampling from the space of the random variables x_i , according to the given PDFs. The method has the advantage that it is simple, universally applicable and does not require any modification to the available computational tools. It is important to note that while the method converges to the exact stochastic solution since the number of samples goes to infinity, the convergence of the average error estimate is slow. Therefore thousands or millions of data samples may be required to obtain accurate estimates.
Several method have been developed to accelerate the Monte Carlo approach. One of the most successful MCM variants is the Latin hypercube sampling approach [30], already discussed in section 2.3.1.
LHS is a stratified sampling technique in which the variation range of each input uncertain variable is divided into N_s “equal probability" segments, where N_s is the required number of samples. The segments relative lengths are individuated by the specified probability distribution function ‘shape’ (e.g. uniform implies equal width segments, normal presents tiny segments near the mean and larger segments toward the tails); the algorithm selects a random sample from each of these ‘equal probability’ segments for every uncertain variables. Then the selected N_s values for each of the individual input parameters are combined in a shuffling operation to create a set of N_s parameter vectors (whose size is the parameters number) with a specified correlation structure. A characteristic feature of the resulting sample set is that each row and column in the hypercube of partitions has exactly one sample.
Since the total number of samples is exactly equal to the number of partitions used for every uncertain variable, an arbitrary number of desired samples is easily settled (compared to less flexible approaches in which the total number of samples is a product or exponential function of the number of intervals for each variable, as happens in many classical design of experiments methods).

In Fig. 2.9 N_s random samples are drawn, one from each of the intervals in which the input uncertain variables (x_1 and x_2) are divided. In LHS the convergence is faster than MCM because the occurrence of low probability samples is reduced. Moreover the LHS samples provide optimal coverage of the parameter space [31], preventing the typical Monte Carlo clusters and holes which in the end lead to a slower convergence of the sampling-based technique.

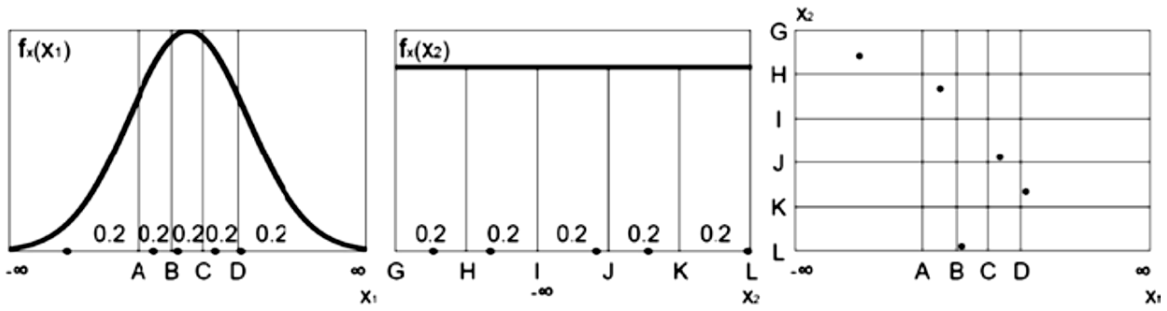

Fig. 2.9 - Example of Latin hypercube sampling applied to N_s = 5 and 2 random variables (x_1 presents a Gaussian PDF while x_2 has a uniform probability density distribution) [19]

2.3.5. Surrogate-Based Uncertainty Quantification

Many uncertainty quantification methods are computationally costly. For example, the sampling-based uncertainty quantification often requires many function evaluations to obtain accurate estimates of the statistical moments or percentage values of a response function probability distribution.

One approach to overcome the computational cost of sampling is to evaluate the "true" function on a fixed set of samples, then use these sample evaluations (DoE) to create a surrogate model or metamodel (RSM) of the underlying "true" function and finally perform random sampling (using thousands or millions of samples) on the approximation to obtain estimates of the mean, variance, and percentiles of the response functions. However, it is fundamental to pay attention when using surrogate-based methods for UQ; in general there is not a unique, straightforward approach to incorporate the surrogate fitting error into the uncertainty estimates of the output produced by sampling the metamodel.
Giunta et al. [32, 33] discussed some of the related issues: the first literature reference [32] shows that statistics of a response based on a surrogate model are less accurate, and sometimes biased, for metamodels constructed on very small sample sizes. However, in many cases the surrogate-based UQ performs well and sometimes generates more accurate estimates of the output statistical quantities.
The second bibliographic reference [33] provides more details on the interaction between sample type and response surface type: e.g., are some response surfaces more accurate if built on a particular sample type? Usually there is not a strong dependence of the surrogate performance with respect to sample type, but some sample types perform better when considering some metrics and not others; much of this work is empirical and application dependent.
The general rule of thumb is that performing surrogate-based uncertainty quantification it is highly recommended to try a variety of surrogates and examining diagnostic goodness-of-fit metrics. To provide a practical example, Dakota UQ tools return some indices that allow the user to determine if the matrix containing the trend basis functions (see section 2.3.2 before) is ill-conditioned, voiding the "warranty" of the surrogate model.

In Fig. 2.10 a practical example of the Surrogate-Based Uncertainty Quantification workflow is shown:

- the first phase (A) deals with the definition of the input variables PDF: in this case Gaussian distributions were assigned to the tip clearance values at rotor leading edge and trailing edge;
- in the second phase (B) the input probability distributions are given to the sampling based UQ method which is applied to the response surface (coloured with a contour plot). The metamodel was generated through the RSM (Gaussian Process) starting from a 64-sample design of experiments (blue points); clustered red points in Fig. 2.10B represent the result of the LHS performed for the uncertainty quantification. In this application the samples number for UQ analysis is two order of magnitude greater than the corresponding number used for DoE generation;
- the input uncertainties propagate through the metamodel leading to the PDFs of the response function, which are extracted in the third phase (C).

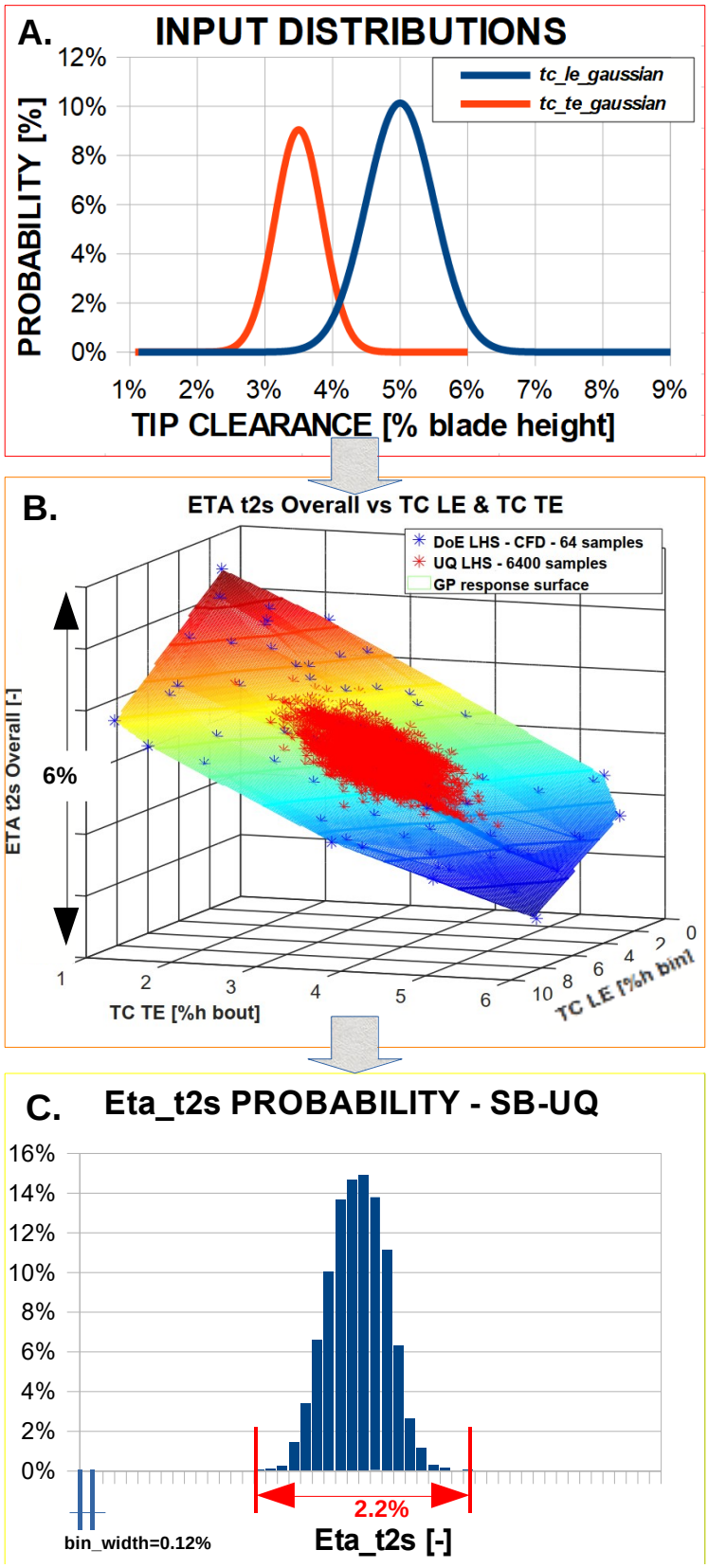

Fig. 2.10 - Example of Surrogate-Based UQ applied to a twin scroll turbine (tip clearance values made non-dimensional for confidentiality reasons)

2.4. Mesh-based uncertainty analysis: Grid Convergence Index method

A fundamental prerequisite of any numerical simulation is the mesh dependence analysis. The influence of the mesh resolution on CFD simulation results must be considered: in fact, grid spacing effects can be responsible for the poor prediction of complex flow structures (i.e. shock waves intensity and position, secondary flows, etc.) and consequently of integral parameters such as stagnation losses.
It is necessary to remark from the beginning that the "perfect mesh" cannot be generated: once the main target of the numerical activity has been identified, the grid control parameters are defined to capture the essential flow phenomena. Moreover the quality of the mesh must be consistent with the chosen numerical approach with a focus on analysis type (steady/unsteady) and turbulence modelling: e.g. the boundary layer development is strongly affected by the computational tool order of accuracy, by the selected turbulence model and also by the grid resolution close to the wall.
Error estimates and uncertainty estimates are related but not equivalent:

- an error estimate is intended to provide an improvement to the result of a computation. For example, if the outcome of an heat transfer coefficient calculation using a particular grid is f and the error estimate is ε, then an improved value (closer to the true value 'f_t') is $f - \varepsilon$;
- an (expanded) uncertainty estimate $U_{x\%}$ is intended to provide a statement that the interval $f \pm U_{x\%}$ defines a range within which the true (mathematical) value of f_t probably falls, with probability of $x\%$. Quantifying this probability is the goal of uncertainty estimation.

The most common uncertainty target for both experiments and computations is ~95% probability that the true value f_t is within the interval $f \pm U_{95\%}$, where $U_{95\%}$ is the estimate of the (expanded) uncertainty at the 95% confidence level.
According to the characteristics of the Gaussian distribution (section 2.3.3), the 95% target confidence level is compatible with the $\pm 2\sigma$ range for a normal PDF; however, it is important to clarify immediately that the concept and the semi-empirical methods presented below do not depend on the assumption of Gaussian distribution or any other distribution.
Uncertainty estimates ($U_{95\%}$) can be calculated following a five-step procedure for the application of the 'Grid Convergence Index' (GCI) method [34]. The GCI determines the grid influence on the evaluation of a specific parameter; it represents the numerical uncertainty connected to the spatial filter and can be compared to the experimental uncertainty. The leading concept is to estimate the error included in the selection of a specific computational mesh with respect to a reference solution obtained through an asymptotic approach. The main steps are summarized below:

1) define a rule for the calculation of a representative cell dimension denoted 'h'.
   For example for three-dimensional, structured, geometrically similar grids (not necessarily Cartesian):

$$h = [(\Delta x_{max})(\Delta y_{max})(\Delta z_{max})]^{1/3} \tag{2.15}$$

   Instead for unstructured grids it is possible to define:

$$h = \left[\left(\sum_{i=1}^{N} \Delta V_i\right)/N\right]^{1/3} \tag{2.16}$$

where N is the total number of cells used for the computations and ΔV_i stands for the volume of the '$i-th$' cell. From equations (2.15) and (2.16) h is usually defined as the cubic root of the mean value of the elements volume;

2) select three significantly different grid resolutions: for example coarse, medium and fine resolution (denoted respectively by the suffixes 3 , 2 and 1) and run simulations to determine the values of key variables to the target of the simulation study (e.g. a variable φ). One of the constrains of this procedure is that the grid refinement factor $r = h_{coarse}/h_{fine}$ (ratio between the h values of two consecutive meshes) is greater than 1.3 (a number based on experience and not on some formal derivation). It is highly recommended to refine the mesh as isotropically as possible, i.e. not to use different grid refinement factors in different directions (e.g. $r_x = 1.3$ and $r_y = 1.6$); otherwise misleading observed order of accuracy (p – see definition below) values are obtained;
3) compute the apparent (or observed) order of the method from reference [35]:

$$p = \frac{1}{\ln r_{21}} \left| \ln \left| \frac{\varepsilon_{32}}{\varepsilon_{21}} \right| + q(p) \right| \tag{2.17}$$

$$q(p) = \ln \left(\frac{r_{21}^p - s}{r_{32}^p - s} \right) \tag{2.18}$$

where $\varepsilon_{32} = \varphi_3 - \varphi_2$, $\varepsilon_{21} = \varphi_2 - \varphi_1$, $r_{21} = h_2/h_1$, $r_{32} = h_3/h_2$ (with $h_1 < h_2 < h_3$) and $s = sign(\varepsilon_{32}/\varepsilon_{21})$. The observed order of accuracy can be calculated imposing $q(p) = 0$ for $r = constant$; in case of $r \neq constant$ instead, equations (2.17) and (2.18) can be solved using fixed point iteration with the initial guess of $q = 0$.
Three different mesh resolutions should be satisfactory for the calculation of the observed order p if some of the values of the predicted variable φ on the three grids are in the asymptotic region for the simulation series. Important factors are the resolution of the initial mesh and where is the expected value of φ as a function of the resolution of the mesh;
4) compute the extrapolated values through the apparent order of accuracy:

$$\varphi_{21,ext} = \left(r_{21}^p \varphi_1 - \varphi_2 \right) / \left(r_{21}^p - 1 \right) \tag{2.19}$$

5) calculate and report the approximate relative error in dimensionless form (2.20), the estimated extrapolated relative error (2.21) and finally the 'fine' (associated to the finest grid resolution) Grid Convergence Index (2.22):

$$e_{21,app} = \left| \frac{\varphi_1 - \varphi_2}{\varphi_1} \right| \tag{2.20}$$

$$e_{21,ext} = \left| \frac{\varphi_{21,ext} - \varphi_1}{\varphi_{21,ext}} \right| \tag{2.21}$$

$$GCI_{21,fine} = \frac{F_s \cdot e_{21,app}}{r_{21}^p - 1} \tag{2.22}$$

where F_s indicates the Factor of Safety.

Roache [35] recommended a value for $F_s = 1.25$, but only when the GCI calculation is performed using at least three grid resolutions and the observed p. Roache suggested this value based on empirical studies, concluding that a value of $F_s = 1.25$ results in a GCI with a 95% confidence interval. Further experience in hundreds of CFD cases (more than 500 proven cases) by dozens of research groups has supported this empiricism [35, 36, 37, 38]: a value of $F_s = 1.25$ is therefore recommended with three-grid studies involving a "structured" refinement of the grid. It is important to highlight that a base mesh can belong to the 'unstructured' type, but the sequence of meshes (coarse, medium, fine) generated for the GCI may derive from a 'structured' refinement of the grid.
Whenever the computed observed order of the method p (equation 2.17) falls below 1.0, it is still possible to assign an uncertainty band assuming p = 1.0. In this way, two calculations can be provided, one with the observed p (<1) and one with p = 1.0, as a measure of the sensitivity of the error band to the apparent order of accuracy p.
The form of the GCI is theoretical, but the use of absolute values for estimated errors and the factor F_s are based on the examination of several hundred CFD case studies. The empirical tests resulted in the determination of conservatism in 95% of the cases, corresponding to $GCI = U_{num}$ with a confidence level of 95%.

An example of application [39] of the presented GCI calculation procedure is summarized in Tab. 2.1. The case study concerns steady, turbulent flow over a backward facing step simulated on non-uniform structured grids with the total number of cells defined by three grid resolutions (N_1 , N_2 and N_3). The variable selected for the evaluation of uncertainties is the dimensionless reattachment length (L) at a specific location of the fluid domain.

Tab. 2.1 – Example of GCI calculation procedure for a backward facing step [39]

N_1	18000
N_2	8000
N_3	4500
r_{21}	1.5
r_{32}	1.33
φ_1	6.06
φ_2	5.97
φ_3	5.86
p	1.53
$\varphi_{21,ext}$	6.17
$e_{21,app}$	1.50%
$e_{21,ext}$	1.71%
$GCI_{21,fine}$	1.46%

The above calculations lead to the conclusion that the value of the reattachment length would be more correctly reported as $L = \varphi_1 \pm (GCI_{21,fine} \cdot \varphi 1)$, i.e. $L = 6.06 \pm 0.09$.

The presented methodology can be applied to structured and unstructured grid types. In the latter case, a systematic or "structured" refinement of the mesh brings the algorithm to the best results. Another example of application of the GCI calculation procedure is reported in Appendix A, which deals with the determination of the numerical uncertainty derived from the mesh of some characteristic performance parameters of the twin entry volute investigated in this doctoral thesis.
It should be emphasized that the grid convergence index does not provide any information on the accuracy of the code itself: the code must be verified for the same class of problems and validated against experimental data.
In conclusion, the analysis presented in this section highlights that a reliable treatment of mesh-dependent uncertainties in CFD campaigns must be included in the optimization tools commonly used by the Industry. Consequently, high-fidelity computational fluid dynamics simulations should include the evaluation of the grid spacing impact on global parameters of the system under examination, followed by model assessment and uncertainty quantification.

2.5. Operational and geometrical uncertainty analysis in CFD

The previous paragraph deals with numerical uncertainty; recalling the uncertainties classification made in paragraph 2.1, two uncertainty sources remain to be discussed: operational and geometric.
The UQ analysis within a simulation environment that embeds CFD is becoming an effective approach for industrial use thanks to the concurrent development of both soft-computing methods and computer performance. The use of CFD coupled to optimization algorithms for the automatic design optimization of industrial components is nowadays a mature technology [40, 41].
One of the main issues addressed in any engineering design problem is to predict the performance of the component or system as accurately and realistically as possible. The off-design behaviour of a system is not only related to the deterministic variation of the input parameters, but also to the aleatory uncertain which can characterize the input data and the geometrical tolerances. Hence, in order to improve the accuracy and the reliability of the numerical predictions, it is necessary to understand how the uncertainties can affect the results of the problem under investigation. This is one of the main targets of uncertainty quantification analyses, with direct positive fall-out on engineering problems.

A well known problem by CFD users is the exact knowledge of boundary conditions to perform numerical simulations. As an example, chapter 5 deals with the influence of the discharge pressure on the operating conditions, flow structure and performance of a supersonic de Laval nozzle. Another application concerns instead the effects of the gas chemical composition on the expansion nozzle performance.
Considering instead the turbomachinery field, the various components are subject to non-uniform conditions, the distribution of which must be carefully studied: chapter 3 deals with the effect of flow non-uniformities at rotor inlet on the performance of twin scroll radial turbines.
Another fundamental aspect to be considered in every simulation is represented by the differences between the real geometrical model (the actual manufactured machine) and the simulated one (the CAD model).
The computational domain used in CFD to simulate a gas turbine and the real control volume are not identical. This is due to two main reasons:

1. the actual machine is different from the designer's technical projects due to manufacturing (epistemic) and assembling (aleatory) uncertainties;
2. usually the computational domain does not simulate all geometric characteristics, such as fillets.

It is noteworthy to mention the problem arising from tip clearances in rotor rows. Through the rotational periodicity boundary condition, it is possible to perform CFD on a single turbine rotor channel and this means that a single tip clearance dimension must be specified; however, it has been experimentally proved that each blade has a different value of tip gap, which moreover depends on the rotational speed [42]. Consequently, the definition of an average value for the tip clearance represents a mixed epistemic-aleatory uncertainty due, respectively, to the known statistical distribution of the values and the limits of the experimental measure.
On this theme, chapter 6 deals with the analysis of the effects of tip clearance uncertainties on the performance of a twin scroll radial turbine.

2.6. An emerging UQ technique: Polynomial Chaos Expansion

The second UQ approach investigated in this doctoral thesis is the Polynomial Chaos Expansion (PCE), which is based on a multidimensional orthogonal polynomial approximation formed in terms of standardized random variables.
Wiener introduced first the term 'Polynomial Chaos' (PC) expansion in 1938 in his work on the decomposition of Gaussian stochastic processes [43]; then Ghanem and Spanos [44] combined the use of PC with finite element method for modelling the uncertainty for various solid mechanics problems.
Stochastic Expansion methods aim to estimate the functional relationship between response functions and their random inputs using the notions of projection, orthogonality and weak convergence [44, 45]; thus they provide a more thorough uncertainty representation to be used in simulations involving multiple codes.
Polynomial chaos expansions (PCE) use multivariate orthogonal polynomials that are customized to represent peculiar input probability density functions. Several methods can lead to the evaluation of the expansion coefficients: e.g. a spectral projection approach (based on sampling, tensor-product quadrature, etc.) or a regression approach (least squares). Starting from the base, a polynomial of degree $N \in \mathbb{N}$ can be written as:

$$Q_n(x) = a_N x^N + a_{N-1} x^{N-1} + \cdots a_1 x + a_0 \tag{2.23}$$

It is possible to indicate a system of polynomials $\{Q_N(x), \mathrm{N} \in \mathbb{N}\}$ as 'orthogonal' with respect to the function $w(x)$ if it fulfills the 'orthogonality conditions' :

$$\int_D Q_N(x) Q_M(x) w(x) \mathrm{dx} = h_N^2 \delta_{NM} \qquad N, M \in \mathbb{N} \tag{2.24}$$

where D is the support of Q_N, $w(x)$ is a specified weight function, h_N are non-zero constants and δ_{NM} is the Kronecker delta function, where $\delta_{NM} = 0$ if $N \neq M$ and $\delta_{NM} = 1$ if $N = M$.
Tab. 2.2 collects the set of classical orthogonal polynomials which supply an optimal basis for different types of continuous probability distribution. This set belongs to the family of

hypergeometric orthogonal polynomials known as the "*Askey scheme*" [46], for which the Hermite polynomials originally used by Wiener [43] are a subset.
The orthogonality of these basis selections with respect to 'weighting functions' (that correspond to the PDFs of the continuous distributions when placed in a standard form) is the characteristic that makes them "optimal" [47]. As the reader can see in Tab. 2.2, the density and weighting functions are different by a constant factor due to the condition that the integral of the PDF on the support range is one.

Tab. 2.2. – Linkage between the type of generalized Polynomial Chaos and its underlying random variables [47]

Distribution	Density function	Polynomial	Weight function	Support range
Normal	$\frac{1}{\sqrt{2\pi}}e^{\frac{-x^2}{2}}$	Hermite $He_n(x)$	$e^{\frac{-x^2}{2}}$	$[-\infty,\infty]$
Uniform	$\frac{1}{2}$	Legendre $P_n(x)$	1	$[-1,1]$
Beta	$\frac{(1-x)^\alpha(1+x)^\beta}{2^{\alpha+\beta+1}B(\alpha+1,\beta+1)}$	Jacobi $P_n^{(\alpha,\beta)}(x)$	$(1-x)^\alpha(1+x)^\beta$	$[-1,1]$
Exponential	e^{-x}	Laguerre $L_n(x)$	e^{-x}	$[0,\infty]$
Gamma	$\frac{x^\alpha e^{-x}}{\Gamma(\alpha+1)}$	Generalized Laguerre $L_n^{(\alpha)}(x)$	$x^\alpha e^{-x}$	$[0,\infty]$

It is important to note that if all random inputs can be described using independent normal, uniform, exponential, beta, and gamma distributions, it is possible to apply the Askey polynomials directly. Otherwise, if correlations or other distribution types are present, additional techniques are required ('*Numerically generated orthogonal polynomials*' [47]).
The set of polynomials from Tab. 2.2 are used as an orthogonal basis to approximate the functional form between the stochastic response output and each of its random inputs.
The chaos expansion for a response *R* takes the form:

$$R = a_0B_0 + \sum_{i_1=1}^{\infty} a_{i_1}B_1(\xi_{i_1}) + \sum_{i_1=1}^{\infty}\sum_{i_2=1}^{i_1} a_{i_1i_2}B_2(\xi_{i_1},\xi_{i_2}) + \sum_{i_1=1}^{\infty}\sum_{i_2=1}^{i_1}\sum_{i_3=1}^{i_2} a_{i_1i_2\,i_3}B_3(\xi_{i_1},\xi_{i_2},\xi_{i_3}) + \cdots \tag{2.25}$$

where each further set of nested summations corresponds to an additional order of polynomials in the expansion formulation and the random vector dimension is unlimited. Replacing the order-based indexing with a term-based indexing:

$$R = \sum_{j=0}^{\infty} \alpha_j\psi_j(\xi) \tag{2.26}$$

There is a one-to-one correspondence between $a_{i_1i_2\ldots i_n}$ and α_j and between $B_n(\xi_{i_1},\xi_{i_2}\ldots\xi_{i_n})$ and $\psi_j(\xi)$, which are multivariate polynomials that involve products of the one-dimensional polynomials.
The next step consists in truncating the infinite expansion to a finite number of random variables (the input uncertain variables) and to a definite expansion order:

$$R \cong \sum_{j=0}^{P} \alpha_j\psi_j(\xi) \tag{2.27}$$

According to the 'tensor-product' expansion approach [47] polynomial order bounds are applied on a per-dimension basis (no total order limit is applied) and all combinations of the one-dimensional polynomials are included. Furthermore, the tensor-product expansion supports anisotropy in polynomial order for each dimension (variable), so the polynomial order limits for each dimension can be specified independently.
PCE estimates its coefficients α_j using a 'spectral projection' approach, which projects the response on each basis function using inner products and uses the polynomial orthogonality properties to extract every expansion coefficient:

$$\alpha_j = \frac{\langle R, \psi_j \rangle}{\langle {\psi_j}^2 \rangle} = \frac{1}{\langle {\psi_j}^2 \rangle} \int_{\Omega} R \ \psi_j \, \varrho(\xi) d\xi \tag{2.28}$$

where each inner product involves a multidimensional integral over the support range (Ω) of the weighting function.
In particular, $\boldsymbol{\Omega} = \boldsymbol{\Omega}_1 \otimes \cdots \otimes \boldsymbol{\Omega}_n$, with possibly unlimited intervals $\boldsymbol{\Omega}_j \subset R$ and the form of the tensor product of the joint probability density (weight) function $\varrho(\xi) = \prod_{i=1}^{n} \varrho_i(\xi_i)$. The denominator in equation (2.28) is the norm squared of the multivariate orthogonal polynomial, while the numerator is computed numerically using quadrature approach; this technique employs a tensor product of one-dimensional quadrature rules.
In the multivariate case ($n > 1$) for each $f \in C^0(\Omega)$ and the multi-index $i = i_1, i_2, \ldots i_n \in \mathbb{N}^n{}_+$, the full tensor product quadrature formula corresponds to:

$$\begin{aligned} {Q_i}^n f(\xi) &= \left(\mathcal{U}^{i_1} \otimes \cdots \otimes \mathcal{U}^{i_n}\right)(f)(\xi) = \\ &= \sum_{j_1=1}^{m_{i_1}} \cdots \sum_{j_n=1}^{m_{i_n}} f(\xi_{j_1}^{i_1}, \cdots, \xi_{j_n}^{i_n}) \ (\omega_{j_1}^{i_1} \otimes \cdots \otimes \omega_{j_n}^{i_n}) \end{aligned} \tag{2.29}$$

where the above product requires $\prod_{j=1}^{n} m_{ij}$ function evaluations.
When the number of input random variables is limited, full tensor product quadrature is a very efficient numerical tool. On the other hand, approximations based on tensor product grids suffer from the "curse of dimensionality" as the number of collocation points in a tensor grid quickly grows exponentially with the number of input random variables [47].
In chapter 6 the analysis of the effects of tip clearance uncertainties on the performance of a twin scroll radial turbine is performed using the PCE method. In this case Gaussian quadratures are selected using an isotropic approach. This means that the UQ algorithm uses the same quadrature order $m_{ij} = m$ for the input variables (clearance values at rotor leading edge and trailing edge, i.e. two dimensions), resulting in a total of m^n function evaluations to compute the PCE coefficients α_j.
A distinguishing (and positive) feature of the PCE methodology is that the final solution is expressed as a functional mapping and not merely as a set of statistics, as in the case of many nondeterministic approaches (e.g. sampling-based UQ). However, polynomial approaches suffer from the aforementioned curse of dimensionality; so following a general rule of thumb their application is limited to cases where the number of uncertain variables is less than five (such as the one presented in the following chapter 6) since the number of CFD simulations required increases exponentially with the number of input variables [48]. PCE method provides analytic statistical moments of the response functions; nevertheless, cumulative distribution function probabilities are evaluated numerically by sampling (LHS) on the expansion.

Chapter 3

Insight into twin scroll turbines fluid dynamics

The final goal of this PhD thesis is to integrate uncertainty quantification techniques with the CFD simulation of twin entry radial turbines for turbocharging applications. The essential prerequisites for pursuing this objective are:

(1) the detailed study of this kind of turbomachinery, aimed at understanding the parameters which affect their performance and formulating performance prediction methods;
(2) the acquisition of skills in DoE generation, application of the RSM and implementation of uncertainty quantification techniques. This skill set was previously tested on a case study (the supersonic nozzle which is the main topic of chapter 5) in order to set up the workflow that afterwards has been applied to the IFR twin scroll turbines.

Chapter 3 deals with the first (1) step, which in turn is articulated into several research themes:

I) experimental validation of the CFD models [49];
II) quantitative and qualitative evaluation of twin scroll volute losses, definition of flow non-uniformity parameters at impeller inlet and hub to shroud analysis with the formulation of brand new non-uniformity indices [49, 50];
III) study of the influence of the 'backside cavity' (the fluid cavity located behind the impeller upstream of the seals) on turbine performance [49];
IV) development of a numerical method to represent the degree of reaction. The analysis of the CFD results obtained from three different turbines subject to various operating conditions (different rotational speeds and admission conditions) highlights the reliability limits of some performance prediction methods frequently proposed in literature. For the sake of brevity, this research topic is not addressed in this chapter, but the reader can find all the details of the work done on this issue in the paper [51] cited in the bibliography.

3.1. Experimental validation of the twin scroll turbine CFD model

This paragraph concerns a complete (volute and full rotor) CFD model of a twin scroll radial turbine which has been developed to understand the capabilities of current industrial CFD approaches applied to these complex cases. Steady simulations were performed with Ansys CFX® commercial CFD solver in a broad range of working conditions at both full and partial admission (see section 1.3.1), with and without backside cavity. The total to static efficiency and the mass flow parameter (MFP) of the turbine were then calculated and compared with the experimental database to validate the numerical model.

3.1.1. Reference geometry

The "test case" turbine is an IFR twin entry turbine for automotive turbocharging applications; it is classified as a small size radial turbine, capable of generating about ten kilowatts. Geometrical data are confidential therefore all quantities have been reported in the following tables in non-dimensional or reduced form.
Since the turbine in question is twin scroll, the ICE exhaust manifolds are coupled to two volute inlet sections, denoted according to their relative position with respect to the rotor:

hub and shroud side respectively (see Fig. 3.1 below). The volute geometrical parameters are listed in Tab. 3.1 and are interpreted as follows:

- radial extension of the vaneless nozzle was made dimensionless with the radius (r_{1sh}) measured from the center of gravity of inlet duct section which feeds the shroud branch;
- volute area ratio (AR) was obtained by comparing the volute outlet section (A_2) with the total inlet area (A_{1tot}), computed from the sum of shroud and hub side inlet areas (A_{1sh} and A_{1hub} respectively);
- dimensional values refer to the A/r of the volute branches. For the two inlet sections this parameter was calculated using the corresponding radius ($r_{1hub} < r_{1sh}$).

Tab. 3.1 – Twin scroll volute geometrical parameters

Geometric parameter	**Value**
Vaneless nozzle radial extension [-]	0.0252
Volute area ratio ($AR = A_2 / A_{1tot}$) [-]	0.910
A_{1hub}/r_{1hub} [mm]	9.33
A_{1sh}/r_{1sh} [mm]	16.2

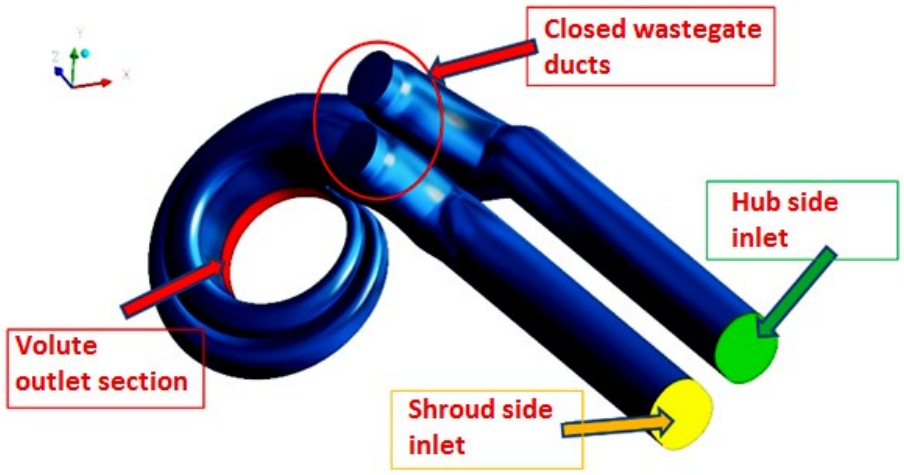

Fig. 3.1 - Position of inlet and outlet sections of the twin entry volute. The exhaust gas bypass ducts are circled in red

The turbine impeller (see following Fig. 3.2b) has $z_b = 9$ blades. The rotor leading edge is cut-off and aligned with the radial direction ($\beta_{b2} = 0°$), while at the trailing edge the blade is swept from hub to shroud, with a metal angle β_{b3} proportional to the radius in order to follow the increase in relative circumferential velocity component (attributable to the peripheral speed variation). All rotor geometrical data reported in Tab. 3.2 have been made non-dimensional with impeller inlet radius r_2, which is not intentionally provided to the reader. The impeller reference dimensions are identified in Fig. 3.2a that shows the meridian section of a generic twin entry radial turbine.
A peculiar feature of the radial machine is the backside cavity, which consists of the volume between the back disk (rotating surface behind the impeller block) and the stationary housing; for better understanding the volume is coloured green in Fig. 3.2b).

Tab. 3.2 - Dimensionless geometric data of the studied centripetal impeller

Geometric parameter	Dimensionless value
Inlet blade height (b_2)	0.299
Outlet blade height (b_3)	0.572
Outlet blade radius (r_3)	0.843
Rotor axial size (l)	0.829
Inlet blade thickness (uniform along blade height)	0.0361
Outlet blade thickness (hub)	0.0675
Outlet blade thickness (shroud)	0.0359

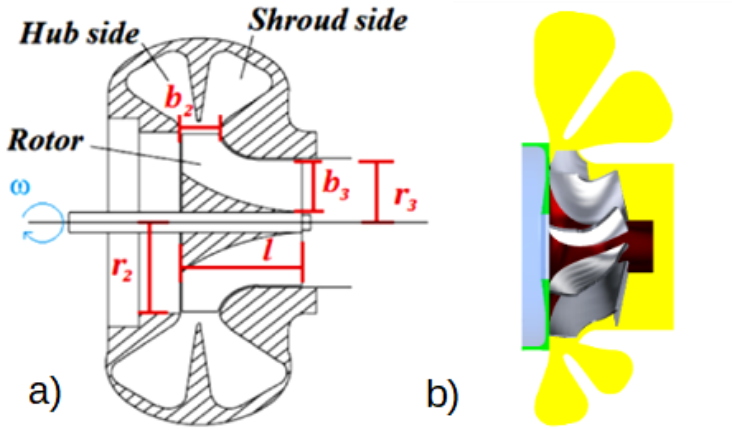

Fig. 3.2 - a) Sketch of the meridian section of a generic twin scroll turbine. b) Rotor view with a yellow cut of the volute and rotor passage, while the backside cavity is in green

3.1.2. Numerical setup

The unstructured grid of the twin scroll volute (Fig. 3.3A) is composed of about 8 million elements (3 million nodes) with a 'tetra size ratio' set to 1.25. Special attention was paid to the accurate resolution of the boundary layer on the walls by mean of 10 prism layers with exponential clustering (height ratio of about 1.4) to the wall. In order to avoid the use of 'wall functions', the height of the first layer has been calculated to get $y+$ close to one.
Concerning the volute mesh quality, the aspect ratio (AR) resulted above 0.5 for the 99.5% of the elements, with the 60% of the cells having an AR>0.95 (where AR=0 indicates that the element has zero area or volume, while AR=1 corresponds to a perfectly regular cell).
An 'H-O-H' (H-topology and O-grid around the blade) structured grid was generated for the rotor with a target value of approximately 500 thousand nodes for the single channel, which is displayed in Fig. 3.3B. Regarding the mesh quality control:

- the 'minimum face angle' was set at 15 [deg], considering as acceptable a percentage of "bad" elements not exceeding 0.1% of the overall mesh;
- the number of constant-size elements and the total number along the blade height were selected to get an expansion rate of about 1.25 (good values between 1.2 and 1.4);
- the 'maximum element volume ratio' was set to 20, while a 'maximum edge length ratio' of 1000 was considered, using the solver 'double precision' option to ensure greater numerical accuracy given the significant cells size variation inside the passage.

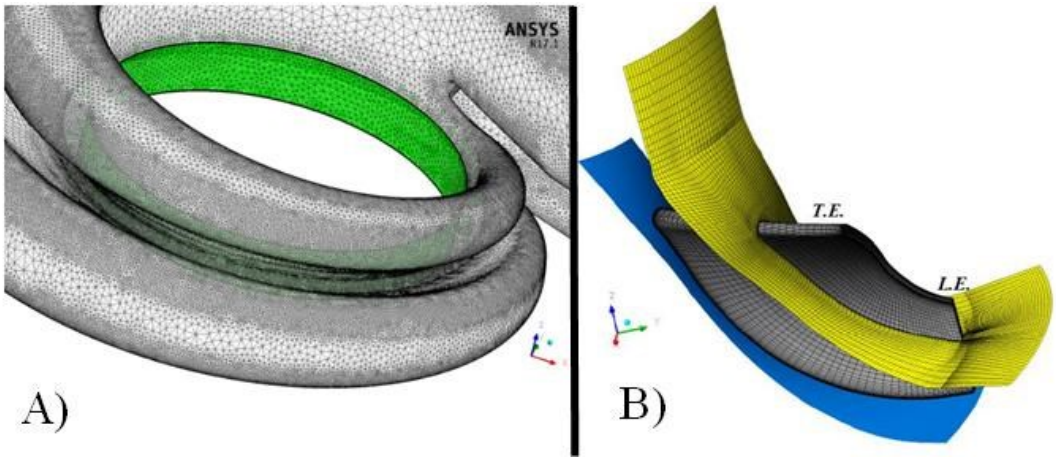

Fig. 3.3 - A) Detail of the unstructured grid on the two volute branches; the volute outlet section is highlighted in green. B) Structured mesh of the single rotor channel

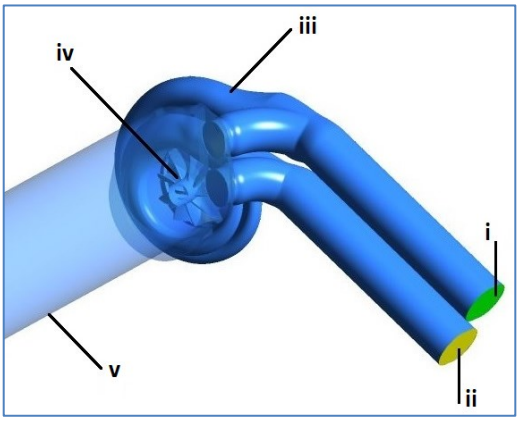

Fig. 3.4 - CFD model: i)-ii) inlet sections, iii) twin entry volute, iv) rotor, v) discharge pipe

The CFD model is divided into three domains (Fig. 3.4): volute, rotor and discharge pipe. Tab. 3.3 summarizes the type of boundary conditions assigned to each computational domain of the numerical model; these are valid for the full admission condition. In partial admission one of the inlets is closed and this condition was simulated by introducing a wall boundary for the non-fed inlet (zero mass flow). Experimental data were used as boundary conditions for inlet total conditions, outlet static pressure and rotational speed.

Tab. 3.3 - Boundary conditions set for the different domains of the CFD model

Volute	• total pressure and total temperature, different for each inlet • flow direction orthogonal to volute inlet sections • 5% inlet turbulence intensity
Rotor	• rotational speed • stationary shroud wall (‘counter-rotating’ at the same rotor speed)
Discharge pipe	• static pressure on outlet section

Steady state calculations were performed with stage (mixing-plane) interfaces between static and rotating domains. This simulation setup is necessary to validate the CFD model

with experimental data obtained at gas stand test bench (therefore without actually coupling the turbine with the ICE). The validation measurements provided by the industrial partner were taken in the test rig keeping the turbocharger insulated to minimize heat losses through the walls; therefore adiabatic option was selected for the 'wall' type boundary conditions, neglecting heat transfer from the fluid domains towards the outside.
The compressible flow model consists in *Reynolds Averaged Navier-Stokes* (RANS) equations; the Shear Stress Transport (SST) model for turbulence closure was adopted due to its higher accuracy and calibration in the code (Ansys CFX®) for turbomachinery applications. In fact, the SST takes into account the transport of turbulent shear stresses, providing very accurate predictions on the trigger and degree of flow separation under adverse pressure gradients. The equations have been solved with the 'high resolution' scheme that has second order accuracy. Finally, the fluid is modeled as a perfect gas with a specific heat C_p=1.15 [kJ/(kg*K)] and a dynamic viscosity that varies with temperature according to Sutherland's law:

$$\mu = \mu_{ref}\left(\frac{T}{T_{ref}}\right)^{\frac{3}{2}}\frac{T_{ref}+Su}{T+Su} \tag{3.1}$$

3.1.3. Boundary conditions: selected operating points

Twin scroll turbines can operate under different admission conditions, as already discussed in section 1.3.1. The experimental validation of the turbine CFD model was carried out considering the same admission conditions tested by the turbo supplier:

- partial admission → one of the two branches is not directly powered by the ICE. The cases studied with mass flow passing through the shroud branch only were denoted 'partial shroud', while in the opposite cases 'partial hub';
- full admission → both volute branches are fed by roughly the same exhaust gas mass flow (differences mainly due to the geometric asymmetry of the two sectors).

Even if the partial admission condition is difficult to achieve under normal engine operating conditions, the partial admission tests are fundamental to evaluate turbine fluid dynamic losses and to translate them into the real pulsating operation of the turbocharger coupled with the ICE.

Tab. 3.4 - Set of cases tested at full and partial admission

Full		**Partial shroud**		**Partial hub**	
N [rpm/(K^0.5)]	PRF	N [rpm/(K^0.5)]	PRF	N [rpm/(K^0.5)]	PRF
N1	1.31	N1	1.56	N1	1.51
	1.37		1.69		1.62
	1.42		1.77		1.69
N2	1.79	N2	2.35	N2	2.18
	1.99		2.72		2.51
	2.15		2.99		2.76
N3	2.54	N3	3.34	N3	3.15
	2.83		3.72		3.49
	3.15		4.35		3.93

Tab. 3.4 presents the set of pressure ratios selected for the different rotational speeds and admission conditions: nine operating points (three for each rotational speed) were individuated over three different iso-speed lines (N1= 'low', N2= 'medium', N3= 'high' speed) to properly cover the turbine working range.
In order to validate the computational model, the main turbine performance parameters (i.e. MFP and η_{ts}) were computed from the CFD results and then compared with the corresponding experimental data. The outcomes of this research activity have been collected in the paper *"Numerical simulation of the performance of a twin scroll radial turbine at different operating conditions"* [49] published in the International Journal of Rotating Machinery.

3.1.4. Full admission validation

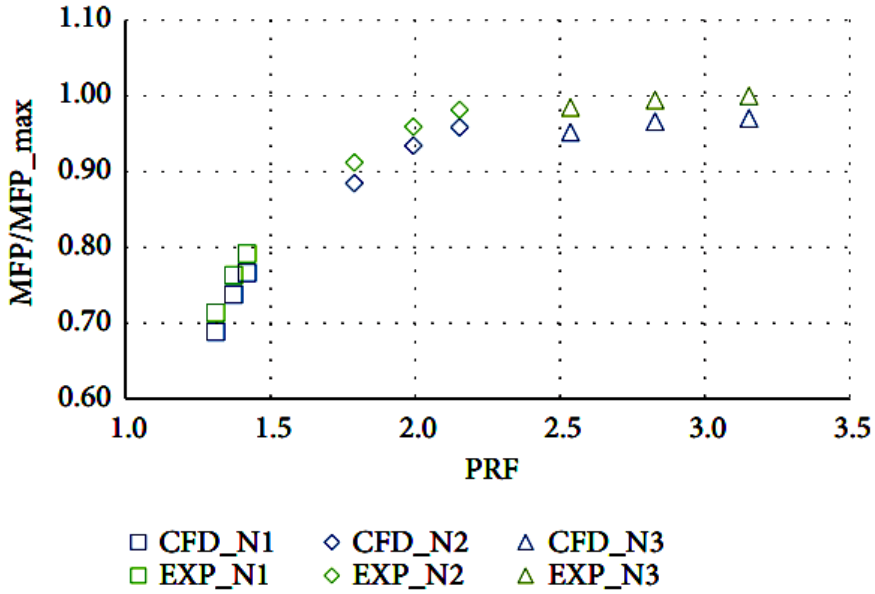

Fig. 3.5 - MFP (referred to the maximum value of the data set) vs. PRF in full admission

CFD full admission results are compared in Fig. 3.5 and 3.6 with experimental data. Regarding the MFP trends comparison, it can be noted that there is a good match between experimental and numerical data (the series of points are very close), with the CFD results which tend to slightly underestimate the mass flow rate measured at test bench.

Tab. 3.5 - Percentage difference (CFD vs. EXP) for MFP values in full admission

N [rpm/(K^0.5)]	PRF	ΔMFP%
N1	1.31	3.53
	1.37	3.34
	1.42	3.18
N2	1.79	2.98
	1.99	2.60
	2.15	2.35
N3	2.54	3.33
	2.83	2.85
	3.15	2.98

From a qualitative point of view, the shape of the measured trends (in green in Fig. 3.5) is well reproduced by the numerical results; moreover, the good match between 'CFD' and 'EXP' data is quantitatively confirmed by the relative percentage differences (see equation (3.2)) reported in Tab. 3.5, which are below 3.5% in all cases examined.

$$\Delta MFP\% = \frac{|MFP_{CFD} - MFP_{EXP}|}{MFP_{EXP}} 100 \tag{3.2}$$

For what concerns the total-to-static efficiency trends, in Fig. 3.6 it is possible to notice that CFD results tend to overestimate measured efficiency values; furthermore, there's a 'shape' discrepancy: numerical results show a tendency that is monotonically decreasing with the PRF on each iso-speed, whereas the experimental data have a peak at medium and high speeds (series 'N2' and 'N3' respectively). In quantitative terms, the relative percentage difference in efficiency, averaged over all the simulated points, is less than 4%.

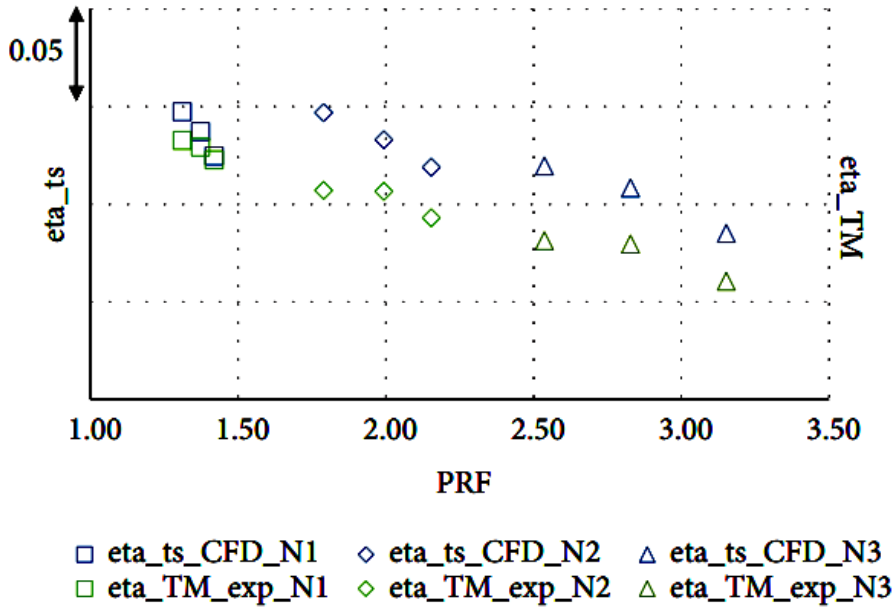

Fig. 3.6 – Total to static (CFD) and Thermo-Mechanical (EXP) efficiency vs. PRF in full admission (for confidentiality reasons the efficiency values are not reported)

In order to correctly understand the efficiency results comparison, it must be remarked that CFD values follow the classic total to static isentropic efficiency definition (see equation (1.32)), while experimental efficiency refers to the so called 'turbine effective efficiency', whose definition is reported below:

$$\eta_{TM} = \eta_{ts} \cdot \eta_m = \frac{P_c}{\dot{m}_{tot}\, C_p\, T_{01} \left[1 - \left(\frac{p_4}{p_{01\,both}}\right)^{(k-1)/k}\right]} \tag{3.3}$$

As discussed in the Master's degree thesis [52], turbo manufacturers usually provide to customers the thermo-mechanical performance (η_{TM}) due to the difficulty to accurately estimate friction and thermal losses, which are nonlinear and highly dependent from the operating point. Their behaviour can explain the trend mismatch shown in Fig. 3.6 among CFD and experimental data.

The careful reader may wonder why no error bars were associated with the measured data in Fig. 3.5 and 3.6. Unfortunately the industrial partner did not provide experimental data with measurement uncertainties as they are confidential data, therefore it was not possible to add this information to the experimental data series. However, the error bars on the MFP and the thermo-mechanical efficiency (η_{TM}) of the turbine can be obtained from the estimate of the expanded uncertainty calculated by the combination of the uncertainties deriving from each term that appears in the formulation of the performance parameters. Some researchers [53, 54] indicate that the measurement uncertainty on the mass flow rate via hot wire is approximately ±1-2% of the calibration range, pressure signals can be detected using strain gauge sensors characterized by an accuracy of 0.14% of the full scale and finally temperature can be measured by means of type K thermocouples placed at the turbine inlet, with uncertainty of ±1.5 [K] including the effects of the cables and the acquisition system.
For sake of completeness, it is useful to point out that in the case of a turbocharger IFR turbine the evaluation of the isentropic efficiency resulting from measurement of thermodynamic quantities at inlet and outlet sections can produce significant errors. In fact, due to the flow distribution at the exit of a radial flow turbine [55], a correct evaluation of the turbine outlet temperature is difficult and this can give high inaccuracies.
Considering the above, the isentropic efficiency of a turbocharger radial turbine is generally assessed by the turbine power (P_t). The use of a dynamometer on the turbine provides a direct measurement, but presents several problems: too narrow range of allowed rotational speeds, difficulty in coupling to different turbines and very sensitive instrumentation required due to the very low torque levels to be measured.
The most frequent option for turbine power assessment is to keep the turbocharger compressor coupled, evaluating the turbine power P_t in equation (3.4) starting from the measurement of the power absorbed by the compressor (P_c) and the estimation of the power dispersion caused by friction in the turbocharger bearings (P_b) and by windage losses (P_w). In this case the turbine power can be expressed as follows:

$$P_t = P_c - P_b - P_w \tag{3.4}$$

where:

- the compressor power (P_c) can be detected by direct method through pressure and temperature measurements at inlet and outlet sections, provided that the piping system is properly insulated [56]
- the mechanical friction losses in bearings (P_b) are generally evaluated by their geometry and turbocharger working conditions [57];
- the windage power losses (P_w) are calculated by theoretical and empirical correlations based mainly on friction losses of rotating disks [58].

Taking into account the above, the thermo-mechanical efficiency of the turbine was computed according to equation (3.3) from the measurement of the power absorbed by the compressor and of some thermodynamic quantities at turbine inlet.

As a final comment, it is noteworthy to remark the consistency of the simulated data in comparison with the experimental ones: as visible in Fig. 3.5 and 3.6 it seems that the 'predicted' turbine gives the same power of the 'measured' one with less mass flow and more efficiency (this is indeed a common trend).
Overall, the results presented in this section lead to the conclusion that the CFD model is able to correctly simulate the behaviour of the turbine studied in full admission.

3.1.5. Partial admission validation

In case of partial admission the CFD values of the mass flow parameter slightly overestimate the corresponding experimental values (the opposite was noted in Fig. 3.5 for full admission), as shown in Fig. 3.7. The shape of the measured trends is well reproduced by numerical data and quantitatively the percentage differences (always below 4.5% - see Tab. 3.6) attest to the reliability of the CFD model developed.

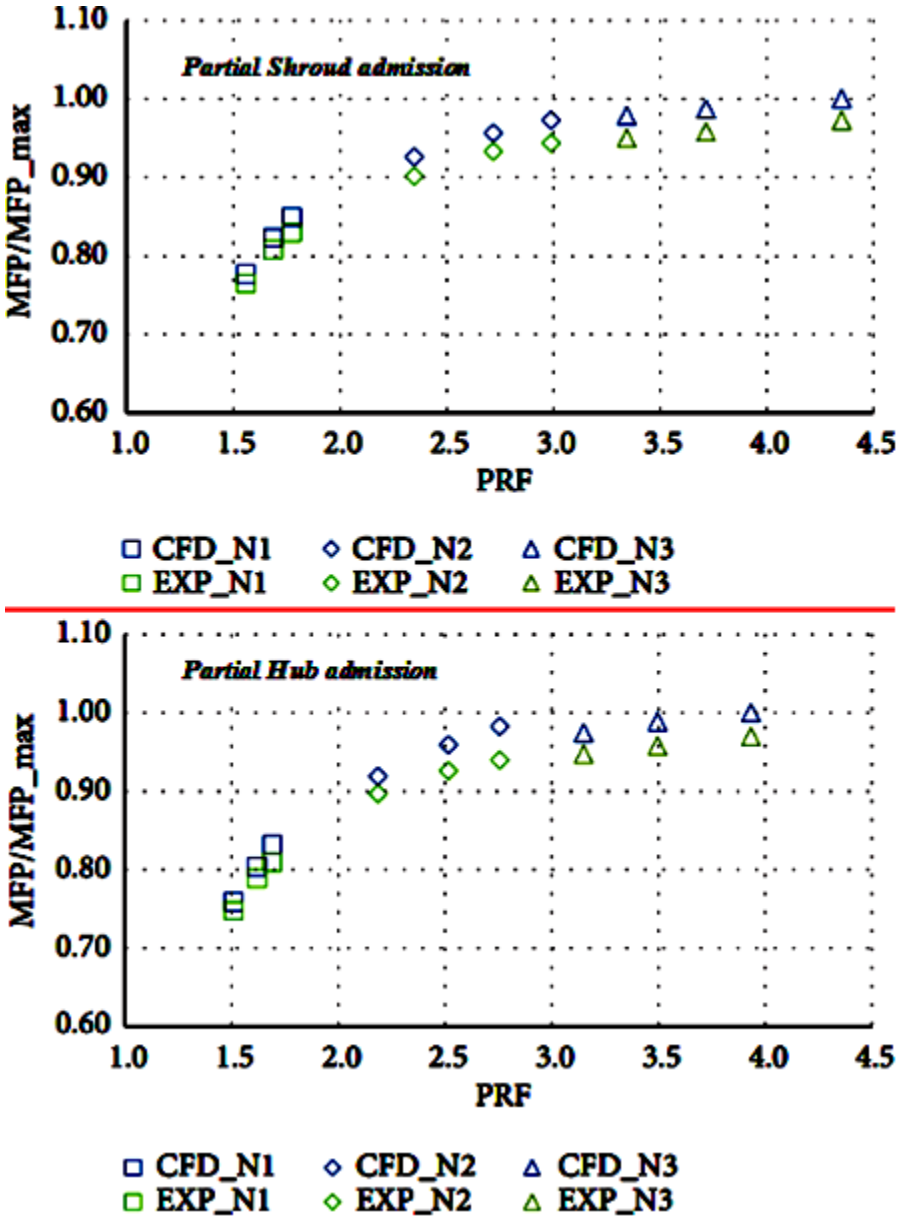

Fig. 3.7 - MFP (referred to data set maximum value) vs. PRF in partial admission cases

Considering the total-to-static turbine efficiency, in partial admission the numerical model shows the same behaviour already examined in equal admission: CFD data overestimate experimental measurements (see Fig. 3.8). The same explanation given above for the full admission points can be repeated here.

Tab. 3.6 - Percentage difference (CFD vs. EXP) for MFP values in partial admission

N	**Partial Shroud**		**Partial Hub**	
[rpm/(K^0.5)]	***PRF***	***ΔMFP%***	***PRF***	***ΔMFP%***
N1	1.56	1.55	1.51	1.62
	1.69	1.87	1.62	1.85
	1.77	2.35	1.69	2.76
N2	2.35	2.71	2.18	2.44
	2.72	2.53	2.51	3.58
	2.99	3.12	2.76	4.56
N3	3.34	3.05	3.15	2.90
	3.72	3.02	3.49	3.23
	4.35	2.84	3.93	3.12

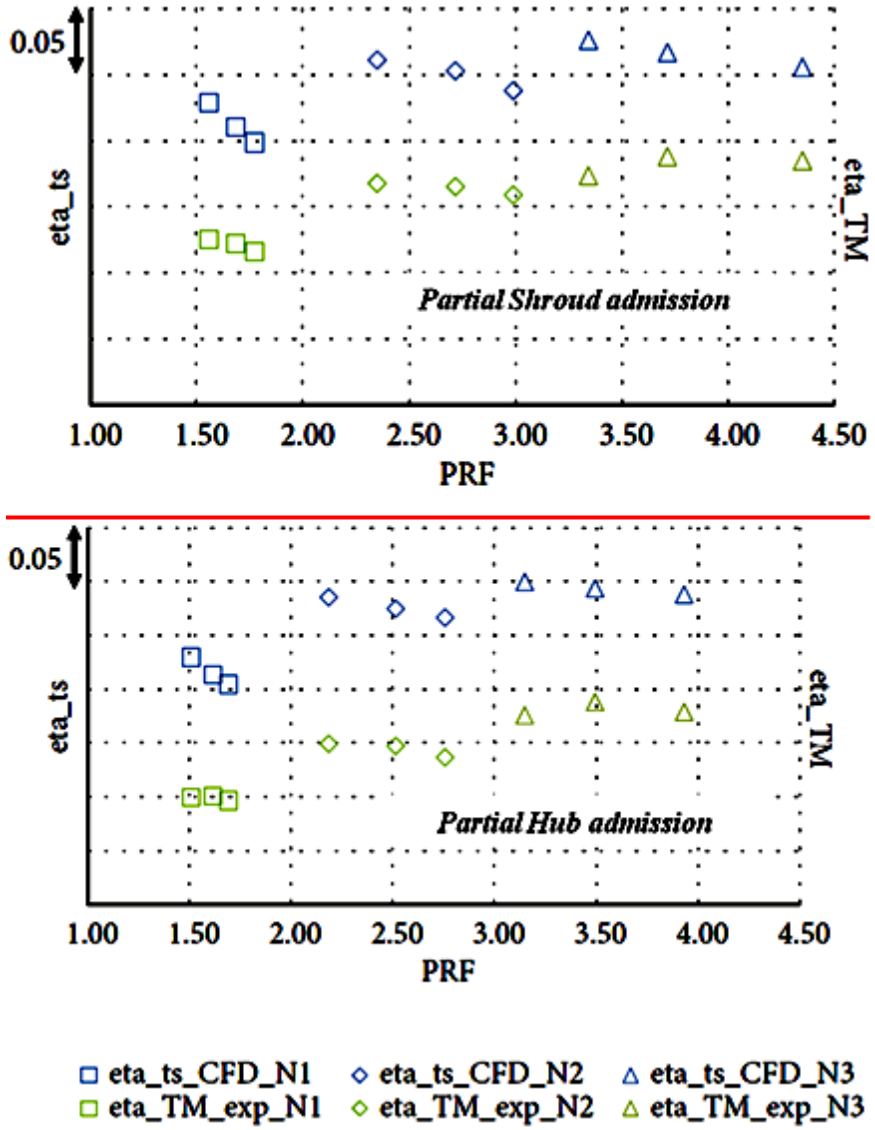

Fig. 3.8 – Total to static (CFD) and Thermo-Mechanical (EXP) efficiency vs. PRF in partial admission cases (for confidentiality reasons the efficiency values are not shown)

3.2. Twin scroll volute fluid dynamic characterization

Once the CFD model has been validated, it's time to analyze the fluid dynamic behaviour of the component that most characterizes twin entry radial turbines, that is the volute.
The main target of this section is the twin scroll volute characterization, i.e. the analysis of the total pressure drops through the twin scroll volute and the study of how the exhaust gases are distributed from this component to the impeller over a broad range of operating points. In particular, the attention was focused on rotor feeding conditions in order to understand how much the volute affects turbine overall performance, influencing entropy production of the downstream components.
For completeness, the research work presented in this paragraph refers to a paper [50] presented at the TurboExpo congress held in Oslo in 2018; the CFD model is derived from the one validated in paragraph 3.1. A single rotor channel was simulated with the rotational periodicity boundary condition applied on passage side walls and the discharge pipe was replaced by a simple axial extrusion of the rotor domain outlet. This simplified and computationally lighter version of the numerical model is denoted in the following as *"Scroll + single channel model"* (which is shown in Fig. 3.9). The numerical setup (including mesh, type of boundary conditions applied to the domains, fluid properties, turbulence model, etc.) is the same previously presented in 3.1.2.

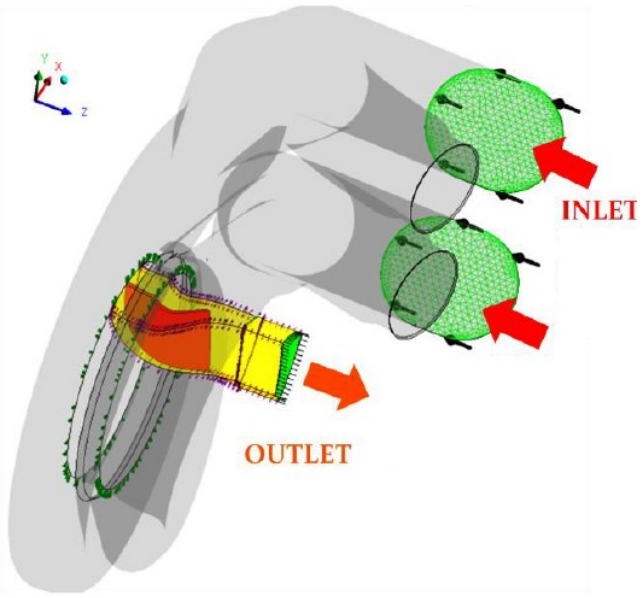

Fig. 3.9 – Scroll + single channel model: the two volute inlets and the model outlet are green, while the impeller blade is orange inside the yellow rotor passage

A fundamental step consists in the definition of significant control sections of the volute in order to extract as much information as possible from CFD data post-processing, which makes possible to take detections that on experimental side would require very sophisticated (and sometimes unfeasible) measurement setups.
Tab. 3.7 summarizes the operating points selected, over the entire working range, from the experimental data set of performance maps. The calculations made on the twin scroll turbine relate to three sets of 'reduced iso-speeds': $N_{rid} = 2688 - 4030 - 5040$ (low, medium and high rotational speed respectively).

Tab. 3.7 - Reduced or non-dimensional BCs values for the Scroll + single channel model

Equal		Partial Shroud		Partial Hub	
N_rid [rpm/K^0.5]	PRF	N_rid [rpm/K^0.5]	PRF	N_rid [rpm/K^0.5]	PRF
2689.2	1.31	2684.5	1.36	2685.0	1.29
2686.0	1.37	2686.9	1.44	2689.3	1.35
2687.3	1.42	2688.4	1.49	2688.0	1.39
4034.1	1.79	4034.5	1.88	4035.2	1.67
4029.4	1.99	4030.8	2.12	4030.8	1.85
4030.2	2.15	4031.3	2.30	4031.4	1.99
5042.4	2.54	5041.9	2.55	5042.4	2.24
5039.2	2.83	5038.5	2.80	5040.6	2.46
5036.7	3.15	5041.8	3.25	5039.5	2.72

The division of this paragraph into subsections follows the volute characterization, that is split into three 'phases':

1. quantitative and qualitative assessment of volute losses;
2. definition of non-uniformity flow parameters;
3. hub to shroud analysis and introduction of brand new non-uniformity indices.

3.2.1. Quantitative and qualitative assessment of volute losses

The total pressure values at the inlets and outlet of the volute were calculated through post-processing as mass flow weighted average on the corresponding control sections. Then the dimensionless total pressure drop across the volute was defined as follows:

$$\frac{\Delta p_t}{p_{t1}} = \frac{p_{t1both} - p_{t2}}{p_{t1both}} \tag{3.5}$$

this parameter relates the total pressure drop due to friction losses (energy equation in 'mechanical' form $dp_0/\rho = -dL_a$ - no work exchange in a static component) to the 'both' volute inlet total pressure, i.e. calculated through equation (1.29).
It was intentionally chosen not to use the 'traditional' loss coefficient used for turbines ($\Delta p_t/p_{d2}$) because for each admission condition analyzed (e.g. 'equal') the volute inlet total pressure vary significantly with the reduced speed, leading to some issues in the comparison among operating points at different rotational speeds. In fact, the dynamic pressure at volute exit (p_{d2}) is remarkably higher for the points at maximum N_{rid} and close to choking ('5040' series in Fig. 3.10) compared to those at minimum revs and close to zero mass flow ('2688' series), resulting in a lower value of the corresponding loss coefficient if expressed in the 'traditional' formulation. This would give higher loss coefficient values for the low reduced speed points (usually with higher efficiency) despite the lower total pressure losses in absolute value (Δp_t).
Considering the above, an alternative definition (equation (3.5)) of the loss coefficient has been introduced, which relates the volute total pressure losses to the amount of 'energy' (total pressure) available at turbine stator inlet. This choice is even more valid if different admission conditions are considered (as in this case): at similar rotational speeds and mass flow rates, very different total pressure values are required at volute inlets, also in relation to the asymmetry of the studied twin scroll volute. For example, in order to maintain the

same rotor speed and overall mass flow, partial shroud admission conditions require higher inlet total pressure than partial hub ones.

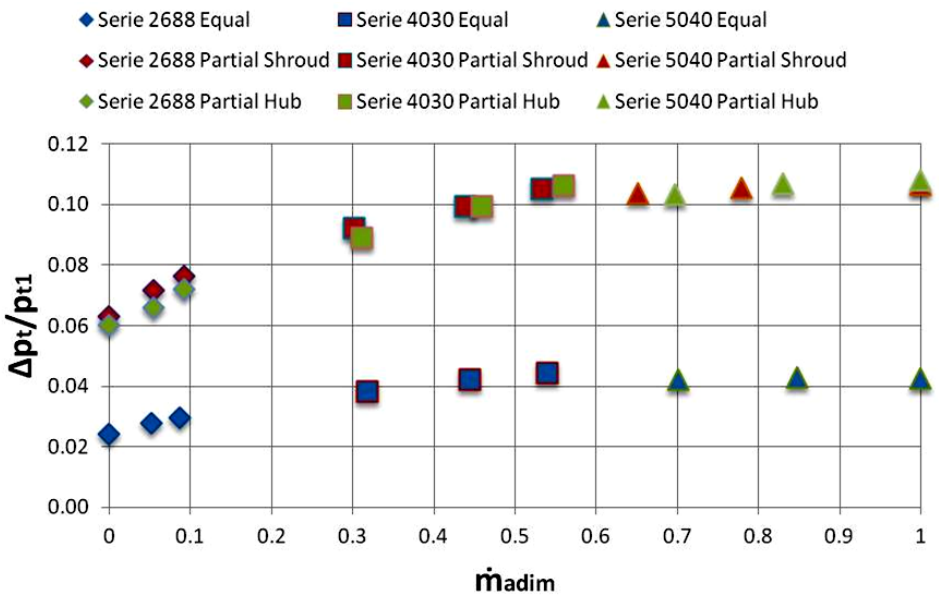

Fig. 3.10 – Overall ('both') dimensionless total pressure drop of the volute

The first comparison is made between the extreme cases of equal and partial admission (see Fig. 3.10). Mass flow values are expressed in non-dimensional form as $\dot{m}_{adim} = (\dot{m} - \dot{m}_{MIN})/(\dot{m}_{MAX} - \dot{m}_{MIN})$, where $\dot{m}_{MIN}$ and $\dot{m}_{MAX}$ are respectively the minimum and maximum mass flow rates calculated for each admission condition; therefore the points at $\dot{m}_{adim} = 1$ correspond to three (equal, partial hub, partial shroud) different $\dot{m}_{MAX}$ values. As expected, the total pressure drop across the volute increases with the rotational speed and also with the mass flow rate along each iso-speed line. Furthermore, it can be noted that in partial admission cases the relative increase in the loss coefficient between low (N_{rid} =2688) and medium (N_{rid} =4030) speed is more pronounced than in full admission.

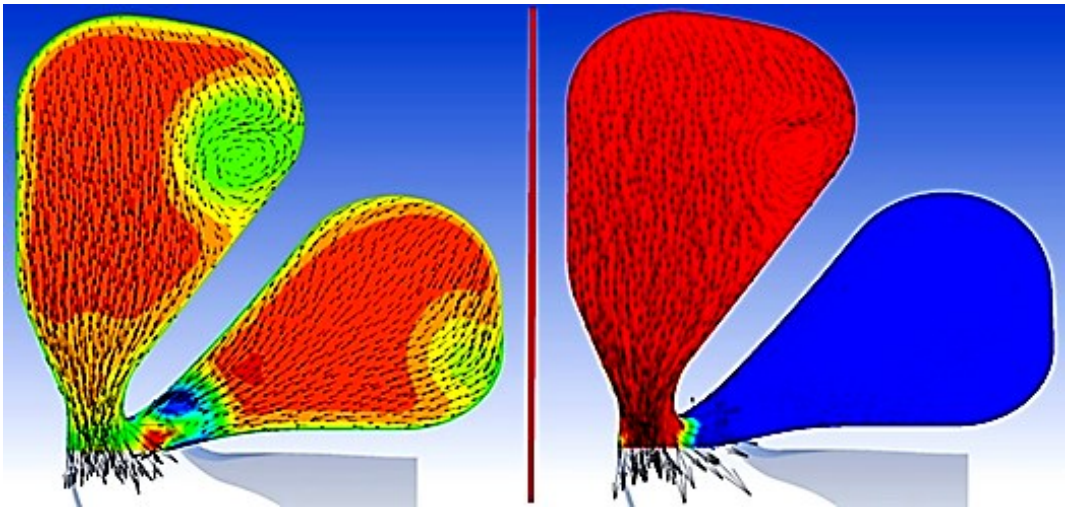

Fig. 3.11 – Comparison of total pressure contours (fixed scale) on the same volute cross section: equal admission on the left, partial hub admission on the right

As shown in the comparison proposed in Fig. 3.11, partial admission is characterized by higher fluid dynamic losses due to marked recirculation in the unpowered branch; coherently the values of dimensionless total pressure drop in partial admission are remarkably higher than the corresponding at full admission (Fig. 3.10).

In an attempt to correlate the geometry of each scroll with its associated losses, it is also interesting to calculate the total pressure losses across each limb taken individually. To this target, two surfaces of revolution (identified in Fig. 3.12) were introduced upstream of the vaneless nozzle (constant height channel between volute and rotor), in order to uniquely identify each volute branch outlet. The loss coefficient for each volute limb was then computed as in equation (3.5) by the ratio between the total pressure drop across the single scroll and its inlet total pressure (i.e. $\Delta p_{t\ hub}/p_{t1\ hub}$ if the hub side branch is considered).

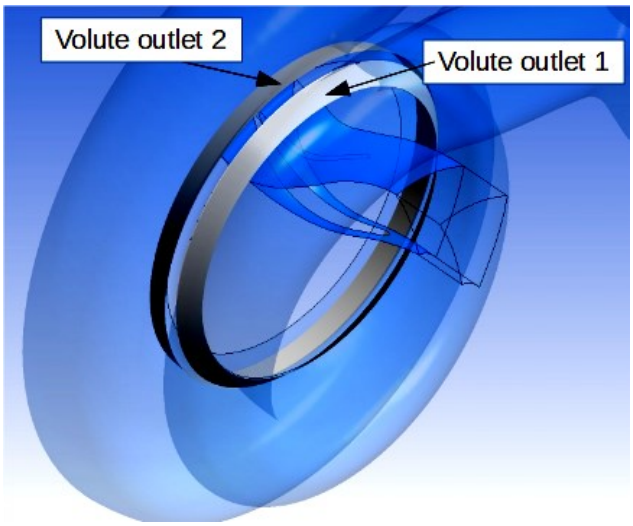

Fig. 3.12 – Revolution surfaces that identify each scroll outlet (1=shroud - 2=hub side)

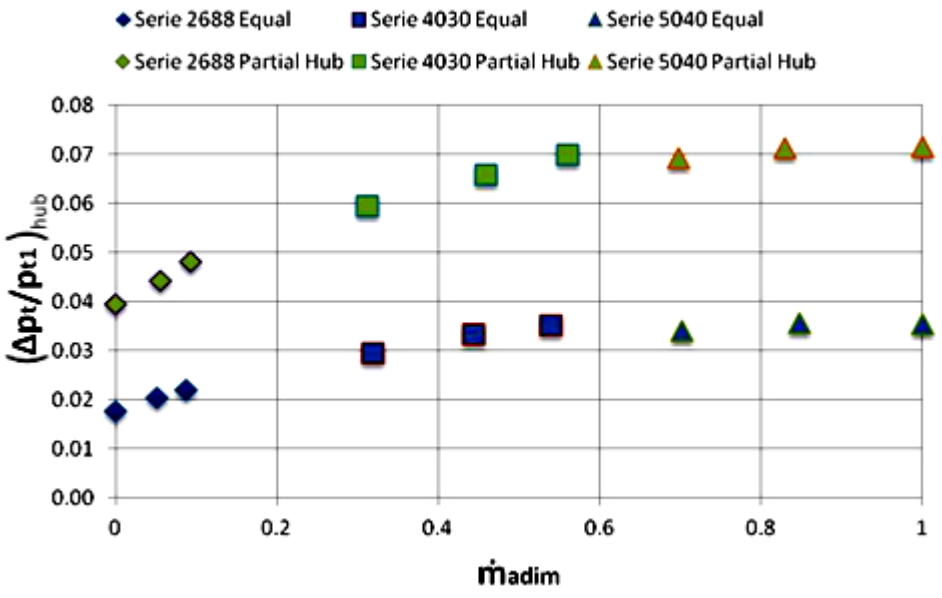

Fig. 3.13 – Dimensionless total pressure drop of the hub side branch only

The analysis highlights that in partial admission the non-dimensional losses in the powered volute branch are about double with respect to the corresponding ones in equal admission. Furthermore, comparing Fig. 3.13 and Fig. 3.14 the influence of the individual scroll shape on losses is evident: shroud side produces more entropy than the hub side branch and this is mainly due to the volute cross section asymmetry in the meridian plane.

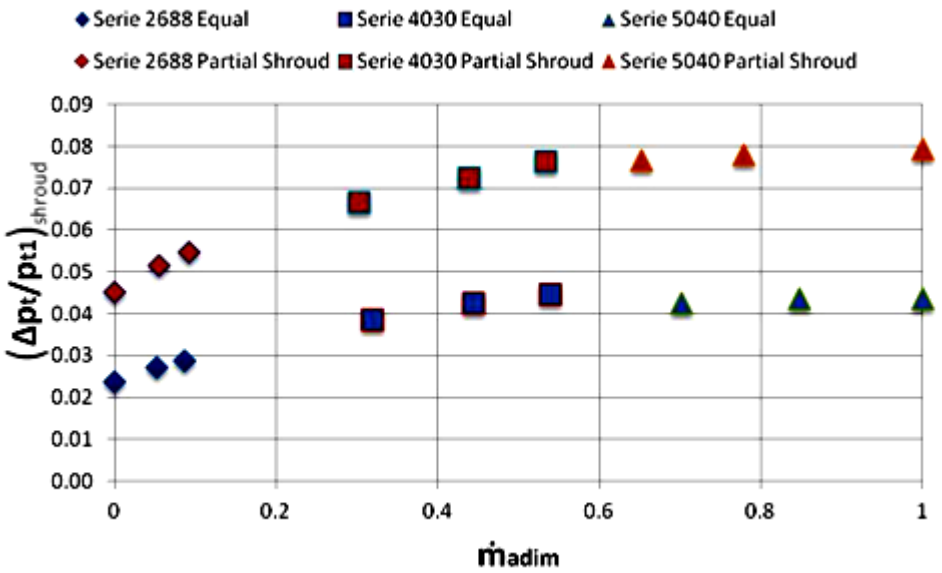

Fig. 3.14 – Dimensionless total pressure drop of the shroud side branch only

In confirmation of the above, Fig. 3.15 shows the behaviour of the flow on a volute cross section enlarged in the region between the scrolls divider septum and the rotor leading edge: in partial shroud admission the 'back flow' condition (described at Chapter 1 in Fig. 1.15) is much more evident if compared to partial hub admission. The greater losses of the shroud side branch taken individually find a clear explanation observing the twin scroll volute in meridian view (as in Fig. 3.15): the marked inclination of the shroud limb towards axial direction promotes the recirculation in the no flow branch.

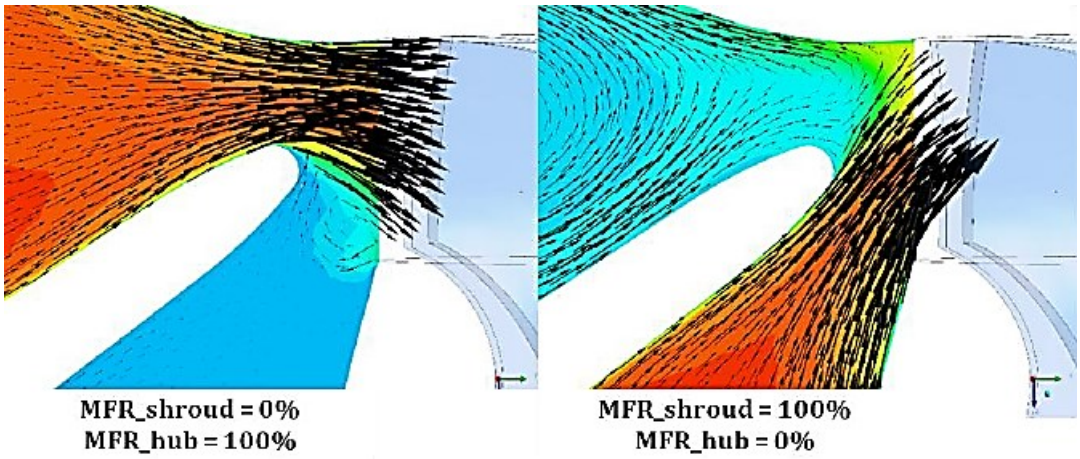

Fig. 3.15 – Total pressure contours and velocity vectors projected on a volute cross section: comparison between opposite cases of partial admission

3.2.2. Non-uniformity flow parameters

Twin scroll volutes characterization proceeds in the second phase with the identification of parameters that can give an insight into the exhaust gas distribution at volute outlet: a greater flow unevenness at wheel inlet leads to performance penalties for the rotor and therefore for the whole machine. The term 'performance' is intended hereafter not only as a synonym of efficiency, but also of turbine flow capacity.
The first non-uniformity flow parameter was identified in the ratio between area-weighted average and mass-weighted average of the swirl flow angle (α) at volute outlet.

$$c_m = \sqrt{c_x^2 + c_r^2} \tag{3.6}$$

$$\alpha = arctan(c_\vartheta / c_m) \tag{3.7}$$

$$\alpha Ratio = \alpha_{area} / \alpha_{mass} \tag{3.8}$$

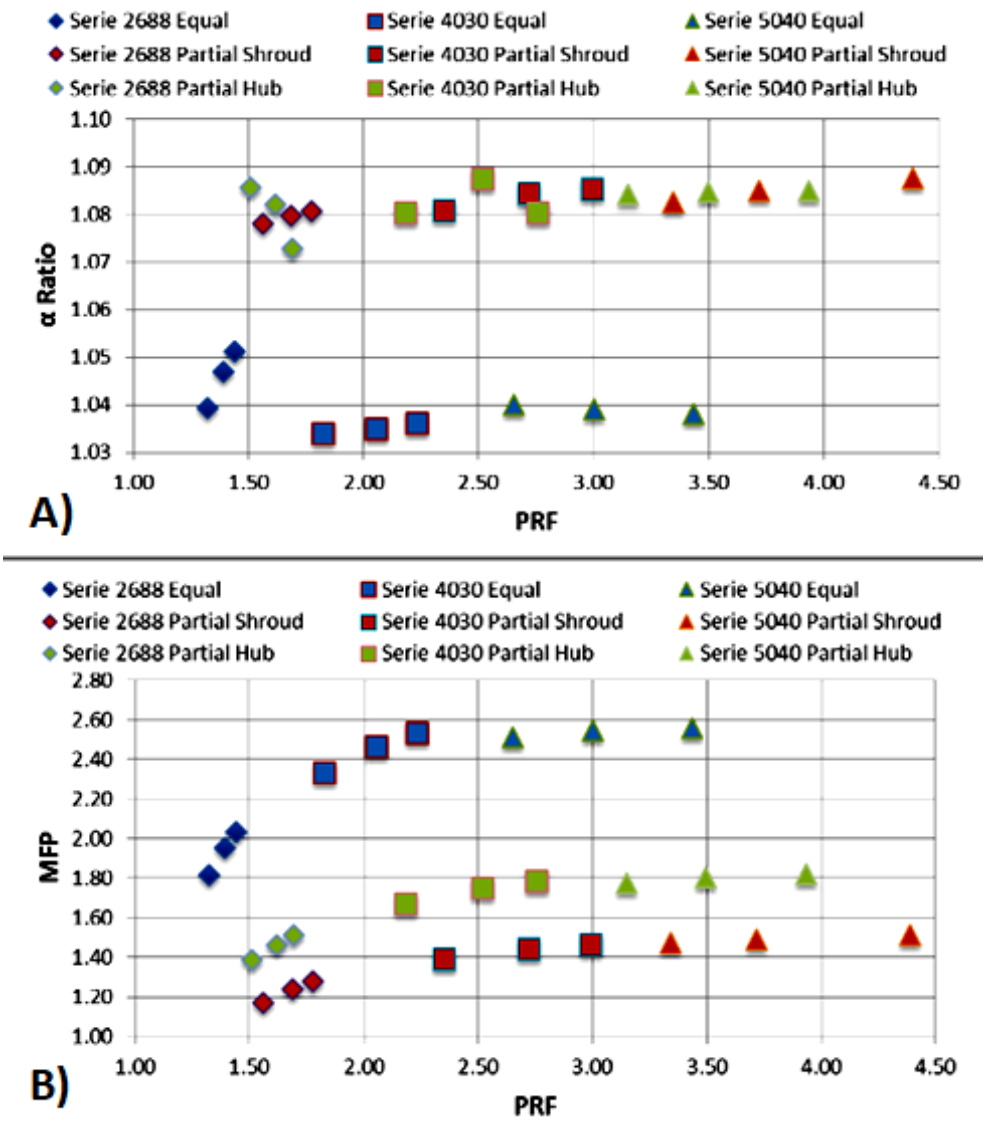

Fig. 3.16 – (A) Absolute flow angle ratio. (B) Mass flow parameter

Fig. 3.16A shows that the partial admission conditions lead to greater flow non-uniformity than equal admission; moreover a small difference in $\alpha Ratio$ means a rather different flow capacity, as confirmed by the MFP dataset comparison (Fig. 3.16B).
A better understanding of the discussed trends stems from Fig. 3.17, which shows the comparison of the radial velocity contours at the mixing plane (stator-rotor interface): the more mass flow locally varies, the more mass-weighted average α value diverges from the area-weighted average one. Since in an IFR turbine the mass flow rate at rotor inlet is given by the radial velocity component, a contour of this variable is meaningful of the $\alpha Ratio$ behaviour.

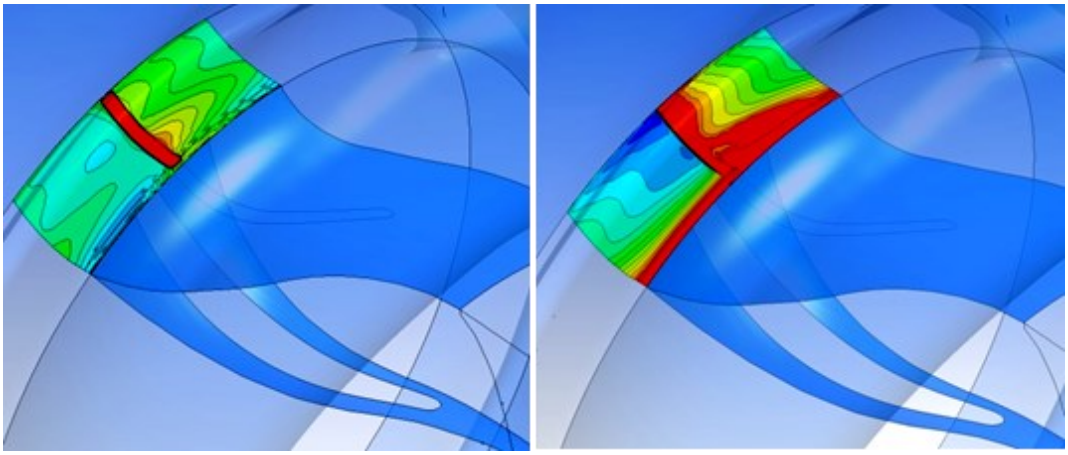

Fig. 3.17 - Radial velocity contours at rotor inlet: equal admission on the left and partial shroud admission on the right

The second non-uniformity flow parameter introduced is the axial to radial velocity ratio:

$$VR_{x-r} = \frac{c_x}{c_r} \tag{3.9}$$

this parameter quantifies how much the actual exhaust gas direction is different from the ideal case of purely radial flow at rotor inlet. The velocity ratio is therefore a good indicator of the turbine expected performance, despite the fact that velocity values have been averaged on rotor inlet section and this does not guarantee a complete local analysis.
In Fig. 3.18 the axial to radial velocity ratio values are compared according to:
A) the type of admission condition, on three different reduced speeds;
B) the way in which the overall mass flow is split into the two scrolls (20% Sh - 80% Hub, 40% Sh - 60% Hub, 60% Sh - 40% Hub, 80% Sh - 20% Hub).

Observing trends in Fig. 3.18A it is clear that equal admission cases show a very small absolute value of axial velocity compared to the radial component, in contrast with the partial shroud admission conditions, where the two components are almost equivalent (velocity ratio near one). Partial hub admission points, on the other hand, are characterized by intermediate absolute values of VR_{x-r} with respect to the other admission conditions, but of opposite sign: this is due to the positive sign of the axial speed component at rotor inlet, while radial component is always negative because it is directed towards rotor axis.
It is also interesting to comment on the unequal admission results, that are compared with those of equal admission in Fig. 3.18B:

- high shroud scroll mass flow ratios ($MFR_{sh} = \dot{m}_{sh}/\dot{m}_{tot}$) result in an increase of the axial velocity absolute value, hence of the VR_{x-r} ;

- in case of slightly unbalanced admission towards the hub side branch, the axial velocity decreases in absolute value leading to very positive results: the '40Sh 60Hub' (i.e. $MFR_{sh} = 40\%$ and $MFR_{hub} = 60\%$) series shows VR_{x-r} values lower than those of the equal admission series;
- high hub scroll mass flow ratios ($MFR_{hub} = \dot{m}_{hub}/\dot{m}_{tot}$) result in axial velocity sign change, thus causing negative values of VR_{x-r} (see the '20Sh 80Hub' series).

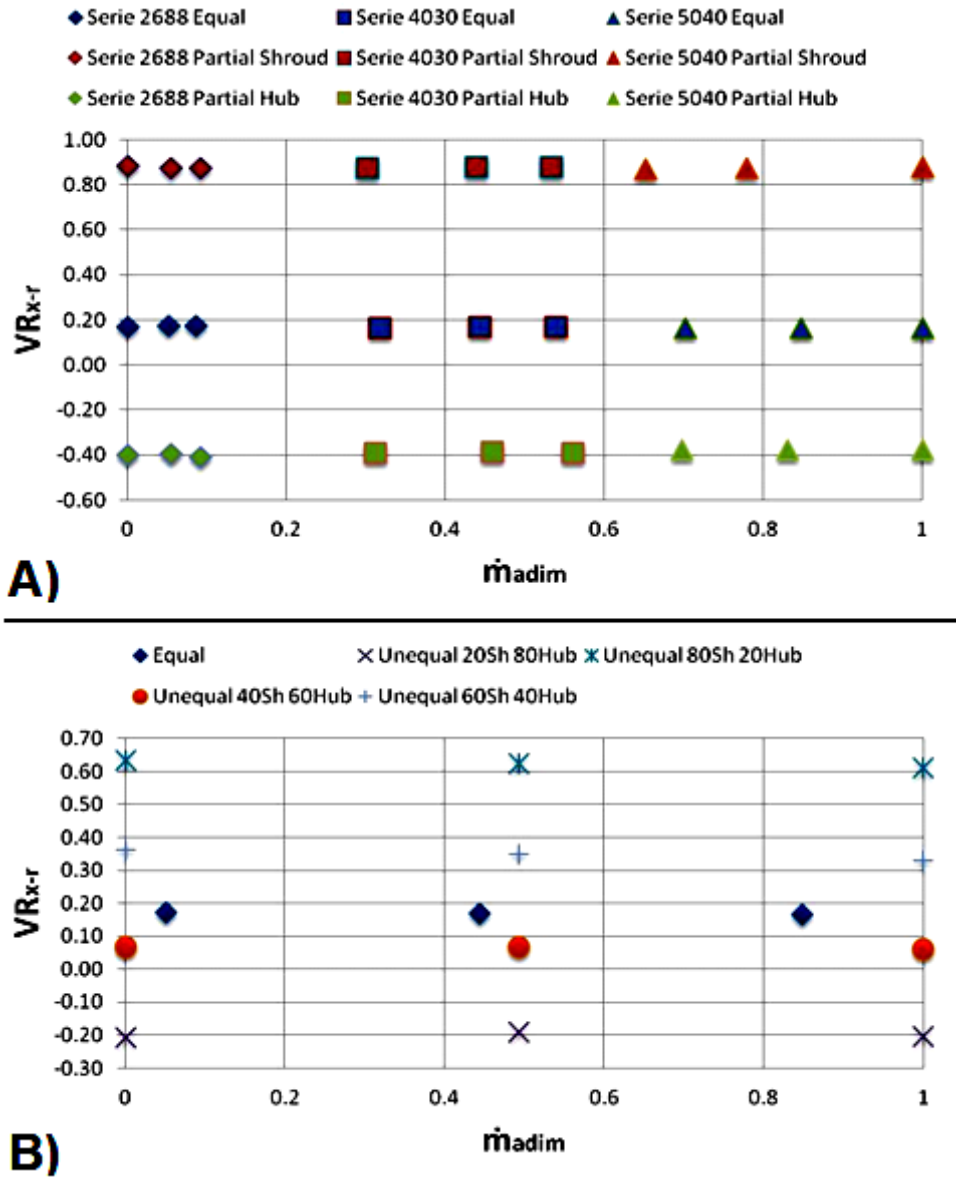

Fig. 3.18 – Axial to radial velocity ratio at rotor inlet in various admission conditions

The comparison between partial shroud admission operating point at $\dot{m}_{adim} = 1$ (Fig. 3.18A) and the corresponding '80Sh 20Hub' unequal admission point (Fig. 3.18B) deserves a final comment: if the hub side volute branch is fed with at least 20% of the overall turbine mass flow it is possible to significantly align the flow discharged from the volute to the radial direction, bringing the twin scroll radial turbine closer to ideal theoretical operation.

3.2.3. Hub to shroud analysis and definition of brand new non-uniformity indices

In order to generalize the analysis and make it applicable and comparable with other studies, in this section an appropriate non-dimensional index is introduced in an attempt to correlate the turbine performance to the studied flow non-uniformity at rotor inlet. To this purpose, the hub-to-shroud span at wheel inlet was divided into 21 sampling points to systematically compare the results from the CFD database. Fig. 3.19 shows the flow angle trends along the span (0% = hub - 100% = shroud) at rotor inlet:

a) in partial shroud admission (Fig. 3.19a) the α values are uniform up to 60% of the span; beyond this value a drastic reduction of the swirl flow angle can be noted. This is caused by an heavy flow velocity unevenness towards the shroud, which is the most crucial region for high work exchange;
b) in partial hub admission (Fig. 3.19b) flow angle variations along inlet blade height are limited and the spanwise mean value is comparable with that measured near the shroud.

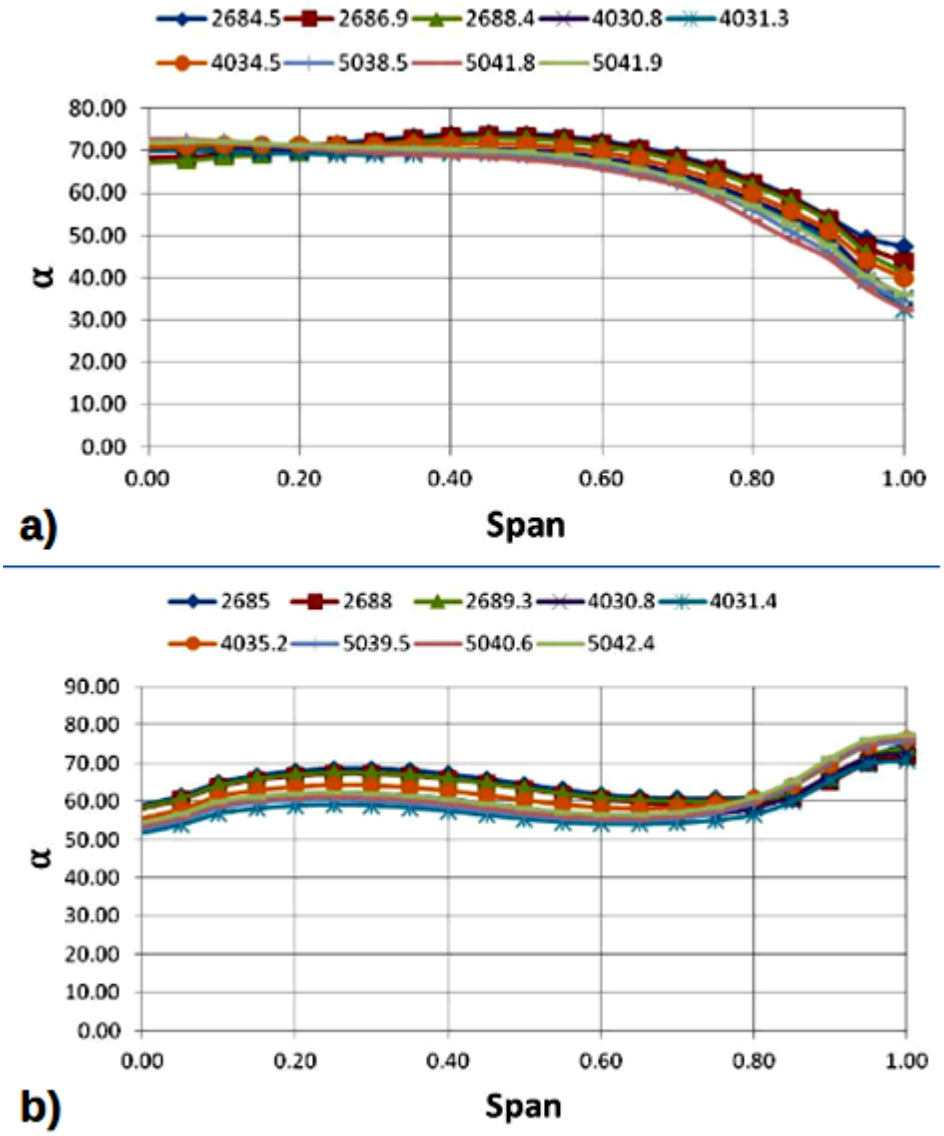

Fig. 3.19 – Flow angle spanwise trends for partial admission: a) shroud, b) hub side

The physical explanation for the different hub to shroud distribution of the swirl angle can be found in its formula (equation (3.7)): α is in fact inversely proportional to meridian velocity. In particular, the radial component (c_r) in partial shroud admission drastically increases near the shroud (see the right half of Fig. 3.17), thus reducing the value of the flow angle. This is due to the convexity of the shroud surface which generates a strong flow acceleration in this zone. In the partial hub case instead, this effect is felt much less since most of the flow rate is discharged towards the impeller from the rotor hub side and therefore the spanwise distribution of alpha is more uniform.

According to the experience gained on the database, a set of five percentage values of span (10-25-50-75-90%) were considered a proper discretization for flow non-uniformity index assessment. Furthermore, it should be remembered that a greater flow distortion close to the rotor shroud is more critical than a non-uniformity toward the hub, due to the different peripheral speed values that affect the work exchange within the streamtubes.
The index is therefore defined as a weighted average, based on the position along the span (weights increasing towards the shroud), of α_n deviations from mean value ($\bar{\alpha}$), as below:

$$\alpha_{index} = \frac{1}{(n.v. \cdot \bar{\alpha})}[\,0.1|\alpha_{10} - \bar{\alpha}| + 0.25|\alpha_{25} - \bar{\alpha}| + 0.5|\alpha_{50} - \bar{\alpha}| + \\ + 0.75|\alpha_{75} - \bar{\alpha}| + 0.9|\alpha_{90} - \bar{\alpha}|] \tag{3.10}$$

where *n.v.*=5, $\bar{\alpha}$ is the mean value of the swirl flow angle at rotor inlet and α_n corresponds to the flow angle computed at the *n-th* percentage of the span (0% = hub - 100% = shroud).

The strong radial orientation of the hub side scroll determines an almost constant flow angle along the span in partial hub admission (as already shown in Fig. 3.19b), consequently $\alpha Index$ values are significantly lower than the corresponding in partial shroud admission. A good connection between $\alpha Index$ and turbine performance is confirmed by Fig. 3.20 and Fig. 3.21: in fact partial shroud admission working points present higher $\alpha Index$ values that match to lower total to static efficiency.

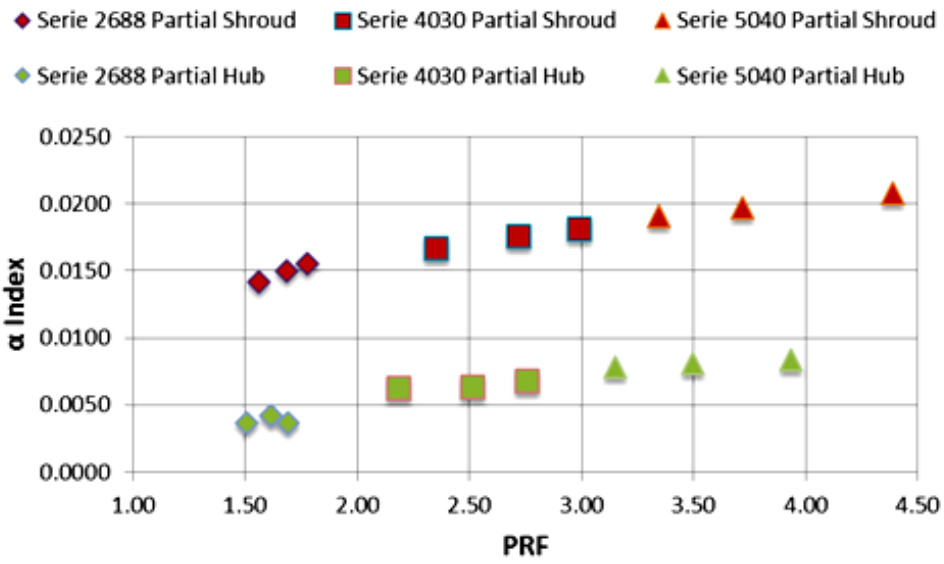

Fig. 3.20 – Flow angle index trends in partial admission cases

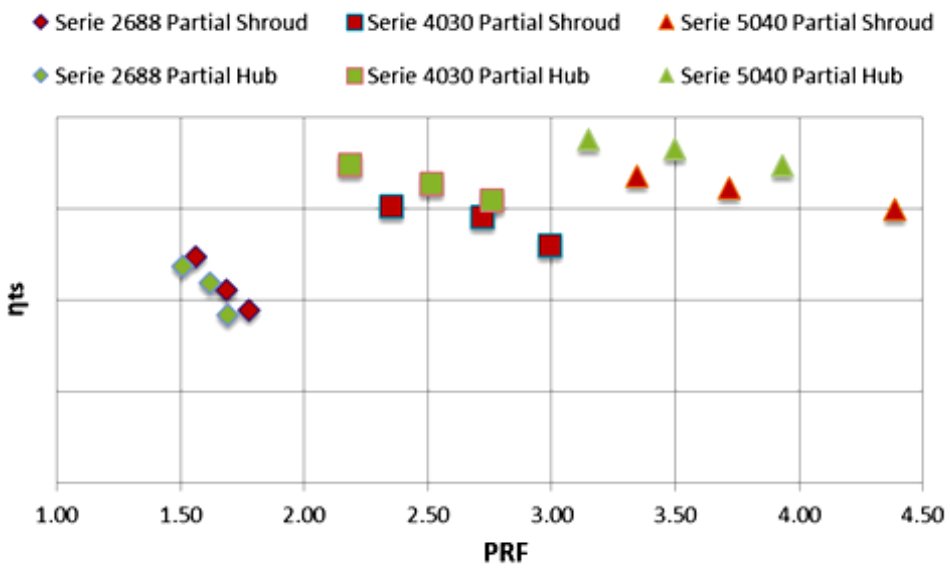

Fig. 3.21 – Total to static efficiency trends in partial admission cases

The careful reader may note that the distortion suffered by the flow in partial shroud admission has less influence on efficiency at $N_{rid} = 2688$: in this case, in fact, the peripheral speed is lower and the absolute circumferential velocity at rotor inlet is proportionally less affected by the drastic decrease in the flow angle at the shroud (Fig. 3.19a). Therefore at the minimum reduced speed the total to static efficiency remains slightly higher in partial shroud admission because this condition feeds the rotor privileging the shroud area, where the streamtubes exchange more work to the wheel.
It is worth noting that full admission operating points are intentionally excluded from the comparison because the 'equal' turbine flow capacity is very different from partial admission cases (see Fig. 3.16B). Therefore, even if the $\alpha Index$ is expected to be very close to zero in equal admission functioning, it is not reasonable to achieve higher efficiency than in partial admission conditions, since the mass flow rate through the turbine is rather different.

3.3. Backside cavity influence on turbine performance

This paragraph deals with the influence of the backside cavity on twin scroll turbine fluid dynamic behaviour: the cavity was introduced into the 3D CFD complete model (volute and full rotor – see Fig. 3.4) in order to understand its effect on performance parameters. The outcomes of this research work have been published in the International Journal of Rotating Machinery [49].
The numerical setup and the set of operating points are the same as previously described in sections 3.1.2 and 3.1.3 respectively; since pressure boundary conditions are kept equal to those of the already presented 'no cavity' cases, overall mass flow is not remarkably affected by the cavity; therefore the performance parameter chosen to compare the cases with or without backside cavity is the total-to-static efficiency.
For a correct interpretation of the results presented in this paragraph it is important to specify that the CFD model including the fluid cavity upstream of the seal does not simulate a leakage flow through the seal itself, but only the windage losses inside the cavity. This choice is crucial to isolate the fluid dynamic effect of the backside cavity on

turbine performance, without taking into account the performance drop caused by a certain flow rate bypassed through the seal.
In partial shroud admission the presence of the backside cavity seems to have a positive influence on turbine efficiency. A qualitative assessment of the flow field shown in Fig. 3.22 leads to the conclusion that the cavity mitigates the back flow condition typical of partial shroud admission for this twin scroll volute, resulting in slightly higher total to static efficiency values (see following Fig. 3.24B).

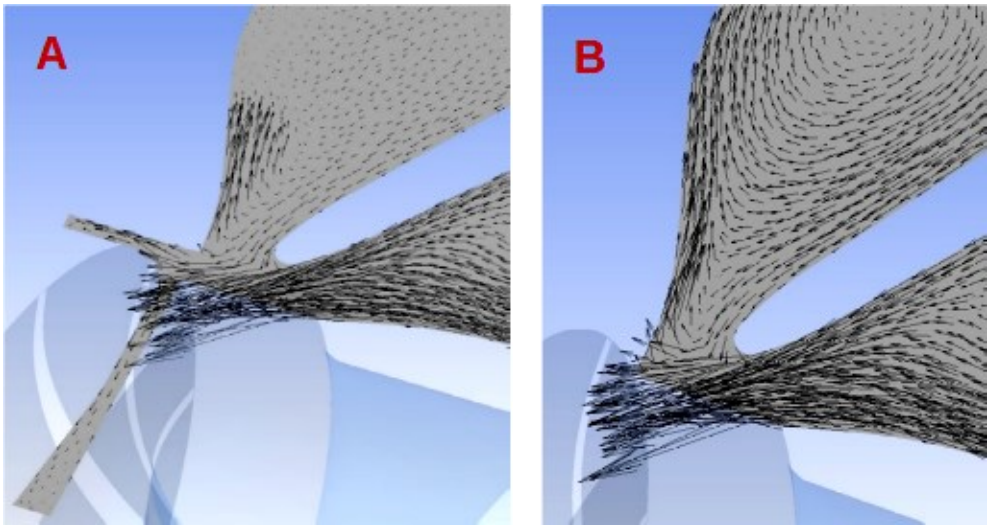

Fig. 3.22 – Velocity vectors projected on a volute cross section for partial shroud admission: A) with and B) without backside-cavity

The numerical evidences highlight that the presence of the cavity alters the flow structure at the rotor inlet: following the same approach already proposed in 3.2.3 for the $\alpha Index$, an additional performance index based on hub to shroud total pressure distributions has been introduced. The goal is to correlate the flow structure at the rotor inlet with the turbine performance in presence of backside cavity; since the total pressure is linked to the amount of energy potentially extractable from the streamtubes, a large spanwise variation of this quantity at rotor inlet affects turbine efficiency.
The index is therefore defined as an average of the absolute values of 'local' deviations of total pressure from spanwise mean value ($\bar{p}_t$), as below:

$$p_{t\,index} = \left(\frac{1}{n.v. \cdot \bar{p}_t}\right)[|p_{t\,5} - \bar{p}_t| + |p_{t\,20} - \bar{p}_t| + |p_{t\,40} - \bar{p}_t| + \\ + |p_{t\,60} - \bar{p}_t| + |p_{t\,80} - \bar{p}_t| + |p_{t\,95} - \bar{p}_t|] \tag{3.11}$$

where $p_{t\,n}$ is the total pressure post-processed at the corresponding *n-th* percentage value of the span (0% = hub - 100% = shroud) and $n.v.$ is the number of span locations considered for the $p_{t\,index}$ calculation (n.v. = 6 in equation (3.11)).
The careful reader may note that in this case the total pressure local deviations from hub to shroud mean value are not weighted with the relative position along inlet blade height. In fact, backside cavity effects on flow field are concentrated on the hub side, hence a formulation similar to equation (3.10) would result in a significant minimization of the influence of total pressure non-uniformity in that specific zone.

It is important to stress that this brand new index does not replace α_{index}, which remains valid for the evaluation of volute performance, but improves the description of flow non-uniformities at rotor inlet in presence of backside cavity.

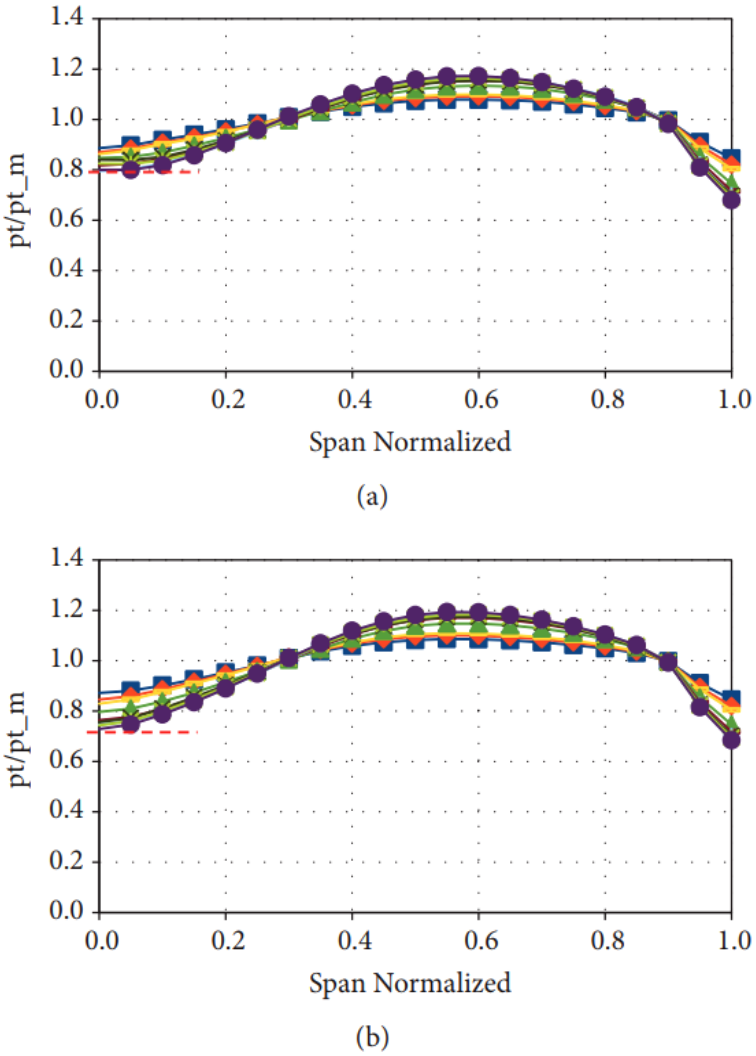

Fig. 3.23 – Partial shroud admission: spanwise total pressure trends (a) with and (b) without cavity (the different colors refer to various rotational speeds)

The hub to shroud total pressure distributions at rotor inlet are plotted in Fig. 3.23 for both cases with and without cavity. It can be noted that total pressure values are reported in non-dimensional form as the ratio (pt/pt_m) between local and average spanwise value for all tested rotational speeds. The dimensionless total pressure trends evidence that in partial shroud admission when the backside cavity is not included in the CFD model (Fig. 3.23b) the total pressure values near hub endwall (close to zero span position) are generally lower than those measured with cavity (Fig. 3.23a) and this difference is more evident at high rotational speeds. This seems to suggest that the presence of the cavity in case of partial shroud admission leads to an improvement in the performance of the turbine, with less unevenness in the spanwise total pressure profile at rotor inlet.
Starting from the hub to shroud total pressure data, the non-uniformity index was calculated and the resulting trends as a function of the PRF are reported in Fig. 3.24a. The

p_{tindex} shows a good correlation with the turbine total-to-static efficiency (Fig. 3.24b): higher total pressure index values match to lower efficiency and vice versa. The trends also confirm that in partial shroud admission the turbine has higher efficiency when the cavity is included in the CFD model.

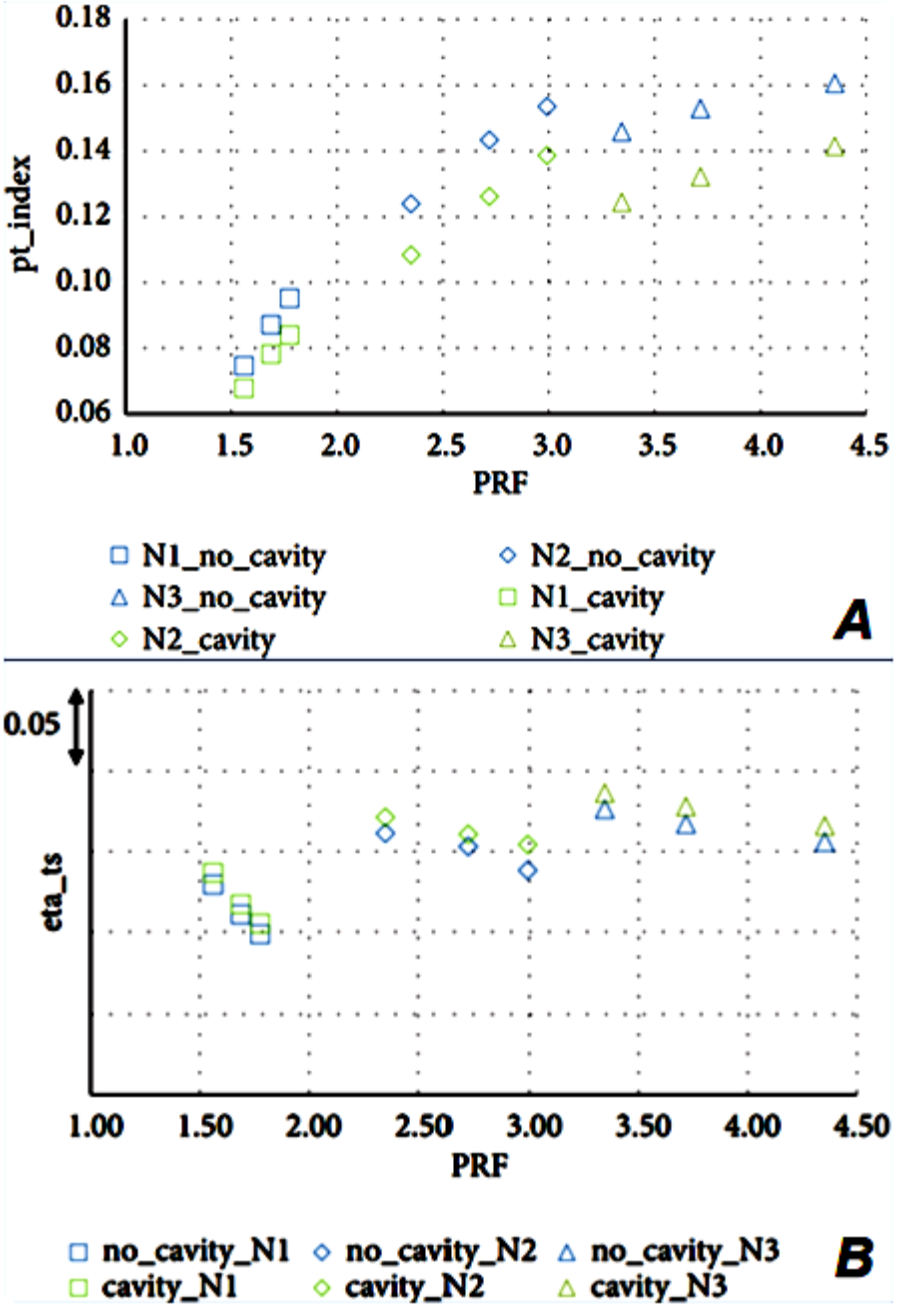

Fig. 3.24 – Cavity effect in partial shroud admission: A) total pressure index vs. PRF; B) total to static efficiency vs. PRF

Once the case of partial shroud admission has been discussed, the opposite operating condition is considered. As shown in the following Fig. 3.26, in partial hub admission the local values of total pressure referred to the respective spanwise averaged value (pt_m) are higher near the hub region in absence of cavity, unlike what was previously noted.

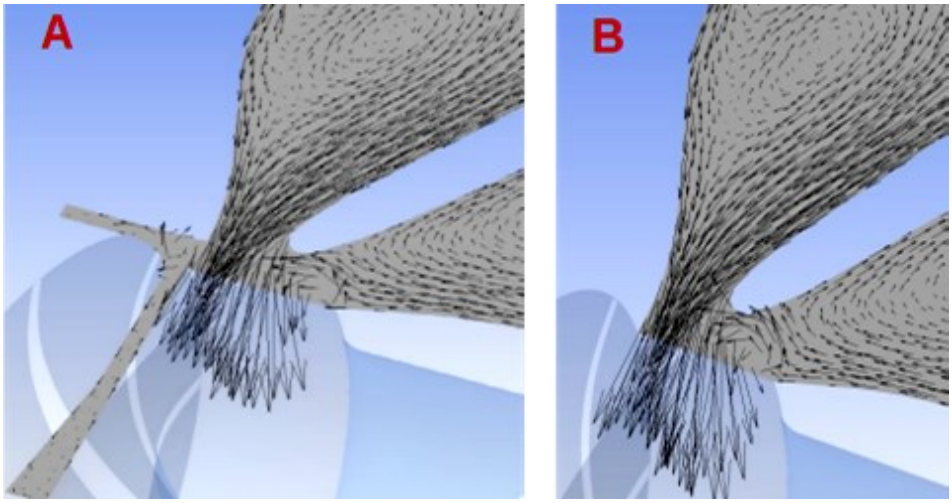

Fig. 3.25 – Velocity vectors projected on a volute cross section for partial hub admission: A) with and B) without backside cavity

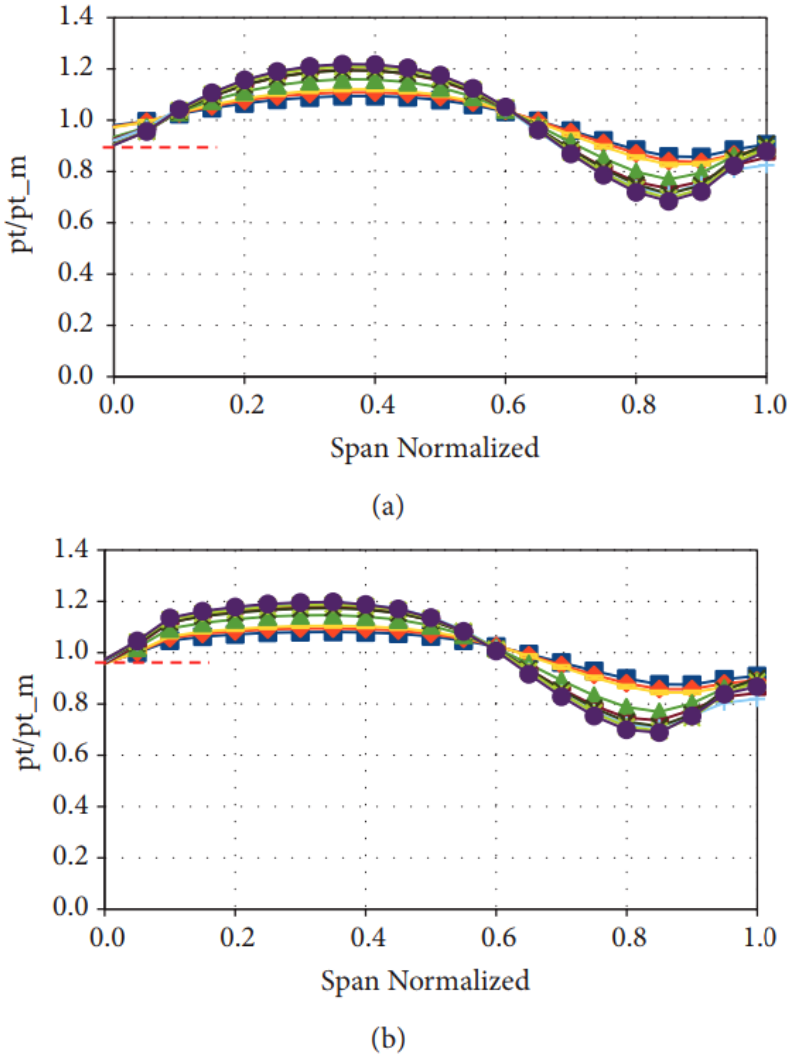

Fig. 3.26 – Partial hub admission: spanwise total pressure trends (a) with and (b) without cavity (the different colors refer to various rotational speeds)

The total pressure hub to shroud distributions in Fig. 3.26 show that in partial hub admission the backside cavity tends to slightly increase the unevenness in the spanwise total pressure profile at rotor inlet; thus in presence of cavity lower values of the total to static efficiency are expected. The goodness of the correlation existing between p_{tindex} and total to static efficiency is confirmed once again in Fig. 3.27: higher values of the index (with cavity in this case) match to lower efficiency and vice versa.

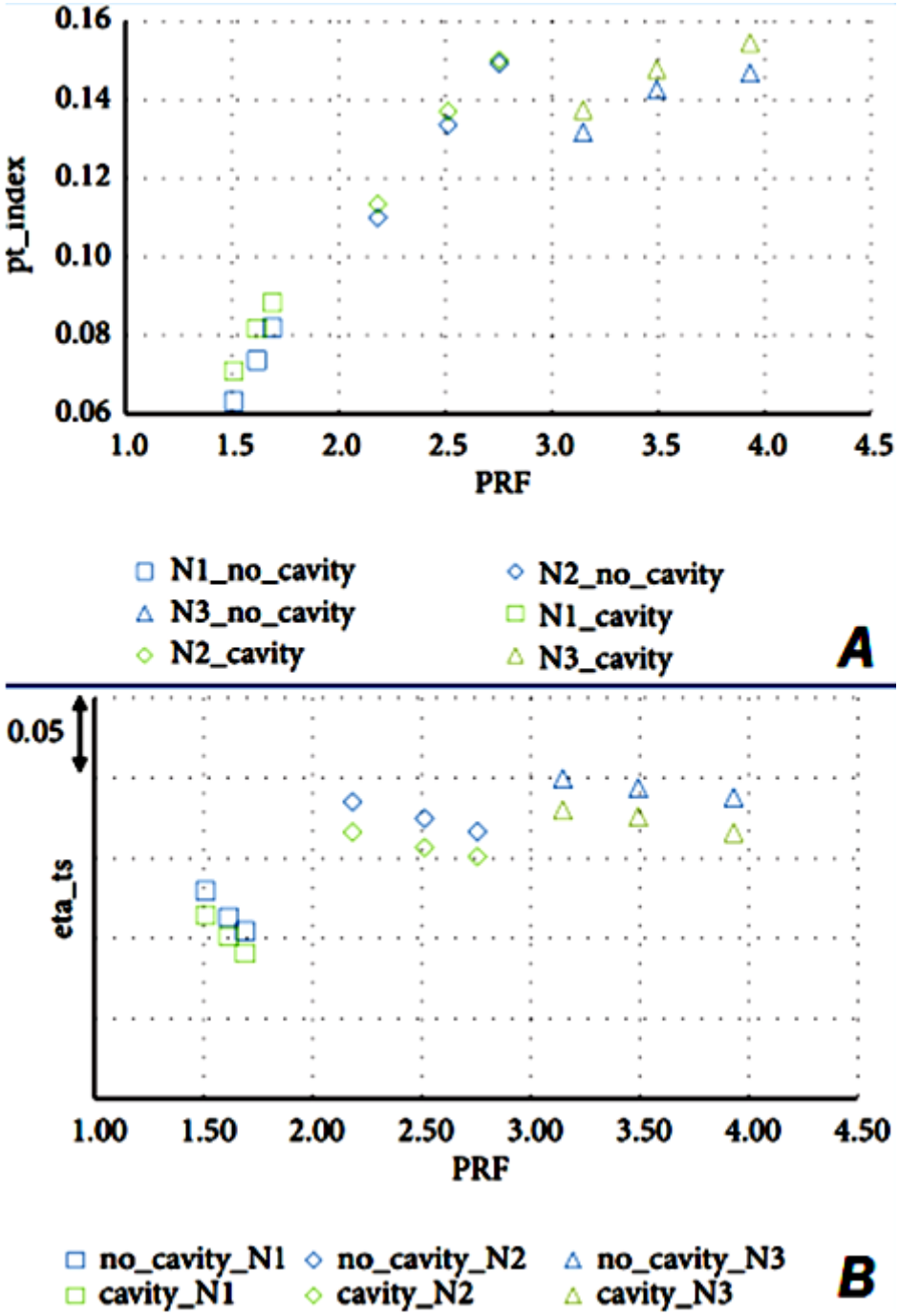

Fig. 3.27 – Cavity effect in partial hub admission: A) total pressure index vs. PRF; B) total to static efficiency vs. PRF

The cases with or without backside cavity are now considered separately, analyzing the turbine performance difference in partial 'shroud' and 'hub' admission by mean of the total pressure index. In both cases it can be noted that the flow non-uniformity index is well correlated with the total to static efficiency:

1. in absence of cavity (Fig. 3.28) partial shroud admission points present higher p_{tindex} values hence lower efficiency than partial hub admission cases;
2. in presence of cavity (Fig. 3.29) turbine performance are affected up to the point that the 'no cavity' efficiency trends are reversed (compare Fig. 3.28b and 3.29b): the cavity gifted radial turbine shows better performance in partial shroud admission rather than in partial hub admission. This is confirmed by the respective values of the total pressure index.

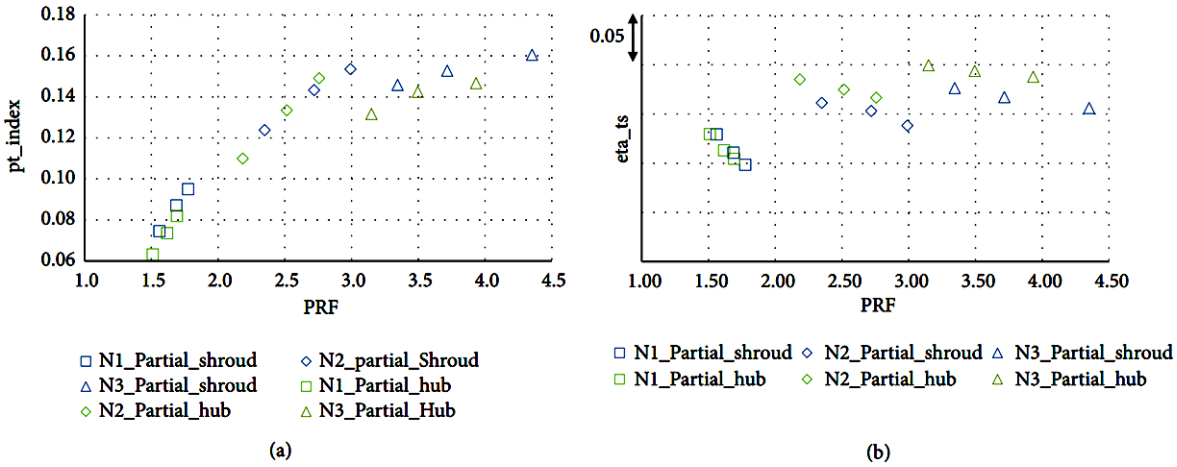

Fig. 3.28 – Performance comparison between partial shroud and partial hub admission without backside cavity: a) total pressure index; b) total to static efficiency

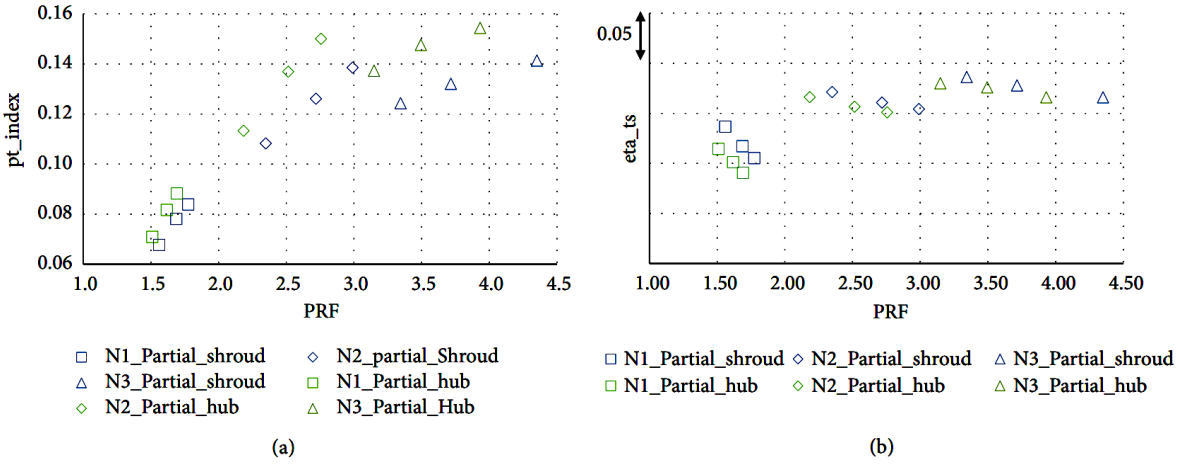

Fig. 3.29 – Performance comparison between partial shroud and partial hub admission with backside cavity: a) total pressure index; b) total to static efficiency

These results highlight the importance of the cavity in this specific volute configuration. The proposed performance index, which is based on the spanwise distribution of total pressure at rotor inlet, has demonstrated its effectiveness in predicting the performance of

the turbine under examination, correlating directly to the total to static efficiency of the machine.

As a final comment of this chapter, the peculiar twin scroll volute configuration, thanks to its strong geometrical asymmetry, facilitated the detailed investigation of flow structures in partial admission and the introduction of flow distortion parameters that would be effective for the design optimization of twin entry volutes.

Chapter 4

A software platform for the application of UQ techniques to CFD simulations

After a deep study of twin scroll turbines fluid dynamic behaviour, this chapter deals with the development of an in-house software platform to apply uncertainty quantification techniques to CFD simulations. The aim is to integrate UQ models and methodologies (which combine mathematics, statistics and engineering) used by some academic research centers with well established commercial CFD solvers.
The open source toolkit 'Dakota' was identified as the appropriate code for the part regarding the generation of the DoE, the application of the Response Surface Methodology and the use of Uncertainty Quantification techniques.
For what concerns the fluid dynamic solver, Dakota has been interfaced with:

1) Ansys Fluent® (the application of the resulting platform is the topic of chapter 5);
2) Ansys CFX® (the results of this layout are discussed in chapter 6).

The use of two different CFD codes stems from the intention to show the application of UQ techniques to different cases of industrial interest, each of which must be treated with a specific solver. On the one hand Fluent has many customization options that make it suitable for the supersonic nozzle because a specific solver setting is required; on the other hand, CFX is the proper code for turbine simulation thanks to its dedicated "Turbo-mode".

4.1. Dakota overview: a toolkit for uncertainty quantification

The acronym 'DAKOTA' stands for *"Design and Analysis toolKit for Optimization and Terascale Applications"*; it is a general-purpose software toolset for performing design of experiments, sensitivity analysis, optimization and uncertainty quantification on HPC (high performance computers). Dakota downloads are provided for Windows® and Linux®; alternatively, Dakota can be built from the source code to customize it with additional packages. When compiling from source, Windows users should typically use a '*.zip'* Dakota source archive, while Unix-based OS users should typically use a Dakota '*.tar.gz'* source archive to avoid issues with source generation utilities and line ending conversion.
Dakota is developed and supported by U.S. Sandia National Labs, it is well documented [28, 47, 59] and comes with many tutorials. The software releases are freely available worldwide via GNU General Public License. Dakota capabilities include:

- parameter studies, to explore the effect of parametric changes within simulation models in order to evaluate the characteristics of the simulation itself (e.g. smoothness), that in turn influence the choice of specific algorithms in further analyses (e.g. UQ);
- Design of Experiments (DoE) and Design and Analysis of Computer Experiments (DACE), to probe the parameter space of an engineering design problem, but with the main target of a good coverage of the input parameter space (e.g. LHS);
- Sensitivity Analysis (SA);
- Uncertainty Quantification (UQ), to calculate probabilistic information on the response functions based on simulations performed according to user-specified probability distributions of the input parameters;
- optimization via gradient-based methods, derivative-free local and global methods, to minimize costs or maximize system performance, as predicted by the simulation model, subject to constraints on input variables or secondary simulation responses;

- Surrogate based optimization (SBO) and Surrogate based uncertainty quantification (SBUQ), to use approximate representative models of an expensive high-fidelity model as computationally cheap stand-ins for optimization or UQ purposes;
- Matlab®, Scilab and Python™ interfaces.

The reader may ask, why use Dakota and not Matlab, Scilab, Octave, Python? The main reasons can be summarized in the following list:

- generic interface to black box solvers;
- scalable parallel computations from desktop to clusters;
- extensively validated;
- fully scriptable;
- simulation failure capturing;
- restart capabilities;
- parallel asynchronous or concurrent evaluations.

Fig. 4.1 summarizes the typical loop for uncertainty quantification applied to computational fluid dynamics: first of all the design variables are passed to the black box solver (Fluent or CFX in the cases studied) which numerically solves the Navier-Stokes equations reaching convergence on the quantities of interest of the UQ problem. The QoI are then collected by Dakota, which evaluates the statistics of the response functions of the engineering problem and generates new input variables according to the algorithm and the design space defined by the user inside Dakota input file.

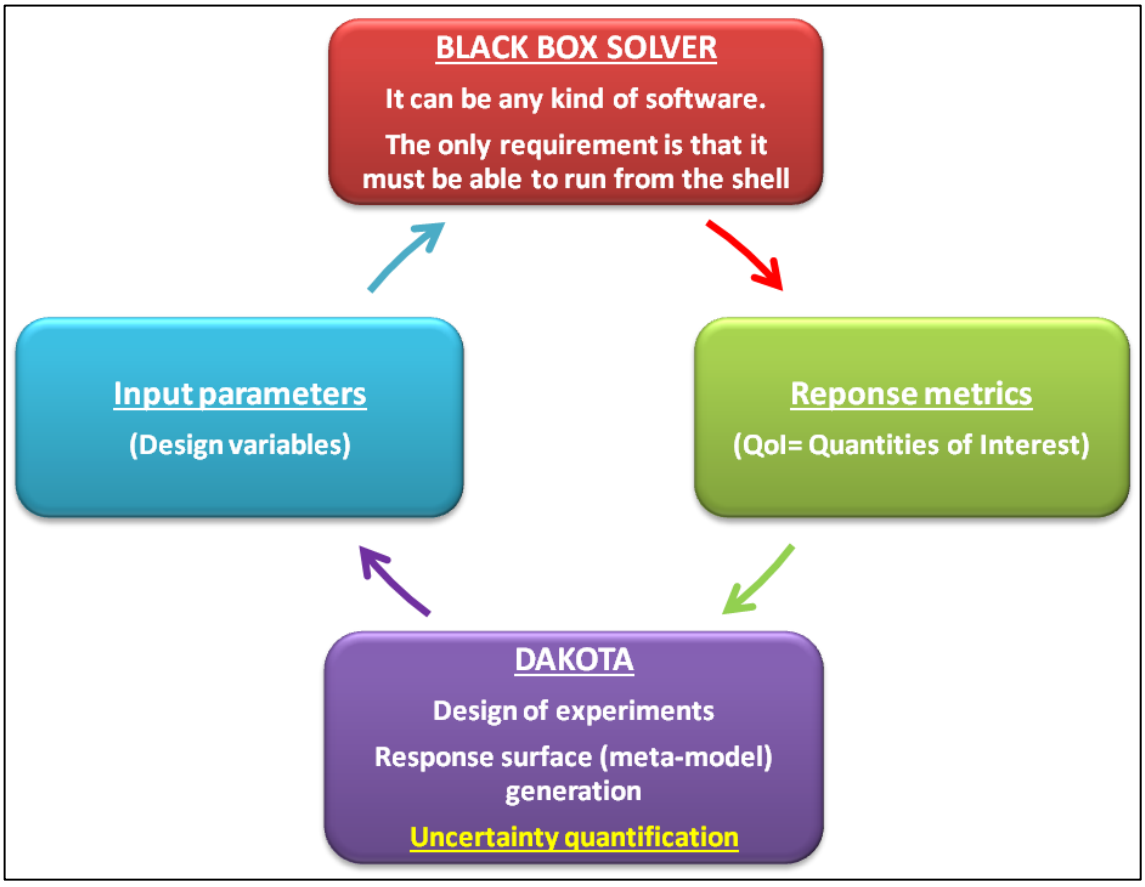

Fig. 4.1 – Uncertainty quantification loop

4.2. Dakota input file

Dakota can be run from a UNIX® or Windows® command prompt; it uses a single input file, with the extension '*.in*'. In this input file the user can formulate the problem, that is: variables, method to use and responses. Additionally, it is possible to define the interface to the black box solver (which also depends on the operating system) and the environment.
If the user misspells something or uses a keyword that does not exist in the input file, Dakota will list the available options; furthermore, if the user forgets a mandatory entry in the input file, Dakota will complain and will ask for that value. Optional entries will use the default values; in general, it is possible to refer to the documentation for more information about the compulsory and optional entries of each method.
The diagram in Fig. 4.2 shows the essential elements that make up the structure of the Dakota input file (for the sake of brevity the script details are omitted).

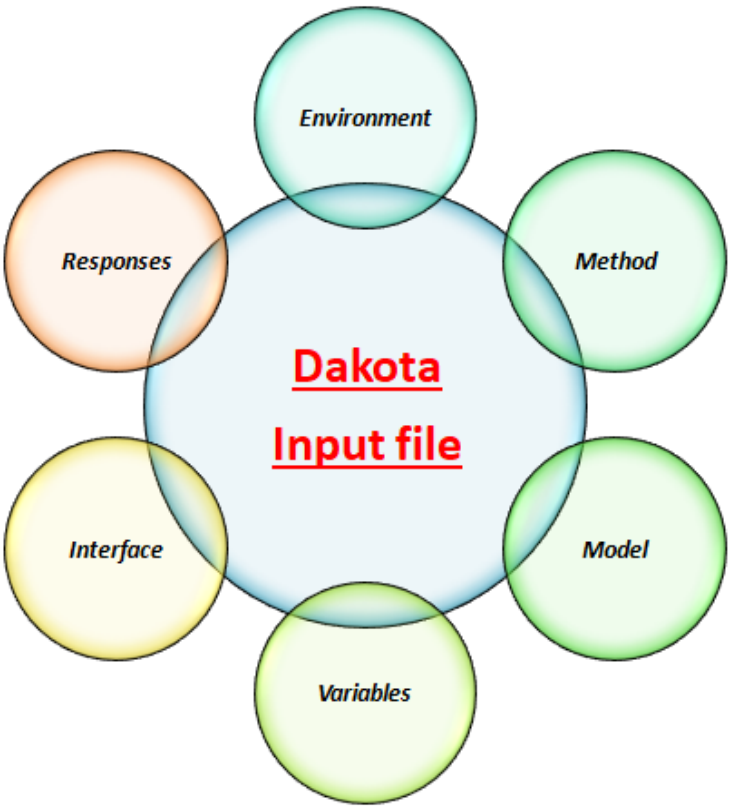

Fig. 4.2 – 'Key' subsets of Dakota input file

The '*environment*' and '*method*' keywords identify the sections in which the algorithm is defined: *environment* concerns general settings (graphical and tabular output), while *method* indicates the method used, such as the Latin hypercube sampling (LHS), and relative specific settings.
A '*model'* provides a logical unit for determining how a set of variables is mapped into a set of responses. The model allows the user to specify a single interface or to manage more sophisticated mappings involving surrogates or nested iterations.
The '*variables*' section defines the parameters (design variables) that are provided as input to the simulation; the user must indicate the lower and upper bounds of each variable, thus identifying the design space. In a UQ problem it is also necessary to establish the

probability distribution function associated with each input variable: e.g. in case of a Gaussian, this is uniquely defined by mean value and standard deviation.
Another fundamental aspect to define inside the *variables* field are the '*descriptors'*, i.e. the identifiers of each variable of the problem, which must appear in the '*.template'* file (that can be a file related to geometry, mesh, or CFD model). The values of the variables are passed in input to the *.template* file by Dakota at each iteration of the loop (Fig. 4.1), according to the predetermined *method*.
The '*interface*' field is necessary to map from variables to responses; the *'system'* call interface has been a workhorse for many years and it is well tested, but the *'fork'* interface supports additional capabilities and it is recommended when managing asynchronous simulation code executions. In the '*interface*' block of the input file the user defines [60]:

- the level of parallelism through the keywords *'asynchronous'* and *'evaluation_concurrency'*. The latter defines the number of concurrent simulations performed on the HPC (concurrent simulations are an efficient way to exploit computational resources);
- the '*analysis driver'* (details at paragraph 4.3), i.e. a shell script which is essential for interfacing Dakota with the black box solver or external programs in general. In this entry the user executes the simulation script which provides to call the programs, manipulate files and do the post-processing. This script contains the instructions of how to copy the input generated by Dakota ('*params.in'*) to the input format needed by the simulator program. In addition, through this script the user redirects the simulation output file ('*results.out'*) to Dakota for reading;
- the '*work_directory'*, i.e. a directory created by Dakota at each evaluation, with optional tagging ('*directory_tag'*) and saving ('*directory_save'*). Everything will be done in the working directory and all evaluations are relative to the current working directory. If the *directory_tag* keyword is used, Dakota will add a period and the function evaluation number to the working directory names ('*workdir.N'*). Tagging is most useful when multiple function evaluations are running simultaneously;
- *'copy_files'*, i.e. an entry which defines the directory where all files needed to run the simulation are located. The location of this directory is in reference to the case directory (*'templatedir/*'*).

The final section of Dakota input file deals with the '*responses'*, i.e. model output(s) to be studied or the response metrics. In a UQ problem these are the QoI for which the evaluation of probability distribution functions is required; even in this case it is essential to assign an acronym (*descriptor*) to each output, so that it can be uniquely identified by Dakota within the loop.

4.3. Analysis driver: connecting Dakota to external codes

This paragraph is dedicated to an in-depth analysis of the typical structure of the analysis driver. The '*simulator_script'* file provides pre- and post-processing functionality in order to transfer the input parameters from Dakota to a selected external code and to extract the response values of interest from the simulator's output file for return to Dakota.
In this section some references are taken from the simulator script (developed for Windows® environment) which is part of the UQ platform used to evaluate the effect of uncertainty on the tip clearance of the rotor of a twin scroll turbine (see more in chapter 6).
A fundamental prerequisite for operation in Windows is the setting of some programming languages including Python and Perl; furthermore, the definition of specific 'environment variables' of the operating system is required.

The main elements of any simulation interface (*'system call', 'fork', 'direct'*) are (Fig. 4.3):

- an input filter (*'I Filter'*) to insert the Dakota parameters into the input files required by the simulator program;
- one or more analysis drivers (*'Analysis Code/Driver'*);
- an output filter (*'O Filter'*) to resume the raw data from the simulation results and compute the target response data set.

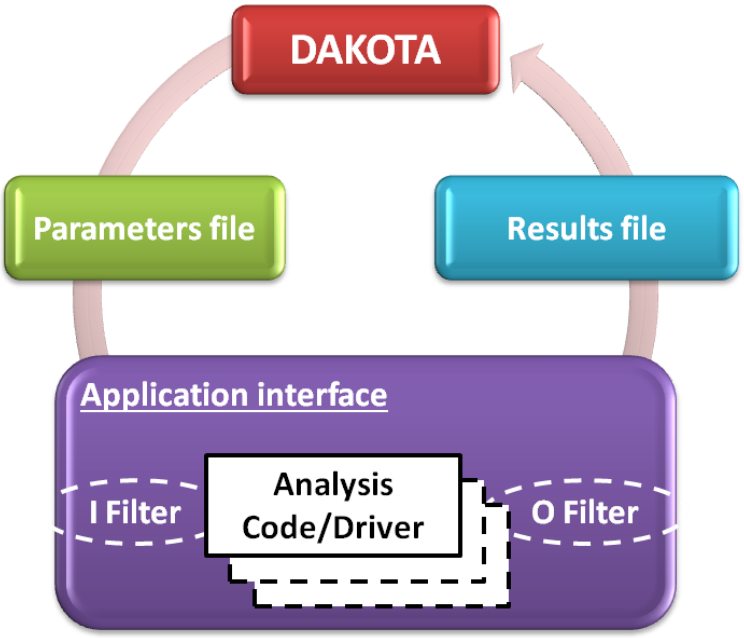

Fig. 4.3 – The 'black box' interface between Dakota and a user-supplied simulation code with the components of the simulation interface

Two cases can be distinguished:

- single analysis code → detached input and output filter facilities are seldom used and it is often convenient to merge these pre- and post-processing functions in a single script;
- multiple analysis drivers → input and output filter facilities provide a convenient means to handle non-repeated portions of the pre- and post-processing for multiple analyses. This means that pre- and post-processing tasks that must be performed for each run can be executed within the individual analysis drivers, while shared pre- and post-processing tasks that are performed only once for the analysis set can be carried out within the input and output filters.

The first part of the analysis driver file is usually dedicated to pre-processing. Dakota is packaged with two 'template' processing tools that are intended for use in the pre-processing phase of analysis drivers:

a) the first, '*pyprepro*', features simple parameter substitution, setting of fixed variable names and provides full access within templates to the entire Python programming language [28]. As such, templates may contain loops, conditionals, lists, dictionaries, and other characteristics of the Python language;
b) the second, '*dprepro*', uses the same template engine as *pyprepro* and additionally understands Dakota's parameter file formats. In particular, when using *dprepro* in an analysis driver, Dakota variables become available for use within templates; this is the case of the UQ platforms illustrated in the next paragraphs 4.4 and 4.5.

Some further details on the operating logic of an analysis driver are provided to the reader considering, as reference case, the analysis driver set up for the UQ analysis on the rotor tip clearance effect for a twin entry turbine (discussed at chapter 6). In this case the pre-processing section of the simulator script can be summarized in the following steps:

1) at first Python is called to run *dprepro* that passes the values of the input parameters (*params.in* file from Dakota) to the *.template* file, inside which the descriptors of the input variables are located. The descriptors are clearly recognizable within the file because they are included in braces, as in Fig. 4.4.

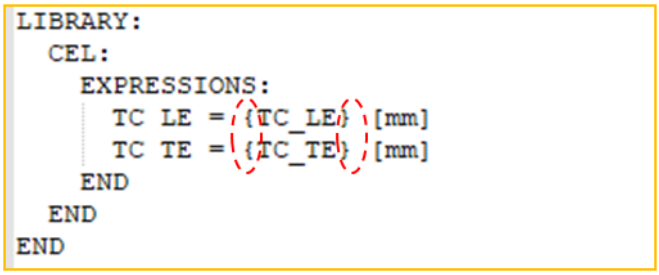

Fig. 4.4 – Extract from the '.template' file: input variables identified by curly brackets

The result of this first step is the generation of the *'.tst'* file that contains the setting for the generation of the rotor structured mesh in Ansys TurboGrid®. At each loop of the analysis the geometry at the rotor tip is modified starting from the '*.curve'* files (which define by points the hub, the shroud and the blade via stacking sections). For all cases it is correct to use the same mesh setup (target passage mesh size, number of elements in the 'O' around the blade, etc.) since the modified geometric parameters involve slight variations in the geometry (contained within millimeters in the specific case);

2) the second step is the generation of the rotor mesh, a process launched in batch through the '*MESH_ROTOR_VARIABLE_TC.tse'* file (see Fig. 4.5) which recalls the *.tst* returned at the first step and produces the rotor mesh file ('*.gtm')*. The structured rotor grid with the new clearance values is then imported into Ansys CFX-Pre® for the generation of the CFD model;

3) the final step of the pre-processing phase is up to the '*.pre'* file, which in turn needs:
   - *.gtm* for the rotor mesh to be imported in CFX-Pre;
   - *'.cfx'*, an intermediate save format for not yet complete CFD models, which already contains the twin scroll volute and exhaust pipe meshes (that are not subject to geometrical variations);
   - '*.ccl'* file which imports the CFD model settings, i.e. boundary conditions of the simulated point, operating fluid properties, turbulence model, number of iterations, timestep, etc.

The output of the pre-processing section is the '*.def'* file, i.e. the CFX-Pre file format to be imported into the numerical solver (Ansys CFX-Solver Manager®).

The second part of the analysis driver file concerns the launch of the simulation and the solution post-processing to extract the values of the response functions of interest. The CFD solver loads the case ('*TWIN_SCROLL_ROTOR_SINGLE_CH.def*') and runs the simulation in parallel on the calculator cores. A detail that can speed up convergence is the initialization of the calculation with a result file ('*.res'*) obtained from a simulation conducted a priori with an example rotor mesh. Once the calculation is completed, the next step is post-processing, performed in batch through a macro.

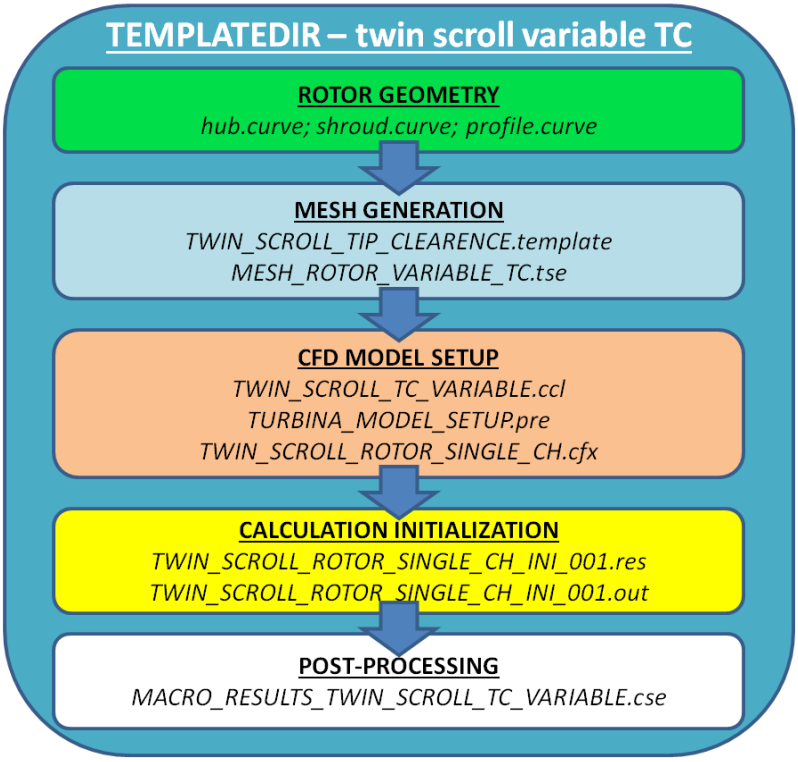

Fig. 4.5 – Template folder structure for the UQ analysis on the rotor tip clearance effect

The *'MACRO_RESULTS_TWIN_SCROLL_TC_VARIABLE.cse'* file imports the results file generated at each iteration of the analysis loop and contains a Perl language script (compatible with Ansys CFD-Post® Command Editor) to extract the selected output data of the problem from the results of the numerical solution and then to print these information in a text file named *'risultati.txt'*. However, this output file is not what is passed to read in Dakota for two reasons:

- at each calculation performed it is possible to save much more post-processing information than the limited set of response functions defined in Dakota;
- the result file to be passed to Dakota for UQ analysis must contain the values of the selected response functions in a predefined order, established at the assignment of the descriptors for the *responses* in the final part of the Dakota input file.

For the reasons listed above it is therefore necessary to insert Perl language instructions in the final part of the analysis driver in order to:

- recognize each of the response functions within *'risultati.txt'* by the name assigned to each output (e.g. "Corrected Mass Flow");
- obtain the corresponding value from the *'risultati.txt'* file;
- print the values in predetermined order in the '*results.tmp'* file, i.e. a temporary file whose values are then passed to Dakota results file (*'results.out'*), closing the analysis loop.

The extrapolated response function values (*'results.out'*) are inserted next to the values of the input parameters (*'params.in'*) on each row of the DoE output results table (*'table_out.dat'*); it is therefore possible to plot 3D surfaces from DoE results through a program suitable for the elaboration of numerical data (e.g. Octave) in order to assess the sensitivity of the quantities of interest to the input parameters.

4.4. UQ platform for Ansys Fluent® : supersonic nozzle case

The input/output files and shell scripts needed to use Dakota have been detailed in the previous sections. This paragraph now focuses on the structure of the UQ platform developed for the uncertainty quantification analysis conducted on a supersonic de Laval nozzle, whose results are the main subject of chapter 5. In this case a Surrogate-Based UQ technique was applied, involving two steps:

1) the generation of a DoE with a sufficiently large number of samples and such as to guarantee optimal coverage of the design space;
2) the application of the response surface methodology and the use of the sampling-based UQ technique on the generated surrogates.

In the first step (Fig. 4.6) the input parameters (*params.in*) generated by Dakota input file according to the selected algorithm (e.g. Latin hypercube sampling) are passed to *dprepro*, which performs the pre-processing phase once called by the analysis driver.
The *'workdir.N'* folder is generated from the template folder *('templatedir')*, where '*N*' stands for the *N-th* loop iteration (i.e. the *N-th* sampling point of the design space). Each working directory contains a *'.cas'* file (Fluent format for the CFD model) in which the nozzle mesh has already been loaded; the CFD model is edited via '*Fluent_auto.jou'*, i.e. a journal file generated at each loop by copying the input parameters values inside the '*Fluent_auto.template'* (that is located in the template folder).

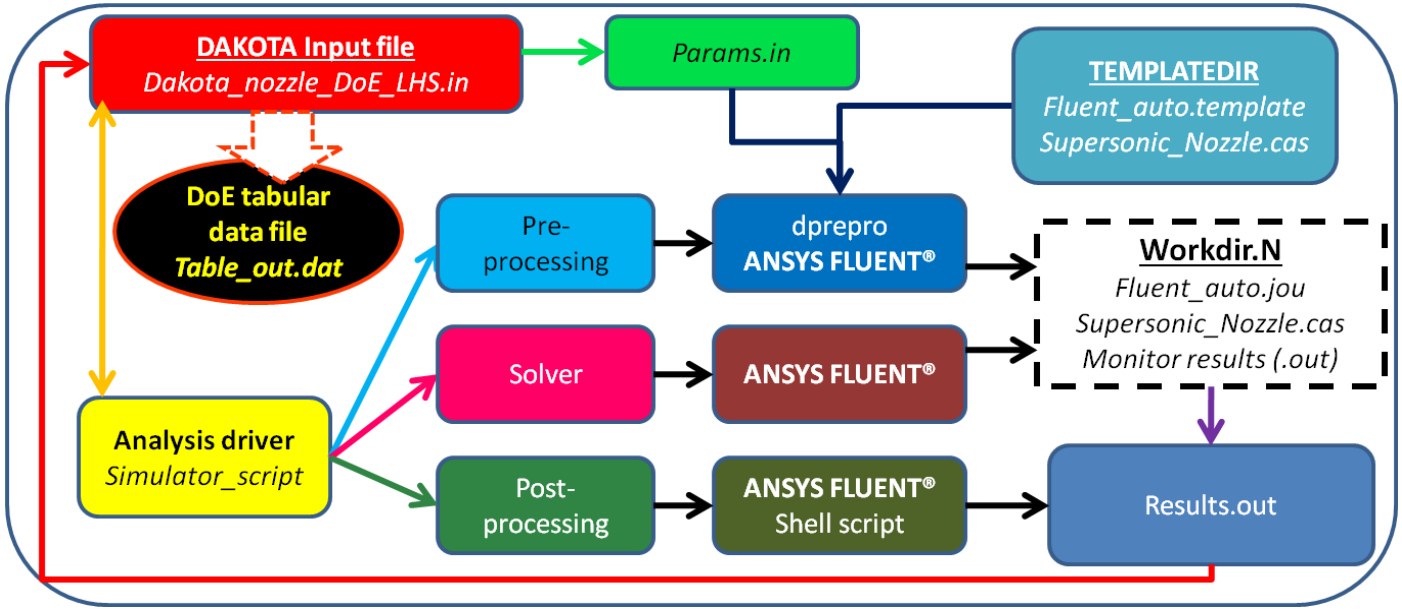

Fig. 4.6 – Dakota coupled to Ansys FLUENT® - 1st step: DoE generation loop

Once the solver input file is written with the updated boundary conditions, the '*simulator_script'* launches the calculation and the quantities of interest are printed in monitoring files ('*Monitors.out'*) at each iteration of the numerical solution of the Navier-Stokes equations. The analysis driver then executes a sequence of post-processing instructions that lead to the generation of a results file formatted according to what has been specified in Dakota input file. The loop ends when the output file (*'Results.out')* is passed to Dakota, which in turn inserts the quantities of interest next to the input parameters on each line of the DoE tabular data file (*'Table_out.dat').*

In the second step (Fig. 4.7) the analysis driver is basically a dummy file necessary for Dakota to work and the template folder is empty. In fact this time the analysis driver does not have to perform any analysis, since the previously generated DoE dataset is used to build the metamodel. Nevertheless, new input parameters and results are visible in Fig. 4.7 because the uncertainty quantification is performed through LHS. The input parameters (*params.in*), taken within the design space and according to user-defined probability distributions, are used to sample the generated surrogates, while the '*Results.out'* file is the process outcome. The output file is finally used by Dakota to:

- build the tabular file containing inputs and outputs for all the sampling points of the response surfaces *('table_UQ_surr.dat');*
- calculate the probability distributions of the response functions and evaluate their statistical quantities, the ultimate goal of the platform.

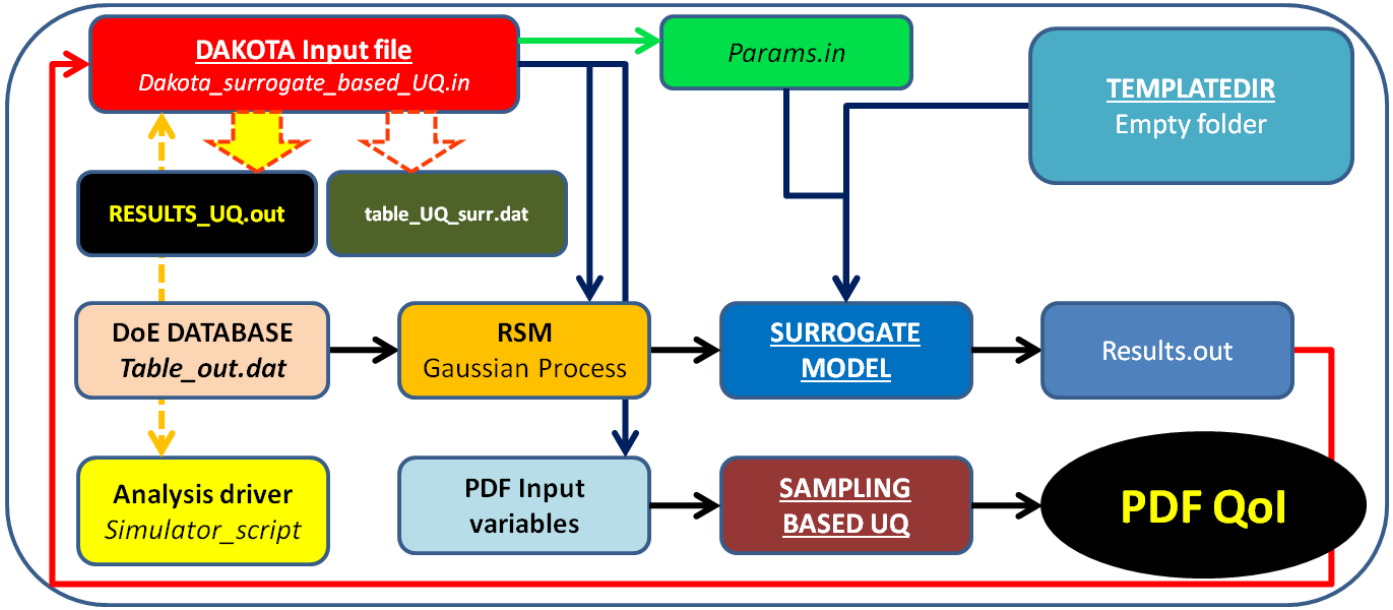

Fig. 4.7 – 2nd step: RSM and sampling-based UQ

The careful reader may note that inside the flowcharts presented in this paragraph no reference is made to the validation of the surrogates. This choice is intentional to simplify the understanding of the workflows; obviously, once the surrogate models have been generated and the PDFs of the outputs have been computed, different methodologies are applied to test the reliability of the metamodels and consequently validate the results obtained from the UQ analysis (see the applications in chapters 5 and 6). More specifically, Dakota allows to calculate diagnostic metrics of surrogate models on the basis of the estimated prediction error (e.g. by cross-validation or with respect to a challenge data set).
A final noteworthy comment concerns the number of sampling points (CFD simulations) necessary to obtain a reliable surrogate. Said that this number is certainly connected to the characteristics of the system to analyze and to the number of input variables of the problem, a practical method to test the goodness of the metamodel consists in:
(1) generate a surrogate with a certain number of sampling points;
(2) perform "checking" CFD simulations in points not used for the metamodel generation;
(3) compare the CFD results with those obtained by sampling the surrogate.
If the prediction error is lower than the level of accuracy with which the response functions have to be estimated, the number of sampling points can be considered sufficient.

4.5. UQ platform for Ansys CFX® : twin scroll turbine case

This paragraph deals with the UQ platform set up for the application of different uncertainty quantification methodologies to the rotor tip clearance effect in a twin scroll radial turbine (subject of chapter 6). Alongside the well-tested UQ procedure based on sampling of response surfaces, it was decided to try a method of increasing interest in the UQ research area, namely the polynomial chaos expansion (PCE – theory details at section 2.6). Therefore in the following the SB-UQ platform is illustrated first and then the PCE.

4.5.1. Surrogate-Based UQ platform for Ansys CFX®

The same steps illustrated at section 4.4 for the supersonic nozzle are repeated here for the radial turbine; however a higher level of sophistication is added to the previous platform because the input parameters are no longer boundary conditions of the CFD model, but geometric variables. This entails a greater complexity of the 'template' directory structure (see Fig. 4.5), which must also contain the files necessary to create the mesh to be imported into the fluid dynamic model. The template directory shown in Fig. 4.8 is the same displayed with more details in Fig. 4.5. During the pre-processing phase the '*.tst'* file (containing rotor mesh setup details) is generated starting from the '*.template'* located inside the template folder; inside '*.tst'* file the input variables are updated for each DoE sample according to the values generated by Dakota input file and then passed to '*params.in'*. Once the rotor channel structured mesh is generated ('*.gtm'* file), CFX-Pre is called by the analysis driver which executes the CFD model setting instructions contained in '*TURBINA_MODEL_SETUP.pre'*. The CFX-Solver Manager® input file ('*.def*' format) is then written and the CFD simulation is performed starting from an initialization results file. The post-processing phase uses CFD-Post® to load a user-defined macro ('*.cse'*) which extracts the main information from the solver output file ('*.res'*). Finally a Perl language script formats the *'results.out'* file to be read in Dakota, which in turn writes the DoE tabular data file.
For what concerns the 2nd step of the Surrogate Based-UQ procedure, the same algorithm and structure shown in Fig. 4.7 for the supersonic nozzle are valid for the turbine case.

The main changes are located inside the Dakota input file, which contains different input variables, probability distributions, response levels, response functions, etc.

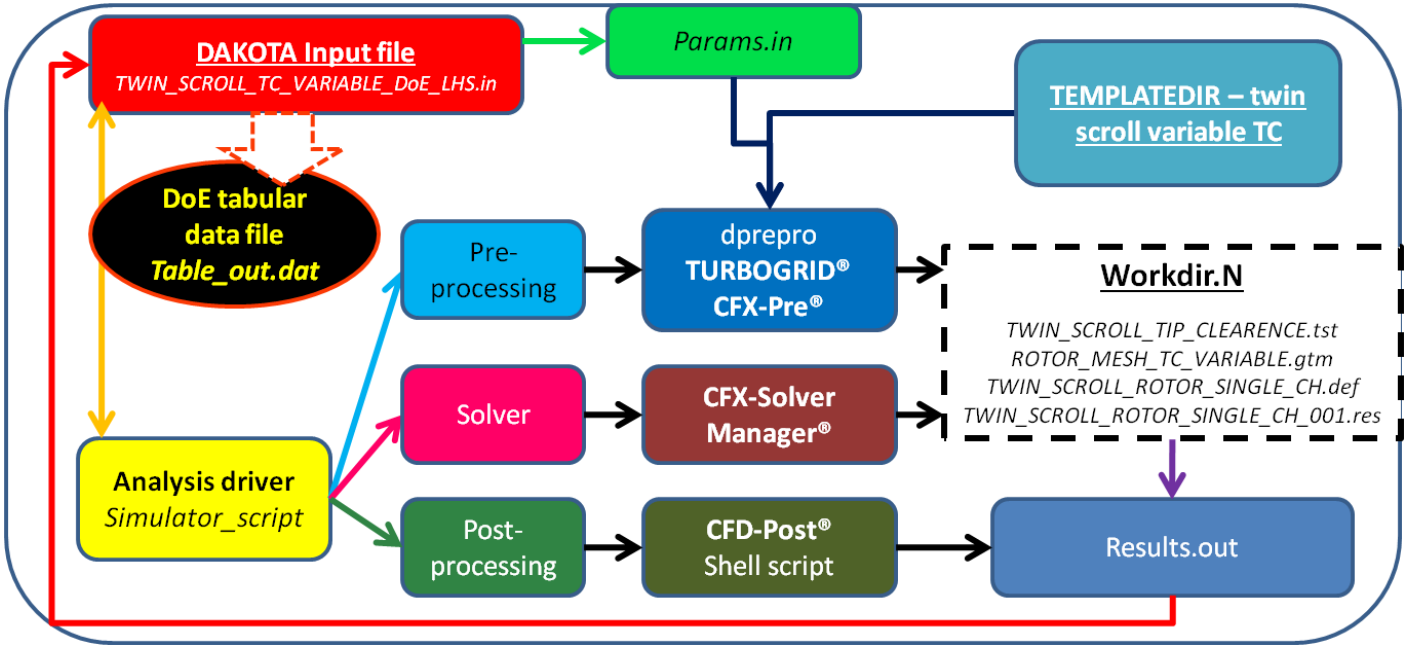

Fig. 4.8 – Dakota coupled to Ansys CFX® - 1st step: DoE generation loop

4.5.2. PCE UQ platform for Ansys CFX®

In this case the structure of the template folder and analysis driver coincides exactly with that already illustrated (Fig. 4.5) for the UQ method based on sampling of metamodels. The main differences are instead in the algorithm used: the uncertainty this time is quantified through a single logic block, i.e. with a single Dakota input file. As mentioned in section 2.6, PCE method estimates its coefficients using a spectral projection technique; numerical approximations are performed using a quadrature approach and this requires the specification of the *'quadrature_order'* of the method. In this application case the Gaussian quadratures are selected using an isotropic approach. Therefore the UQ algorithm uses the same quadrature order (denoted by 'm') for the input variables (clearance values at rotor leading edge and trailing edge, i.e. two dimensions), resulting in a total of m^2 function evaluations to compute the PCE coefficients.

Inside the *method* section of Dakota input file it is necessary to specify the number of response levels for all quantities of interest of the UQ problem; furthermore, if the user wants that Dakota computes response functions probability distributions with a pre-established discretization, the response levels for each response function must be specified bin by bin.
In conclusion of this chapter, Fig. 4.9 shows the structure of the platform prepared for the application of the UQ technique based on PCE method: a single logic block contains all instructions necessary to pass from input variables PDFs to the statistics of the output responses.

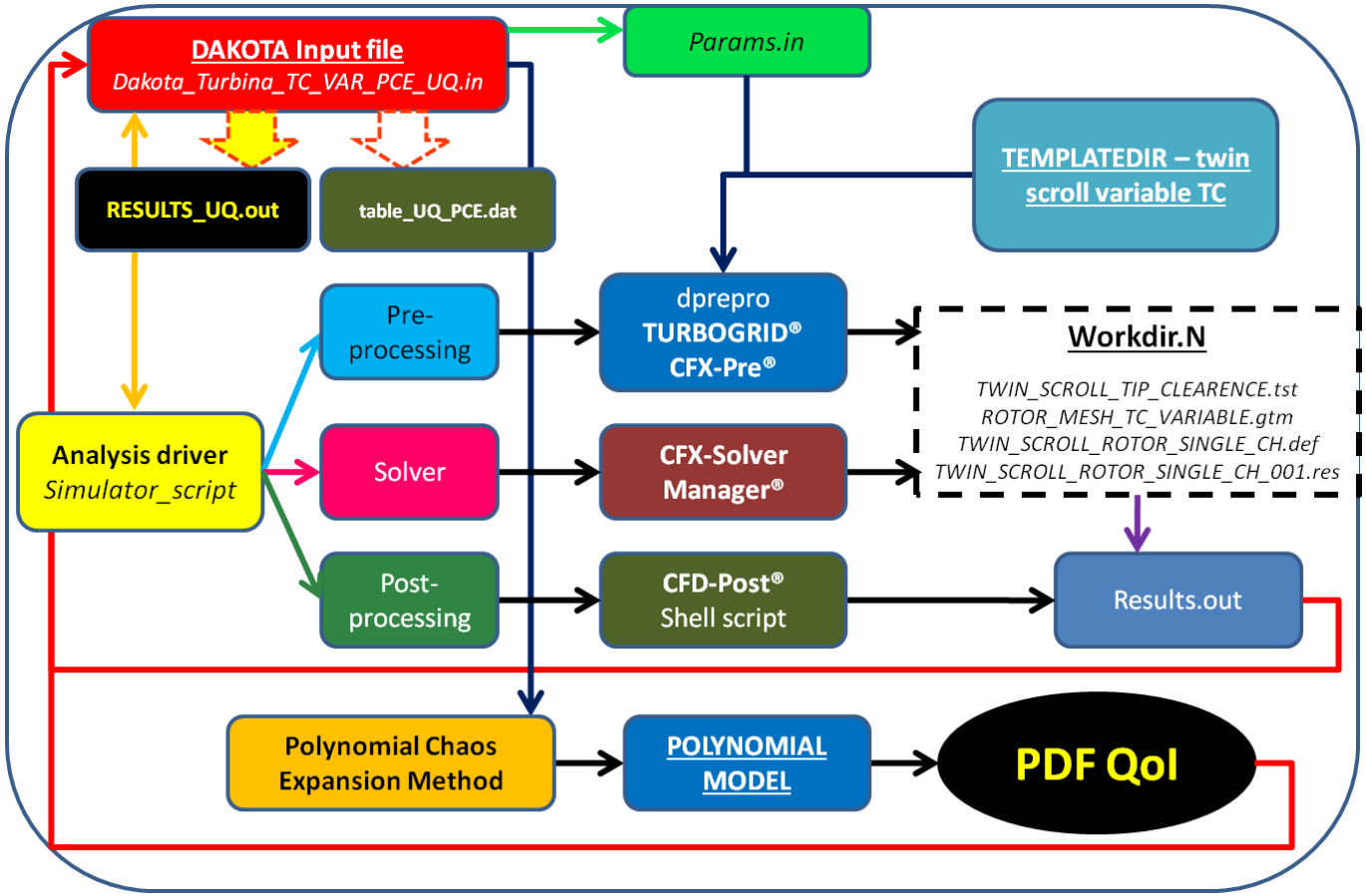

Fig. 4.9 – Dakota coupled to Ansys CFX® - UQ platform for Polynomial Chaos Expansion

Chapter 5

Uncertainty quantification approach on numerical simulation for supersonic jets performance

The performance prediction of a component or system under investigation is the main issue of any engineering design problem, due to the variability of operating conditions or the uncertainty on input data (boundary conditions or geometric tolerance).
In this chapter the propagation of uncertainty on boundary conditions through a numerical model of supersonic nozzle is investigated. The evaluation of the statistics of the problem response functions is performed following 'Surrogate-Based Uncertainty Quantification' (see more in paragraph 2.3.5); this approach involves two steps:

1) the generation of a surrogate starting from a DoE in order to approximate the nozzle "physical" model (expensive to simulate);
2) the application of the UQ technique based on LHS to the metamodel.

Probability density functions are introduced for the inlet boundary conditions in order to quantify their effects on the output nozzle performance. The physical problem considered is very relevant for the experimental tests on the UQ approach because of its high non-linearity: a small perturbation of the input data can drive the solution to a completely different output condition.
The CFD simulations and the uncertainty quantification were performed by coupling the open source toolkit 'Dakota' with the commercial CFD software 'Ansys Fluent®', as described in detail in paragraph 4.4. The novelties of the proposed methodology can be summarized as follows:

- development of an in-house procedure to connect an open source tool set which supports UQ techniques, such as Dakota, with a widely used commercial code such as Ansys Fluent. As well known, the application of UQ methods to CFD has been recently introduced in the field of fluid dynamic simulations only in the research field, while industrial design procedures and codes currently do not include uncertainty quantification techniques applied to CFD simulations;
- although the sampling-based UQ approach is not a brand new technique, the application of this method to an industrially interesting case, such as that of supersonic overexpanded jets, is shown. The reader can verify that there are few available results in literature on this issue.

The adopted procedure demonstrates the applicability of advanced simulation techniques (such as UQ analysis) to industrial technical problems. Furthermore, the analysis highlights the practical use of uncertainty quantification techniques in predicting the performance of a nozzle design affected by off-design conditions with fluid dynamic complexity due to strong non-linearity.
In the context of the doctoral thesis, the supersonic nozzle also represented a test case to refine the workflow necessary for the application of uncertainty quantification methodologies. The experience gained on the convergent-divergent duct facilitated the identification of the most suitable UQ techniques to be applied to the CFD simulation of twin entry radial turbines.
The UQ applications shown in this chapter have been published in the journal Algorithms with the paper "*Uncertainty Quantification Approach on Numerical Simulation for Supersonic Jets Performance"* [61].

5.1. Introduction and literature review

In recent years an important part of the research in numerical simulations, in many engineering sectors, has been dedicated to the performance prediction of systems and components in off-design conditions. The behaviour of a system or component that experiences conditions different from those for which it was designed is on the one hand due to the deterministic variation of input parameters and on the other hand to the aleatory uncertainty which affects both input data and geometric tolerances.
In this scenario it is fundamental to know how uncertainties can influence the results of the problem under investigation with the purpose to improve the accuracy and the reliability of the numerical simulations.

Computational Fluid Dynamics (CFD) is one of the disciplines in which UQ is increasingly applied within a simulation environment. The parallel evolution of both soft-computing methods and computer performance made UQ analysis a potential improvement of conventional industrial design procedures, which often include CFD simulations. The development of the Response Surface Methodology (RSM) has significantly enhanced the effectiveness of design optimization based on simulation [62, 63] as an industrial standard or for data mining and diagnostic applications [64, 65]. The same RSM approach can be used to develop very efficient frameworks for UQ analysis [66].
A contribution to this field is given in this chapter with reference to one of the most interesting examples of compressible flow thanks to its high non-linearity: the adiabatic flow in a variable section duct. It is a relevant case for its physical and mathematical background, and it has also a wide range of engineering applications. The best known application is for spacecraft propulsion in aircraft engines or in supersonic wind tunnel [67]. Convergent–divergent nozzles are also applied in gas burners [68, 69] and in supersonic water separators for natural gas purification [70, 71].
The preliminary design of a supersonic nozzle (de Laval nozzle) is based on the basic gas dynamic equations to obtain a reference, ideal, operative condition of fully expanded jet [67]. However, the theory is based on some assumptions, such as isentropic flow conditions, that may affect the actual nozzle performance. In addition, the real operating conditions (pressure, temperature, gas mixture composition, etc.) can cause a significant change in the flow structure and in the generation of shock waves, with direct fall-out on nozzle performance.

The main goal of this chapter is to answer to the following questions: a small variation of some input parameters can remarkably affect the performance of a designed convergent–divergent nozzle? Can UQ methods help to quantify the above effect and give more insight into the nozzle behaviour?
The uncertainties propagation through the CFD model of the nozzle was performed using the automated procedure developed by the author within Dakota open source platform (see section 4.4). The selected UQ approach is a ‘surrogate-based’ approach: a response surface was generated from a DoE and then the Latin hypercube sampling (LHS) was applied to the metamodel to perform the UQ analysis. The choice of a surrogate model is highly effective in reducing calculation times when a sampling-based UQ method is adopted: in fact, a large number of response function evaluations is required to generate converging statistics.
The LHS method was used for both DoE generation and UQ analysis. In this case the Latin hypercube sampling was preferred to the basic Monte Carlo method because LHS is a

sampling method that converges more quickly and also ensures better coverage of the design space.
The surrogate model was generated through the Gaussian Process approach (theoretical details in section 2.3.2) which uses a Gaussian correlation function with parameters that are selected by Maximum Likelihood Estimation; by definition [28] this correlation function results in a response surface that is C^{∞}-continuous.

In a first application an optimized nozzle geometry with supersonic airflow is considered. The commercial software Ansys Fluent® was used to run a series of CFD simulations to identify the influence of the discharge environment pressure on nozzle operating condition, flow structure and performance. A perturbation range of the discharge static pressure was chosen with respect to the critical gas dynamic condition, where the normal shock wave is positioned at the nozzle exit section (denoted as 'r2' state in classical literature). The choice of this particular condition is related to the performance drop that occurs if the shock wave moves into the divergent part of the nozzle. After a preliminary sensitivity analysis, a full UQ approach was applied to quantify the effects of the input variable (ambient static pressure) distribution on nozzle performance.
A second application considers the flow of natural gas in a convergent–divergent nozzle to understand the effects of uncertainty on gas chemical composition on nozzle expansion performance. The gas composition variation may occur on a daily or seasonal basis, according to the geographical area and pipeline used [72]; this is a serious problem for several industrial applications, where large quantities of natural gas are treated and energy consumption is an issue [73, 74]. The same investigation approach of the first case study was applied, confirming the effectiveness of the UQ analysis.

5.2. CFD model settings

The fluid domain consists of a 2D axisymmetric de Laval nozzle with an expansion volume ("environment" in Fig. 5.1) at the exit, which represents the discharge environment at constant pressure. The CFD model is consequently setup as 'axisymmetric', i.e. the RANS equations were solved using an 'axis' boundary condition (indicated in Fig. 5.1), as common practice in literature [75].

A structured grid was generated for the spatial discretization: as shown in Fig. 5.2, a grid refinement was performed near the nozzle wall in order to ensure a y+ value close to one. The Reynolds Averaged Navier-Stokes Equations (RANS) in the steady form were solved numerically with the addition equation for the turbulence closure. The two equations k-ω SST turbulence model was selected according to previous experience in the application case. This turbulence model in fact allows a good accuracy both in proximity and far from the walls, correctly predicting the trigger and the degree of flow separation under adverse pressure gradients.
A second order upwind scheme was chosen for the spatial discretization because when the flow is not aligned with the structured mesh (e.g. oblique shock waves), the first-order convective discretization is not appropriate.
Total inlet conditions (pressure and temperature) were applied at nozzle inlet, while the discharge pressure (p_s) was assigned to each side ('1', '2' and '3' in Fig. 5.1) of the expansion volume which models the nozzle discharge environment.

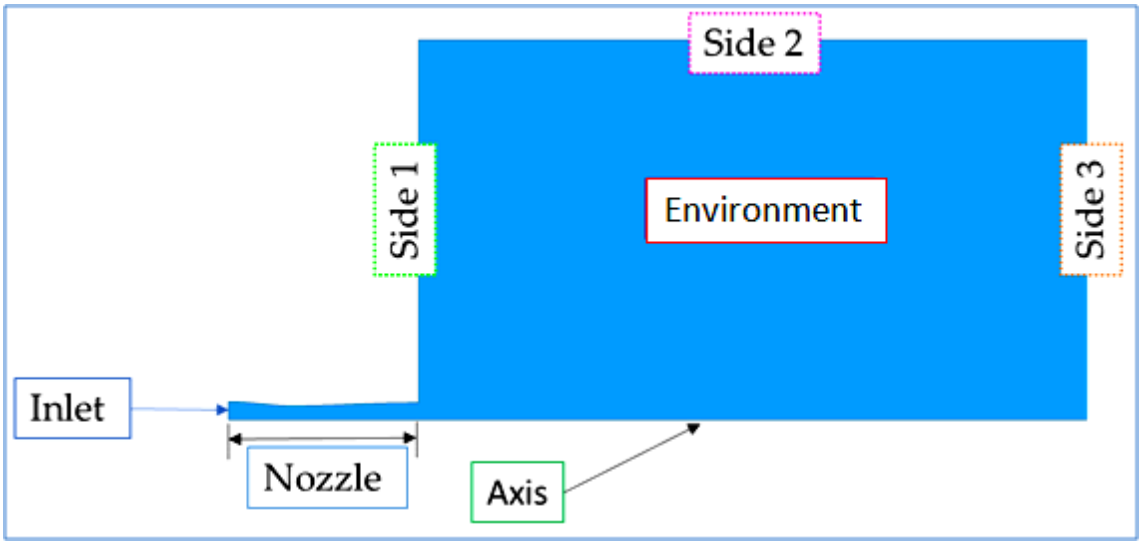

Fig. 5.1 - Supersonic nozzle CFD model: fluid domain

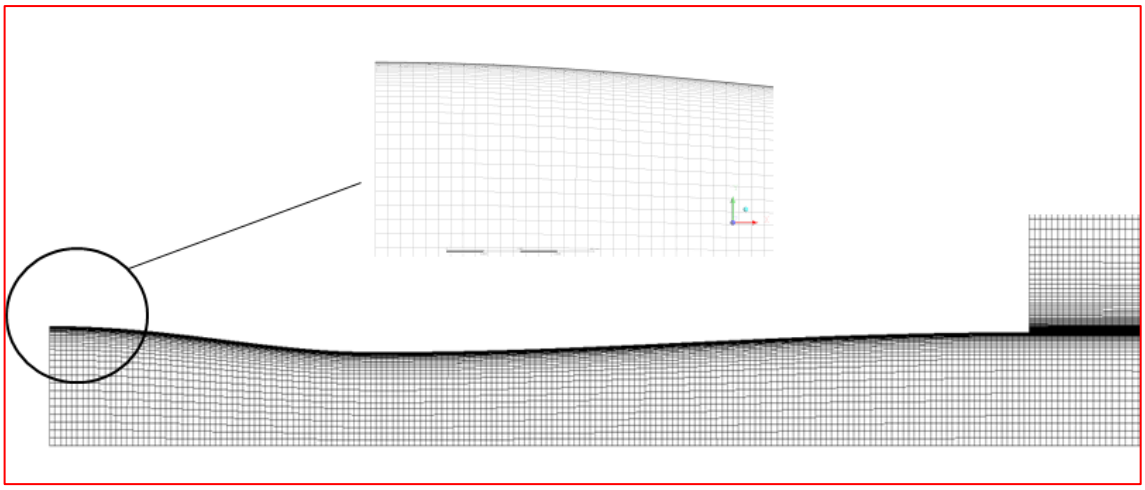

Fig. 5.2 - Nozzle mesh (an enlargement of the grid near wall in the miniature)

The set of BCs assigned to the fluid domain is summarized in Tab. 5.1 below:

Tab. 5.1 - Boundary conditions for the supersonic nozzle CFD model

Fluid domain region	**BCs type**
Nozzle inlet	total pressure and total temperature
Environment side walls	discharge static pressure and temperature
Nozzle walls	no slip condition; adiabatic

In the first part of the research work, the operating fluid is air modeled as an ideal compressible gas with constant C_p. Sutherland's law with three coefficients (equation (5.1)) is adopted to simulate the variation of the dynamic viscosity with temperature.

$$\mu_{air} = \mu_{ref\ air}\left(\frac{T_{air}}{T_{ref\ air}}\right)^{\frac{3}{2}}\left(\frac{T_{ref\ air} - Su_{air}}{T_{air} - Su_{air}}\right) \tag{5.1}$$

In the second part of the chapter the working fluid is instead natural gas; even in this case the fluid is treated as an ideal and compressible gas. The dynamic viscosity is calculated through Sutherland's law with suitable coefficients for methane.

5.3. Background work: some concepts of supersonic nozzle theory

The supersonic convergent-divergent duct was selected as first test case of UQ applications because on the one hand it is a computationally cheap two-dimensional case (and this is very important if a sampling-based UQ technique is applied) and on the other hand it is a highly difficult case to converge due to the complexity of its fluid dynamic structure. For this last reason, in fact, an accurate tuning of the numerical model was required a priori, even using a well tested commercial CFD code like Fluent®.
The background work also consists in the 1D design of a convergent-divergent nozzle in a specific theoretical reference condition, usually indicated as 'r3' and relative to the case of perfectly expanded nozzle or 'supersonic isentropic solution' (see Fig. 5.3 - no shock waves in the divergent duct or in the outside jet).

Tab. 5.2 – Nozzle boundary conditions at design point

Design BCs	
$T_{t1}\ [K]$	600.0
$p_{t1}\ [Pa]$	300000
$p_s\ [Pa]$	50000
$\dot{m}\ [kg/s]$	0.200

The selected boundary conditions (see Tab. 5.2 – where the mass flow rate is the target) represent a realistic operating condition which allows the realization of the aforementioned 'r3' since the p_s/p_{t1} ratio is lower than 0.528 ('critical' pressure ratio for air fluid).

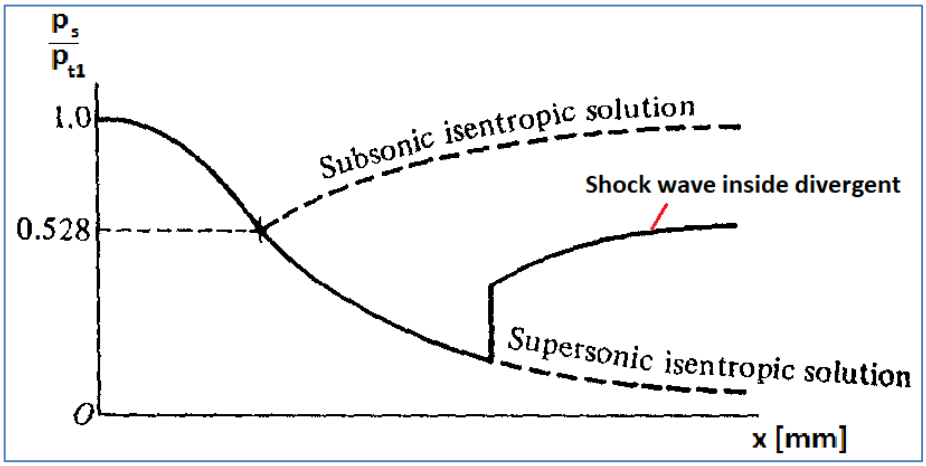

Fig. 5.3 - Gas dynamic theory of de Laval nozzle

Another fundamental aspect to certify the validity of the results discussed in the following paragraphs is the validation of the CFD model, which consists in checking that the 'r3' state is actually verified at the design point. The results of these 'background' calculations are shown below:

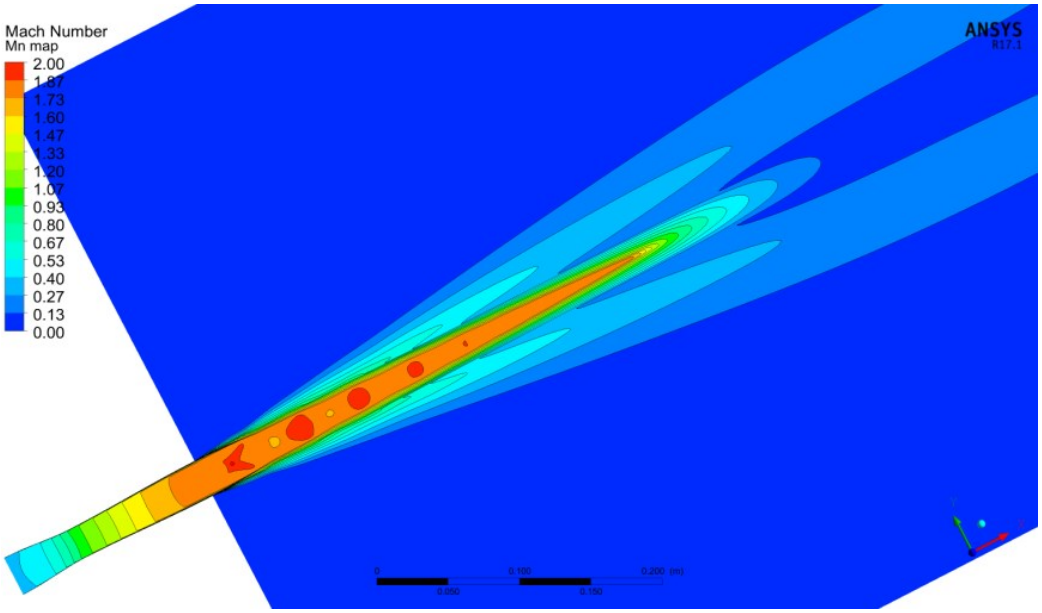

Fig. 5.4 – Mach number map on nozzle meridian plane at design point (p_s=50000 [Pa]). Case with viscous nozzle walls

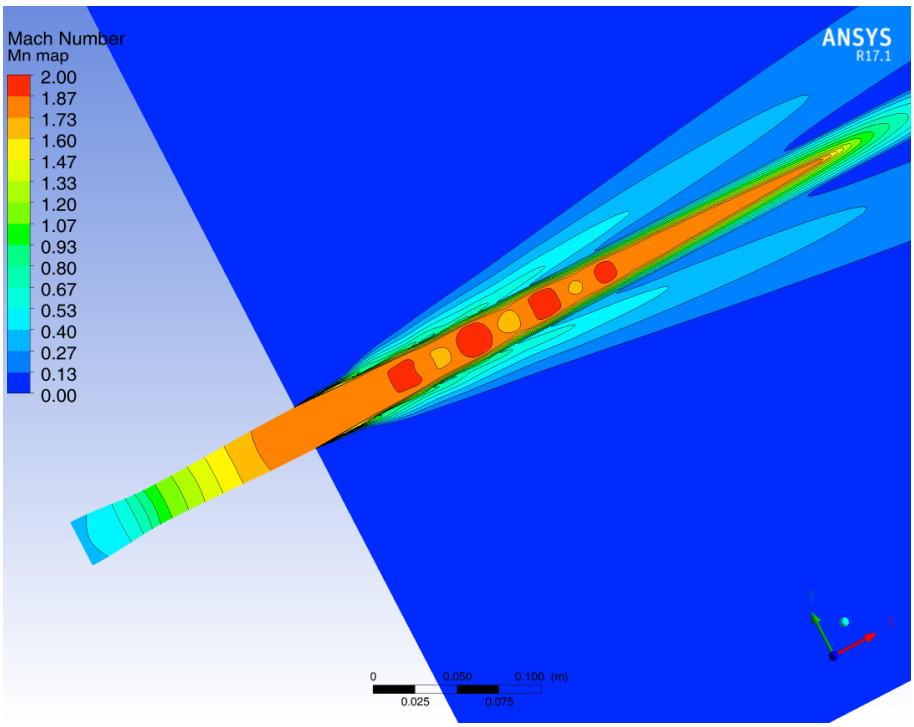

Fig. 5.5 - Mach number map on nozzle meridian plane at design point (p_s=50000 [Pa]). Case with inviscid nozzle walls

It should be remembered that the isentropic solution 'r3' can be verified only in the adiabatic case without losses. However, this analytically achievable condition is very difficult to be reproduced numerically due to the discretization error.
In order to test if the solution tends to the 'r3' ideal case by adapting the CFD model to the 'zero losses' condition, an inviscid run was executed (Fig. 5.5). The same pressure ratio ($p_{t1}/\ p_s$) of the viscous case was applied, verifying that the mass flow at nozzle outlet converges on the same target $\dot{m} = 0.2\ [kg/s]$. Comparing Fig. 5.4 and Fig. 5.5 it is clear that in the inviscid run the first shock wave is further forward inside the jet, approaching the ideal case. Hence, even conditioning nozzle walls as adiabatic (zero heat flux) and free slip (no viscous losses), the presence of weak shock waves in the jet is considered acceptable if a viscous model is used for the numerical setup (as in the case discussed).
The CFD model is then tested in another gas dynamic theoretical reference condition (involved in the next UQ analysis), denoted as 'r2' (R_{II} in Fig. 5.6) and corresponding to the case with shock wave located at the exit of the divergent duct.

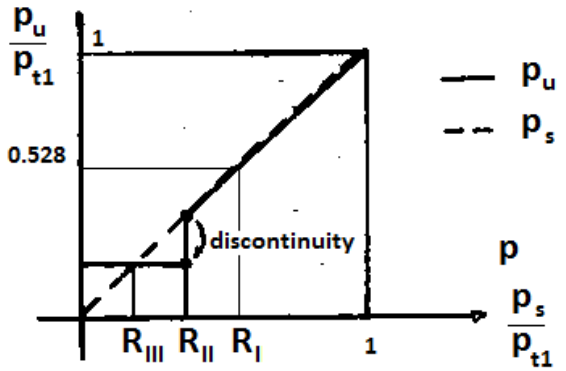

Fig. 5.6 – Nozzle exit pressure (p_u) versus discharge environment pressure (p_s)

The 'r2' condition was selected because, as shown in Fig. 5.6, it represents a discontinuity for the nozzle exit static pressure (p_u); in fact from this point on, the reduction of the discharge environment pressure (p_s - which was coherently chosen as the input uncertain variable in the first part of the UQ application) results in a nonlinear nozzle exit pressure (p_u) drop. For this theoretical reason, a discontinuity in nozzle performance can be expected around the 'r2' state, that therefore becomes an interesting operating condition around which to perform the UQ analysis. The CFD model validation is completed once it has been verified that the calculated nozzle flow structure uniquely corresponds to the theoretical one: this is clearly checked in the next Fig. 5.7c (corresponding to p_s =100[kPa]), that displays a shock wave at nozzle exit, as required by gas dynamic theory.

5.4. UQ analysis on nozzle discharge pressure

In this first part of the UQ application, an optimized nozzle geometry with supersonic airflow is considered. CFD simulations were performed in order to investigate the influence of the discharge pressure (p_s) on the nozzle flow structure and performance. The discharge environment pressure was varied in a predefined range around the gas dynamic condition 'r2', characterized by a normal shock wave located at divergent duct exit.
This paragraph can be divided into two subsets: first the sensitivity analysis and then the UQ approach application. The final goal is the quantitative assessment of the influence on nozzle performance of uncertainty on boundary conditions.

5.4.1. Sensitivity analysis on discharge pressure

The value of the discharge pressure (p_s) has a remarkable impact on the nozzle flow structure, especially in determining the position and strength of the shock wave: this is evident by referring to the 'r2' state, where the shock wave is located at nozzle exit section [67]. As proof of the reliability of the CFD model, comparable results were obtained in similar conditions in the experimental case by Zapryagaev et al. [76].
Fig. 5.7 shows Mach number contours for five different p_s values (80-120 [kPa]) around the 'r2' condition. The flow structure and the shock wave location change significantly even with a small difference of 10 [kPa] (about 10% of the pressure interval mean value).

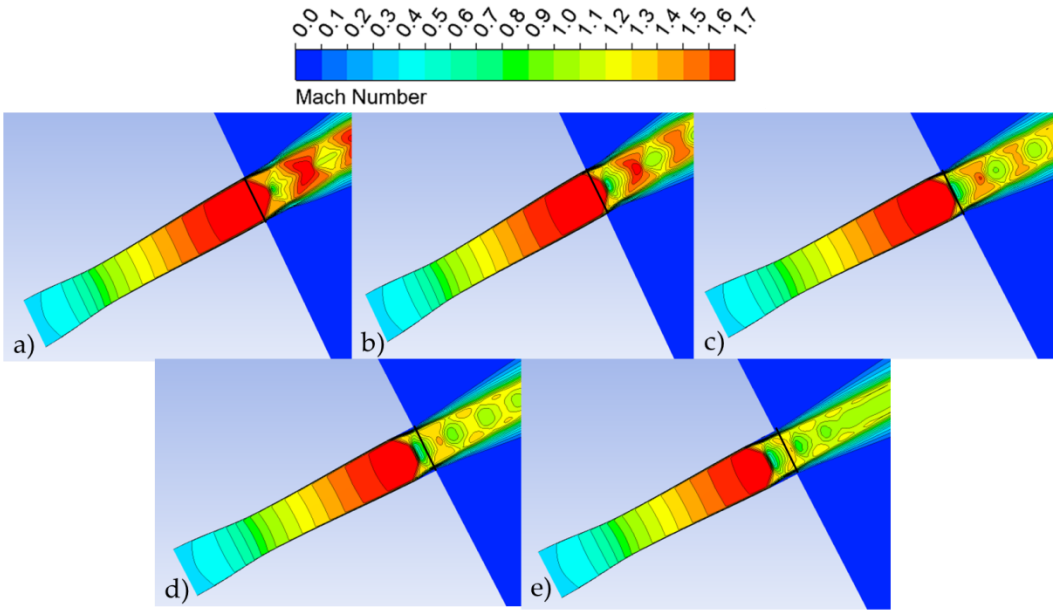

Fig. 5.7 - Mach number contours for five p_s values: (a) 80kPa, (b) 90kPa, (c) 100kPa, (d) 110kPa, (e) 120kPa. The black line identifies nozzle exit section

The performance variation of the nozzle within the above range is further confirmed by the charts in Fig. 5.8 (p_s as variable parameter on curves): it is evident that the position of the shock wave close to nozzle exit is affected by the small change in the discharge pressure.

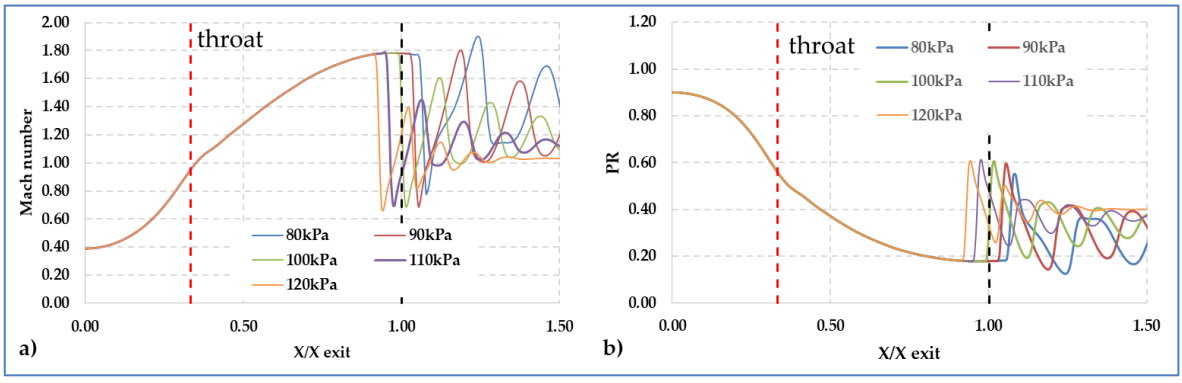

Fig. 5.8 - (a) Mach number and (b) PR versus the dimensionless axial coordinate

$$PR = p_s/p_{t\,in} \tag{5.2}$$

Another important parameter which corroborates the performance variation is the Δp_t (equation (5.3)), i.e. the nozzle total pressure drop, that quantifies the mechanical losses due to viscous and compressible flow effects. The total pressure drop can also be referred to the dynamic pressure at nozzle outlet in the form of loss coefficient (denoted by ξ).

$$\Delta p_t = p_{t\,in} - p_{t\,out} \tag{5.3}$$

Tab. 5.3 – Nozzle total pressure drop values with respect to the operating condition

CASE	Discharge Pressure (p_s) [kPa]	Δp_t [Pa]	ξ
a	80	19270	8.8%
b	90	20145	9.6%
c	100	31926	19.6%
d	110	32675	21.9%
e	120	34972	22.5%

Tab. 5.3 links each case shown before in Fig. 5.7 with the nozzle corresponding crossing losses: the total pressure drop tends to increase with discharge static pressure in a nonlinear way (see the difference between cases 'a' and 'b' compared to that between 'b' and 'c'); this is related to the location of the shock wave (inside/outside the convergent–divergent duct). The nozzle off-design behaviour makes the UQ analysis useful for studying the component response to a non-deterministic input variable.

5.4.2. Surrogate model cross validation and uncertainty quantification results

This section concerns the uncertainty quantification analysis carried out considering the discharge pressure as the input uncertain variable, while the Mach number at nozzle exit (M_{exit}) and the total pressure drop (Δp_t) are the Quantities of Interest (QoI), i.e. the output performance parameters of the problem.
The fully automated procedure implemented inside Dakota environment (section 4.4) was applied. A DoE in the pressure range 80-120 [kPa] was performed for the two QoI using LHS method; in order to correctly approximate the 'physical' (numerical) model, N_{DoE}=121 samples were chosen within the design space. The discharge pressure values provided by Dakota were used as the input variable in Fluent CFD software, which returned the corresponding response functions values (see Fig. 5.9). Equations (5.4) to (5.6) show the problem 'normalized' variable and responses (denoted by superscript '*'):

$$p_s^* = \frac{p_s - p_{s\,min}}{p_{s\,max} - p_{s\,min}} \tag{5.4}$$

$$M_{exit}^* = \frac{M_{exit} - M_{exit\,min}}{M_{exit\,max} - M_{exit\,min}} \tag{5.5}$$

$$\Delta p_t^* = \frac{\Delta p_t - \Delta p_{t\,min}}{\Delta p_{t\ max} - \Delta p_{t\,min}} \tag{5.6}$$

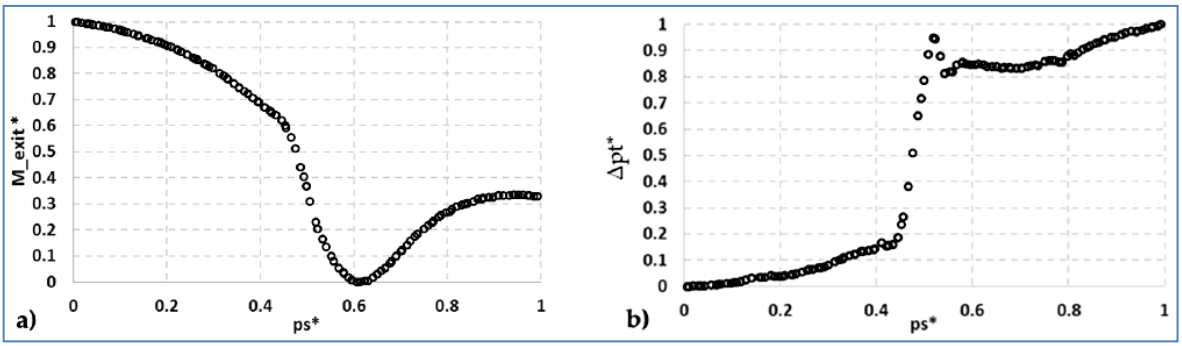

Fig. 5.9 – Normalized response functions with respect to the input variable: (a) Mach number at nozzle exit; (b) nozzle total pressure drop

Kriging or 'Gaussian Process' method was applied and the response surfaces for the above functions were generated from the training points provided by the DoE. The UQ analysis was then performed through LHS method, sampling the surrogates with N_{UQ}=10^3 points. In order to ensure the reliability of metamodels and consequent UQ results, a 'cross-validation' analysis was conducted.

In Dakota the type of cross-validation which can be carried out is the '*k-fold cross-validation'*: at first, the DoE dataset is divided into *k* partitions and *k* metamodels are generated, each by excluding the *k-th* partition of training data. Every surrogate is then tested at the points that were excluded in its generation and finally the user-specified diagnostic metrics are computed with respect to the data kept out [28].
In the case under examination, a particular type of k-fold cross-validation was performed, i.e. the *'Leave-one-out cross-validation'* or *'Prediction Error Sum of Squares'* (PRESS). In this special instance, the number of partitions is equal to the number of sampling points.
The results obtained from this analysis, collected in Tab. 5.4, include the root mean squared, the mean absolute value and the maximum absolute value of the prediction error (calculated between the 'observed' value and the surrogate model prediction for the training points).

Tab. 5.4 – Diagnostic metrics of the response surfaces cross validation

Metrics	$\boldsymbol{M_{exit}}$	$\boldsymbol{\Delta p_t}$ **[Pa]**
Root mean squared (RMS)	4.15×10^{-3}	175.2
Mean absolute value	2.84×10^{-3}	97.9
Maximum absolute value	1.70×10^{-2}	739.7

In addition, three operating points were randomly selected in the UQ database of N_{UQ}=10^3 samples and then simulated with the CFD solver. The corresponding fluid dynamic results for the QoI were assigned in input to Dakota as a *'challenge set of data'*. The metrics calculated with respect to this dataset are reported in Tab. 5.5.
The outcomes of the previous validation analyses were supplemented by the calculation of the relative percentage errors (Tab. 5.6) between the response function values extracted from CFD simulations and those coming from sampling of the surrogate models; the results once again certify the reliability of the metamodels.

Tab. 5.5 - Diagnostic metrics of the response surfaces tested on a challenge set of data

Metrics	M_{exit}	Δp_t [Pa]
Root mean squared (RMS)	5.06×10^{-4}	189.7
R squared	0.998411	0.97978
Mean absolute value	4.57×10^{-4}	119.2
Maximum absolute value	7.00×10^{-4}	327.9

Tab. 5.6 - Relative percentage error between CFD simulation results and corresponding surrogate model values on three randomly selected samples

p_s [Pa]	M_{exit} percentage error	Δp_t percentage error
80870	0.043%	−0.053%
100451	0.015%	0.964%
117848	0.042%	−0.056%

Once the validity of the surrogates is confirmed, the results of the UQ analysis are considered. In a first application, a uniform distribution of the variable p_s was chosen as the input probability density function: in this case any pressure value within the established range has the same chance to occur. The results of the uncertainty propagation through the surrogate models are the discretized PDFs of the outputs (M_{exit} and Δp_t), displayed in Fig. 5.10. It is immediately clear that the PDFs of the QoI are very far from the uniform distribution assigned to the input variable (p_s). The physical explanation of these non-uniform PDFs is that the state 'r2' corresponds to the case p_s=100 [kPa], i.e. the mean of the probability distribution of the input uncertain variable.
As demonstrated by the PDFs of the exit Mach number and total pressure drop, around 'r2' two kinds of solutions are highly probable (Fig. 5.10):

I. high M_{exit} and low Δp_t → overexpanded jet with shock waves outside the nozzle;
II. low M_{exit} and high Δp_t → shock waves inside the divergent duct.

This means that even with a uniform probability density of the input variable, the most frequent flow structures can be limited to two main ranges of M_{exit} and Δp_t.

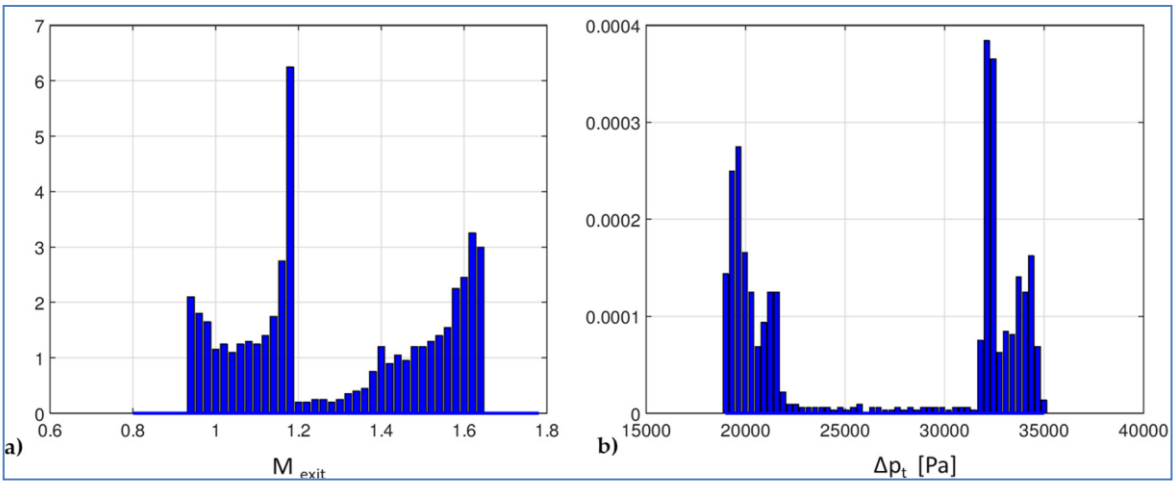

Fig. 5.10 – Uniform input PDF. Discretized PDFs of the two outputs: (a) M_{exit} ; (b) Δp_t

In order to test the reliability of the UQ analysis results, a second case with an increased number of samples (N'_{UQ}=10^4, i.e. one order of magnitude greater than the first attempt) was considered. The comparison between the bar diagrams obtained with different number of samples is reported in Fig. 5.11 for the two QoI: differences between the discretized distributions are detectable, but they are so small that the results of the UQ analysis with N_{UQ}=10^3 samples can be considered satisfactory.

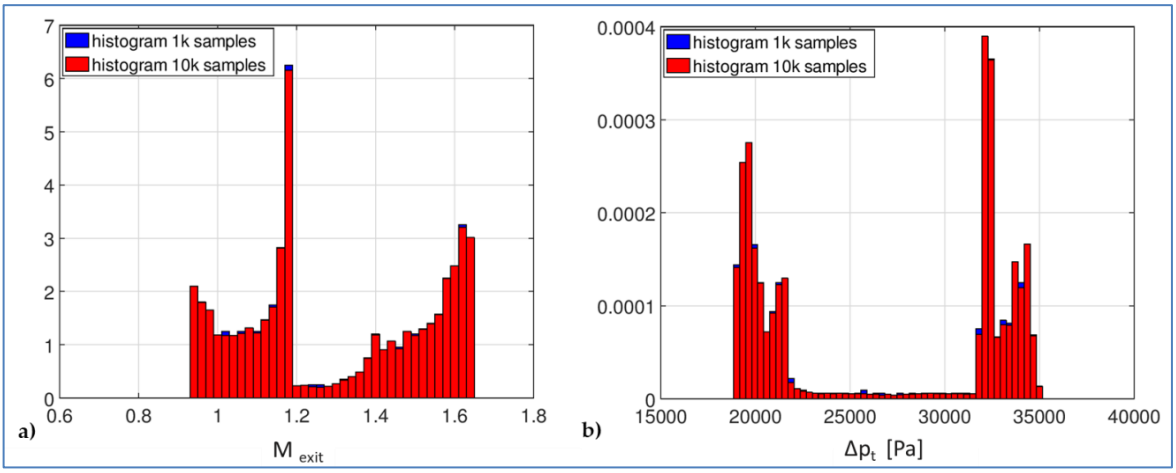

Fig. 5.11 - Uniform input PDF. Comparison between the discretized PDFs obtained with 10^3 and 10^4 samples for the two outputs of the UQ problem: (a) M_{exit} ; (b) Δp_t

After this first application of the UQ approach, another case was simulated: this time a normal distribution is assigned to the input uncertain variable (p_s) with a mean value *'m'* (100 [kPa]) centered on the variation range previously considered and a standard deviation *'σ'* chosen to simulate a small perturbation of the discharge pressure: e.g. $\sigma \approx 1\%$ of the mean value. The resulting probability density function is shown below:

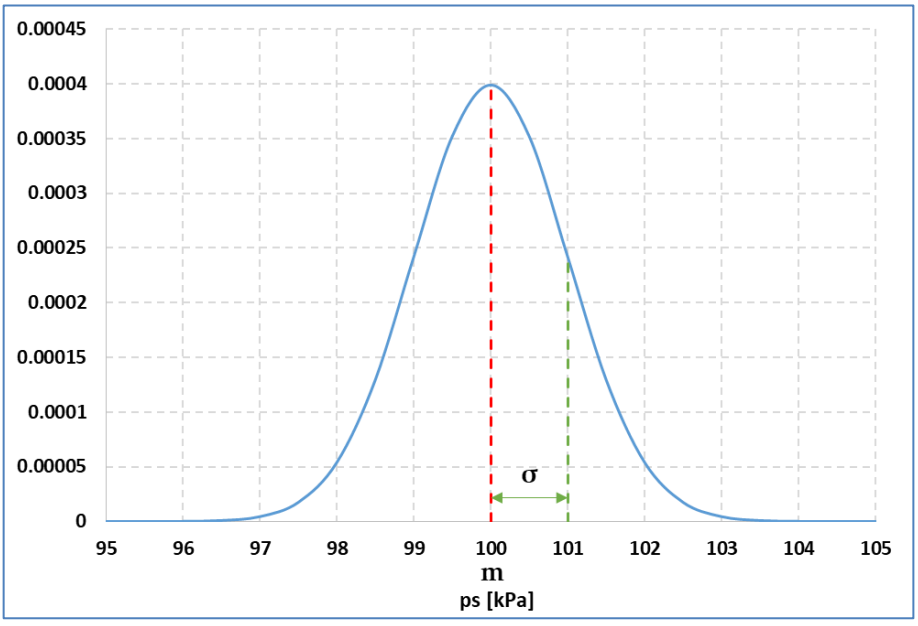

Fig. 5.12 - Gaussian PDF of the input uncertain variable (discharge pressure)

Using again the LHS method for the uncertainty quantification (N_{UQ}=10^3 samples as before), the discretized probability distributions of the response functions (Fig. 5.13) were obtained. It is evident, especially for nozzle crossing losses, that even in this case the output PDFs are different from the input one (normal distribution); Tab. 5.7 collects the values of the statistical moments computed for the output probability density functions.
The red curve on each bar diagram in Fig. 5.13 represents the 'reference' Gaussian continuous trend, i.e. associated with the mean and standard deviation values of each output discretized PDF returned by Dakota. When compared to the normal PDF (in red line), the M_{exit} probability density function is more flat (negative value of Kurtosis) and slightly asymmetric. The distribution of Δp_t is instead shifted to the right (negative Skewness) and more pointed (positive Kurtosis) than the corresponding Gaussian PDF.

Tab. 5.7 - Statistical features of the output discretized PDFs

Statistical Moments	$\boldsymbol{M_{\text{exit}}}$	$\boldsymbol{\Delta p_t}$
Mean	1.2	3.1x10^4[Pa]
Standard Deviation	0.1	3.2x10^3 [Pa]
Skewness	0.013	−0.98
Kurtosis	−0.8	0.05

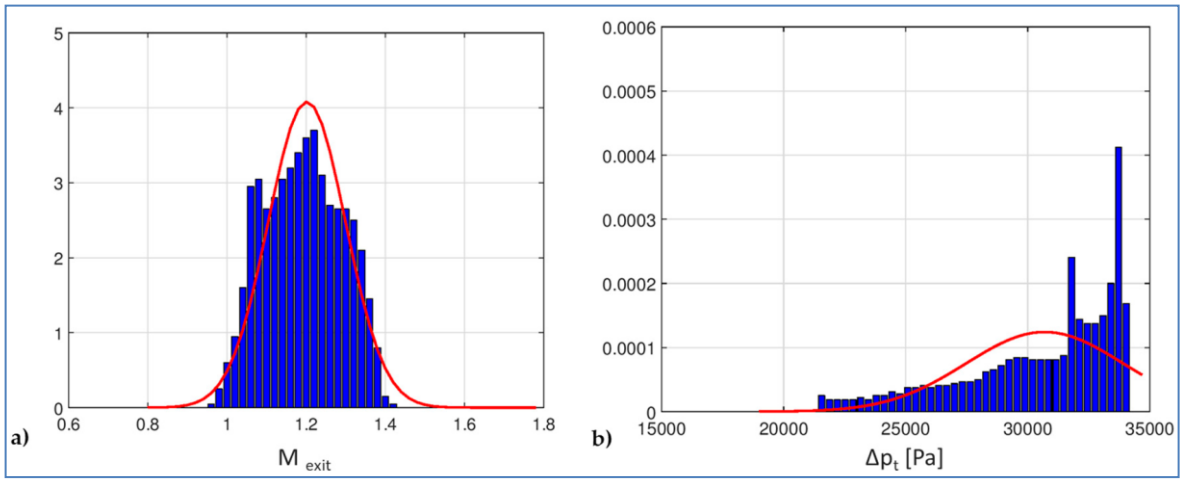

Fig. 5.13 – Gaussian input PDF. Discretized PDFs of the two outputs: (a) M_{exit} (b) Δp_t . The corresponding Gaussian distributions (same mean and σ) in red line

The results analysis suggests that in this case the QoI are spread over a wider range of values. Therefore, a small variation in the input discharge pressure from the reference 'r2' discharge pressure (that is approximately 100 [kPa]) can significantly change the operating condition, and consequently, the performance of the nozzle.
The comparison between the bar diagrams of the output PDFs with N_{UQ}=10^3 and N'_{UQ}=10^4 samples is shown in Fig. 5.14. Even with a different type of PDF for the input uncertain variable, it can be noted that the increase in the number of samples used for the LHS method does not considerably affect the discretized PDF of the output nor the corresponding Gaussian distribution, which remains almost unchanged (black and magenta lines in Fig. 5.14 are superimposed).

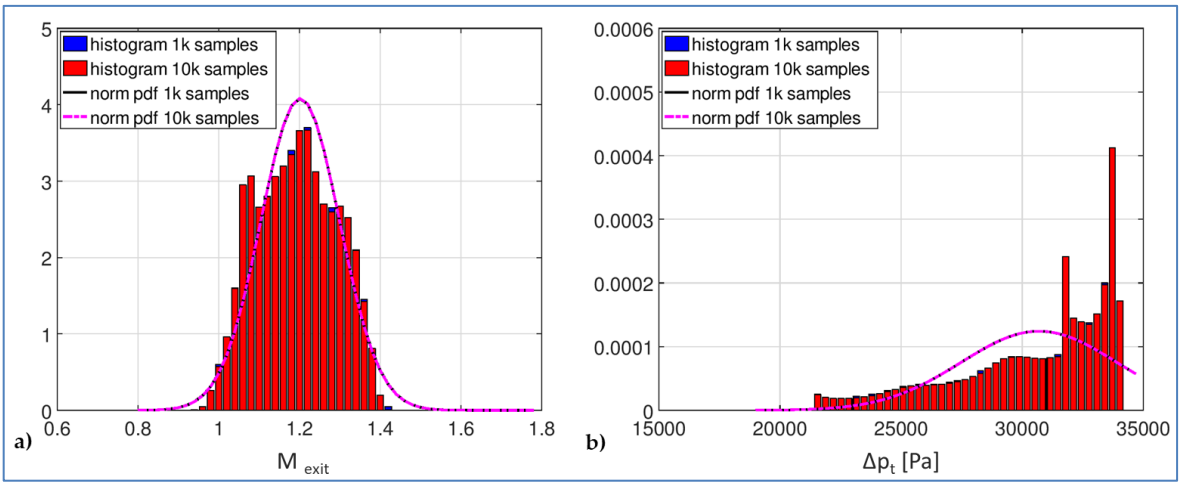

Fig. 5.14 – Gaussian input PDF. Comparison between the PDFs obtained with 10^3 and 10^4 samples for the two outputs:(a) M_{exit} ; (b) Δp_t (lines for the Gaussian reference)

In conclusion, the comparison of the discretized PDFs obtained for the same response function (M_{exit} or Δp_t), but with different input variable probability distributions (uniform vs. Gaussian) is presented.

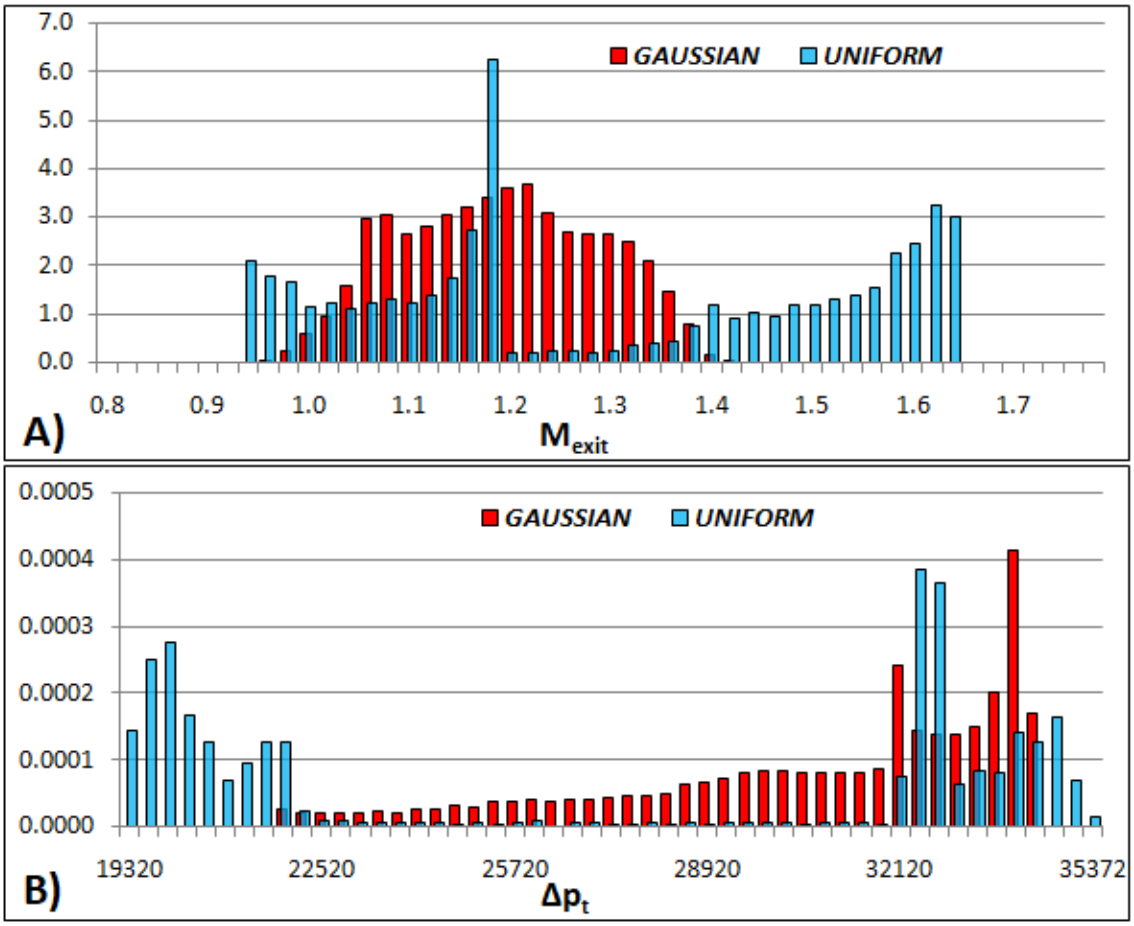

Fig. 5.15 – Comparison between the PDFs obtained with the two different types of input probability distribution. A) Nozzle exit Mach number; B) total pressure drop

As the reader can see, in Fig. 5.15A the probability distribution of the exit Mach number is remarkably affected by the input PDF, with a more concentrated probability density in the case of Gaussian input (red bars) and much more distributed for uniform input. However, it should be noted that the peak of probability is in both cases located around $M_{\text{exit}} = 1.2$.
For what concerns the nozzle total pressure drop (Fig. 5.15B), the two high probability regions, already commented in the case of uniform input, disappear for Gaussian input. In the latter case, in fact, only one region with greater probability can be identified (above 30 [kPa] of total pressure drop). Moreover, in this area the amplitude of the probability peaks is very similar between the two cases (Gaussian or uniform input).
Analyzing the results of this last comparison as a whole, it can be concluded that the type of input PDF assigned to the UQ problem significantly affects the output probability distributions of this nonlinear behaviour system.

5.5. UQ analysis on gas properties

The effects of the fluid chemical composition on nozzle performance are investigated in this second part of the UQ application. As already discussed in the introduction paragraph, the gas composition variation simulates a real and serious scenario for several industrial applications. To confirm the effectiveness of the proposed UQ approach, the same steps of the first case study (where p_s was the uncertain variable) are repeated here.

5.5.1. Sensitivity analysis on gas composition

The purpose of this paragraph is to quantify the effect of uncertainty in natural gas composition on nozzle performance. The natural gas case is of particular interest in the industrial field: the actual chemical composition of the natural gas sent to a site is not constant and both the pipeline used and the geographic region of extraction play a crucial role in its uncertainty. Tab. 5.8 summarizes some reference data of the most interesting gas mixtures for the Italian market [72]: four different 'real' natural gas compositions were selected and their properties calculated. The input uncertain variables were identified in the specific heat at constant pressure (C_p) and the molecular weight (MW) of the mixture. The choice of these properties is related to the option of the 'fluid specification' in the CFD code (still using the ideal gas law), that allows an easier automation of the simulation process through scripting. Another property of interest for the application case, deriving from the aforementioned fluid properties (C_p and MW) and from the operating temperature, is the speed of sound ($a = \sqrt{kRT}$) whose value is reported in Tab. 5.8 below.

Tab. 5.8 - Natural gas compositions and properties according to the extraction region [72]

Composition [%Vol]	**Italian**	**Libyan**	**North Europe**	**Russian**
Methane	99.61%	87.41%	91.58%	98.08%
Ethane	0.06%	9.81%	4.82%	0.98%
Carbon Dioxide	0.02%	1.88%	1.23%	0.10%
Others	0.31%	0.90%	2.37%	0.84%
Properties	**Italian**	**Libyan**	**North Europe**	**Russian**
C_p [J/(kg K)]	2214	2031	2057	2154
MW [kg/kmol]	16.1	19.5	18.2	16.2
a [m/s]	636.9	592.9	606.4	626.9

Four CFD simulations were performed, varying the fluid composition but keeping the other boundary conditions (inlet total pressure and temperature, discharge pressure) constant; thus the nozzle pressure ratio was set close to the gas dynamic condition 'r2' (shock wave at nozzle exit).

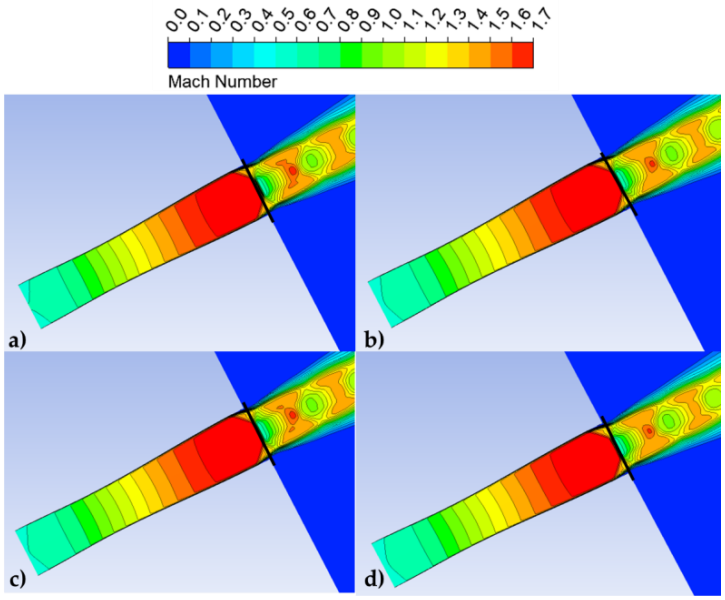

Fig. 5.16 - Mach number contours for different natural gas mixtures: (a) Italian, (b) Libyan, (c) NorthEurope and (d) Russian

Comparing the results in Fig. 5.16 with those relating to the sensitivity analysis on discharge pressure (Fig. 5.7), it is evident that fluid properties (C_p and MW) have a lower influence on the flow structure and Mach number values inside the nozzle. This is also confirmed by the charts in Fig. 5.17, where Mach number and Pressure Ratio trends along nozzle axis are displayed (gas extraction region as the variable parameter on curves). The graphs are enlarged at nozzle exit section, where a slight change in the shock wave position can be noted, due to the different properties of the tested gas mixtures.

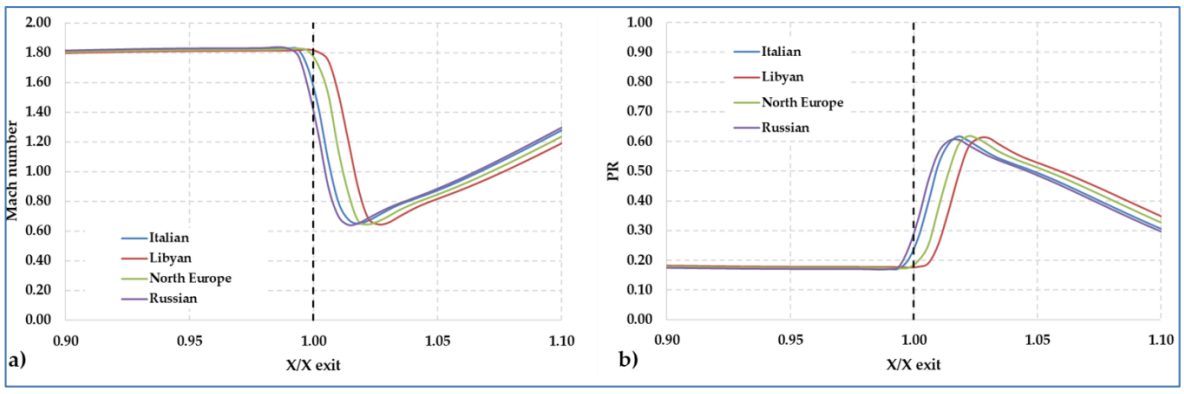

Fig. 5.17 - a) Mach number and (b) PR versus the dimensionless axial coordinate

On the other hand, due to gas composition change, a significant variation of the nozzle crossing losses is detected within the examined dataset (more than 10 [kPa] in Tab. 5.9).

Tab. 5.9 - Nozzle crossing losses variation with gas mixture composition

Natural gas extraction region	Δp_t **[Pa]**	ξ
Italian	31100	18.4%
Libyan	21407	11.3%
North Europe	23933	12.9%
Russian	33579	20.8%

5.5.2. Surrogate model cross validation and uncertainty quantification results

The UQ analysis on gas properties was performed with the same approach used for the first application (section 5.4.2). The variation range of the input parameters (design space) was identified from the preliminary sensitivity analysis: the specific heat at constant pressure varies inside the interval C_p=2031-2214 [J/(kgK)], whereas the molecular weight in the range MW=16.1-19.5 [kg/kmol]. The QoI selected for UQ analysis are again nozzle exit Mach number (M_{exit}) and total pressure drop (Δp_t – equation (5.3)).
The DoE was generated with N_{DoE}=121 samples according to LHS algorithm. The resulting scattered distributions of the response functions are shown in Fig. 5.18, where the input uncertain variables are normalized (MW^* and $C_p{}^*$) as in equations (5.7) and (5.8).

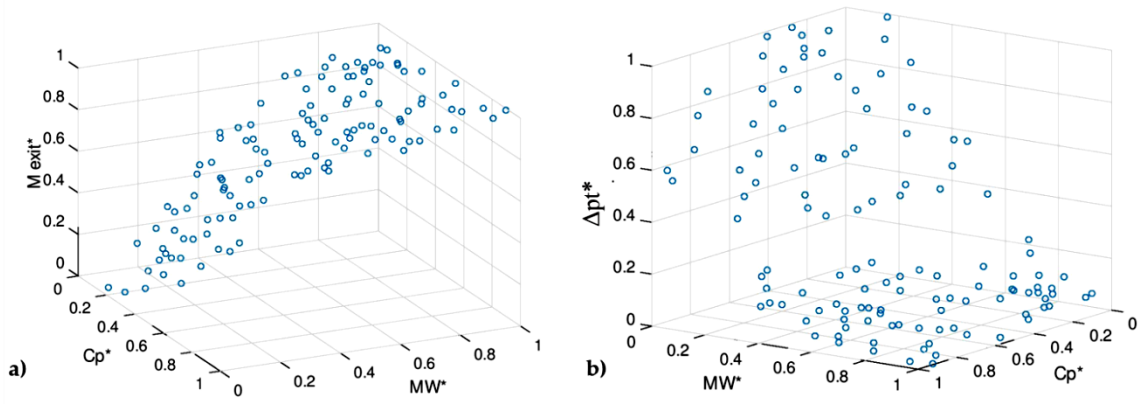

Fig. 5.18 – Normalized response functions with respect to input variables. (a) Mach number at nozzle exit; (b) nozzle total pressure drop

$$MW^* = \frac{MW - MW_{min}}{MW_{max} - MW_{min}} \tag{5.7}$$

$$C_p{}^* = \frac{C_p - C_{p_{min}}}{C_{p_{max}} - C_{p_{min}}} \tag{5.8}$$

The surrogate models were generated using Kriging method on the DoE dataset: the resulting response surfaces are shown in Fig. 5.19. Even in this application the PRESS results confirm the reliability of metamodels and consequent UQ outcomes (see Tab. 5.10). CFD results on three randomly selected points from the N_{UQ}=10^3 samples were given in input to Dakota as a *'challenge set of data'* for the generated metamodels: the diagnostic metrics are collected in Tab. 5.11, while the relative percentage errors are in Tab. 5.12.

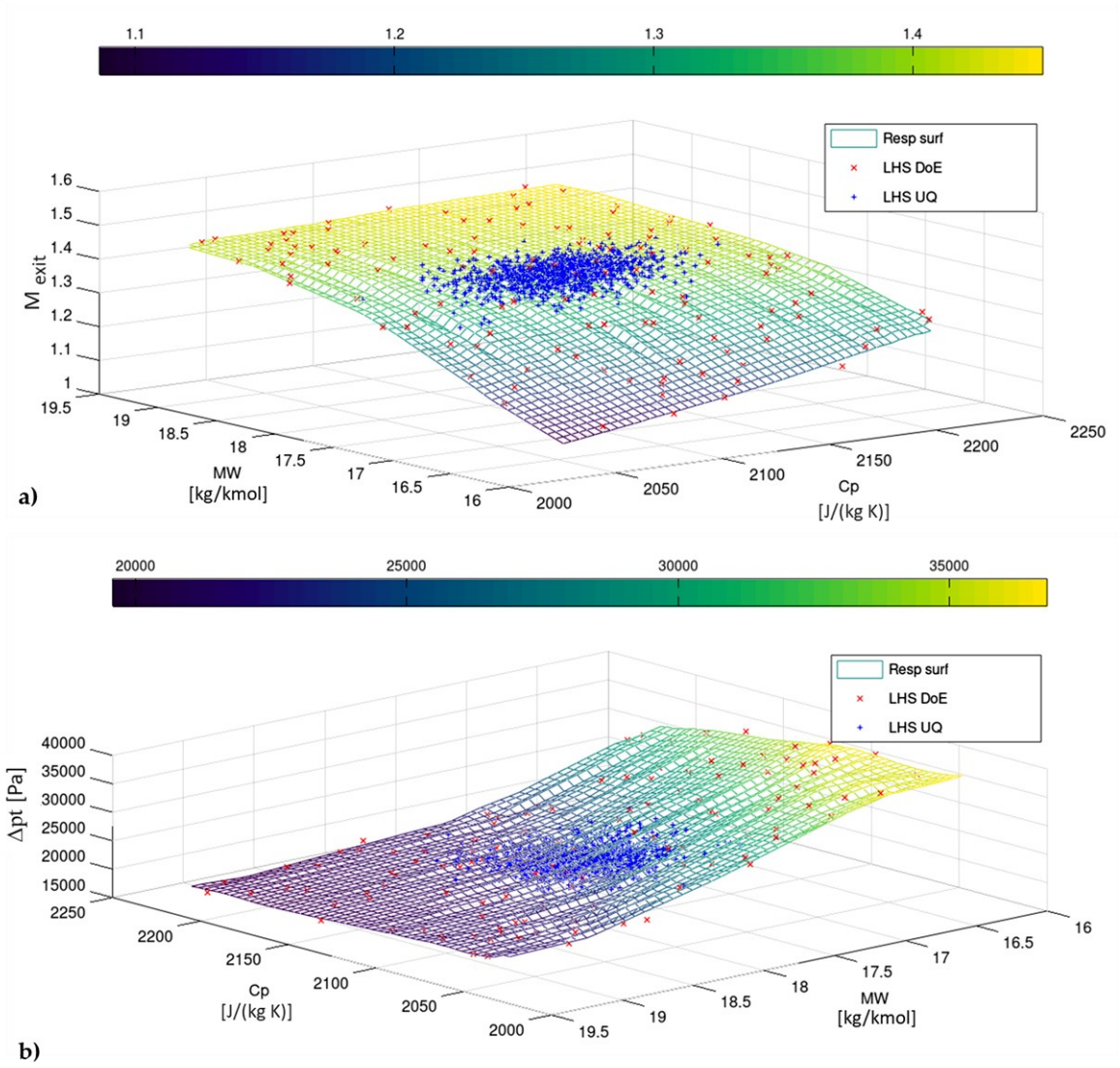

Fig. 5.19 - Response surfaces generated through Gaussian Process for: (a) M_{exit} ; (b) Δp_t

Tab. 5.10 – Diagnostic metrics of the metamodels cross validation

Metrics	$\boldsymbol{M_{\text{exit}}}$	$\boldsymbol{\Delta p_t}$ **[Pa]**
Root mean squared (RMS)	$2.87\text{x}10^{-3}$	384.8
Mean absolute value	$1.65\text{x}10^{-3}$	251.2
Maximum absolute value	$1.42\text{x}10^{-2}$	1416.6

Tab. 5.11 - Diagnostic metrics of the response surfaces tested on a challenge set of data

Metrics	$\boldsymbol{M_{\text{exit}}}$	$\boldsymbol{\Delta p_t}$ **[Pa]**
Root mean squared (RMS)	$1.17\text{x}10^{-3}$	283.7
R squared	0.916084	0.806983
Mean absolute value	$9.99\text{x}10^{-4}$	192.6
Maximum absolute value	$1.81\text{x}10^{-3}$	483.2

Tab. 5.12 - Relative percentage error between CFD simulation results and corresponding surrogate model values on three randomly selected samples

C_p [J/(kg K)]	MW [kg/kmol]	M_{exit} percentage error	Δp_t percentage error
2099	17.53	−0.13%	1.80%
2113	17.95	0.06%	−0.39%
2159	18.01	0.02%	−0.02%

Once again the reliability of the response surfaces is confirmed by low values of the relative percentage errors.
After the surrogates validation process, the UQ results are then considered. The sampling-based UQ analysis was implemented according to the LHS method (N_{UQ}=10^3 samples) in order to evaluate nozzle response to input statistical distributions. A Gaussian PDF was assigned to both input uncertain variables (C_p and MW). The statistical features of the input PDFs are collected in Tab. 5.13, while Fig. 5.20 displays the respective trends.

Tab. 5.13 – Main statistical characteristics of the input PDFs

Statistical Moments	C_p [J/(kg K)]	MW [kg/kmol]
Mean	2122	17.8
Standard deviation	21.2	0.178

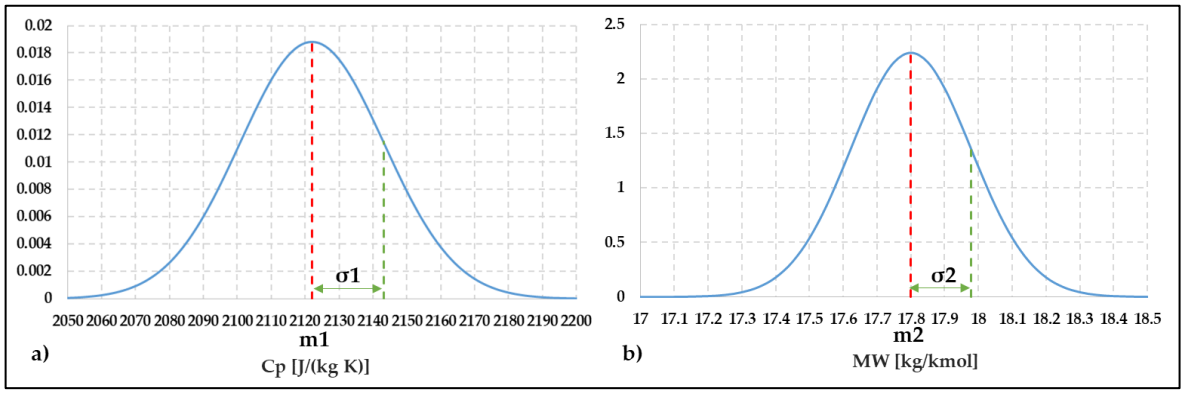

Fig. 5.20 - Gaussian probability density functions of the input variables

The mean values of the input PDFs are indicated with *'m1'* and *'m2'* (red dotted lines in Fig. 5.20), while the standard deviations '*σ1'* and '*σ2'* are about 1% of the corresponding mean values to simulate the effects of a small probability dispersion of the variables involved. The uncertainties propagation through the metamodels leads to the discretized PDFs of the QoI (see Fig. 5.21); the statistical moments of the output probability density functions are summarized in Tab. 5.14.
In Fig. 5.21 the 'shape' of the response functions PDFs is very far from the corresponding reference Gaussian distributions (red line): both of them are more pointed (positive Kurtosis) and slightly shifted from the mean. The variation range of M_{exit} , with the selected inputs, is very narrow, confirming what was previously observed in the sensitivity analysis (section 5.5.1): the nozzle exit Mach number is only slightly influenced by the gas chemical composition.

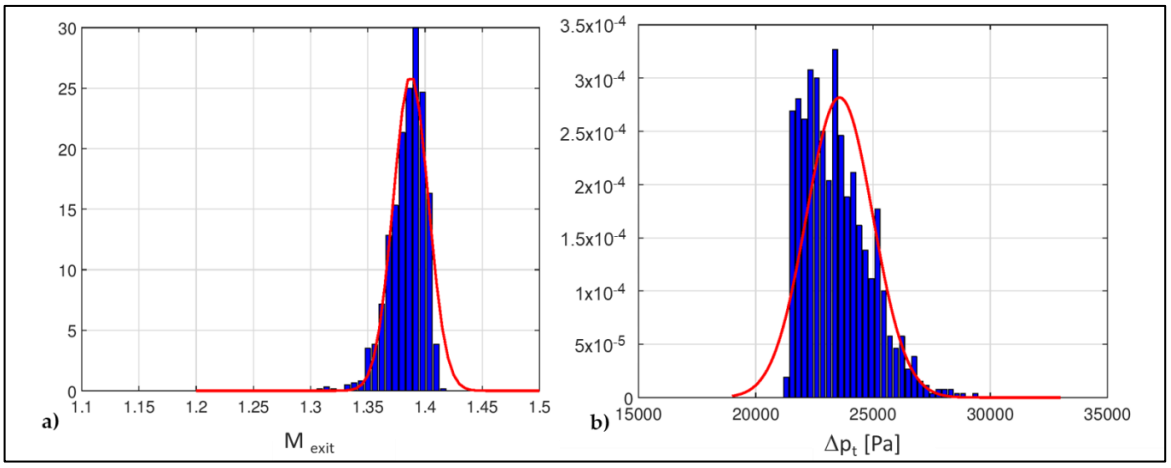

Fig. 5.21 - Discretized PDFs of the two output functions: (a) M_{exit} ; (b) Δp_t . The corresponding Gaussian distributions (same mean and σ) in red line

Tab. 5.14 - Statistical features of the output discretized PDFs

Statistical moments	$\boldsymbol{M_{exit}}$	$\boldsymbol{\Delta p_t}$
Mean	1.39	2.36×10^4 [Pa]
Standard deviation	0.015	1.42×10^3[Pa]
Skewness	−1.00	0.819
Kurtosis	1.73	0.497

It can be noted that even with a small uncertainty in C_p and MW the range of 'possible' total pressure drop (Δp_t) values is quite wide and consequently the probability of falling into a non-optimal operating condition is high.
The skewed probability distributions of the outputs shown in Fig. 5.21 are a direct result of the response surfaces displayed in Fig. 5.19, which exhibit an inflection in both directions of variation of the input parameters. A high sensitivity of the M_{exit} to the mixture molecular weight can be noted, especially at low C_p values inside the design space. However, the exit Mach number response surface tends to flatten as the MW increases from its PDF average value, with M_{exit} approximately constant at high values as the C_p varies. This means that, starting from Gaussians for the input variables, the uncertainties propagation leads to a non-Gaussian probability distribution and in particular to a 'left skewed' (Sk <0) PDF, leaning towards high exit Mach number values. The same reasoning applies to the Δp_t , which is closely correlated to the M_{exit} (high exit Mach numbers match to low total pressure drops because the shock waves remain outside the nozzle). Even in this case the response surface flattens as the molecular weight increases from the input PDF average value, with Δp_t approximately constant at low values as the C_p varies. Consequently, a 'right skewed' (Sk> 0) PDF is obtained with probability density more concentrated towards low Δp_t. In conclusion, the uncertainty on the performance of the designed nozzle could be reduced by shifting the MW variation range upwards, i.e. towards more "humid" and heavier natural gas mixtures (lower percentage in methane). According to the gas dynamic theory, a higher molecular weight translates into a smaller gas constant, so the speed of sound would be lower and with the same nozzle and boundary conditions it would be easier to reach high Mach numbers at nozzle exit, as confirmed by the results presented here.

Finally, to test the accuracy of the UQ analysis results, a second run with a greater number of samples (N'_{UQ}=10^4) was performed.
The comparison between the output PDFs bar diagrams with N_{UQ}=10^3 and N'_{UQ}=10^4 samples is reported in Fig. 5.22: very small differences confirm that N_{UQ}=10^3 samples are sufficient to accurately determine the probability density functions of the system responses.

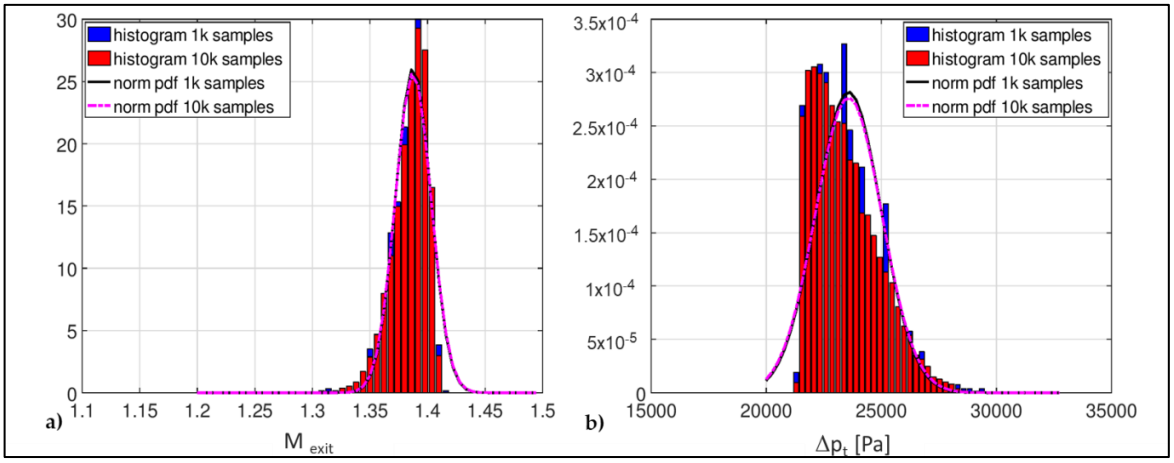

Fig. 5.22 - Comparison between the PDFs obtained with 10^3 and 10^4 samples for the two outputs:(a) M_{exit} ; (b) Δp_t (black and magenta lines for the Gaussian reference)

5.6. Conclusions

The quantitative analysis of the influence on supersonic nozzle performance of the uncertainty on selected input variables leads to the conclusions summarized below.
The perturbation of the discharge environment pressure (p_s) within a range centered on the gas dynamic state 'r2' results in a remarkable alteration of the flow structure inside the nozzle, even with a pressure variation of a few thousand pascals, i.e. few percentage points (3% if uncertainty is considered as '3σ') with respect to the discharge pressure of the 'r2' state. This is confirmed by the UQ analysis: with a uniform uncertainty of the input variable (p_s), the performance parameters (exit Mach number and total pressure drop) can assume a broad range of possible values. If a Gaussian uncertainty is considered, it can be observed that, even with a small pressure change, a significant variation in the output parameters is detectable: the resulting statistical distributions are very far from the input one, due to the strong non-linearity of the physical problem under investigation.
The study of the effects of uncertainty on natural gas composition (C_p, MW) showed that fluid properties have a slight influence on the flow structure of the convergent-divergent duct, but can remarkably affect nozzle crossing losses. The UQ analysis with Gaussian probability distributions of the input variables highlighted a limited effect on the Mach number at nozzle exit and a non-negligible influence on the total pressure drop, which showed a rather large probability dispersion. The statistical distributions of the output responses differ from the normal probability distribution functions of the input variables due to the uncertainties propagation through the nonlinear model.

The proposed workflow for UQ analysis, implemented with the Dakota platform, has demonstrated its effectiveness in a quantitative evaluation of the effect of changes in input parameters on the response functions of the engineering design problem; it can be applied to other cases with the same structure.

Chapter 6

Uncertainty quantification methodologies applied to the rotor tip clearance effect in a twin scroll radial turbine

The experience gained with the supersonic nozzle test case has facilitated the identification of some uncertainty quantification techniques for the final application of this doctoral thesis, namely the study of the effect of geometric uncertainties on the performance of twin scroll radial turbines for turbocharging. This chapter focuses on geometrical sources of uncertainty in the field of CFD applied to twin scroll radial turbines; in particular, the effect of uncertainties in rotor tip clearance values at blade leading edge and trailing edge on turbine selected performance parameters was investigated.
The analysis shows the use of the Surrogate-Based Uncertainty Quantification platform that has been configured by the author inside Dakota environment (for more details see section 4.5.1). The second UQ approach selected for this application is the Polynomial Chaos Expansion (PCE) method, particularly suitable for the case under examination since its effectiveness is high especially if the number of uncertain variables is limited.
The comparison of the results coming from the different approaches and the discussion of the positive and negative aspects related to each technique lead to interesting findings, which are proposed as guidelines for future UQ applications on the topic of CFD applied to radial turbines. The research work presented in this chapter has been published in the journal Fluids with the paper entitled "*Uncertainty Quantification Methodologies Applied to the Rotor Tip Clearance Effect in a Twin Scroll Radial Turbine"* [77].

6.1. Introduction and literature background

Uncertainty quantification is the science of characterizing and reducing uncertainties in both computational and real world applications, a tool for determining how likely certain outcomes are if aspects of the system are not completely known; while the models and methodologies (which combine mathematics, statistics and engineering) are used throughout academia, the practice has not yet been integrated into professional engineering workflows. The uncertainty propagation through the CFD model supports engineers to determine whether system outputs will meet the requirements, what the extreme probabilities really are and which inputs have the most significant effect on output PDFs.
A fundamental aspect to be considered in every simulation consists in the differences between the real geometrical model (the actual manufactured machine) and the simulated one (the CFD model): the computational domain used in CFD to simulate a turbine and the real control volume are not identical. In the industrial world geometrical uncertainties are the so-called "allowed manufacturing deviations from the desired geometry". Such deviations are inevitable as a 'perfect' production would have very high costs. In this scenario, UQ can be used to determine the maximum manufacturing deviation from the expected geometry that causes an acceptable gap from the target performance.
One of the most delicate geometric aspects concerning radial turbines is undoubtedly the tip clearance, i.e. the gap between the rotor tip and the shroud surface (stationary housing). Usually, in order to limit tip leakage flows, thus optimizing turbine performance, clearances are kept very close; in this context small geometrical variations, e.g. induced by severe operating conditions, may be responsible of appreciable performance variations.
It is noteworthy to mention that many authors [78, 79] have already investigated the variability of gaps, fillets and small geometric details due to turbomachinery operating conditions. The epistemic uncertainties of a numerical model represent the level of

uncertainty in reproducing a physical system or phenomenon, while the aleatory uncertainties are an intrinsic property of the system being analyzed. Following this definition, turbulence modelling is an epistemic uncertainty whose effect has been extensively investigated at the rotor tip by Krishnababu et al. [80].
This chapter deals with the aleatory operational uncertainties to which the tip clearances (at blade leading and trailing edge) of a twin entry turbine impeller are subject: centrifugal, thermal, assembly and wear effects can significantly affect tip gap values. The turbine under investigation is used for automotive turbocharging and the numerical model for the simulation of this turbine, validated with experimental data [49], has been already presented in paragraph 3.1. The uncertainties propagation through the CFD model of the turbine was performed using an automated procedure (section 4.5) developed with Dakota, an open source toolset provided with a large number of optimization and uncertainty quantification utilities.
Response surface methods have been widely used for design optimization approaches [62, 63], but the same techniques can also be very useful in the field of UQ methods based on sampling, in order to bypass the high computational cost generally required to generate converging statistics of the outputs. The first application of UQ methodologies follows a 'Surrogate-Based' approach already tested on the case study addressed in chapter 5. This method consists, at first, in the evaluation of the objective functions on a fixed set of samples (DoE), then the results are used to generate a surrogate model (RSM) of the underlying "true" functions. In the final step random sampling (using thousands of samples) is performed on the metamodel to obtain estimates of the response function statistics (mean, variance, etc.).
The second UQ approach investigated is the Polynomial Chaos Expansion (PCE), which is based on a multidimensional orthogonal polynomial approximation where the final solution is expressed as a functional mapping in terms of standardized random variables. This polynomial approach is particularly valid for the problem under examination since there are only two input variables; in fact the major limitation of the PCE is that the number of CFD simulations needed increases exponentially with the number of inputs.
At first, based on experience gained on twin entry radial turbines [49, 50, 51, 52], some key performance parameters were chosen as response functions for the UQ analysis. According to available experimental/CFD data on radial turbines for turbocharging applications, the input probability density functions assigned to the rotor tip clearances were selected considering physically suitable values for both the average values and the standard deviations. The propagation through the CFD model of the input uncertainties on rotor tip clearances led to the PDFs of the outputs; then the statistical distributions provided by the two UQ methods (Surrogate-Based and PCE) were compared.
The ultimate goal is to identify the pros and cons of each UQ technique applied to the numerical simulation of twin entry radial turbines and then to propose some guidelines for the future integration of UQ approaches into industrial design workflows.

6.2. Turbine CFD model

In this application the commercial CFD platform Ansys CFX® was coupled to the open source Dakota for its UQ capabilities. The turbine selected for the UQ analysis is a twin scroll inflow radial turbine for turbocharging applications. Geometrical and performance data are confidential, therefore all quantities are reported in non-dimensional or reduced form in the following; for further geometric details on volute and rotor, the reader can refer to 'Reference geometry' in section 3.1.1. The same details provided in subparagraph 3.1.2

on the generation of the computational grids and their quality metrics apply here.
The twin scroll volute (Fig. 6.1) was discretized with an unstructured mesh (prism layers added to ensure correct boundary layer resolution), as shown in Fig. 6.1, while a structured grid was generated for the rotor. The leading edge ('L.E.') and trailing edge ('T.E.') of the blade are indicated in Fig. 6.2.

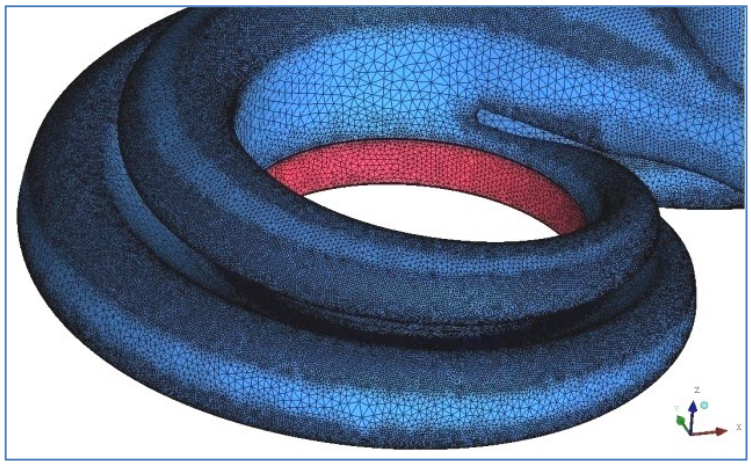

Fig. 6.1 – Unstructured surface grid on the two volute branches. Volute outlet in magenta

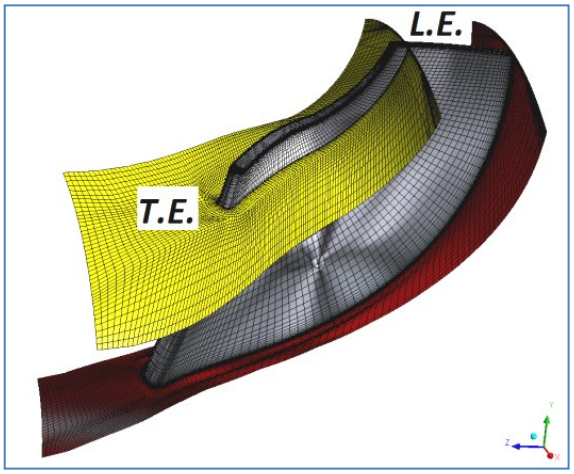

Fig. 6.2 - Rotor channel structured surface mesh with volume mesh cut plane (in yellow)

The CFD model is divided into three domains (Fig. 6.3) and the set of assigned boundary conditions is summarized in Tab. 6.1.

Tab. 6.1 – Turbine CFD model BCs. Numbers define 'in-out' control sections

Domain	Boundary conditions
Volute (1-2)	- inlet total pressure and temperature - flow direction orthogonal to volute inlets
Rotor channel (2-3)	- rotational speed - rotational periodicity on passage side walls - counter-rotating shroud wall
Discharge pipe (3-4)	- static pressure on tailpipe outlet section

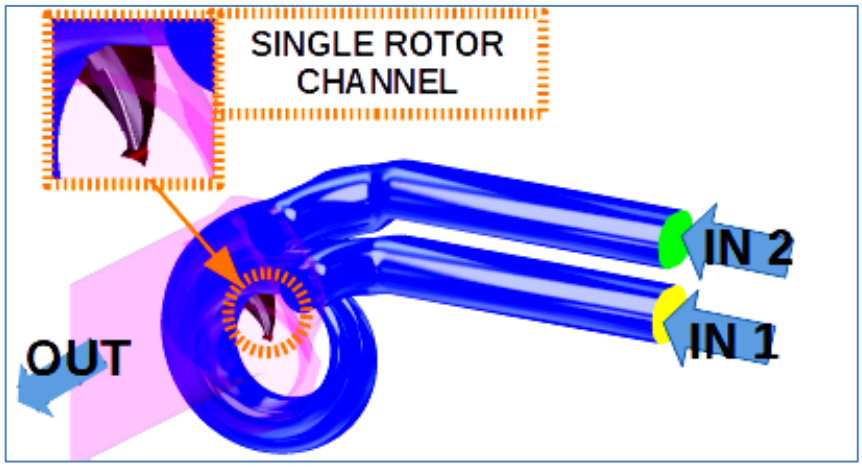

Fig. 6.3 - CFD model of the twin scroll turbine

The careful reader may object on the CFD model configuration that the volute delivers to the wheel a not perfectly uniform flow in tangential direction. On the one hand the adoption of a single rotor channel with periodicity conditions is a simplification necessary to lighten the weight of the simulations (especially in the perspective of building a reliable surrogate), on the other hand the performance could differ considering the full 360-deg rotor. Therefore, it should be noted that some of the results shown in the next paragraphs may be influenced by the simplifications assumed in the calculations.
Simulations were performed with steady-state flow condition and in full admission (for more details on twin entry admission conditions see section 1.3.1). In order to isolate the effects of rotor tip clearance uncertainties on turbine performance parameters, a fixed operating condition was calculated; more specifically, a working point at maximum rotational speed and near choking was selected from the experimental maps provided by the industrial partner. This choice is motivated by the fact that the highest stress conditions for the turbine are promoted by:

- high internal combustion engine exhaust gas temperature → thermal stress;
- high peripheral speed values → centrifugal stress;
- high flow momentum variation and flow leakage in the backside cavity → maximum thrust on bearings.

These factors can significantly affect the 'nominal' rotor tip clearance values, which have been assumed as the mean values of the corresponding probability density functions.

6.3. Input uncertainties and response functions

The input variables of the uncertainty quantification problem are two: the rotor tip clearance values at blade leading and trailing edge respectively.

Tab. 6.2 - Uncertainty range and statistical features of the input parameters

Metrics	TC_{LE} [$\%h_{bin}$]	TC_{TE} [$\%h_{bout}$]
Min	1.00%	1.00%
Max	9.00%	6.00%
Mean (μ)	5.00%	3.50%
Standard deviation (σ)	0.50%	0.35%

The average values and variation ranges of the input variables derive from physically-based assumptions on the geometric data of the turbine provided by the industrial partner. The assigned clearances were therefore validated in relation to the actual rotor tip gap values, which are confidential. For this reason all tip clearance data in Tab. 6.2 have been 'scaled' with the respective blade heights ('h_{bin}' at L.E. and 'h_{bout}' at T.E.).

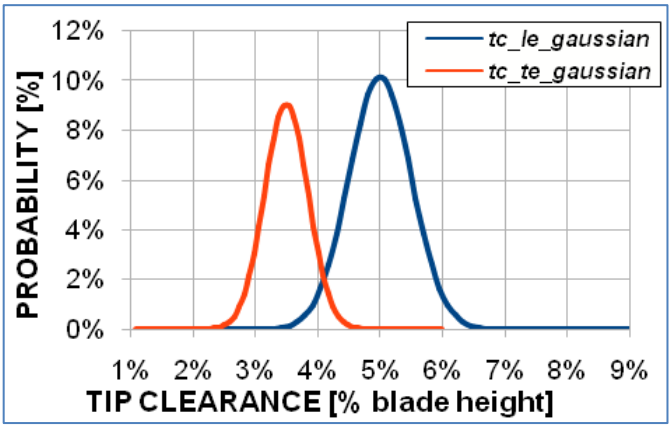

Fig. 6.4 - Gaussian probability distributions of the input variables

Gaussian probability distributions (Fig. 6.4) were assigned to the two input variables, with standard deviation (σ) equal to 10% of the corresponding mean value ('μ'). According to the definition of Gaussian (or 'normal') probability density function in equation (6.1), the 99.73% of input samples is concentrated inside the ± 3σ range centered on the mean value. Therefore in Tab. 6.2 the 'Min' and 'Max' clearance values only identify the uncertainty limits of the input variables, since the samples used for the UQ analysis will be almost totally included in the ranges: $TC_{LE} = 3.5 - 6.5\ \%h_{bin}$ and $TC_{TE} = 2.45 - 4.55\ \%h_{bout}$. On the one hand the maximum clearance values inside the aforementioned ranges can realistically correspond to the cold blade, i.e. to the turbine start-up phase (when the internal combustion engine is fired up), on the other hand the minimum values simulate the conditions of maximum stress (when the blade tip is very close to the shroud).

$$f_{normal}(x) = \frac{1}{\sqrt{2\pi}\sigma} exp\left[-\frac{1}{2}\left(\frac{x-\mu}{\sigma}\right)^2\right] \tag{6.1}$$

$$\sigma = \sqrt{\sum_{i=1}^{N} \frac{1}{N-1}(x_i - \mu)^2} \tag{6.2}$$

The rotor clearance uncertainties are a consequence of the deformation of turbine blades during service. Two main factors can explain this phenomenon:

1) thermal stress, stronger at the LE where the hot gases have not yet undergone the rotor expansion which causes a remarkable pressure and temperature drop;
2) centrifugal stress (quadratic with rotational speed), stronger at the TE where the blade extends mainly in the radial direction, along which the centrifugal force acts.

At the blade leading edge the variation range ('Min-Max') assigned to the rotor tip clearance is greater in terms of blade height percentage and this is related to a third factor, i.e. the axial thrust on rotor bearings. On this issue many authors investigated [81, 82] and

concluded that the thrust contribution of the leakage flow in the rotor backside cavity is usually higher than the momentum variation contribution due to blade flow deflection. The overall thrust tends to push the impeller toward the shroud at the LE, resulting in a further reduction of the existing gap (while at TE the axial thrust has no effect on tip clearance).
The response functions selected for this UQ problem are twin scroll radial turbine performance parameters, whose definitions are reported below for completeness:

- 'overall' expansion ratio, i.e. the ratio between volute inlet total pressure and tailpipe outlet static pressure. In the present turbine volute inlets cross sections are the same, thus it is valid to derive from equation (1.27) the following:

$$PRF = \frac{p_{t1\,sh} + p_{t1\,hub}}{2p_4} \tag{6.3}$$

- rotor expansion ratio (PRF_{rotor}), which has the same definition reported in equation (6.3) but uses the static pressure measured at rotor outlet (p_3) instead of the turbine tailpipe outlet pressure (p_4);
- mass flow ratio, i.e. the ratio between the mass flow through one of the two branches and the overall mass flow processed by the turbine:

$$MFR_{sh} = \frac{\dot{m}_{sh}}{\dot{m}_{tot}};\ MFR_{hub} = \frac{\dot{m}_{hub}}{\dot{m}_{tot}} \tag{6.4}$$

- mass flow parameter, used to estimate turbine flow capacity. In case of twin entry turbines the MFP is calculated through the mass flow ratios to consider the contribution of each volute branch ('hub' or 'shroud' rotor side) on total mass flow:

$$MFP = \dot{m}_{tot}\frac{\sqrt{MFR_{sh}T_{t1sh} + MFR_{hub}T_{t1hub}}}{\frac{p_{t1sh} + p_{t1hub}}{2}} \tag{6.5}$$

- 'overall' total to static efficiency, i.e. the ratio between the actual total enthalpy drop ($h_{01} - h_{04}$) and the total to static enthalpy variation in case of isentropic transformation from volute inlets to tailpipe outlet;

$$\eta_{ts} = \left[1 - \left(\frac{T_{t1}}{T_{t3}}\right)\right] \Big/ \left[1 - \left(\frac{1}{PRF}\right)^{\left(\frac{k-1}{k}\right)}\right] \tag{6.6}$$

- 'rotor' total to static efficiency, which has the same definition reported in equation (6.6) but uses the rotor expansion ratio (PRF_{rotor}) instead of the overall one (PRF).

In conclusion four response functions were identified: PRF_{rotor}, MFP, $\eta_{t2s\,rotor}$ and η_{t2s}.

6.4. Results

The uncertainty quantification workflow synthetically involves the following steps:

I. the UQ algorithm provides the rotor tip clearance values at blade leading and trailing edge, selecting them within the respective variation ranges based on the input probability density functions specified inside Dakota input file;
II. the rotor mesh is then generated and imported into the computational model (Ansys CFX® platform);
III. the CFD simulation is performed and finally the response functions values are extracted through post-processing in order to be passed to the UQ algorithm.

This section deals with the comparison of the results achieved using two different uncertainty quantification approaches: Surrogate-Based UQ and Polynomial Chaos Expansion. For the theoretical concepts underlying these two techniques, the reader can refer to chapter 2, while paragraph 4.5 contains more details on the UQ platform specifically configured for this case study.

6.4.1. Surrogate-Based UQ main outcomes

At first, a 64-sample Design of Experiments (DoE) was generated with the Latin hypercube sampling method: a suitable number of numerical simulations is necessary to obtain, through RSM, a metamodel which is a good approximation of the true 'physical' model (the turbine CFD model). Then the input probability distributions described in paragraph 6.3 were passed to the Surrogate-Based UQ method (LHS is again used for sampling) which was applied to the surrogates to finally evaluate the response function statistics. An example of response surface generated with the SB-UQ approach is reported in Fig. 6.5 for the overall total to static efficiency of the twin scroll turbine (equation (6.6)).

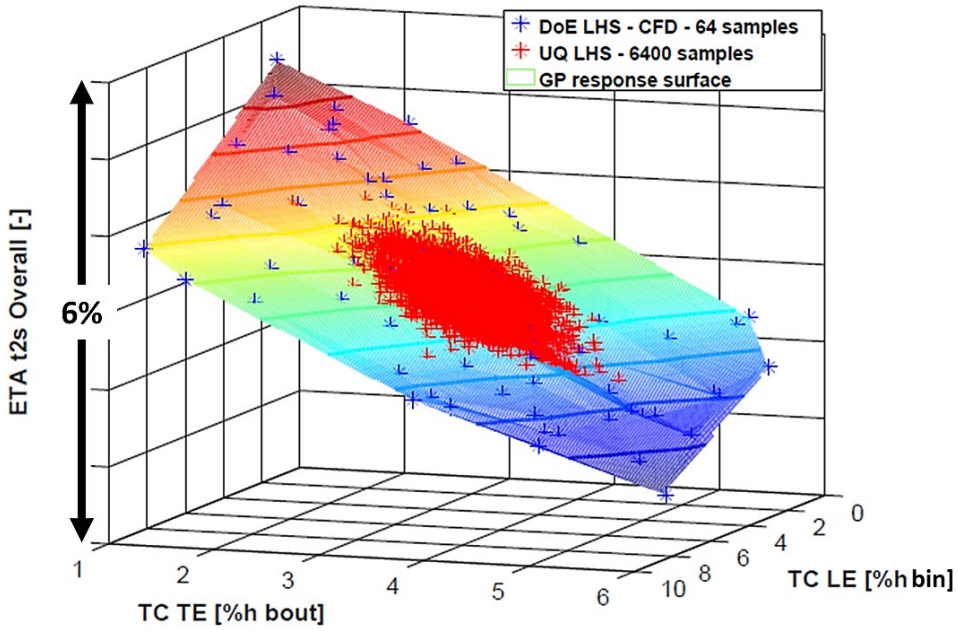

Fig. 6.5 - SB-UQ: overall total to static efficiency response surface and samples (DoE/UQ)

Fig. 6.5 shows the contours on the response surface to visualize the overall variation of the turbine efficiency as a function of the input parameters (rotor tip clearances at blade LE and TE). The blue scattered points represent the N_{DoE} = 64 points of the DoE, which correspond to 64 different combinations of rotor clearance values, i.e. to a database of 64 CFD simulations. This computational effort is necessary to build a reliable surrogate of the numerical model through the RSM (Gaussian Process).
In order to compute the statistics of the response function, the SB-UQ algorithm performs on the metamodel N_{UQ} = 6400 function evaluations (two orders of magnitude greater than those used for DoE), represented by the red dot cloud in Fig. 6.5. The overall efficiency variation inside the DoE is about 6% (see Fig. 6.5 vertical axis), but most of the sampling points of the UQ method fall within a smaller range, quantifiable by the efficiency PDF.

The resulting discretized probability distribution of the overall efficiency is plotted in Fig. 6.6, where each interval of the histogram corresponds to a 0.12% efficiency difference. The input uncertainties (Fig. 6.4) are mapped in an efficiency variation range of 2.2%, within which it is possible to fall with non-zero probability. This is a significant outcome: in a fixed operating point, subject to rotor tip clearance uncertainty (see Tab. 6.2), the overall efficiency variability is approximately 2%.

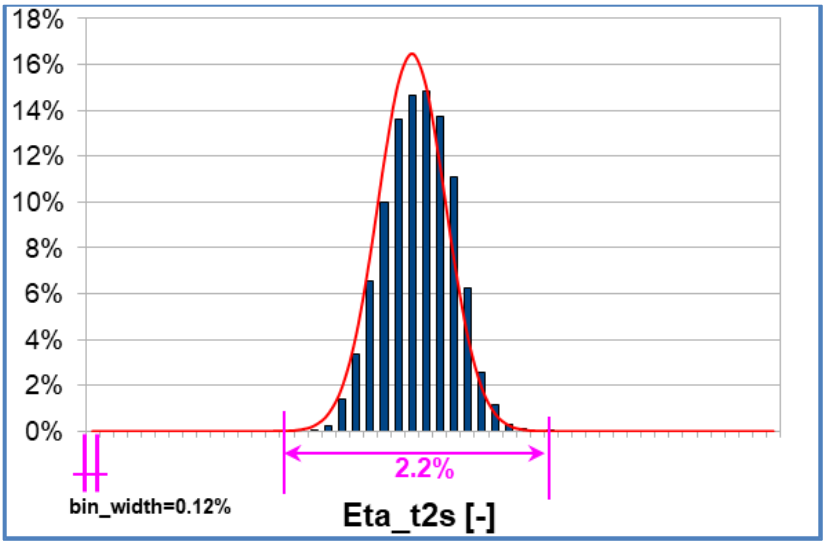

Fig. 6.6 - SB-UQ: overall efficiency probability bars (in blue) and corresponding reference Gaussian trend (same mean and standard deviation) in red line

Rotor total to static efficiency (i.e. calculated using the 'rotor' expansion ratio instead of the 'overall' expansion ratio) has a slightly different behaviour and larger sensitivity within the DoE (7% of variation), as shown in Fig. 6.7.

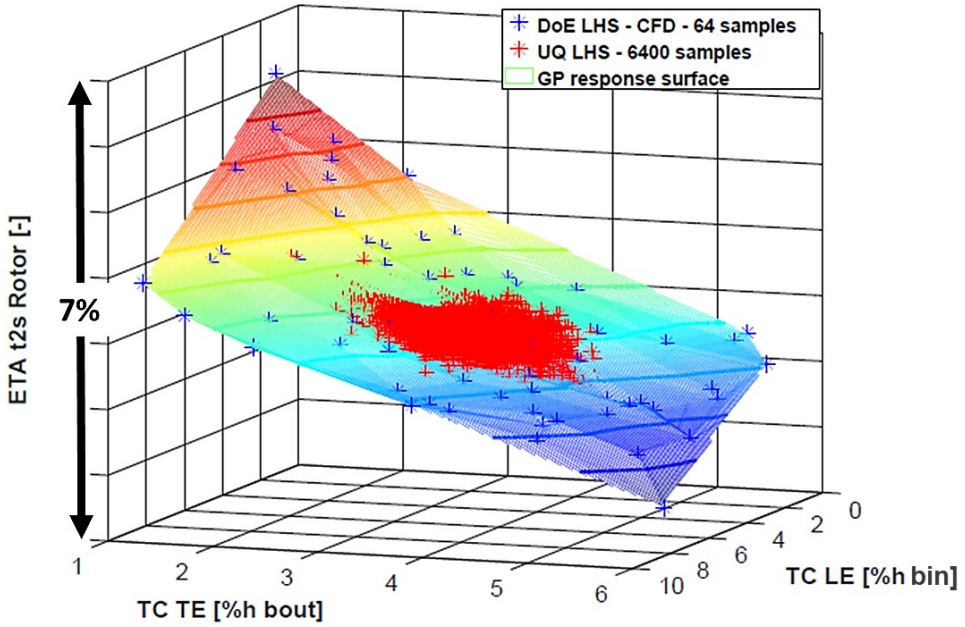

Fig. 6.7 - SB-UQ: rotor total to static efficiency response surface and samples (DoE/UQ)

The rotor efficiency higher sensitivity (compare Fig. 6.5-6.7) can be explained considering that tip gap variations directly affect the rotor efficiency, while the stage efficiency also includes volute and tailpipe losses which tend to mitigate the effect of rotor tip clearance change. The comparison between the two different definitions of efficiency continues with the analysis of the respective discretized probability distributions: the rotor total to static efficiency PDF is more pointed and less dispersed than the 'overall' one (see Fig. 6.6–6.8).

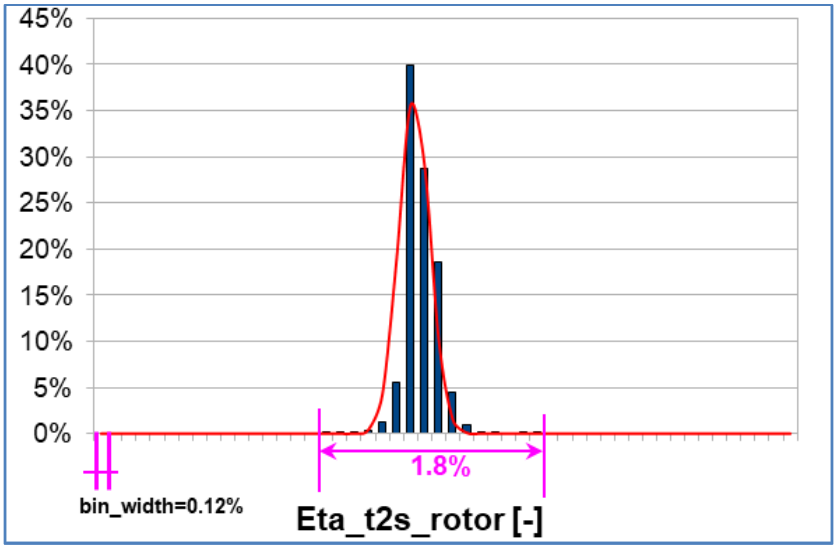

Fig. 6.8 - SB-UQ: rotor efficiency probability bars (in blue) and corresponding reference Gaussian trend (same mean and standard deviation) in red line

By examining Fig. 6.5 and 6.7 it can be noted that the turbine efficiency (overall or rotor only) presents a greater sensitivity with respect to variations in tip clearance at blade TE: in fact, by setting a tip gap value at the LE, the efficiency absolute variation is approximately 3% against a small 1-1.5% in the opposite case (i.e. fixing a tip gap value at the TE). In conclusion, the gradient (and therefore the slope) of the efficiency response surfaces is remarkably higher in the direction of variation of the TE tip clearance.
Among the statistical quantities provided by the UQ analysis, the 'Skewness' (equation (6.7)) and the 'excess Kurtosis' (equation (6.8)) are computed as follows:

$$Sk = E\left[\left(\frac{R_i - \mu_i}{\sigma_i}\right)^3\right] \cong \frac{1}{{\sigma_i}^3}\left[\sum_{k=1}^{N_p}(r_{ik} - \mu_i)^3\omega_k\right] \tag{6.7}$$

$$Ku = E\left[\left(\frac{R_i - \mu_i}{\sigma_i}\right)^4\right] - 3 \cong \frac{1}{{\sigma_i}^4}\left[\sum_{k=1}^{N_p}(r_{ik} - \mu_i)^4\omega_k\right] - 3 \tag{6.8}$$

where μ_i is the mean, σ_i is the standard deviation and E is the 'expectation operator'.

The skewness (Sk) is a measure of the asymmetry of the probability distribution of a real-valued random variable about its mean, while the excess Kurtosis (Ku) describes the shape of a PDF with respect to the Gaussian distribution (which has Ku=0).
The corresponding values of these statistical moments are reported in next Tab. 6.3 and the following considerations can be drawn:

- overall efficiency → comparing the discretized probability function with the corresponding reference Gaussian it is clear that the distribution is 'left-skewed' (Sk<0), i.e. the left tail is slightly longer and the mass of the distribution is shifted on the right of Fig. 6.6. Furthermore, Ku<0 and the distribution is defined 'platykurtic' because it is flatter than the corresponding Gaussian, resulting in thinner tails;
- rotor efficiency → the distribution is 'right-skewed' (Sk>0), i.e. the right tail is longer and the mass of the distribution is shifted on the left of Fig. 6.8. In this case Ku>0 and the distribution is defined 'leptokurtic' because it is more pointed than the corresponding Gaussian, resulting in thicker tails.

Tab. 6.3 - SB-UQ: statistical moments of 3rd and 4th order for the total to static efficiency referred to the rotor only or to the overall turbine respectively

Quantity of interest	**Skewness (Sk)**	**Excess Kurtosis (Ku)**
ETA_t2s_Overall	−0.0195	−0.3046
ETA_t2s_Rotor	0.2982	2.3968

The difference between the probability distributions of efficiency calculated for the rotor only and for the whole stage can be explained comparing the respective response surfaces. In Fig. 6.7 the surface has an inflection at the rotor tip clearance average values; since the input distributions are Gaussian, the majority of UQ samples falls around their mean values (where the response surface flattens) resulting in a more concentrated probability density for the rotor efficiency. The aforementioned inflection in rotor efficiency is due to the peculiar behaviour of the rotor pressure ratio, whose response surface is shown in Fig. 6.9.

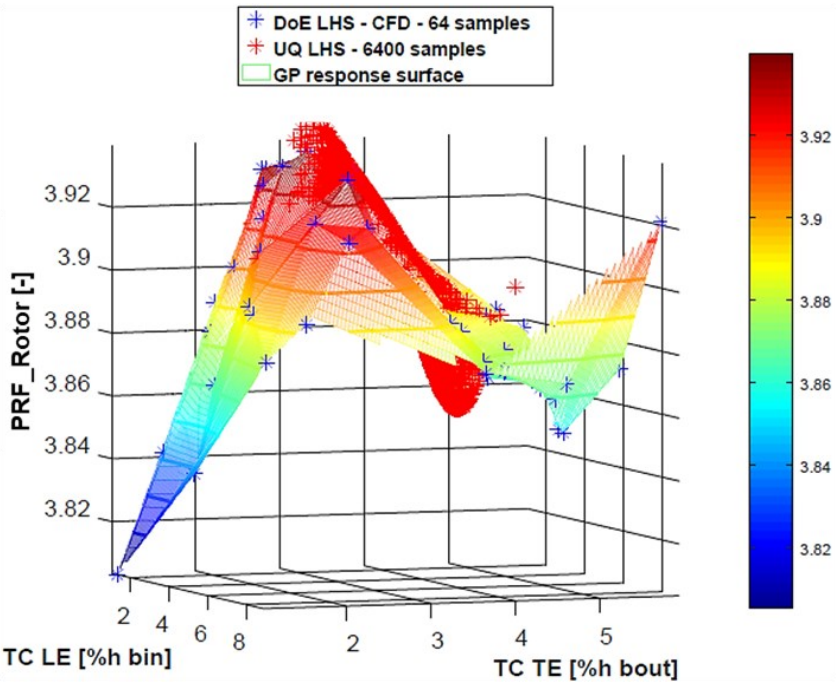

Fig. 6.9 - SB-UQ: rotor pressure ratio response surface and samples (DoE/UQ)

The PDF of the PRF_{rotor} obtained with the UQ analysis is displayed in Fig. 6.10, where the input uncertainties are mapped in a variation range of 0.1, equal to 2% of the mean value of the distribution. The rotor pressure ratio probability distribution is almost uniform within this interval with the highest probability peaks at around 8%.

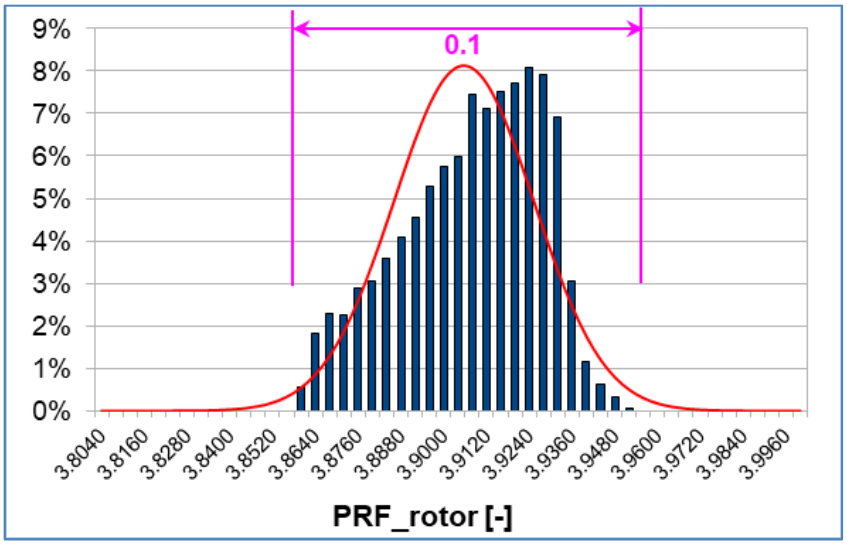

Fig. 6.10 - SB-UQ: rotor pressure ratio probability bars (blue) and corresponding reference Gaussian trend (same mean and standard deviation) in red line

Fig. 6.11 shows the response surface of the mass flow parameter with the data set points; it is evident from the surface gradient that the tip gap at blade trailing edge (TC_{TE}) has a greater influence on the MFP than the tip gap at blade leading edge (TC_{LE}).

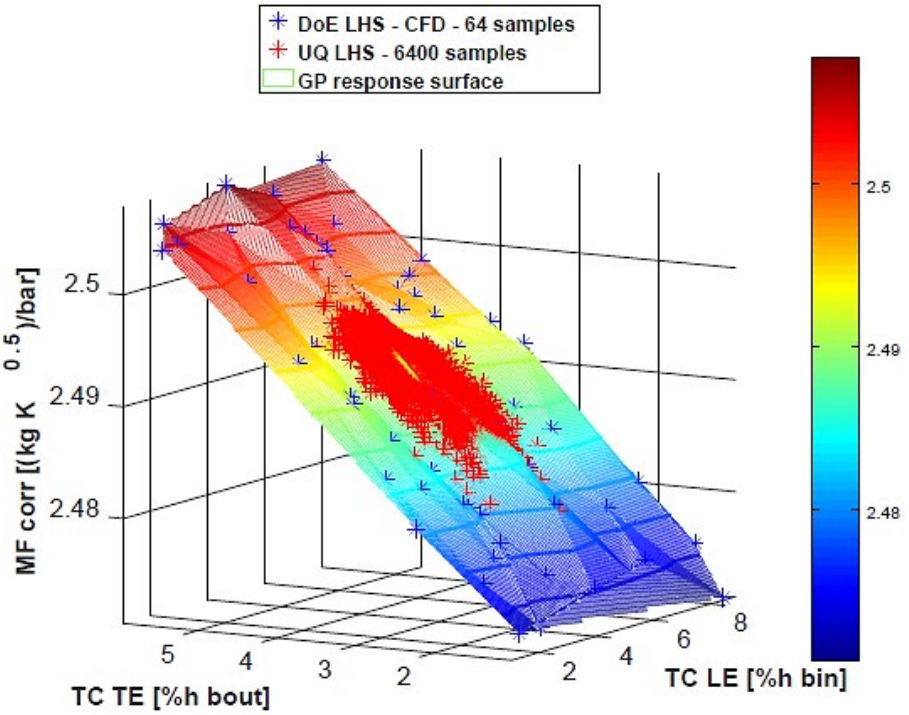

Fig. 6.11 - SB-UQ: mass flow parameter response surface and samples (DoE/UQ)

The rotor tip clearance reduction at blade trailing edge (i.e. TE blade tip closer to the shroud surface) leads to an appreciable decrease of the mass flow parameter, namely of the turbine exhaust gas processing capacity. This result agrees perfectly with the radial turbine design theory, which teaches that the aerodynamic blockage in the exducer (final part of the blade) limits the impeller blades number (see paragraph 1.2.2).
The discretized probability distribution of the MFP is shown in Fig. 6.12. The 6400 results of the sampling-based UQ algorithm are concentrated in a small range of 0.02 [(kgK^0.5)/bar], equal to 0.8% of the mean value of the distribution. Overall, it can be noted that rotor tip gap uncertainties have a limited impact on turbine mass flow, which is only slightly affected by tip clearance uncertainty at blade trailing edge.

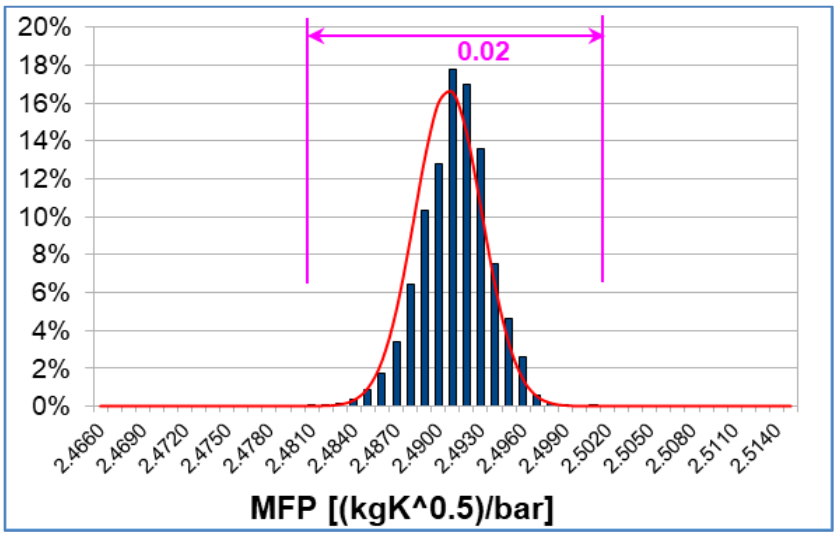

Fig. 6.12 - SB-UQ: mass flow parameter probability bars (blue) and corresponding reference Gaussian trend (same mean and standard deviation) in red line

Although in this case the MFP sensitivity to rotor tip gap uncertainties is limited (overall variation within the DoE of about 1.5% of the mean value), it should be noted that the trailing edge tip clearance may have a stronger impact if a diffuser is placed downstream of the wheel, limiting the turbine permeability through diffuser blockage.

6.4.2. Surrogate model validation

The surrogate models given by Dakota's 'Surfpack' toolset allows to compute diagnostic metrics based on the differences between the 'observed' value $o(x_i)$, and the metamodel prediction $p(x_i)$ for the training points x_i [28]. Three types of 'error' can be distinguished:

1) simple prediction error with respect to the training data. In this case the points x_i are those used to train the model;
2) prediction error estimated by cross-validation, when the points x_i are selectively omitted from the build;
3) prediction error with respect to challenge data, which are supplementary points x_i provided by the user.

The resulting metrics must be interpreted very carefully: e.g. in case of interpolatory models, like that used in this case for the surrogates generation, simple prediction error (1) will almost always be zero and therefore must be neglected, while options (2) and (3) remain valid to compute diagnostic metrics.

As done in chapter 5 for the UQ analysis on the supersonic nozzle, a cross-validation was performed for the radial turbine metamodels in order to verify their reliability.
At first the *k-fold* cross-validation is considered: the results obtained from a '*4-fold'* cross-validation are reported in Tab. 6.4 including the root mean squared, the mean absolute value and the maximum absolute value of the prediction error (calculated between the CFD value and the surrogate model prediction for the training points). The determination coefficient (R^2) is meaningful for polynomial models, but less for other model types.
It should be noted that the average and maximum absolute values of the prediction error (last two rows of Tab. 6.4 and 6.5) are reported in relative percentage form with respect to the corresponding mean values of the 64-point DoE.

Tab. 6.4 – Diagnostic metrics for the 4-fold cross validation of response surfaces

Metrics	$\boldsymbol{\eta_{ts}}$	$\boldsymbol{\eta_{ts\_rotor}}$	$\boldsymbol{PRF_{rotor}}$	$\boldsymbol{MFP}$ **[kgK^0.5/bar]**
Root mean squared (RMS)	5.766 x10^{-4}	1.428 x10^{-3}	1.794 x10^{-2}	1.356 x10^{-3}
Mean absolute value (%mean value)	0.08%	0.20%	0.33%	0.04%
Maximum absolute value (%mean value)	0.30%	0.97%	1.52%	0.15%

The results of the '*4-fold'* cross-validation attest to the reliability of the metamodels, with average errors never above 0.5% and maximum errors contained within 1.5%.
In addition, the *'Prediction Error Sum of Squares'* (PRESS) was performed.

Tab. 6.5 - Diagnostic metrics for the Leave-one-out cross validation (PRESS) of surrogates

Metrics	$\boldsymbol{\eta_{ts}}$	$\boldsymbol{\eta_{ts\_rotor}}$	$\boldsymbol{PRF_{rotor}}$	$\boldsymbol{MFP}$ **[kgK^0.5/bar]**
Root mean squared (RMS)	5.116 x10^{-4}	1.339 x10^{-3}	1.738 x10^{-2}	1.393 x10^{-3}
Mean absolute value (%mean value)	0.07%	0.17%	0.29%	0.04%
Maximum absolute value (%mean value)	0.27%	1.03%	1.71%	0.15%

The diagnostic metrics in Tab. 6.5 further confirm the outcomes of the *4-fold* cross validation. As expected, the maximum error increases slightly (1.71%) because in this case the number of partitions used to assess the statistics corresponds to the number of training points. Nevertheless, maximum errors within 2% are considered acceptable and certify the validity of the UQ results already discussed in section 6.4.1.
The SB-UQ approach will therefore be taken as a reference to evaluate the quality of the PDFs obtained with PCE of different orders in the next paragraph.

6.4.3. PCE: comparison of the results obtained from different polynomial orders

Polynomial chaos expansions (PCE) use multidimensional orthogonal polynomial approximation formed in terms of standardized random variables. In the present case study

all random inputs can be described using independent normal, uniform, exponential, beta and gamma distributions, hence Askey polynomials (see paragraph 2.6) can be directly applied. The set of polynomials are used as an orthogonal basis to approximate the functional form between the stochastic response output and each of its random inputs. It should be remembered that although the PCE method provides analytic statistical moments of the response functions, the cumulative distribution function probabilities are evaluated numerically by sampling (LHS) on the expansion.
In this application the Gaussian quadratures have been selected using an isotropic approach because the two input variables have the same physical meaning. This means that the UQ algorithm uses the same quadrature order $m_{ij} = m$ for the input variables (n= 2 dimensions), resulting in a total of m^n function evaluations to compute the PCE coefficients (α_j): e.g. for a 4th order $4^2 = 16$ CFD simulations are needed.

The Polynomial Chaos Expansion technique requires the user to specify the expansion order of the multivariate polynomial approximation and the polynomial order bounds for each input variable. The GP algorithm previously used in the Surrogate-Based approach (section 6.4.1) requested a 2nd order polynomial for the trend function of each response function and the highest total polynomial order of any term in the trend function was two. However, if no information on the response functions behaviour is available, what is the proper polynomial order for each QoI of the UQ problem? To answer this question it is essential to compare the output PDFs resulting from different PCE orders.
In this section the results of a 2nd, 3rd and 4th order polynomial expansion are compared to give some guidelines for future UQ applications on twin scroll radial turbines. Starting from the η_{ts}, the comparison among the respective discretized PDFs is shown in Fig. 6.13.

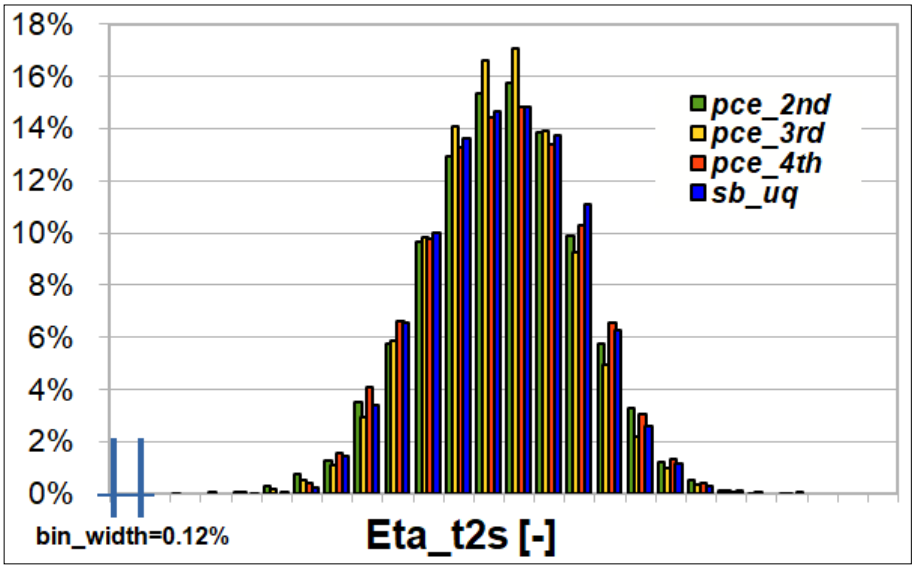

Fig. 6.13 - PCE vs. SB-UQ: overall efficiency probability distributions obtained from polynomial expansions of different orders compared to the 'Surrogate-Based' reference

It is interesting to note that the PDFs obtained with 2nd and 4th order PCEs are more similar near the mean value, while 3rd order polynomial expansion PDF differs from the previous ones, with higher probability peaks close to the probability distribution mean value. If the

SB-UQ diagram bars are taken as reference, the closest PDF stems from the 4th order PCE, especially considering the central bars, associated with the highest probability levels.
In order to provide the reader with a quantitative idea of the maximum error made in estimating the probability distribution of a QoI with a certain PCE order, the PDFs are compared using the same response levels for each quantity of interest. This means that for a given QoI the probability of occurrence inside a definite bin, estimated with a determined order of the PCE, was compared with the corresponding one (same bin) coming from the SB-UQ method. Once this operation was performed, the 'maximum absolute (no sign) probability differences' were identified and collected in a table. For example, considering the probability differences between the discretized trends obtained with the PCE and the SB-UQ 'reference' distribution in Tab. 6.6, the 3rd order PCE gives the most different PDF from SB-UQ prediction, while 2nd and 4th order polynomial expansions differ by 0.4%.
At this point, is it worth doing 16 CFD simulations instead of 4 (minimum number required by 4th and 2nd order PCE respectively) for such a small improvement? The answer to this question can only be given by considering the set of all response functions.

Tab. 6.6 - Overall efficiency maximum probability differences from SB-UQ reference

Eta_t2s : max. absolute probability difference - PCE vs. SB-UQ		
2nd	**3rd**	**4th**
1.22%	2.22%	0.83%

Fig. 6.13 and Tab. 6.6 highlight an important outcome: with the 2nd order PCE it is possible to get an overall efficiency probability distribution which differs from the SB-UQ 'reference' by a maximum of 1%. Therefore, the PCE technique allows to obtain optimal probability predictions with a much lower computational effort: from 64 CFD simulations needed for the metamodel-based approach to just 4 simulations for the 2nd order PCE.

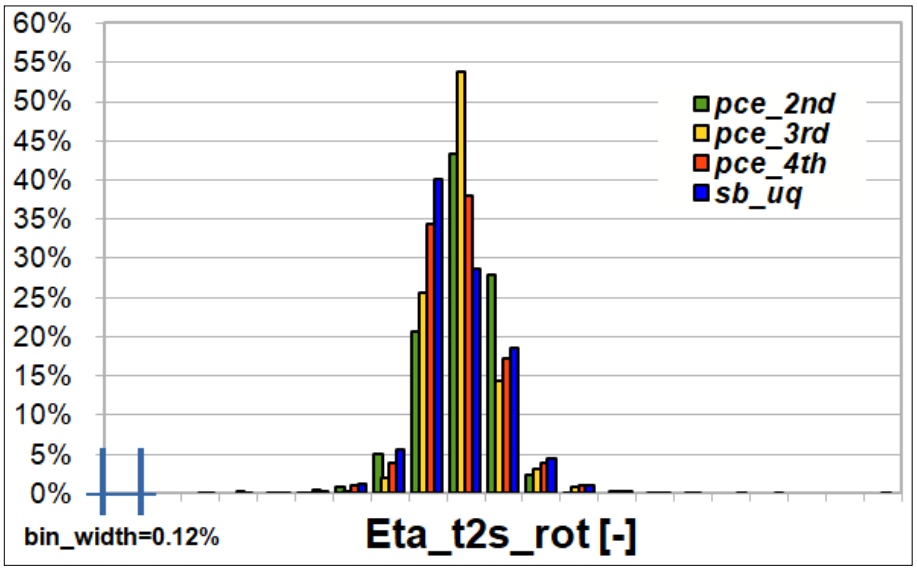

Fig. 6.14 - PCE vs. SB-UQ: rotor efficiency probability distributions comparison

The discretized PDFs of the $\eta_{t2s\,rotor}$ in Fig. 6.14 show that the 3rd order polynomial expansion still provides the most pointed distribution, as noted for the overall efficiency. Moreover, lower order (2nd and 3rd) PCEs give more concentrated probabilities around the PDFs mean value, while 4th order PCE and SB-UQ display a greater probability dispersion. In this case the probability differences with respect to SB-UQ reference indicate a larger gap between the 2nd and 4th order polynomial PDFs, as confirmed by Tab. 6.7; the maximum probability difference of the 2nd order PCE is twice that of the 4th order PCE. The wider gap found between rotor efficiency PDFs suggests the use of a 4th order PCE.

Tab. 6.7 - Rotor efficiency maximum probability differences from SB-UQ reference

Eta_t2s_rot : max. absolute probability difference PCE vs. SB-UQ		
2nd	**3rd**	**4th**
19.39%	25.13%	9.31%

All PCE-derived probability distributions for the rotor pressure ratio differ in shape from the SB-UQ reference; furthermore, lower order (2nd and 3rd) polynomial expansions lead to greater probability dispersion within the dataset, as shown in Fig. 6.15 below.

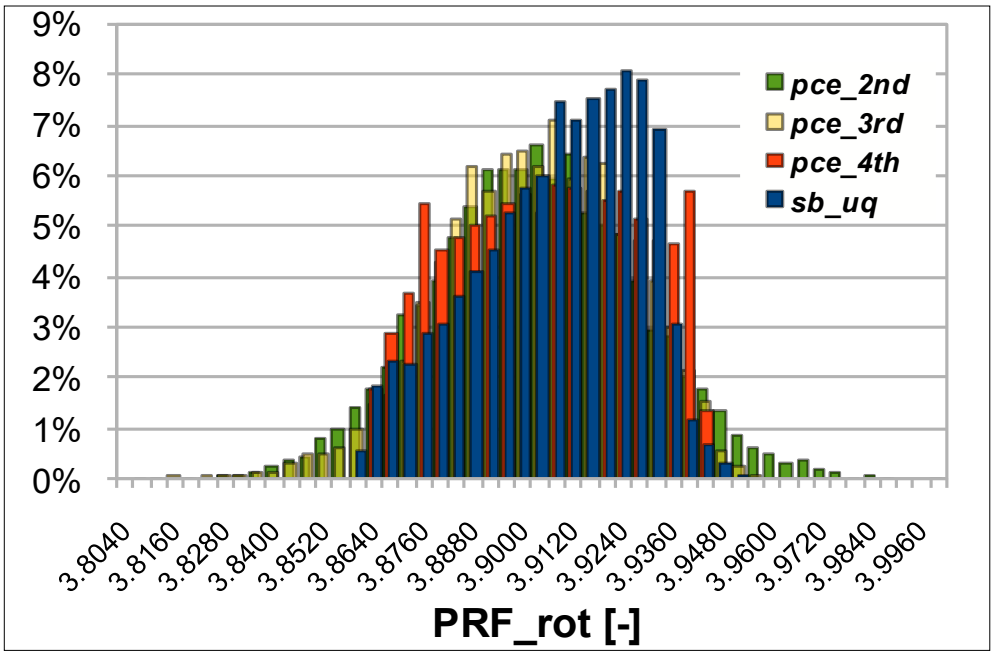

Fig. 6.15 - PCE vs. SB-UQ: rotor pressure ratio probability distributions comparison

Tab. 6.8 - Rotor pressure ratio maximum probability differences from SB-UQ reference

PRF_rot : max. absolute probability difference PCE vs. SB-UQ		
2nd	**3rd**	**4th**
4.52%	3.25%	3.98%

Considering the maximum absolute probability differences reported in Tab. 6.8 for the rotor pressure ratio, the gap from the SB-UQ reference is always around 3–4% for all PCE orders. Nevertheless, it should be stressed that the 4th order PCE is the one that best fits qualitatively to the results of the SB-UQ, as shown in Fig. 6.15.

Finally, the mass flow parameter is examined: the PDFs are almost entirely contained in a range of amplitude equal to 0.8% of the mean value of the distribution (see Fig. 6.16). Analyzing the data in Tab. 6.9 it can be concluded that quantitatively the 4th order PCE is the solution that best approximates the probability distribution given by the Surrogate-Based UQ approach, with a maximum error of about 3%.

Tab. 6.9 - Mass flow parameter maximum probability differences from SB-UQ reference

MFP : max. absolute probability difference PCE vs. SB-UQ		
2nd	**3rd**	**4th**
5.58%	9.59%	3.34%

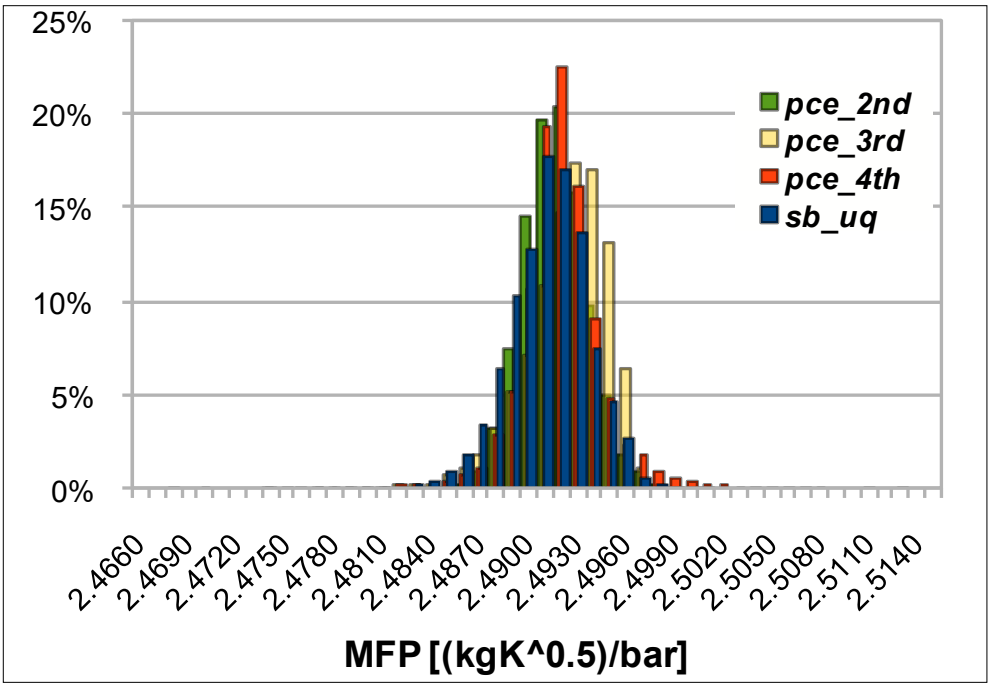

Fig. 6.16 - PCE vs. SB-UQ: mass flow parameter probability distributions comparison

As a general conclusion of the analysis of uncertainty quantification results:

- two UQ approaches (Surrogate-Based and PCE) were studied and compared;
- the results of the UQ method based on metamodels were validated through cross validation and taken as a reference for evaluating PCE capabilities;
- the best polynomial chaos expansion order for the case of the twin scroll turbine was identified in the 4th order and validated using the results of the Surrogate-Based UQ approach.

Conclusions and perspectives

The doctoral thesis achieved the prescribed purposes as a result of a well-defined planning of the research activity.
The detailed fluid dynamic characterization of twin entry turbines allowed to understand the main parameters which typify and influence their fluid dynamic performance. In addition, the formulation of brand new parameters and indices related to the fluid dynamic performance of the twin scroll volute offers the possibility of future improvements in automated procedures for design optimization of twin entry radial turbines.
The development of an in-house platform for UQ analysis, first tested on the industrially interesting test case of the supersonic nozzle, represents a relevant scientific contribution in the perspective of introducing UQ approaches in consolidated industrial design and verification processes.
The application of the UQ platform to the CFD simulation of a twin scroll radial turbine with geometric uncertainties in the rotor tip clearances at blade leading edge and trailing edge demonstrated the capabilities and large potential of these numerical techniques for turbomachinery design purposes. The Surrogate-Based UQ approach is a well established UQ technique for several applications, while the use of Polynomial Chaos Expansion is very attractive, as it requires a much lower number of individuals in the CFD database; nevertheless, the order of the polynomial strongly affects the final distributions.
The effects of rotor tip gap uncertainties were quantified and the overall results were confirmed by radial turbine design practice.
The UQ analysis applied to twin scroll radial turbines provides the designer with more realistic information on expected performance at a given working point by introducing the effects of operational geometric uncertainties into CFD simulation. Performance data associated with uncertainty margins allow designers to better correlate simulated data with actual performance.

The doctoral thesis proved to industry the high potential of UQ methodologies in making the prediction of the expected performance of a component subject to several sources of uncertainty more reliable.
The application of uncertainty quantification techniques to CFD is therefore proposed as a new industrial standard for research and development departments.

References

[1] Marelli S., Academic year 2015/2016, Lecture notes for the course of Propulsion Systems with Reduced Environmental Impact, University of Genoa - Polytechnic School.

[2] Della Volpe R., 2011, Macchine, Liguori editore, Napoli.

[3] Newton P., Romagnoli A., Martinez-Botas R., Copeland C., Seiler, M., June 2014, A Method of Map Extrapolation for Unequal and Partial Admission in a Double Entry Turbine, ASME. J. Turbomach., 136(6): 061019.

[4] Chiong M. S., Rajoo S., Romagnoli A., Costall A. W., Martinez-Botas R. F., 2016, One-dimensional pulse-flow modeling of a twin-scroll turbine, Elsevier Energy, Volume 115, Part 1, Pages 1291-1304.

[5] Hajilouy-Benisi A., Rad M., Shahhosseini M. R., 2009, Flow and performance characteristics of twin-entry radial turbine under full and extreme partial admission conditions, Arch Appl Mech 79, 1127–1143.

[6] Whitfield A., Baines N. C., 1990, Design of radial turbomachines, Longman Scientific & Technical.

[7] Barnard M.C.S., Benson R.S., 1968, Radial gas turbines, Proceeding IME 183 part 3N, 59-70.

[8] Chappie P.M., Flynn P.F., Mulloy J.M., January 1980, Aerodynamic Design of Fixed and Variable Geometry Nozzleless Turbine Casings, Journal of Engineering for Power, 102: 141-147.

[9] Scrimshaw K. H., Williams T. J., 1984, Size effects in small radial gas turbines, ASME paper 84-GT-215.

[10] Dixon S.L., 2005, Fluid mechanics and thermodynamics of turbomachinery, Elsevier Butterworth–Heinemann, Oxford.

[11] Stanitz J.D., 1952, Some theoretical aerodynamic investigations of impellers in radial and mixed flow centrifugal compressors, Trans ASME 74: 473-497.

[12] Sovran G., Klomp E.G., 1967, Experimentally determined optimum geometries for rectilinear diffusers with rectangular, conical, or annular cross-section, In Sovran G (ed) Fluid Mechanics of Internal Flows, Elsevier.

[13] Schorn N., 2014, The Radial Turbine for Small Turbocharger Applications: Evolution and Analytical Methods for Twin-Entry Turbine Turbochargers, SAE Int. J. Engines 7(3):1422-1442.

[14] Baines N. C., Hajilouy-Benisi A., Yeo J. H., 1994, The Pulse Flow Performance and Modelling of Radial Inflow Turbines, Proceedings of the Institution of Mechanical Engineers, 5th International Conference on Turbocharging and Turbochargers, Paper No. C484/006/94.

[15] Romagnoli A., June 2010, Aerodynamic and thermal characterization of turbocharger turbines: experimental and computational evaluation, PhD Thesis, Department of Mechanical Engineering, Imperial College London, pp. 95-104.

[16] Romagnoli A., Martinez-Botas R. F., Rajoo S., 2011, Steady state performance evaluation of variable geometry twin-entry turbine, Elsevier International Journal of Heat and Fluid Flow, Volume 32, Issue 2, pp. 477-489.

[17] U.S. Department of Energy, 2009, Scientific Grand Challenges for National Security: The Role of Computing at the Extreme Scale, p. 135.

[18] Iaccarino G., 2011, Introduction to uncertainty representation and propagation, AVT-193 Short Course on Uncertainty Quantification, NATO Research and Technology Organization.

[19] Montomoli F., Carnevale M., D'Ammaro A., Massini M., Salvadori S., 2015, Uncertainty Quantification in Computational Fluid Dynamics and Aircraft Engines, Springer, pp. 61-65, 70.

[20] AIAA (American Institute of Aeronautics and Astronautics), 1998, Guide for the Verification and Validation of Computational Fluid Dynamics Simulations, AIAA G-077-1998, Renston,VA.

[21] Ghanem R., Doostan A., 2006, On the construction and analysis of stochastic models: characterization and propagation of the errors associated with limited data, Journal of Computational Physics, 217:6381.

[22] Cavazzuti M., 2013, Optimization Methods: From Theory to Design - Scientific and Technological Aspects in Mechanics, Springer, p. 33-34.

[23] Box G. E. P., Wilson, K. B., 1951, Experimental attainment of optimum conditions, Journal of the Royal Statistical Society, 13, 1–45.

[24] Mackay D. J. C., 1997, Introduction to Gaussian processes, Technical report, Cambridge University, Cavendish Laboratory.

[25] Rasmussen C. E., Williams C. K. I., 2006, Gaussian processes for machine learning, Cambridge: MIT Press.

[26] Cressie N. , 1991, Statistics for Spatial Data, John Wiley and Sons, New York.

[27] Koehler J. R. , Owen A. B. , 1996, Computer experiments, Handbook of Statistics, volume 13 (Ghosh S. and Rao C. R. editors), Elsevier Science, New York.

[28] B. M. Adams, W. J. Bohnhoff, K. R. Dalbey, J. P. Eddy, M. S. Ebeida, M. S. Eldred, J. R. Frye, G Gerarci, R. W. Hooper, P. D. Hough, K. T. Hu, J. D. Jakeman, M. Khalil, K. A. Maupin, J. A. Monschke, E. M. Ridgway, A. Rushdi, J. A. Stephens, L. P. Swiler, J. G. Winokur, D. M. Vigil, and T. M. Wildey, Updated May 2018, Dakota, a multilevel parallel object-oriented framework for design optimization, parameter estimation, uncertainty quantification, and sensitivity analysis: Version 6.8 User's Manual. Technical Report SAND2014-4633, Sandia National Laboratories, Albuquerque, NM.

[29] Iaccarino G., 2018, Uncertainty quantification in computational science, STO-AVT-VKI Lecture Series on Uncertainty Quantification in Computational Fluid Dynamics – AVT 326, Short Course on Uncertainty Quantification, von Karman Institute for Fluid Dynamics, Belgium.

[30] Helton J., Davis F., 2000, Sampling-based methods for uncertainty and sensitivity analysis, Technical Report SAND99-2240, Sandia National Laboratories, Albuquerque, NM.

[31] Helton J., Davis F., 2003, Latin hypercube sampling and the propagation of uncertainty in analyses of complex systems, Elsevier Reliability Engineering & System Safety, Volume 81, Issue 1, pp. 23–69.

[32] Giunta A. A., McFarland J. M., Swiler L. P., Eldred M. S., September-December 2006, The promise and peril of uncertainty quantification using response surface approximations, Structure and Infrastructure Engineering, 2(3-4):175–189.

[33] Swiler L., Slepoy R., Giunta A. A., May 1-4 2006, Evaluation of sampling methods in constructing response surface approximations, Proc. 47th AIAA/ASME/ASCE/AHS/ASC Structures, Structural Dynamics, and Materials Conference, number AIAA-2006-1827, Newport, RI.

[34] Celik I. B., Ghia U., Roache P. J., Freitas C. J., Coleman H. W., Raad P. E., 2008, Procedure for Estimation and Reporting of Uncertainty due to Discretization in CFD Applications, ASME Journal of Fluids Engineering, Editorial, Vol. 130, No. 7, July 2008, pp. 078001-1– 078001-4, 4 pages.

[35] Roache P. J. , 1998, Verification and Validation in Computational Science and Engineering, Hermosa Publishers, Albuquerque.

[36] Roache P. J., January 2003, Error Bars for CFD, AIAA Paper 2003-0408, AIAA 41st Aerospace Sciences Meeting, Reno, Nevada.

[37] Eça L., Hoekstra M., Roache P. J., June 2007, Verification of Calculations: an Overview of the Second Lisbon Workshop, AIAA Paper 2007-4089, AIAA Computational Fluid Dynamics Conference, Miami.

[38] Roache P. J., July 2003, Conservatism of the GCI in Finite Volume Computations on Steady State Fluid Flow and Heat Transfer, ASME Journal of Fluids Engineering, Vol. 125, No. 4, pp. 731–732.

[39] ASME V&V, 2009, Standard for Verification and Validation in Computational Fluid Dynamics and Heat Transfer, ASME V&V 20-2009, p. 15.

[40] Cravero C., Dawes W.N., 2-5- June 1997, Throughflow design using an automatic optimization strategy, ASME Turbo Expo 1997, Orlando (USA).

[41] Barsi D., Costa C., Cravero C., Ricci G., June 16-20, 2014, Aerodynamic design of a centrifugal compressor stage using an automatic optimization strategy, ASME paper GT2014-26465, Asme Turbo Expo, Dusseldorf (D).

[42] Lavagnoli S., Maesschalck C., Andreoli V., 2016, Design considerations for tip clearance control and measurement on a turbine rainbow rotor with multiple blade tip geometries, Journal of Engineering for Gas Turbines and Power, 139(4), 042603.

[43] Wiener N., 1938, The homogeneous chaos, American Journal of Mathematics, 60(4), 897–936.

[44] Ghanem R. G., Spanos. P. D., 1991, Stochastic Finite Elements: A Spectral Approach, Springer-Verlag, NewYork.

[45] Ghanem R., Red-Horse J. R., 1999, Propagation of probabilistic uncertainty in complex physical systems using a stochastic finite element technique, Physica D: Nonlinear Phenomena, Volume 133, Issues 1–4, pp. 137–144.

[46] Askey R., Wilson J., 1985, Some basic hypergeometric orthogonal polynomials that generalize Jacobi polynomials, Mem. Amer. Math. Soc. 319, Providence, RI.

[47] Brian M. Adams, Mohamed S. Ebeida, Michael S. Eldred, Gianluca Geraci, John D. Jakeman, Kathryn A. Maupin, Jason A. Monschke, J. Adam Stephens, Laura P. Swiler, Dena M. Vigil, Timothy M. Wildey, William J. Bohnhoff, Keith R. Dalbey, John P. Eddy, Joseph R. Frye, Russell W. Hooper, Kenneth T. Hu, Patricia D. Hough, Mohammad Khalil, Elliott M. Ridgway, Justin G. Winokur, Ahmad Rushdi, Updated May 2018, Dakota, a multilevel parallel object-oriented framework for design optimization, parameter estimation, uncertainty quantification, and sensitivity analysis: Version 6.8 Theory Manual. Technical Report SAND2014-4253, Sandia National Laboratories, Albuquerque, NM.

[48] Montomoli F., Carnevale M., D'Ammaro A., Massini M., Salvadori S., 2019, Uncertainty Quantification in Computational Fluid Dynamics and Aircraft Engines – Second Edition, Springer.

[49] Cravero C., De Domenico D., Ottonello A., 2019, Numerical Simulation of the Performance of a Twin Scroll Radial Turbine at Different Operating Conditions, Hindawi International Journal of Rotating Machinery, vol. 2019, Article ID 5302145.

[50] Cravero C., La Rocca M., Ottonello A., 2018, Performance Characterization of a Twin Scroll Volute for Turbocharging Applications, Proceedings of the ASME Turbo Expo 2018: Turbomachinery Technical Conference and Exposition. Volume 2B: Turbomachinery, ASME Paper GT2018-75522, V02BT44A010, Oslo, Norway.

[51] Cravero C., De Domenico D., Ottonello A., 2019, Investigation on the Degree of Reaction in Twin Scroll Radial Turbines at Different Operating Conditions for Turbocharging Applications, Proceedings of the ASME Turbo Expo 2019: Turbomachinery Technical Conference and Exposition. Volume 2B: Turbomachinery, ASME Paper GT2019-90285, V02BT44A004, Phoenix, AZ, USA.

[52] Ottonello A., February 2017, CFD analysis of the performance of a twin entry radial turbine for turbocharging, Master's degree thesis in Mechanical Engineering, University of Genoa.

[53] Olmeda P., Tiseira A., Dolz V., García-Cuevas L.M., 2015, Uncertainties in power computations in a turbocharger test bench, Measurement, Volume 59, pp. 363-371.

[54] Marelli S., Capobianco M., 2011, Steady and pulsating flow efficiency of a waste-gated turbocharger radial flow turbine for automotive application, Energy, Volume 36, Issue 1, pp. 459-465.

[55] Vavra MH., 1965, Problems of fluid mechanics in radial turbomachines, VKI Course Note 55-3.

[56] Benson R.S., Scrimshaw K.H., 1965-1966, An experimental investigation of non-steady flow in a radial gas turbine, Proc Inst Mech Engrs, 180. Part 3J, Paper 23.

[57] Capobianco M, Gambarotta A., 1986, Un metodo per la determinazione dell'efficienza di gruppi turbosovralimentatori di motori a combustione interna, 41_Congresso ATI. Napoli, Italy [in Italian].

[58] Dialy J.W., Nece R.E., 1960, Chamber dimension effects on induced flow and frictional resistance of enclosed rotating disk, ASME Trans Ser D;S82.

[59] Brian M. Adams, Mohamed S. Ebeida, Michael S. Eldred, Gianluca Geraci, John D. Jakeman, Kathryn A. Maupin, Jason A. Monschke, J. Adam Stephens, Laura P. Swiler, Dena M. Vigil, Timothy M. Wildey, William J. Bohnhoff, Keith R. Dalbey, John P. Eddy, Joseph R. Frye, Russell W. Hooper, Kenneth T. Hu, Patricia D. Hough, Mohammad Khalil, Elliott M. Ridgway, Justin G. Winokur, Ahmad Rushdi, Updated May 2018, Dakota, a multilevel parallel object-oriented framework for design optimization, parameter estimation, uncertainty quantification, and sensitivity analysis: Version 6.8 Reference Manual. Technical Report SAND2014-5015, Sandia National Laboratories, Albuquerque, NM.

[60] Pralits J., Academic year 2017/2018, Lecture notes for the course of Advanced fluid dynamics, University of Genoa - Polytechnic School.

[61] Cravero C., De Domenico D., Ottonello A., 2020, Uncertainty Quantification Approach on Numerical Simulation for Supersonic Jets Performance, Algorithms 2020, Volume 13, Issue 5, 130.

[62] Cravero C., Macelloni P., Briasco G., 5–11 June 2012, Three-dimensional design optimization of multi stage axial flow turbines using a RSM based approach, Proceedings of the ASME Turbo Expo, Copenhagen, Denmark, ASME paper GT2012-68040.

[63] Cravero C., 26–28 June 2013, Turbomachinery design optimization based on metamodels, Proceedings of the 4th Inverse Problems Design and Optimization Symposium IPDO-2013, Albi, France.

[64] Campora U., Capelli M., Cravero C., Zaccone R., 2015, Metamodels of a Gas Turbine Powered Marine Propulsion system for Simulation and Diagnostic Purposes, J. Nav. Arch. Mar. Eng. 2015, 12(1), 1–14.

[65] Campora U., Cravero C., Zaccone R., 2018, Marine Gas Turbine Monitoring and Diagnostics by Simulation and Pattern Recognition, Int. J. Nav. Arch. Ocean Eng. 2018, 10(5), 617–628.

[66] Anderlini A., Salvetti M.V., Agresta A., Matteucci L., 2019, Stochastic sensitivity analysis of numerical simulations of injector internal flows to cavitation modeling parameters, Comput. Fluids 2019, 183, 130–147.

[67] Anderson J.D., 1990, Modern Compressible Flow, 2nd ed.; McGraw Hill: New York, NY, USA, pp. 147–179.

[68] Laws C.J., 2003, A Simple Method for the Design of Gas Burners Injectors, Proceedings of the Institution of Mechanical Engineers, Part C: Journal of Mechanical Engineering Science, Volume 217, Issue 2, pp. 237-246.

[69] Ogawa H., Boyce R.R., Isaacs A., Ray T., 2010, Multi-Objective Design Optimisation of Inlet and Combustor for Axisymmetric Scramjets, Open Thermodynamics Journal, Volume 4, pp. 86–91.

[70] Karimi A., Abdi M.A., 2009, Selective dehydration of high-pressure natural gas using supersonic nozzles, Chemical Engineering and Processing: Process Intensification, Volume 48, Issue 1, pp. 560–568.

[71] Yang Y., Li A., Wen C., 2017, Optimization of static vanes in a supersonic separator for gas purification, Fuel Processing Technology, Volume 156, pp. 265–270.

[72] Available online, accessed on 20 January 2020, https://misura.snam.it/portmis/coortecDocumentoController.do?menuSelected=4300.

[73] Basso D., Cravero C., Reverberi A.P., Fabiano B., 2015, CFD Analysis of Regenerative Chambers for Energy Efficiency Improvement in Glass Production Plants, Energies, Volume 8, Issue 8, pp. 8945–8961.

[74] Arnulfi G.L., Cravero C., Marini M., 11–15 June 2012, Analysis of the operating mode influence onto energy consumption of a natural gas storage plant, Proceedings of the ASME Turbo Expo 2012: Turbine Technical Conference and Exposition. Volume 6: Oil and Gas Applications; Concentrating Solar Power Plants; Steam Turbines; Wind Energy, pp. 131-140, Copenhagen, Denmark.

[75] Shimshi E., Ben-Dor G., Levy A., 2009, Viscous simulation of shock-reflection hysteresis in overexpanded planar nozzles, Journal of Fluid Mechanics, 635, 189.

[76] Zapryagaev V. I., Kudryavtsev A. N., Lokotko A. V., Solotchin A. V., Pavlov A. A., Hadjadj A., 2002, An experimental and numerical study of a supersonic-jet shock-wave structure, Proceedings of the International Conference on Methods of Aerophysical Research (11th), Novosibirsk, Russia.

[77] Cravero C., Ottonello A., 2020, Uncertainty Quantification Methodologies Applied to the Rotor Tip Clearance Effect in a Twin Scroll Radial Turbine, Fluids 2020, Volume 5, Issue 3, 114.

[78] Montomoli F., Massini M., Salvadori S., 2011, Geometrical uncertainty in turbomachinery: Tip gap and fillet radius, Computers & Fluids, Volume 46, Issue 1, pp. 362–368.

[79] Satish T.N., Murthy R., Singh A.K., 2014, Analysis of uncertainties in measurement of rotor blade tip clearance in gas turbine engine under dynamic condition, Proceedings of the Institution of Mechanical Engineers, Part G: Journal of Aerospace Engineering, Volume 228, Issue 5, pp. 652–670.

[80] Krishnababu S.K., Newton P.J., Dawes W.N., Lock G.D., Hodson H.P., Hannis J., Whitney C. , 2009, Aerothermal Investigations of Tip Leakage Flow in Axial Flow Turbines – Part I: Effect of Tip Geometry and Tip Clearance Gap. ASME J. Turbomach. 2009, 131(1): 011006.

[81] Raetz H., Kammeyer J., Natkaniec C.K., Seume J.R., 6–10 June 2011, Numerical Investigation of Aerodynamic Radial and Axial Impeller Forces in a Turbocharger, Proceedings of the ASME 2011 Turbo Expo: Turbine Technical Conference and Exposition. Volume 3: Controls, Diagnostics and Instrumentation; Education; Electric Power; Microturbines and Small Turbomachinery; Solar Brayton and Rankine Cycle, ASME Paper GT2011-46360, pp. 919-928, Vancouver, BC, Canada.

[82] Lüddecke B., Nitschke P., Dietrich M., Filsinger D., Bargende M., 15–19 June 2015, Unsteady Thrust Force Loading of a Turbocharger Rotor During Engine Operation, Proceedings of the ASME Turbo Expo 2015: Turbine Technical Conference and Exposition. Volume 8: Microturbines, Turbochargers and Small Turbomachines; Steam Turbines, ASME Paper GT2015-43559, V008T23A022, Montreal, QC, Canada.

Nomenclature

Symbols

a	speed of sound [m/s]
b	blade height [mm]
c	absolute velocity [m/s]
d	derivation symbol
h	specific enthalpy [J/kg], representative cell dimension (GCI), blade height (leading/trailing edge) [mm]
k	specific heat ratio
l	diffuser length [m], rotor axial size [mm]
m	mass [kg], mean value
min	minimum value of a distribution
$\dot{m}$	mass flow rate [kg/s]
p	static pressure [Pa], observed order of accuracy (GCI)
r	radial coordinate, radius [m], grid refinement factor (GCI)
r2	nozzle reference condition: normal shock wave at outlet section
r3	nozzle reference condition: supersonic isentropic expansion
u	peripheral velocity [m/s]
w	relative velocity [m/s]
y+	dimensionless wall distance
z	axial direction [m]
z_b	blade number
A	area [m^2]
AR	area ratio (geometry), aspect ratio (mesh quality)
C_p	static pressure recovery (diffuser), fluid specific heat at constant pressure [J/kgK]
D	diameter [m]
ER_U	unequal expansion ratio
ETA_t2s, ETA_t2s_Overall	overall total to static efficiency
ETA_t2s_Rotor	rotor total to static efficiency
Ku	kurtosis
L	specific work [J/kg]
M	Mach number
MAX	maximum value of a distribution
MFP	Mass Flow Parameter $[(\mathrm{kgK}^{0.5}/\mathrm{s})/\mathrm{bar}]$
MFP_R	Mass Flow Parameter ratio (unequal admission)
MFR	Mass Flow Ratio
MW	Molecular Weight, molar mass [kg/kmol]
N	rotational speed [rev/min], number of samples (DoE, SB-UQ)
P	power [W]
PRF	Pressure Ratio Flow
R	specific gas constant [J/kgK]

Su	Sutherland's coefficient
Sk	skewness
TC_LE	tip clearance at blade leading edge [mm]
TC_TE	tip clearance at blade trailing edge [mm]
T	static temperature [K]
U	uncertainty
VR	Velocity Ratio
X	axial coordinate [m]
α	absolute flow angle [deg]
β	relative flow angle [deg]
β_b	blade metal angle [deg]
δ	half-opening angle of the diffuser
ε	expansion ratio
η	efficiency
ϑ	angular coordinate, crank angle [deg], circumferential direction
λ	incidence factor, admission ratio
μ	dynamic viscosity [Pa s], mean value (Gaussian distribution function)
ξ	dimensionless loss coefficient
π	total pressure loss coefficient (diffuser)
ρ	density [kg/m^3]
σ	standard deviation
φ	flow coefficient
ω	angular speed [rad/s]
Δ	difference, variation
θ	non-dimensional mass flow rates

Superscripts and subscripts

0	total state
1	volute inlet (turbine inlet) section, nozzle inlet section
2	volute outlet/rotor inlet section
3	rotor outlet/tailpipe inlet section
4	diffuser/tailpipe outlet (turbine outlet) section
95%	associated with a 95% probability of occurrence
a	advance, atmospheric, specific work lost in friction
adim	dimensionless
air	referred to air
area	averaged on area
atm	atmospheric
b	blade
bin	blade inlet
bout	blade outlet
both	referred to both twin entry volute branches
c	closing, metal angle
centrifugal	centrifugal force
const	identifies the volute limb at constant pressure ratio (unequal admission)

d	delay, discharge, diffuser, dynamic
effective	effective
exit	outlet nozzle section
exp	experimental
firing	firing sequence
free flow	identifies the volute limb for which the pressure ratio is free to vary (unequal admission)
hub	rotor hub side (identification of the volute branch)
i	inner (annular diffusers)
id, ideal	ideal case
in	inlet nozzle section
limb	generic twin scroll volute branch
m	meridian component
mass	averaged on mass flow
max	maximum value
min	minimum value
normal	referred to a normal or Gaussian distribution
o	opening, outer (annular diffusers)
out	outlet nozzle section
partial	partial admission condition
r	radial
ref	reference value
rel	relative
rid	reduced
rot, rotor	relative to the rotor only
s	isentropic, discharge (static pressure), static condition
sh	rotor shroud side (identification of the volute branch)
ss	isentropic stage
t	total condition, “true” value
tot	overall
ts, t2s	total to static
tt	total to total
twin entry	related to twin entry turbines type
u	unequal
x	axial
x-r	axial to radial
θ, ϑ	circumferential component
*	normalized value
DoE	referred to the Design of Experiments
LE	blade Leading Edge
MAX	maximum value
MIN	minimum value
TE	blade Trailing Edge
TM	Thermo-Mechanical
UQ	referred to the Uncertainty Quantification analysis

Acronyms

BCs	Boundary Conditions
CFD	Computational Fluid Dynamics
CDF	Cumulative Distribution Function
DACE	Design and Analysis of Computer Experiments
DoE	Design of Experiments
ER	Expansion Ratio
GCI	Grid Convergence Index
GP	Gaussian Process
HPC	High Performance Computer
ICE	Internal Combustion Engine
IFR	Inflow Radial
LE	blade Leading Edge
LHS	Latin Hypercube Sampling
MCM	Monte Carlo Method
MFP	Mass Flow Parameter $[(\mathrm{kgK}^{0.5}/\mathrm{s})/\mathrm{bar}]$
MFR	Mass Flow Ratio
MLE	Maximum Likelihood Estimation
P	Pressure side
PC	Polynomial Chaos
PCE	Polynomial Chaos Expansion
PDF	Probability Density Function
PR, PRF	Pressure Ratio Flow
PRESS	Prediction Error Sum of Squares (cross-validation)
QoI	Quantity of Interest
RANS	Reynolds Averaged Navier-Stokes
RMS	Root Mean Square
RSM	Response Surface Methodology
S	Suction side
SA	Sensitivity Analysis
SB	Surrogate-Based
SBUQ, SB-UQ	Surrogate-Based Uncertainty Quantification
SST	Shear Stress Transport
TE	blade Trailing Edge
UQ	Uncertainty Quantification

Appendix A

The kind of uncertainty source leads to a distinction into three main uncertainty categories:
1) operational, such as BCs or fluid properties (see the supersonic nozzle in chapter 5);
2) geometrical, like the rotor tip clearance addressed in chapter 6;
3) numerical, i.e. related to modelling issues and numerical errors.

This appendix concerns a mesh-based uncertainty quantification analysis which shows the application of the Grid Convergence Index method ('GCI'- illustrated in section 2.4) to the twin scroll turbine case (main subject of chapter 6).

Twin entry volute Grid Convergence Index

The goal of this procedure is to quantify the mesh influence on the evaluation of some performance parameters of twin entry radial turbines in order to give an uncertainty estimate $U_{95\%}$ for each of them. By denoting the generic performance parameter with $'f'$, the aim is therefore to provide an interval $f \pm U_{95\%}$ within which the true value $'f_t'$ probably falls, with probability of 95% (confidence level compatible with the range $\pm 2\sigma$ for a Gaussian distribution). The concept underlying the GCI is to calculate the error associated with the use of a certain computational mesh with respect to a reference solution obtained through an asymptotic approach.

At first, three significantly different volute grid resolutions were selected. The GCI procedure recommends not to use different grid refinement factors in different directions, because this results in erroneous observed order of accuracy 'p' (see equation (2.17)). Consequently, in this case the mesh parameters assigned to each geometry patch are kept fixed, while for the global mesh size a 'scale factor' between two consecutive meshes (e.g. coarse to medium or medium to fine) was chosen, in order to refine the volute grid isotropically.

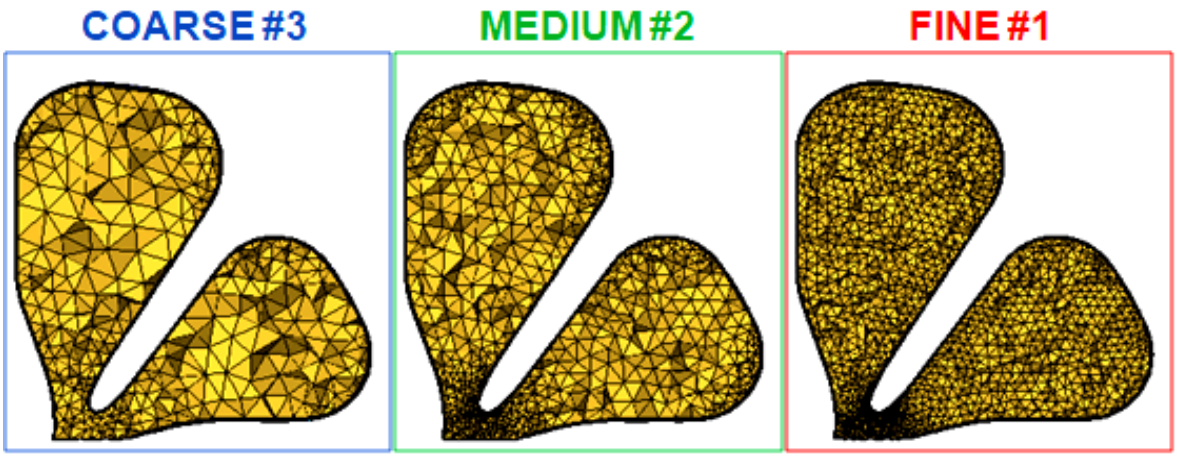

Fig. A.1 – From left to right: coarse, medium, fine mesh resolution on a volute cross cut

Given the geometric complexity of the component, to simulate the twin entry volute it is necessary to generate an unstructured mesh. Equation (2.16) is used to derive, for each grid refinement level, the representative grid dimension *'h'*, which corresponds to the cubic root of the mean value of the elements volume (see Tab. A.1).

A major constraint of the GCI procedure is that the grid refinement factor (ratio between the 'h' values of two consecutive meshes - $r = h_{coarse}/h_{fine}$) must be greater than 1.3. In this specific case it results $r_{21} = h_2/h_1$ = 1.324 and $r_{32} = h_3/h_2$ = 1.525 respectively.

Tab. A.1 – Reference data and representative mesh size for each grid resolution

RESOLUTION	Size [Mcell]	Volume [mm^3]	Representative grid dimension [mm]
FINE #1	10.9	558790	0.372
MEDIUM #2	4.7	558472	0.493
COARSE #3	1.3	558081	0.751

Once the grid resolutions were chosen, CFD simulations at fixed point and in equal admission were perfomed to determine the values of key variables for the twin entry turbine under investigation. However, before calculating discretization errors, it is essential to ensure that the convergence of the calculation is achieved. The rule of thumb is to obtain a reduction of at least three orders of magnitude in the normalized residuals for each solved equation over the entire computational domain. It is important to remember that three different mesh resolutions are considered sufficient for the calculation of the observed order of the method if some of the values of the generic variable $'\varphi'$ predicted on the three grids are in the asymptotic region for the simulation series. The following images show the grid dependency for each performance parameter of the twin scroll volute examined:

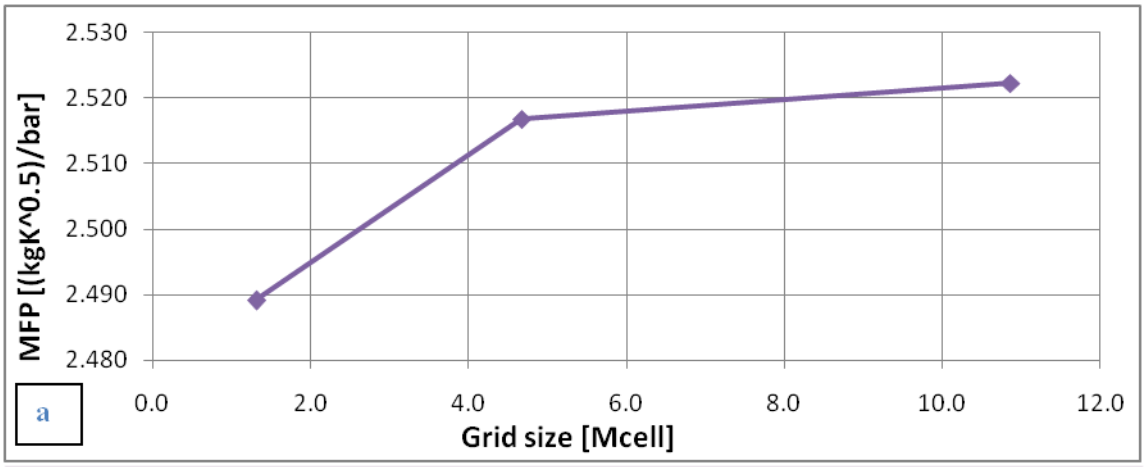

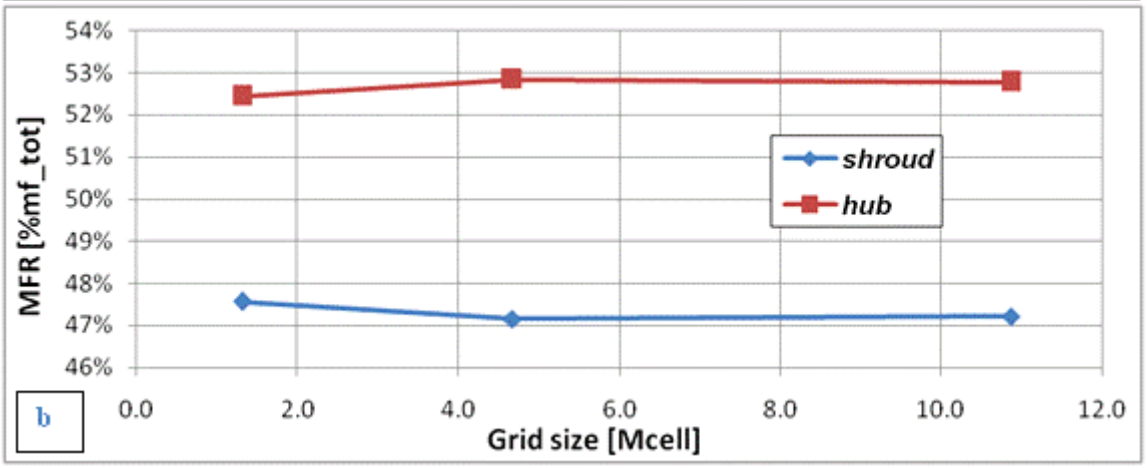

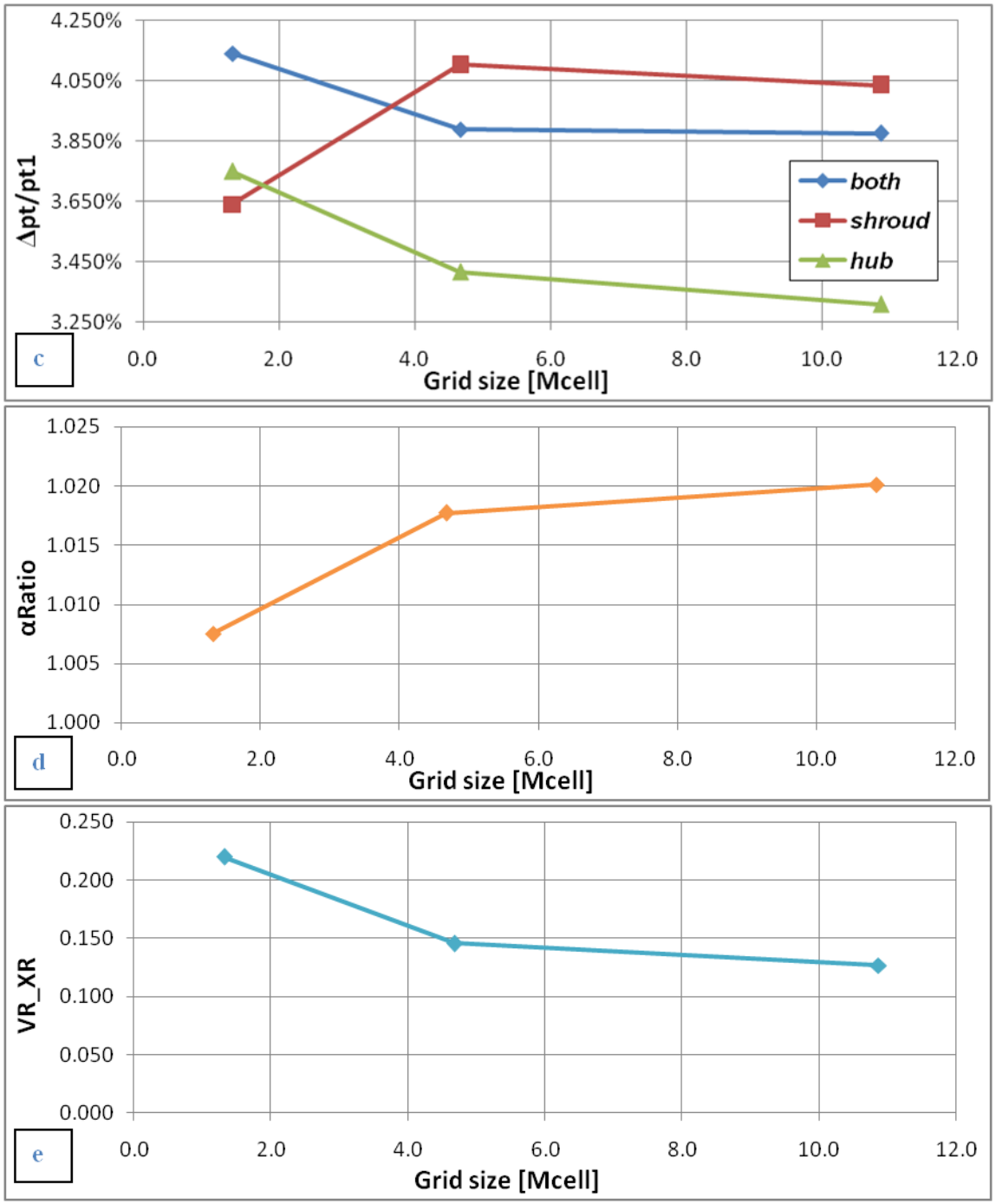

Fig. A.2 – Grid dependency for key twin scroll volute parameters: a) mass flow parameter, b) shroud and hub mass flow ratio, c) both, shroud and hub dimensionless total pressure drop, d) absolute flow angle ratio, e) axial to radial velocity ratio

Tab. A.2 shows the results of the five-step procedure (more details at section 2.4) applied to calculate the mesh-based uncertainty. For each performance parameter of the volute, the following quantities are collected:

- φ_1, φ_2, φ_3 are the values of the parameter whose uncertainty estimation has to be determined, obtained with fine, medium and coarse grid respectively;

- p is the apparent (or observed) order of the method, calculated through a fixed point iterative process;
- e_a^{21} and e_{ext}^{21} respectively represent the 'approximate' and 'estimated' extrapolated relative error in dimensionless form;
- φ_{ext}^{21} or 'extrapolated value' of the variable, that corresponds to the fine grid solution (φ_1) plus the estimated error;
- $GCI\ _{fine}^{21}$ i.e. the grid convergence index associated with the finest grid resolution. This value corresponds to two times the relative standard deviation.

Tab. A.2 – Results summary of the GCI procedure applied to various performance parameters of the twin entry volute

Var.	MFP	MFR_{sh}	MFR_{hub}	$\frac{\Delta p_{t\ both}}{p_{t1\ both}}$	$\frac{\Delta p_{t\ sh}}{p_{t1\ sh}}$	$\frac{\Delta p_{t\ hub}}{p_{t1\ hub}}$	$\alpha Ratio$	VR_{x-r}
φ_1	2.522	47.2%	52.8%	3.9%	4.0%	3.3%	1.0201	0.1269
φ_2	2.517	47.2%	52.8%	3.9%	4.1%	3.4%	1.0177	0.1456
φ_3	2.489	47.6%	52.4%	4.1%	3.6%	3.7%	1.0075	0.2197
p	3.30	4.84	4.92	6.86	4.80	2.02	2.86	2.67
φ_{ext}^{21}	2.526	47.24%	52.76%	3.874%	4.011%	3.166%	1.0221	0.1102
e_a^{21}	0.22%	0.12%	0.11%	0.33%	1.68%	3.25%	0.24%	14.75%
e_{ext}^{21}	0.14%	0.04%	0.04%	0.06%	0.59%	4.46%	0.19%	15.17%
$GCI\ _{fine}^{21}$	0.18%	0.05%	0.04%	0.07%	0.74%	5.34%	0.24%	16.46%

The final results of the GCI method are shown in Tab. A.3 which reports each of the key variables of the simulated twin entry volute with a value ('f' - relative to the finest grid) and the corresponding 'numerical' uncertainty deriving from the mesh resolution. Within these intervals there is a 95% probability of finding the true value 'f_t' of each performance parameter.

Tab. A.3 – 95% probability intervals for each twin scroll volute performance parameter

PARAMETER	FINEST GRID VALUE (f)	±	$U_{95\%}$ (2σ)
MFP	2.522	±	0.005
MFR_{sh}	47.22%	±	0.03%
MFR_{hub}	52.78%	±	0.02%
$\Delta p_{t\ both}/p_{t1\ both}$	3.876%	±	0.003%
$\Delta p_{t\ sh}/p_{t1\ sh}$	4.035%	±	0.030%
$\Delta p_{t\ hub}/p_{t1\ hub}$	3.308%	±	0.176%
$\alpha Ratio$	1.020	±	0.002
VR_{x-r}	0.127	±	0.021

The results shown in Tab. A.2 and A.3 lead to the conclusion that a single parameter has rather large margins of uncertainty in relation to its value, i.e. the axial to radial velocity ratio (VR_{x-r}), which quantifies how much the exhaust gas direction at rotor inlet is different from the ideal case of purely radial flow. This outcome is not surprising because the flow axial velocity at the rotor-stator interface is very low in equal admission, consequently the velocity ratio assumes values close to zero and this tends to amplify the effect of the uncertainty deriving from the grid.

As a general conclusion of this appendix, good practice in computational fluid dynamics should include the evaluation of the grid spacing impact on global parameters, followed by model assessment and uncertainty quantification.